Laser spectroscopy for coherent manipulation and state-specific probing of atoms and molecules

Georgi Dobrev

N° d'ordre NNT : 2016LYSE1083

THÈSE DE DOCTORAT DE L'UNIVERSITÉ DE LYON

opérée au sein de

l'Université Claude Bernard Lyon 1

École Doctorale ED52
Physique et Astrophysique de Lyon

Spécialité de doctorat : Physique
Discipline : Spectrométrie Physique

et préparée en co-tutelle avec

Université St Kliment d'Ohrid, Sofia

Soutenue publiquement le 28/06/2016, par :

Georgi DOBREV

Laser spectroscopy for coherent manipulation and state-specific probing of atoms and molecules

---

Devant le jury composé de :

M. IVANOV Petar, Associate Professor, Sofia University	Examinateur
M. TOKARYK Dennis, Professeur, University of New Brunswick	Rapporteur
M. BLAGOEV Kiril, Professeur, Bulgarian Academy of Sciences	Rapporteur
Mme ROSS Amanda, Directrice de Recherche CNRS, Université Lyon 1	Examinatrice
M. YU Jin, Professeur, Université Lyon 1	Examinateur
M. PASHOV Asen, Professeur, Sofia University	Directeur de thèse
M. CROZET Patrick, Chargé de Recherche CNRS, Université Lyon 1	Co-directeur de thèse

UNIVERSITE CLAUDE BERNARD - LYON 1

Président de l'Université	**M. le Professeur Frédéric FLEURY**
Président du Conseil Académique	M. le Professeur Hamda BEN HADID
Vice-président du Conseil d'Administration	M. le Professeur Didier REVEL
Vice-président du Conseil Formation et Vie Universitaire	M. le Professeur Philippe CHEVALIER
Vice-président de la Commission Recherche	M. Fabrice VALLÉE
Directeur Général des Services	M. Alain HELLEU

COMPOSANTES SANTE

Faculté de Médecine Lyon Est – Claude Bernard	Directeur : M. le Professeur J. ETIENNE
Faculté de Médecine et de Maïeutique Lyon Sud – Charles Mérieux	Directeur : Mme la Professeure C. BURILLON
Faculté d'Odontologie	Directeur : M. le Professeur D. BOURGEOIS
Institut des Sciences Pharmaceutiques et Biologiques	Directeur : Mme la Professeure C. VINCIGUERRA
Institut des Sciences et Techniques de la Réadaptation	Directeur : M. le Professeur Y. MATILLON
Département de formation et Centre de Recherche en Biologie Humaine	Directeur : Mme la Professeure A-M. SCHOTT

COMPOSANTES ET DEPARTEMENTS DE SCIENCES ET TECHNOLOGIE

Faculté des Sciences et Technologies	Directeur : M. F. DE MARCHI
Département Biologie	Directeur : M. le Professeur F. THEVENARD
Département Chimie Biochimie	Directeur : Mme C. FELIX
Département GEP	Directeur : M. Hassan HAMMOURI
Département Informatique	Directeur : M. le Professeur S. AKKOUCHE
Département Mathématiques	Directeur : M. le Professeur G. TOMANOV
Département Mécanique	Directeur : M. le Professeur H. BEN HADID
Département Physique	Directeur : M. le Professeur J-C PLENET
UFR Sciences et Techniques des Activités Physiques et Sportives	Directeur : M. Y.VANPOULLE
Observatoire des Sciences de l'Univers de Lyon	Directeur : M. B. GUIDERDONI
Polytech Lyon	Directeur : M. le Professeur E.PERRIN
Ecole Supérieure de Chimie Physique Electronique	Directeur : M. G. PIGNAULT
Institut Universitaire de Technologie de Lyon 1	Directeur : M. le Professeur C. VITON
Ecole Supérieure du Professorat et de l'Education	Directeur : M. le Professeur A. MOUGNIOTTE
Institut de Science Financière et d'Assurances	Directeur : M. N. LEBOISNE

Софийски университет “Св. Климент Охридски”

ДИСЕРТАЦИЯ

за присъждане на
образователна и научна степен “доктор”

Научно направление: 4.1 Физически науки
Физика на атомите и молекулите

изготвена под двойно научно ръководство
в сътрудничество с
Université Claude Bernard Lyon 1

Георги Симеонов Добрев

Приложения на лазерната спектроскопия за кохерентно манипулиране и изследване на избрани състояния на атоми и молекули

Научни ръководители :
проф. дфзн Асен Пашов
Dr. Patrick Crozet

София, 2016 г.

Résume

Cette thèse, préparée en co-tutelle entre Université Lyon 1 et Université de Sofia St Kliment d'Ohrid, se concentre sur la réalisation expérimentale du contrôle strict de l'état quantique d'atomes et de molécules, appliqué à divers domaines scientifiques tels que l'informatique quantique, la métrologie et l'astrophysique. La première partie de la thèse vise à établir des techniques robustes qui garantiront une grande fidélité pour préparer l'état d'un système quantique particulier. La première étape vers le contrôle cohérent passe, bien sûr, par la conception soignée d'un environnement et par le bon choix d'un système où l'influence des processus de décohérence est limitée. Nous présentons la construction et le développement d'un dispositif à jet atomique de calcium. La conception d'une source laser pour sonder les atomes dans le faisceau atomique est ensuite décrite. La génération avec succès du jet atomique de Ca et sa détection par fluorescence induite par laser ont permis de valider le système d'analyse des schémas d'excitation visant au transfert de population avec une probabilité proche de 100%.

La deuxième partie de la thèse décrit les progrès récents dans l'amélioration de la stabilité de la fréquence relative d'une horloge à fontaine d'atomes de césium. Dans un régime de fonctionnement limité par le bruit quantique de projection, la stabilité à court terme de la fontaine est déterminée par le nombre d'atomes qui participent au cycle d'interrogation de Ramsey. Un piège magnéto-optique tridimensionnel modifié est utilisé pour fournir un faisceau intense d'atomes lents qui à son tour renforce la densité d'atomes chargés dans la mélasse optique de l'horloge atomique. Nous démontrons aussi une technique élégante pour manipuler l'état quantique des atomes de césium dans le faisceau de particules qui permet un contrôle précis de leur vitesse. Cette vitesse se révèle être le paramètre le plus important qui régit le chargement efficace des mélasses optiques. Cette efficacité accrue augmente le rapport signal sur bruit de la mesure de fréquence de la transition d'horloge. Ce faisceau lent fait partie intégrante du dispositif standard primaire de fréquence CSF2, basé à l'Institut national de métrologie allemand (PTB) à Braunsweig , qui contribue aux échelles de temps internationales UTC et TAI, comme l'horloge la plus stable dans le monde.

La troisième partie de la thèse est consacrée à des mesures de fréquence de précision afin de déterminer des constantes magnétiques (facteurs Landé) de molécules hydrure métalliques. En tant que première étape, la conception et la mise au point d'une nouvelle source de pulvérisation cathodique à décharge pour une production efficace de ces molécules est décrite. Les exigences de la source sont de maintenir une répartition homogène des molécules dans le milieu de la décharge, et de fournir une longueur d'absorption bien définie. Le fonctionnement à long terme de la source est demontré par des mesures d'absorption différentielle par laser sur NiH en phase vapeur, en champ nul puis en présence d'un champ magnétique. Par ailleurs, la technique de spectroscopie cw-CRDS est appliquée sur ces radicaux faiblement absorbant, et les co-

efficients d'absorption des bandes rouges de cette espèce sont ainsi mesurés. Dans une autre source à pulvérisation cathodique d'une conception différente, la spectrométrie Zeeman sur les bandes de FeH dans le proche infrarouge est réalisée. Cette dernière molécule est une sonde du champ magnétique dans les étoiles froides.

Abstract

This thesis, prepared in co-tutelle between Universté Lyon 1 and Sofia University St. Kliment Ohridski, focuses on experimental realization of techniques which provide strict control of the quantum state of atoms and molecules with application in various scientific areas such as quantum computing, metrology and astrophysics.

The first part of the thesis aims to demonstrate robust techniques which provide high fidelity in the state preparation of a particular quantum system. The first step towards coherent control is, of course, careful design of an environment and a proper choice of a system where the influence of decoherence processes is limited. We present the construction and development of an atomic beam apparatus operating with calcium. In addition the design of a laser source for probing the atoms in the beam is described. The successful formation of an atomic beam and subsequent detection of laser-induced signal from Ca allowed for the feasibility of the system to be analyzed in a view of accommodation of excitation schemes for population transfer with probability close to 100%.

The second part of the thesis describes recent advances in improvement of the relative frequency stability of a Cs fountain clock. In a quantum-projection noise-limited regime of operation the fountain short-term stability is determined by the number of atoms which take part in the Ramsey interrogation cycle. A modified three-dimensional magneto-optical trap is used to provide an intense beam of slow atoms which in turn boosts the number of atoms loaded in the optical molasses of the fountain clock. We also demonstrate an elegant technique for manipulation of the quantum state of the caesium atoms in the particle beam which provides precise control over the velocity of the atoms. The latter turns to be the most crucial parameter which governs the efficient loading of the optical molasses. As a result of the enhanced loading the obtainable signal-to-noise ratio of the measured frequency of the clock transition is increased more than 6 times. With the slow beam on board the primary frequency standard CSF2, based at the German National Metrology Institute (PTB) in Braunsweig, continues to contribute to the international time scales UTC and TAI now as the most stable clock in the world.

The third part of the thesis is devoted to precision frequency measurements and determination of magnetic constants (Landé factors) of metal-hydride molecules. As a first step the design and the development of a new discharge sputtering source for efficient production these molecules is described. The demands to the source are to sustain a homogeneous distribution of the molecules within the discharge medium, and thus to provide a well defined absorption length. The long-term operation of the source is demonstrated in differential laser absoption experiments with NiH molecules, both in the presence of a magnetic fiefd and in zero field. Furthermore, in another discharge sputtering source of a different design, a cavity-enhanced technique is applied on weakly absorbing NiH molecules, to establish absorption coefficients for the red

bands of NiH. Also Zeeman spectroscopy on the near-IR band of FeH is performed by LIF spectroscopy. The latter molecule being targeted as a molecular probe of magnetic field in cool stars.

Абстракт

Настоящата дисертация, която е изготвена под двойно научно ръководство в сътрудничество между Софийски университет "Св. Климент Охридски" и университета "Клод Бернар" в гр. Лион, Франция, се фокусира върху реализирането на експериментални техники, които осигуряват прецизен контрол върху квантовото състояние на атомни и молекулни системи, с евентуални приложения в разнообразни области на науката като квантовите компютри, метрологията и астрофизиката.

Основната задача, описана в първата част на дисертацията, има за цел да бъдат демонстрирани техники, които предлагат устойчивост и високо ниво на достоверност при приготвянето на квантова система в отнапред зададено състояние, например чрез композитни импулси. Първата и най-важна стъпка към успешната реализация на техниките за кохерентен контрол е, разбира се, създаването на подходяща среда и правилния избор на квантова система, където влиянието на процеси, водещи до разрушаване на кохерентността на системата, е силно ограничено. В тази връзка, тук е представено проектирането и конструирането на експериментална апаратура за получаване на сноп от калциеви атоми. Също така е описано разработването на пълна система, диоден лазер и необходимите електронни устройства за неговата работа, използван за спектроскопия на атомите в снопа. Демонстрирано е успешното получаване на сноп от ^{40}Ca атоми и са представени спектри от лазерно–индуцирана флуоресценция на атомите в снопа. Това позволи да бъде направен подробен анализ на възможността, за в бъдеще, в изградената системата да бъдат приложени техники за възбуждане на атомите, които се характеризират с изключително висока вероятност за преход, която е близо до 100%.

Втората част на тази дисертация представя последните експериментални достижения за подобряване на относителната честотна стабилност на цезиев фонтанен часовник. При определени условия,когато честотният еталон работи в режим, при който стабилността на фонтана е ограничена единствено от квантовия шум на честотното измерване, може да се покаже, че кратковременната стабилност на този еталон се определя и зависи само от броя атоми, които участват в цикъла на Рамзи. Увеличен е броят атоми, зареждани в оптичната меласа на фонтана, чрез използване на сноп от бавни ^{1}33Cs атоми, който се генерира от модифициран магнито-оптичен капан. Демонстрирана е интересна техника за манипулиране на квантовото състояние на атомите в снопа, предоставяйки прецизен контрол върху скоростта на атомите. Последната се оказва най-важния параметър, от който зависи ефективността на процеса на зареждане на оптичната меласа. В резултат на нарастването на броя атоми, участващи в цикъла на фонтана, е постигнато увеличение на съотношението сигнал към шум на измерването на честотата на часовниковия преход над 6 пъти. С така изградената

апаратура на бавния сноп, първичния честотен еталон CSF2, разположен в метрологичния институт PTB в гр. Брауншвайг, Германия, продължава да допринася с измервания за съставянето на международните времеви скали TAI и UTC , но вече като един от най-стабилните микровълнови честотни еталони в света.

Последната, трета, част на тази дисертация е посветена на прецизно измерване на честоти на преходи и определянето на магнитни константи (фактори на Ланде) на молекули на метални хидриди. Тези молекули са от интерес в астрофизиката, тъй като наличието им в атмосферата на студени звезди и слънчеви петна позволява те да бъдат използвани като дистанционни локални проби на магнитни полета в тези звездни обекти. Първоначално е описано разработването на нов вид газоразряден източник за получаване на тези молекули с висока ефективност. Изискванията към такъв тип източник са той да осигурява хомогенно разпределение на молекулите в обема на разряда, което от своя страна предоставя добре дефинирана дължина на поглъщане в средата. Експериментално е демонстрирана стабилността на източника при продължителна работа на разряда и са измерени спектри на диференциално поглъщане на молекули NiH, както при отсъствие, така и при наличие на магнитно поле. В друг тип газоразряден източник, чрез прилагане на свръхчувствителна техника за измерване на поглъщане, са определени коефициенти на поглъщане за състояния от червената ивица на молекулата NiH. Също така е представен експеримент, където са регистрирани инфрачервени Зееманови спектри на молекулата FeH, откъдето са определени фактори на Ланде за голям брой ротационно-вибрационни състояния.

Acknowledgments

This thesis started to lay down roots when I was a bachelor student at Sofia University. I met my thesis supervisor, *Prof. Asen Pashov*, for the first time in the second year of my undergraduate studies. A year later, in 2008, I joined his team at the Optics and Spectroscopy Department, when I received my first assignment: to build electronic drivers for diode lasers. I was fascinated by his enthusiasm in teaching and also by the clever manner in which he explains quite complicated physical phenomena so that it is impossible to misunderstand them. There are countless positive experiences gained through our collaboration and friendship over the last eight years. Starting from the full renovation and equipping of three new laboratories, through the successful completion of my BSc and MSc degrees and the realization of several research projects leading to the many exciting trips around Europe. His presence in my life has been essential and it has had a great impact on my growth as an individual, at both professional and personal levels. His contacts has also opened many doors for me, allowing me to meet and to work with many more magnificent people, amongst them, my co-supervisor, *Dr. Patrick Crozet* from Lyon 1 University.

Dr. Patrick Crozet is another person who is extremely passionate about his profession. His profound knowledge in physics and our insightful discussions about our research have been a constant source of inspiration in finding solutions for the many problems that arose in the MH experiment. His great sense of humour has made for a wonderful work environment. He has taught me a lot about different experimental techniques, alignment and adjustment of dye lasers and Ti:Sapphire lasers and I was lucky to get first-hand practical advice from him. He really knows every single detail of his equipment and how it works. My stay in his lab was a fascinating experience.

I would like to express my deepest gratitude to both, *Asen* and *Patrick*, for their excellent guidance, patience, care and personal dedication. I feel very fortunate to have them as my mentors and meanwhile I was able to gain an immerse amount of knowledge from them.

Dr. Amanda Ross also deserves a special mention. I cannot express my gratitude to her enough, first for encouraging me to apply for the Eiffel scholarship, and later for arranging my stay in Lyon. She provided invaluable help with the daunting "administration française", within the department and in life outside the university. Besides all her duties as a group leader, she has always been there for me. She made my stay in France a truly pleasant experience and I've never felt lonely there. I have always enjoyed our talks, not only about physics, and I appreciate the side effect of significant improvement in my English language skills!

My sincere thanks also go to *Prof. Kiril Blagoev* for his support over the years. For his idea to build the Magneto-optical trap (the first great project in which I was involved) and for his assistance with the preparation of my six-months visit to PTB in

Germany. There, I had the great pleasure to participate in the world-scale research. I would like to express my gratitude to *Dr. Ekkehard Peik* and *Dr. Stefan Weyers* for the opportunity they have given to me and, of course, to *Dr. Vladislav Gerginov* who initiated this collaboration, patiently introduced me to the field of metrology, and shared with me the secrets of timekeeping. They have shown a great deal of trust and supported me throughout the work on the Cs clock project.

Among the other colleagues at PTB I would like to thank *Dr. Nils Huntemann* and *Dr. Christian Sanner* for providing the cavity - stabilized laser, and *Burghard Lipphardt* for making the frequency comb available during the measurements of the CSF2 clock stability. I owe a dept of gratitude to *Dr. Maksim Okhapkin* for his valuable tips when I was designing the servo loop electronics for frequency stabilization of the lasers in the LVIS experiment. Thanks also go to *Michael Kazda* for his responsiveness and cooperation.

Special thanks are due to *Dr. Jérome Morville* and *Prof. Dennis Tokaryk* for their expertise and precious advice on the CRDS experiment. I am also very grateful to *Prof. Alexander Blagoev* and *Assoc. Prof. Stanislav Balouchev* for supporting me during my study at Sofia University by providing a considerable financial aid. I give many thanks to *Assoc. Prof. Alexander Gritzkov* for giving me the oil diffusion pump which became a vital element of the Ca beam experiment. I'd like to express particular thanks to *Nikolay Markov* for being a very approachable and kind person, especially for his assistance for machining of the two Ca ovens.

I would like to thank the members of my scientific committee for their insightful reading of the manuscript and for their constructive criticism and comments.

This thesis would not have been possible without the support from my nearest colleagues at Sofia University. Amongst them, I particularly wish to thank *Ivo Temelkov* for being a great labmate and friend. A special mention goes to *Ivayla Bozhinova* for her support and helpful discussions on the MH experiment and *Snejana Iordanova* for always giving me great advice in the crucial moments when I was stuck with the Mathematica program.

Finally, my warmest and heartfelt thanks are to my family. *Mom* and *Dad*, even though it was hard to be away from you, I always felt your unconditional love and care. *Zori*: you rose to meet the challenge of making many changes to come with me to Germany: thank you! It is hard to express how much I appreciate all the sacrifices you have made, always standing by me and supplying encouragement in the difficult moments. Enjoying a wonderful life with you, I'm looking forward to many more happy and exciting years together!

Financial Support

Parts of my study were initiated within the framework of several research programs which provided partial funding for my work. Here I would like to acknowledge:

Bulgarian Ministry of Education and Science - the Bulgaria-France "RILA" exchange program (project No. 01/07/2014)

French Government - "Mobility of young researchers" and "Eiffel Excellence Scholarship" programs;

ESF - HRD OP (grant BG051PO001-3.3.06-0057);

EURAMET - EMRP (projects No. SIB04 and No. SIB55);

Georgi Dobrev
Sofia, 28.06.2016

Contents

General introduction

This thesis is devoted to the experimental investigation of quantum systems, in a context where coherent manipulation of the internal states of the system is essential.

Quantum coherence describes a state of matter where an ensemble of wavefunctions are in phase with one another, spatially and temporally. It can also be considered broadly as a result of the evolution of the state of a quantum system, free from random perturbations. Coherence, evolution and state superpositions are at the heart of the quantum mechanical description of our world at a microscopic level.

Coherence is a fundamental property of the matter, but its manifestation is usually washed out due to statistical averaging of random interactions between a system and its environment. A real breakthrough in the experimental physics was the invention of the lasers – a source of coherent radiation, which brought to the world the holography, optical communications, frequency metrology and many others. Another great achievement was the realization of a Bose-Einstein condensate (BEC) and the atom laser – a coherent state of the macroscopic matter. Coherence is also one of the fundamental requirements for quantum computing, quantum cryptography and quantum simulations.

In the first part of the thesis the preparation of the experimental setup for coherent manipulation of Ca atoms by composite pulses [A11, A12, A13] is presented. The setup consists of highly collimated atomic beam and frequency stabilized laser system. The atomic beam is selected as a nearly collision–free source of transversely cold Ca ground state ^{1}S atoms. The main idea is to arrange a set of laser beams with controlled phases which cross a highly collimated atomic beam. These beams will be seen by the atoms as a chain of pulses. By special choices of the pulse phases (Electro-optical modulators (EOM) will be used), it should be possible to demonstrate a high probability for excitation of the atoms to their ^{3}P state which is insensitive to variation of laser frequency and intensity in a broad range.

In Chapter 2 the construction of the beam machine is described with the special attention on the design of the Ca ovens and the light detection system. Successful operation of the beam was demonstrated by observation of the intercombination line in ^{40}Ca ^{1}S–^{3}P. The work on this experiment was suspended due to the financial

collapse of the Bulgarian Science Foundation in the period 2010-2012.

In the second part, the performance of a caesium fountain atomic clock has been improved by loading its optical molasses from an intensive beam of cold Cs atoms in a well defined hyperfine state. The atomic beam is produced by a modified magneto-optical trap (MOT) [1], attached to the fountain apparatus. One of the cooling laser beams is retroreflected from a pierced mirror, which leads to an unbalanced cooling force along the corresponding trap axis. This forms a beam of slow atoms that are extracted from the MOT and accelerated towards the optical molasses zone. In this way the number of atoms taking part in the Ramsey cycle of the clock was increased by more than an order of magnitude. The resulting relative frequency stability was estimated to be σ_y (1s) $= 2.7 \times 10^{-14}$ which is limited by the quantum projection noise.

A detailed report on the experimental efforts and the achieved results can be found in chapter 7 of this thesis. A crucial point for this work was to understand the dynamics of the evolution of the atomic state during the interaction with the cooling lasers and the magnetic field and to asses the possible channels of losses, which compromise the loading efficiency of the optical molasses. With this knowledge, an additional pump laser was added to the usual set of cooling and repumping beams in the trap. The pump laser is used to manipulate the atoms that are extracted from the trap. The beam atoms are prepared in a "dark" state, which prevents them from undergoing further acceleration. By careful adjustment of the parameters of the atom – pump laser interaction, it is possible to achieve optimal transfer of the atoms from the MOT to the optical molasses of the fountain clock.

The third part is devoted to extensive study of the Zeeman effect in the FeH molecule. Metal hydrides are observed in the sunspots and in the spectra of cool stars. Due to their strong response to external magnetic fields they, and especially FeH, have been noted as possible probes of magnetic field, particularly for cool stellar objects. For the practical realization of this idea, however, reliable laboratory data are needed covering transitions frequencies, line strengths and effective g factors for every rovibrational level – without them it is impossible to simulate the stellar spectra, which are observed at temperatures, which are very difficult to achieve in Laboratory conditions. Another reason for the need of experimental data is the complicated electronic structure of these molecules which makes the theoretical predictions unreliable.

The experimental study of FeH is presented in Chapter 12. The first experimental challenge was to build a source for laboratory production of FeH. In principle, for determination of the line strength, the source should provide a column of FeH molecules with well defined length and density. For the Zeeman studies the source should be able to accommodate homogeneous magnetic fields along the absorption length. The interaction zone with the laser should be free from emission (in the case of a gas discharge source) to allow laser-induced fluorescence measurements. Several sources are described in Chapter 11 together with the possible areas of their application. It turns out to be difficult to built a universal source, suitable for all types of experiments.

This thesis concentrates on the interaction of FeH in the excited $F^4\Delta_{5/2,7/2}$ elec-

tronic states with magnetic fields. The experiment consisted in a zero magnetic field measurements of the absorption lines in the F-X $(7/2 - 7/2)$ and $(5/2 - 5/2)$ band for a variety of rotational quantum numbers, followed by repeated records in variable magnetic fields up to 5000 G. The splitting of the molecular lines was modelled within the framework of the linear Zeeman effect and effective g-factors have been fitted for more than 30 rovibrational levels of the F state. The experimental results and the comprehensive analysis are presented in Chapter 12.

The data on the g-factors are essential for interpretation of stellar spectra. But for the F-X band in FeH, experimental line-strengths are also missing. The experiments in magnetic field were performed in a hollow-cathode source which is nicely suited for this, but lines strength measurements are difficult due to the badly defined absorption length. So, a part of this thesis, chapter 11, is devoted to construction of a gas-discharge source for MH, suitable for absorption measurements.

First attempts to increase the sensitivity of the existing experimental set up have also been carried out within this study. It is necessary for transitions involving high J levels, which dominate the stellar spectra, but have very low thermal populations at the present working temperatures. The new set-up (chapter 14) is based on cavity ring-down spectroscopy in a high finesse cavity built around the MH source. The set up was successfully tested with NiH.

Part I

Coherent manipulation of Ca atoms

Chapter 1

Introduction

The achievement of coherent time evolution of a quantum system turns out to be more challenging even than the creation and manipulation of a Bose-Einstein condensate. The main obstacle is the decoherence, which occurs due to the coupling of the quantum system with the external world – through spontaneous emission, atom-atom collisions, interactions with unwanted external fields, random fluctuations of the control fields, etc. The efforts of physicists during the last decades to overcome these obstacles resulted in brilliant experimental techniques such as the atom interferometer [A1], photon and spin echo [A2, A3], optical orientation and alignment [A4], adiabatic passage [A5], electromagnetically induced transparency [A6] etc. These techniques revolutionized our understanding of the world ("action at a distance" and Einstein–Podolsky–Rosen entanglement [A7]), the precision spectroscopy (Ramsey method of oscillatory fields [A8]), time and frequency metrology (atomic clocks and time-resolved dynamics of atomic systems [A8]), atom interferometry (atom gravimeters and gyroscopes [A9]), and the studies of cold atom and molecule interactions [A10]. One of the fields where a myriad of applications is expected is that of quantum information processing. Although numerous experimental setups have been built and the concepts have been proven in systems with two or more qubits, there are many remaining experimental challenges and theoretical ideas still in need of their experimental verification and further development.

The algorithms of quantum computing are based on a set of several quantum systems (atoms, molecules etc.) which interact with each other in a controlled way. The main challenges here are (i) to overcome the processes leading to decoherence in the systems, (ii) to achieve very a high fidelity in preparation of given quantum state and (iii) to enable a robust local addressing of a particular quantum system [A11, A12].

There is a variety of proposals how to face these challenges. The decoherence is reduced mainly by appropriate choices of quantum systems and decoherence-free environments. Some of the experiments are performed with chains of trapped ions, quantum dots in solid states, cold atoms in optical lattices, entangled photons etc. [A13]. Careful design of the manipulation schemes of quantum states can also reduce

the decoherence effects (for example by avoiding short living states) [A14].

The success with the high fidelity and local addressing, however is not as significant as that with the decoherence. It has been demonstrated that with an appropriate error correction algorithm, one needs to reduce the error below 10^{-4} to carry out quantum computation [A15]. The local addressing is more successful in isolated systems (trapped ions) than in solid state systems (quantum dots), at the cost of highly complicated experimental setup. Even in a well-designed system such as trapped atoms or ions experiments, the fluctuations of the light intensity, the thermal and trap motion of the atoms, or finite lifetime may affect the achieved fidelity of the state preparation. The problems with the local addressing are connected with the tight confinement (which in turn is necessary due to the weak atom-atom interactions), or due to the type of quantum system used (solid state systems, for example).

Recently, new proposals appeared in the literature [A16, A17, A18] which, in our opinion, have the potential to lead to a significant progress in the coherent manipulation of quantum systems by light fields. They are based on the so called composite pulses. The essence of these proposals from Vitanov and co–workers [A16] is to illuminate a two–level quantum system with a series of light pulses with the same frequency and intensity, but with different phases. By proper fixing of these phases, the authors have shown that the probability for exciting the system can be arbitrarily close to 1 and can be very insensitive to modest shifts in the light intensity and frequency (due to the Doppler effect for example). Moreover, in a follow–up paper [A18] the same group has proposed an application of these ideas to a technique for selective addressing of atoms in a lattice with tight confinement. These ideas, when realized in practice, can lead to a practical, robust quantum computing system with fidelity good enough to implement error correction algorithms.

It is believed that the manipulation of quantum systems with composite pulses has a great potential to fulfil the conditions for a high fidelity and a local addressing. There is a large number of possibilities to combine the composite pulses excitation with existing resonance and adiabatic techniques [A17], thus extending enormously the range of possible applications not only in the field of quantum computing, but also in laser cooling, precision spectroscopy and metrology. Therefore there is a chance to realize a real breakthrough in the field of coherent manipulation of quantum systems.

This part of the thesis addresses the hurdle of high fidelity in the coherent manipulation of atoms, and as a first step we planned to validate the techniques suggested by the theoreticians for coherent manipulation [A16, A17, A18].

The experiments for coherent manipulation should be carried out in a system with as few decoherence processes as possible. This means (i) environment with few or no collisions and external fields and (ii) operation with states with long life times (to reduce the influence of the spontaneous decay). In order to decrease the coupling of the quantum system with the environment the experiments may be carried out in an atomic/molecular beam and in a magneto-optical-, ion- or dipole trap. These two experimental setups offer different experimental conditions and are to some extent complementary. The beams are easier to construct, the signals are in general stronger

(more particles), it is easy to change the species under study, in many cases there are less collisions than in a trap. The atomic traps, however, offer lower temperatures (reduction of the Doppler shift) and longer interaction times.

The contribution described here is leading to an experimental validation of the concept of composite pulses in a calcium atomic beam. The zero electron and nuclear spin of ^{40}Ca (and some other alkaline earth atoms) lead to a simple electronic structure and make this atom very close to the ideal quantum system. Moreover it offers two types of electronic states: singlets and triplets. The lowest triplet state ^{3}P is metastable, with a very long lifetime which gives opportunities for long interaction times without spontaneous decay.

This part of the thesis describes the assembling of an atomic beam machine at the Sofia University, as a prelude to work with composite pulses. My task was to construct a fully operational atomic beam source and then to evaluate the linewidth of the spin-forbidden $4s\,^1S \rightarrow 4p\,^3P_1$ atomic transition, probing the effusive beam of Ca atoms produced in the source with a complete laser system (light source and driving electronics) which I also constructed. The observed linewidth of the atomic transition provides information about the divergence of the atomic beam and the linewidth of the laser itself, and that information will be used to optimize the experimental conditions for future work on quantum control.

Chapter 2

Experiment

The present experiment based on the technique from Ref. [A16] aims to reach two goals: (i) to realize the scheme for quantum control and (ii) to extend the proposed scheme in order to add more flexibility.

The experimental demonstration of the proposed technique for coherent manipulation in Ref. [A16] was planned to be done in an atomic beam with Ca atoms. The main idea is to arrange a set of laser beams with controlled phases which crosses a highly collimated atomic beam. These beams will be seen by the atoms as a chain of pulses. By special choices of the pulse phases (electro-optical modulators (EOM) will be used), it should be possible to demonstrate a high probability for excitation of the atoms to their $^3P_1$ state. In addition, by proper choice of phases a formation of a quantum state as a superposition of the ground ^1S and the ^3P state in Ca with arbitrary mixing coefficients should be possible.

2.1 The Calcium atom

Calcium, Ca, is an alkaline-earth element. It is placed in group II of the periodic table with atomic number $Z = 20$. The atomic structure of the alkaline-earth elements consists of filled inner shells and two electrons in the outermost s shell.

Similarly to the He atom, the two electrons cause the appearance of singlet and triplet states in the fine structure of the atom (see Fig.). The particularly used isotope ^{40}Ca has no nuclear spin and therefore there is no hyperfine structure.

At room temperature calcium is solid and has negligible vapour pressure. The melting point of Ca is $T_{\mathrm{mp}} = 842\,^{\circ}\mathrm{C}$ [A19, p. 4-126]. The following expression can be used for calculating the vapor pressure, P_{vp} in Pascal units, of calcium at a given temperature T, measured in units of Kelvin [A19, p. 4-134] (valid for temperatures below the melting point):

$$\log_{10} P_{\mathrm{vp}} = 15.133 - \frac{9517}{T} - 1.4030 \log_{10} T \,. \tag{2.1}$$

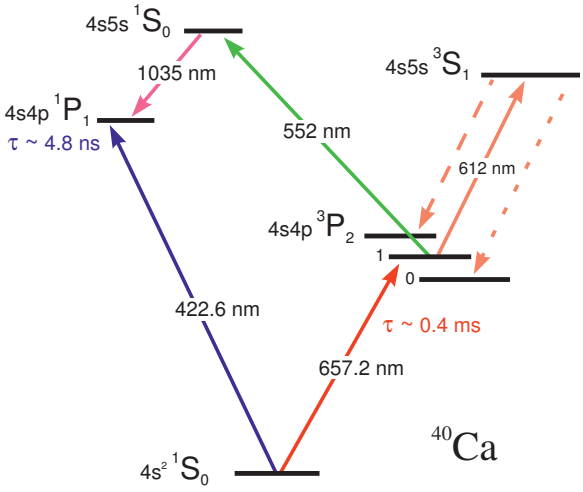

Figure 2.1 Part of the Grotrian diagram for ^{40}Ca.

2.2 Vacuum system

The vacuum system of the beam machine was constructed around two 6-way crosses with standard DN 160 CF flanges, made from stainless steel. Additionally, a gate valve was installed between them to separate the system in two chambers, as shown in Fig. 2.2. The calcium beam source was accommodated inside the first chamber, while the laser-atom interaction and subsequent measurement of the laser-induced fluorescence were intended to occur in the second chamber. The valve allowed the interaction chamber to be isolated when servicing of the oven was needed, for instance refilling with bulk calcium.

The calcium source was mounted on a blank flange which closes the vacuum system at the far end shown on the left-hand side of the drawing in Fig. 2.2. Furthermore, a thermocouple feedthrough was created on the same back end flange for control of the oven temperature. An additional electrical feedthrough was installed on the flange which closes the vertical arm of the source chamber from the top. It was used to connect the current supply wires for the heating elements in the oven assembly, as well as the leads of another thermocouple, which senses the temperature of the atomic source closer to the beam nozzle.

Usually in particle beam experiments the probing light is oriented orthogonally with respect to the beam path. This interaction scheme greatly reduces the Doppler broadening of the spectral lines. The line shape of a particular atomic transition appears broadened by the Doppler effect due to the residual velocity spread of the particles effusing from the oven. A rough estimate for the case of thermal distribution of calcium can be made as follows. At the temperature of the oven, about 600 °C, the mean velocity of the calcium atoms is $\langle v \rangle \approx 680\,\mathrm{m/s}$ which leads to Doppler broadening of the 657 nm line of about $\delta\nu_{\mathrm{FWHM}} = 1\,\mathrm{GHz}$ (full width at half maximum). It is enormous compared to the natural linewidth ($\delta\nu_{\mathrm{nat}} \approx 400\,\mathrm{Hz}$) for the transition

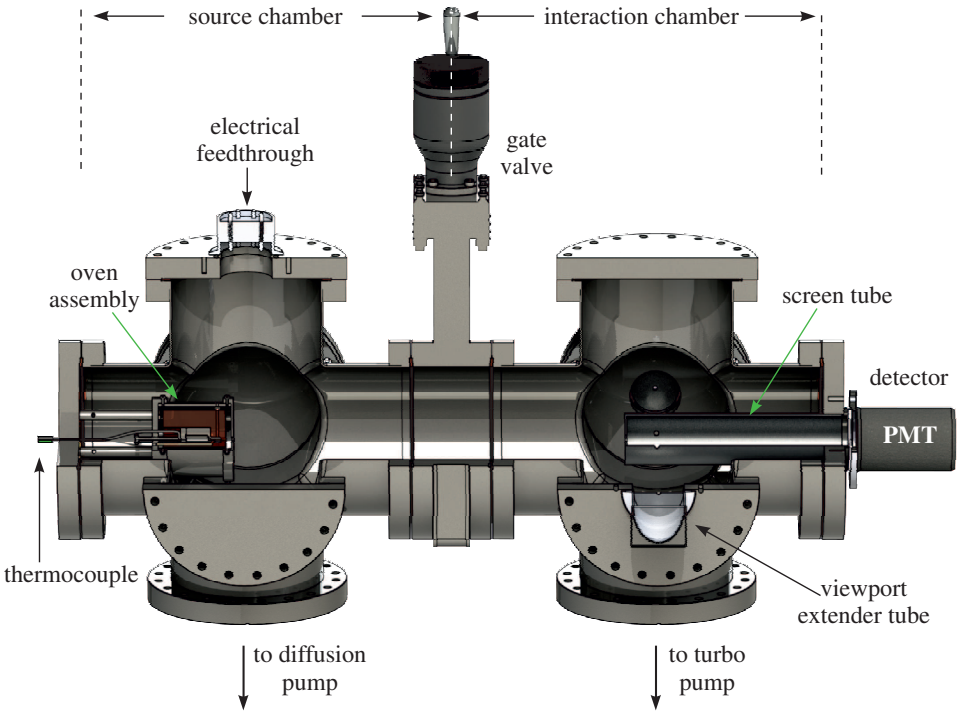

Figure 2.2 Side view of a model drawing of the vacuum chambers of the beam machine (vacuum pumps are omitted).

of interest, $4\,^1S_0 \rightarrow 4\,^3P_1$. In an atomic beam with a collimation ratio of 1:100 the residual Doppler width of the same transition is estimated to be about 10 MHz which is a significant reduction, although far above the natural linewidth.

In order to probe the atomic beam in the described configuration two of the closing flanges in the interaction chamber were equipped with viewports. Each of the viewports is a tube extender with internal diameter of ∅50 mm made of aluminum. A glass window at Brewster's angle was glued on one of the tube ends, while the other end was machined to a standard DN 50 KF vacuum flange so the extensions could be subsequently joined to the bored blank flanges in the horizontal arms of the interaction chamber.

The closing flange at the front end of the vacuum system, shown on the right-hand side of the drawing in Fig. 2.2, was also equipped with a viewport window. There, on the outside the interaction chamber the detector for collecting fluorescence light from the atoms was installed.

Blank flanges were used to terminate all of the remaining arms of the vacuum system except for the free ports at the bottom of both chambers which were used to install the pumps to evacuate the system.

The workhorse in our system is an oil vapour diffusion pump[1] which was connected to the source chamber. The pump has a diameter of the inlet port of 110 mm providing

[1]EDO 160 VEB Hochvakuum Dresden

considerable pumping speed. The pump was loaded with silicone pump fluid type DC704 (Dow Corning), suitable for high vacuum applications in the pressure range down to 10^{-10} mbar. In order to reduce the backstreaming of pump fluid into the vacuum system the pump was equipped with water-cooled baffle[1]. Additionally, a rotary vane pump was installed for baking the diffusion pump and to create the forevacuum in both chambers. A wide range manometer[2], which is a combination of Pirani gauge and Bayard-Alpert ion gauge and covers the range from 1×10^{3} to 1×10^{-10} mbar, was mounted above the diffusion pump, close to the first chamber.

Equivalently, at the same position in the interaction chamber was installed another pumping station[3]. It is a combination of membrane backing pump and turbomolecular pump[4] with diameter of the inlet port of 40 mm. The turbo pump was attached to the 6-way cross through a bored blank flange. Furthermore, along the connection line another Pirani type gauge[5] was installed.

After the whole vacuum system was assembled a flexible heating band was wound around the vacuum parts on the outside. Several days of simultaneously heating of the components, operating an empty oven while continuously evacuating with the pumps allowed outgassing of the metal parts. At the end, the combined gauge below the source chamber indicated a residual pressure of around 1.45×10^{-6} mbar.

2.3 Oven

Perhaps the most challenging part of building the hardware of the beam machine was the design of a reliable atomic vapor source. Two different constructions of an oven were developed and tested through the course of work. They are described in details in the following section.

Initially, the attractive idea to have a source of atoms which is attached to the outside of the main vacuum chamber was adopted, thus providing great flexibility when servicing of the oven was needed. In Fig. 2.3 a model cross section of our first attempt to design the oven is shown.

The body of the source was machined from a single cylindrical piece of stainless steel with length of about 137 mm. Inside the body, close to the back end, a reservoir for calcium with dimensions of $\varnothing 14 \times 41$mm was formed. Additionally, the front end of the reservoir was threaded and a cap, made of the same material, was used to close the container after filling it with bulk calcium. A channel with dimensions of $\varnothing 1 \times 14$mm was bored into the cap which served as an exit for the hot atoms. The heating was provided by six individual cartridge electrical heaters placed in a circumference around the material compartment on the back side of the main body and therefore they are at atmospheric pressure. Furthermore, a standard DN 40 KF

[1] FOW-A 160
[2] ATMION
[3] HiCube 80 Eco Pfeiffer Vacuum
[4] HiPace 80
[5] CVM211

flange was produced at the front end of the body in order to attach the oven to the back flange of the main vacuum chamber. The connection was sealed with an o-ring which required that the connection is kept at substantially lower temperature than the calcium reservoir. Finally the oven was covered with high-temperature insulating wool in order to reduce heat losses.

Unfortunately, along with all of its advantages in terms of easy operation and simple design, the oven did not function properly. It was not possible to achieve a continuous atomic beam from this source because clogging of the nozzle occurred (see the photos in Fig 2.4). When the clogging was encountered for the first time several attempts were made to ensure that the reservoir cap was always kept at the highest temperature compared to the rest of the oven body. However the problem was not fully resolved. Consequently a new oven was designed.

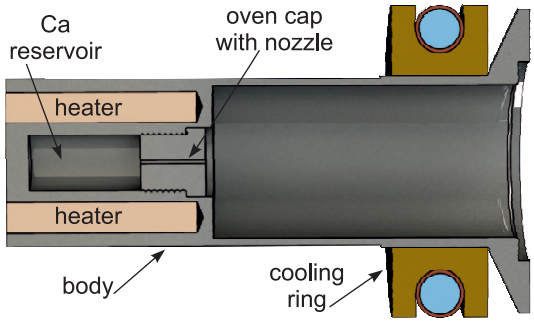

Figure 2.3 Cross section of a model drawing of the initial oven design. The body of the oven is machined from a single piece of stainless steel. The channel drilled in the cap, which closes the container with Ca, serves as an oven nozzle. The connection between the oven and the main vacuum chamber is further cooled with water to preserve the o-ring sealing from degradation due to the high temperature of the oven body.

(a) **(b)**

Figure 2.4 Photos of the oven cap showing a huge amount of calcium deposited on the nozzle – side view (a) and top view (b).

The second atomic beam source was a more sophisticated assembly than the first one and it was designed to be installed inside the main vacuum chamber. The construction is presented in Fig. 2.5.

The calcium reservoir consists of a body (1), where the material compartment (3) and the oven nozzle (4) were formed and a closing cap (2), both made out of stainless steel. Four M3 screws were used to secure the cap to the body together with a nickel seal in between. The outer diameter of the reservoir is 25 mm, which is reduced to ∅6 mm at the front end of the body. In this part a central channel with dimensions of ∅1 × 10mm was produced to create the oven nozzle. Usually calcium comes in a form of pellets and it is loaded in the material compartment, which has dimensions of

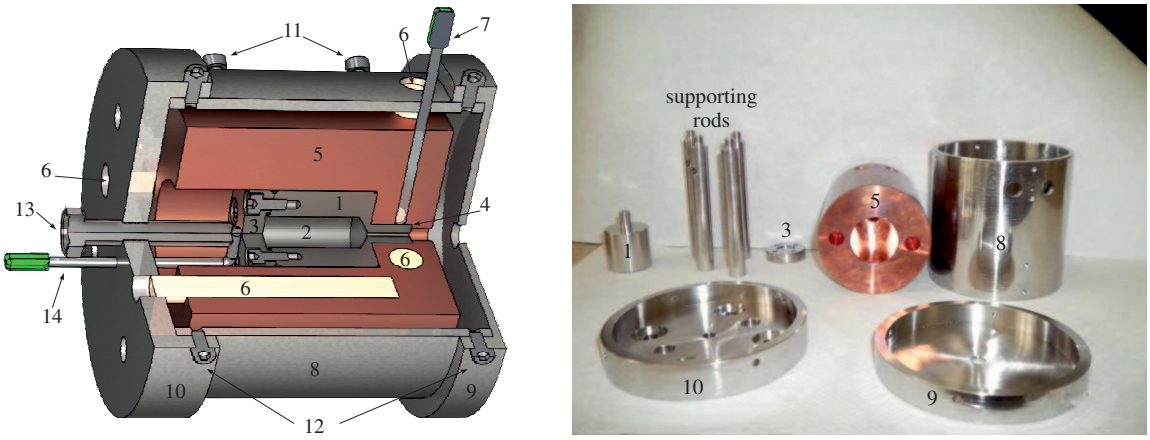

(a) (b)

Figure 2.5 Cross section of a model drawing of the second oven design (a) and a photo of the oven parts (b). The referenced parts are as follows: 1-reservoir body; 2-material compartment; 3-reservoir closing cap; 4-oven nozzle; 5-copper body; 6-cartridge heaters; 7,14 -thermocouples; 8-shield body; 9-shied front end cap; 10-shield back end cap; 11-copper body securing screws; 12-shield caps fixing screws; 13-reservoir secure screw..

$\varnothing 10 \times 25$mm. The container was sealed with a thin sheet of nickel rather than copper, since hot calcium is known to react with copper and leads to material degradation with time [A20]. Nickel melts at temperature $\approx 1455\,^{\circ}$C and its vapour pressure at the temperature of the oven ($\approx 600\,^{\circ}$C) is about 10^{-15} mbar, which is well below the expected vapour pressure for calcium of 1.3×10^{-2} mbar at the same temperature (see Eq. 2.1).

Additionally, several slots of different sizes were produced in a cylindrical piece, $\varnothing 60 \times 63$mm, made out of oxygen–free copper (5). Three channels in a row were bored through the base of the copper piece. The central slot was intended to accommodate the reservoir assembly and the two on the sides were used to fit electrical cartridge heaters (6). Another three channels, orthogonal to the first ones, were produced close to second base of the copper piece. Two additional heaters were inserted into the two end slots, while a K-type thermocouple (7) was plugged into the central slot, all the way in to make a contact with the oven nozzle. The exceptionally good heat conductivity of copper metal provided rather uniform heating along the length of the reservoir. Furthermore, the two heaters at the front ensured higher temperature of the exit channel than the rest of the reservoir part and thus preventing clogging of the nozzle.

Since thermal radiation emitted from the oven would disturb the measurement process by inducing noise in the detector it was mandatory to provide proper shielding of the oven.

The shield assembly consists of three parts - a hollow cylindrical body (8), front end cap (9) and back end cap (10), all constructed from stainless steel. The copper

cylinder was secured inside the shield body by six M3 screws (11), which formed three-point support systems at two different cross sections along the assembly axis. In addition three more openings were made close to the front end of the shield body to match the relevant slots for the heaters (6) in the copper piece inside.

The shield caps were fixed to the body (6) with four M3 screws (12) each. Furthermore, a hole with diameter of 6 mm was pierced in the center of the front end cap in order to clear a path for the atoms effusing from the oven. Seven more openings were made in the back end cap respectively. Four of them were used to attach the whole oven assembly to the back end flange of the vacuum system with supporting rods, made of stainless steel, as shown in Fig. 2.6. Another two holes were needed to make a pass for the electrical wiring of the other pair of heaters. The last central opening in the back end cap was threaded to allow for an M6 screw (13) to secure the calcium reservoir inside the copper body from behind. The second role of the screw was to secure the tip of an additional thermocouple (14) by pressing it to the reservoir cap.

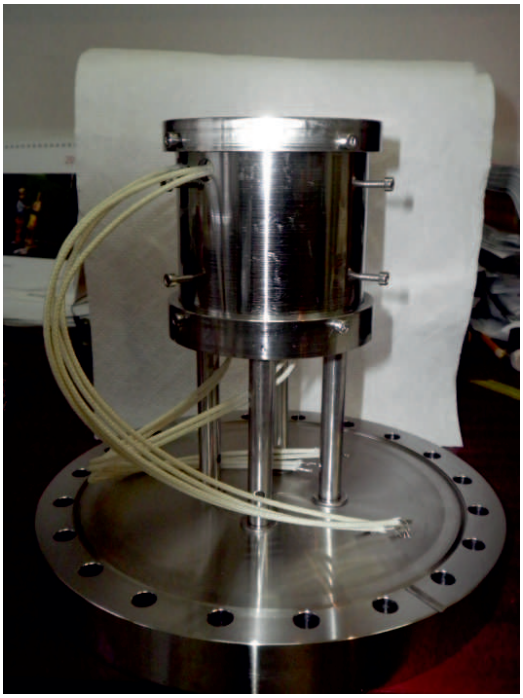

Figure 2.6 A photo of the oven assembly attached to the back end flange of the source chamber.

Moreover, the shiny surface finish of the shield enclosure, left from the machining process, helped to limit the heat loss due to thermal radiation. The test of the new oven showed its ability to held up a constant difference in the temperature of the nozzle and the reservoir cap of about 10 °C as indicated by the two thermocouples.

2.4 Laser system and detector

The presence of calcium atoms in the interaction chamber was checked by means of detecting a signal from laser-induced fluorescence. This required the design and assembly of a complete laser system - light source and control electronics, plus an appropriate detector. These two components of the experimental setup are presented here.

The employed laser system for probing the atoms is based on a Fabry-Pérot (FP) laser diode operated in an extended cavity configuration (ECDL). Typically, the output wavelength of semiconductor lasers can be tuned a few nm around a specified

central value for the particular diode value [A21]. Tuning is accomplished by changing either the current flowing through the diode, which causes change in the refractive index of the crystal medium, or by changing the physical dimensions of the crystal structure (FP resonator), with temperature (heating or cooling) for instance.

Another characteristic of the output radiation is the laser linewidth. The optical cavity of a solitary laser diode is formed by the crystal itself and it is relatively short ($\approx 100\,\mu m$). The low reflectivity of the laser diode facets leaves an optical cavity with a rather poor quality factor Q, which results in radiation linewidth typically on the order of a few tens of MHz. This limitation can be overcome by running the laser in an extended cavity, and introducing external optical feedback to the diode.

There exists a variety of implementation schemes of the ECDL configuration based on reflective gratings [A22, A23], transmission gratings [A24], volume holographic grating [A25] or narrow interference filters [A26, A27]. We chose the first option. I have used this design in other experimental studies before (setting up a magneto-optical trap with rubidium atoms, developed at the Bulgarian Academy of Sciences) and they have proved to be very reliable. Also the hardware components for building the extended resonator were readily available.

The laser diode[1] used in our setup had specified output optical power of 50 mW at 660 nm. The extended resonator was realized by introducing additional optical feedback to the semiconductor medium from a reflective diffraction grating placed in Littrow configuration [A28]. The Littrow scheme is shown in Fig. 2.7a. The grating does not only provide spectral selectivity to the back-reflected light but also leads to an increase of the overall Q factor of the laser cavity and respectively to a narrower laser linewidth, usually bellow 1 MHz. Additional impact on the spectral width of the laser light also have factors such as thermal fluctuations of the laser cavity, mechanical vibrations, noise in the supplying electronics.

The mechanical construction of our ECDL and its housing box were entirely produced from aluminum and it can be seen in the photo in Fig. 2.7b. The laser diode and a collimating lens were fitted together into the laser head block. The diffraction grating was mounted on a separate "tuning fork"-like element. The laser head and grating mount were attached to the base part of the laser below which a thermo-electric element (TE) for stabilizing the temperature of the extended resonator was installed. The other side of the TE was put in thermal contact with the base plate of the housing box of the laser. The coarse alignment of the optical feedback from the grating was accomplished with a micrometric screw placed in the grating mount, while a piezoelectric transducer (PZT) was used for fine adjustment.

The electronics package for the laser included temperature controller, current controller, ramp generator and high-voltage (HV) amplifier. The temperature servo loop controller regulated the current flow through the TE element and assured temperature stability of the extended resonator to better than 0.01 K. The current controller delivered low noise constant electric current for operating the laser diode. The ramp

[1] HL6544FM

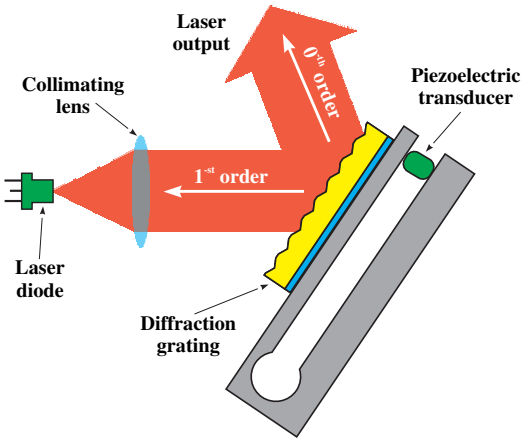

(a) ECDL in Littrow configuration.

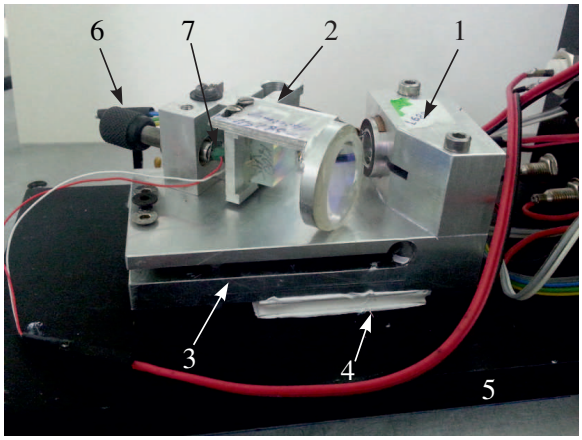

(b) Photo of the diode laser. 1 - laser head; 2 - grating mount; 3 - laser base; 4 - TE cooler; 5 - base plate of the housing box; 6 - alignment screw; 7 - PZT.

Figure 2.7

generator was used to generate a triangular waveform signal. Part of this signal was fed to the modulation input of the current controller while another part was directed to the HV amplifier which served as a driver for the PZT. The main goal is to choose proper multiplication factors for both signals such that the frequency shift of the laser mode caused by the change in diode current and by the different orientation of the grating individually are now synchronized. Finally, the ECDL laser was able to run in a single mode with a mode-hop-free range of about 10 GHz.

The detector utilized in the experiment was a head-on type photomultiplier tube[1] (PMT) with spectral sensitivity in the range 300 to 830 nm. The detector was positioned such that it was able to collect most of the scattered photons from the ^{40}Ca atoms, therefore its input window was oriented towards the oven. The excitation was taking place at a distance of about 20 cm from the viewport window of the interaction chamber.

Usually, the photomultiplier tubes are designed for detection of extremely low light levels, thus implying huge amplification of the signal at their output. Therefore, their response and the obtainable signal-to-noise ratio (SNR) greatly depends on how well the extraneous sources of radiation are suppressed. Special care was taken for shielding the detector from the ambient light in the room. Furthermore, an interference bandpass filter[2] (bandwidth of 10 nm FWHM, centered at 660 nm) was placed at the front of the PMT to further reduce the level of noise caused by thermal radiation from the oven seen by the detector.

The laser beam was traversing the interaction chamber through the windows of

[1] ФЭУ-79
[2] FB660-10

the extender tubes. Although, they were placed at Brewster's angle it was hard to tailor the polarization of the laser beam ideally and still the detector was exposed to scattered photons from multiple reflections in the windows and the interior walls of the chamber. A significant reduction of the noise level was achieved by placing apertures inside the tube extenders. Additional cylindrical screen (screen tube) was introduced inside the vacuum chamber such that the atomic beam was travelling along the axis of the cylinder. Two holes were made on the wall of the tube to clear a path for the laser beam.

Although such an arrangement limited the possibility to vary the orientation of the exciting laser with respect to the path of the atoms at that time the experiment was focused on checking for presence of atoms and therefore our main concern was to reduce the noise on the detector.

2.5 Detection of LIF signal from ^{40}Ca atomic beam

A schematic diagram of the experimental setup is shown in Fig. 2.8. The output light from the ECDL laser was directed to pass successively through two wedge beam splitters (BS) resulting in one transmitted and four reflected beams. One of the reflected beams was coupled to an optical fiber input of a wavemeter[1] (WS-5) with absolute accuracy of 3 GHz. The second reflection from the beam splitter was coupled to a low-finesse confocal Fabry-Pérot interferometer (CFPI) with free spectral range (FSR) of 375 MHz. The output light of the CFPI was detected on a photodiode whose response was observed on an oscilloscope.

The other two reflections from the second beam splitter were sent to a setup for differential measurement of absorption in iodine molecule (I_2). One of the beams was transmitted through a glass vapor cell filled with iodine, while the other served as a reference. Both beams were detected on two separate photodiodes. The output signals of the photodiodes were fed to the inputs of a differential amplifier an the resulting waveform was observed on the oscilloscope.

The wavemeter and the iodine absorption lines served as a rough marker for the instantaneous laser frequency. On the other hand the interference fringes from the CFPI were used for fine calibration of the frequency scale when signals from LIF were analysed.

Light transmitted through the two beam splitters was sent to the beam machine to perform spectroscopy measurements. Before entering the vacuum system the amplitude of laser beam was modulated with an optical chopper (rotating disc) in order to use a phase-sensitive detection of the fluorescence signal from the ^{40}Ca atoms.

To probe the atomic beam, the laser frequency was swept slowly around the frequency of the $4\,^1S_0 \rightarrow 4\,^3P_1$ transition. The width of the scan was about 150 MHz and the scan speed was 1.8 MHz/s as indicated by the green triangular waveform in Fig. 2.9. At the same time the response of the confocal interferometer to the fre-

[1] WS-5 HighFinesse

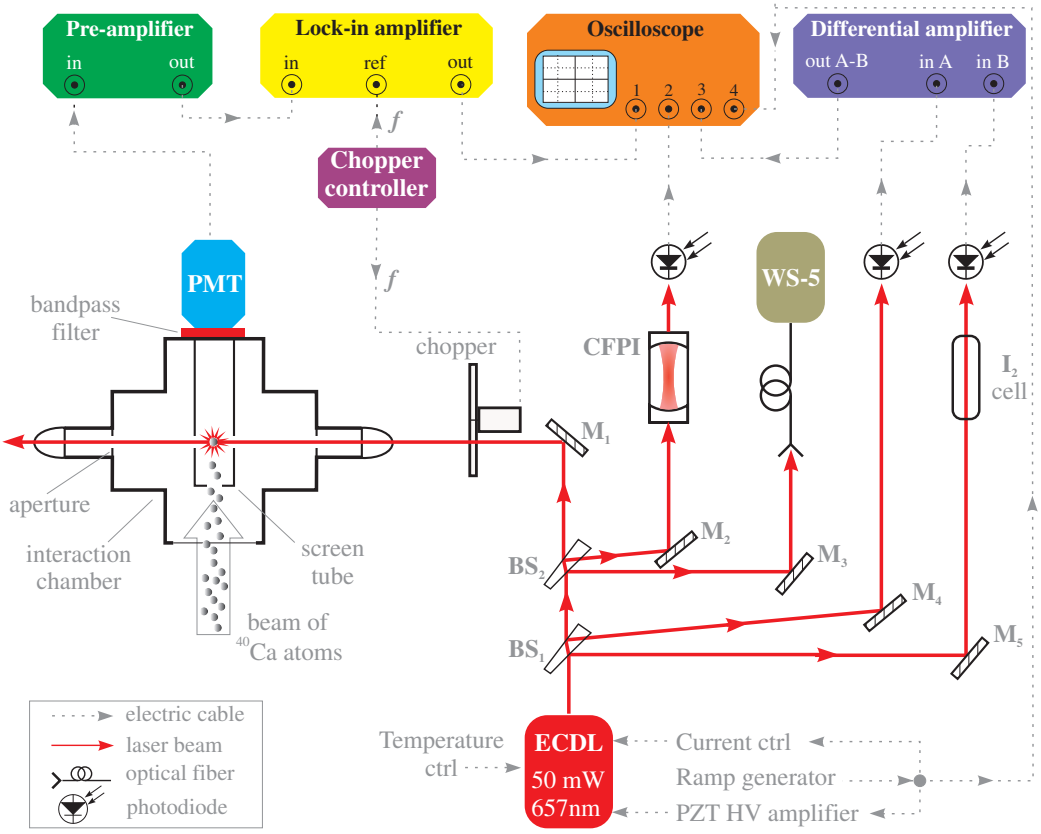

Figure 2.8 Experimental setup for measuring LIF signals from ^{40}Ca atoms in the beam machine.

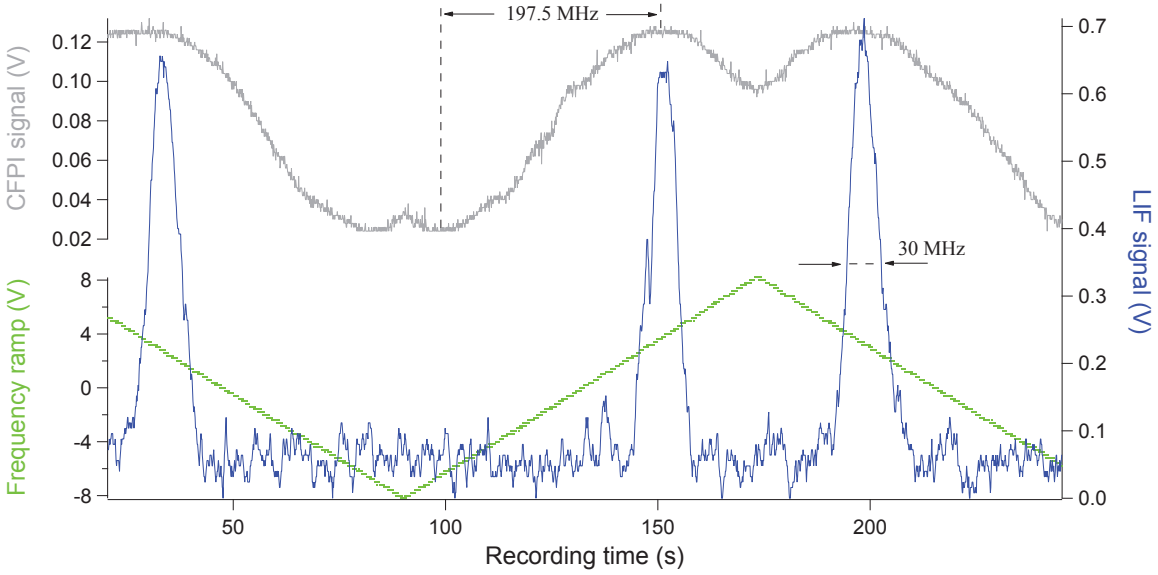

Figure 2.9 Signal from LIF.

quency scan was recorded on the oscilloscope and it appears as the grey trace at the top in Fig. 2.9.

The fluorescence, which resulted from the interaction of the laser light with the atoms from the particle beam, produced a signal at the output of the photomultiplier. First, this signal was passed to a pre-amplifier stage with a conversion factor of 0.5 V/µA. Then, the resulting signal was fed to the input of an analog lock-in amplifier[1]. Finally, the output of the lock-in was recorded on the oscilloscope and it was depicted as a blue trace in Fig. 2.9 under the following conditions: the amplitude modulation of the laser beam was done at a frequency of 250 Hz; the time constant of the lock-in amplifier was set to $\tau = 0.1$ s. Furthermore, the temperature of the atomic source was 600 °C, as indicated by the thermocouple at the back of the calcium reservoir, and the manometer below the source chamber showed pressure reading of 3×10^{-6} mbar.

The recorded spectrum was calibrated in frequency assuming a linear response of the laser output frequency within a half FSR of the CFPI while linearly sweeping the driving current of the laser diode. The full width at half maximum of the observed line was estimated to be about 30 MHz, which appears somewhat larger than the expected result from such type of experiments. This was most likely due to the divergence of the particle beam, and a rough estimate of the induced Doppler shift due to non-zero transverse velocity of the atoms in the beam is given in the conclusions section below.

[1] 420 Dual Phase Lock-in Amplifier Scitec Instruments

2.6 Conclusions and future plans

As a result of the work on this part of the thesis a new laboratory was built in the Department of Optics and Spectroscopy. A beam machine was designed and assembled, together with the accompanying optical tables, lasers, electronics and vacuum systems.

The performance of the beam was successfully demonstrated with the weak intercombination $4\,^1\mathrm{S}_0 \rightarrow 4\,^3\mathrm{P}_1$ transition in Ca.

However a full characterization of the atomic beam, in terms of beam divergence, velocity of the atoms and atomic flux, is still needed.

Regarding the beam divergence, assuming that the velocity of the atoms in the oven obeys Maxwell-Boltzmann distribution, then the mean velocity is given by

$$\bar{v} = \sqrt{\frac{8\,R\,T}{\pi\,M_{\mathrm{Ca}}}}\,,$$

where $R = 8.3\,\mathrm{J/(K\,mol)}$ is the gas constant, $T \approx 873\,\mathrm{K}$ in the oven temperature, and $M_{Ca} \approx 40\,\mathrm{g/mol}$ is the molar mass of calcium atom. This expression leads to a mean velocity of the atoms emerging from the oven nozzle of $\bar{v} \approx 680\,\mathrm{m/s}$.

Supposing an uniform spatial (angular) distribution of the atoms that exit the nozzle form a cone whose apex lies at the center of the nozzle channel, and the apex angle is 11.4°. The atom-laser interaction occurs 446 mm further away from the cone apex, which would result in a transverse velocity component of about $\approx 67.7\,\mathrm{m/s}$, and a Doppler-shifted resonance of about 103 MHz respectively. The estimated linewidth of 30 MHz shows that the spatial distribution of the atoms is actually narrower than the assumed one here, and the nozzle itself acts as a collimator. However, for implementing the scheme for coherent control it is necessary first to evaluate the divergence of the particle beam, and then to provide further collimation, if needed, by installing apertures along the path of the atoms.

Another aspect of the characterization of the atomic beam is the atom flux. Only an approximate calculation of the atomic flux is provided here. The number of atoms emerging from the nozzle per unit time can be expressed as:[A29, p13]

$$Q = (1/\kappa)\frac{1}{4} n\,\bar{v}\,A_s\,,$$

where A_s is the area of the nozzle opening, $\bar{v}$ is the mean velocity of the atoms, n is the number of atoms per unit volume(in the oven). The geometrical factor $(1/\kappa)$, for a long channel nozzle such as ours, is

$$(1/\kappa) = \frac{8}{3}\frac{r}{l}\,,$$

where $r = 0.5\,\mathrm{mm}$ is the radius of the channel opening and $l = 10\,\mathrm{mm}$ is the channel length. At a temperature of 600 °C the vapour pressure of Ca is $\approx 1.3\,\mathrm{Pa}$ that leads to a value for the concentration of calcium atoms in the oven of $10^{20}\,\mathrm{atoms/cm^3}$.

Finally, the expected total number of atoms leaving the oven per second is $Q \approx 2 \times 10^{15}$ atoms/s. It is difficult to acquire a sensible figure of the actual atomic flux from the recorded fluorescence signals since the scattered photons that reach the detector come from not very well defined volume. The probing laser excites the atoms 20 cm before the window of the vacuum chamber where the photomultiplier is placed. Given the natural lifetime of the excited state of about 0.4 ms and the mean velocity of the atoms of 680 m/s it follows that on average an atom will travel 27 cm before a transition back to the ground state occur i.e. the atom will hit the end flange of the vacuum chamber before scattering a photon.

The working beam machine will allow the work on the coherent manipulation of Ca atoms by composite pulses to be continued. One needs to improve the frequency stability of the diode lasers and arrange several beams with controllable phases to cross the atomic beam. Additionally a theoretical work is needed to estimate the requirements for the laser systems. Given the mean velocity of the atoms $\bar{v} = 680$ m/s and an interaction distance between the laser beams of 1 cm, the interaction time with the composite pulses is about 15 μs so the laser frequency should be stable to better than 10 kHz in order to ensure stable phase within the interaction time. This rough estimate shows that the major challenge in the future experiments may be to reach such a level of the laser linewidth. Therefore close collaboration with the theoretical group is important to estimate reliably the proper experimental conditions.

References for Part I

[A1] T. M'uller et al. "Versatile compact atomic source for high-resolution dual atom interferometry". *Phys. Rev. A* 76.6 (2007), p. 063611.

[A2] N. Gisin, S. A. Moiseev, and Ch. Simon. "Storage and retrieval of time-bin qubits with photon-echo-based quantum memories". *Phys. Rev. A* 76 (1 2007), p. 014302.

[A3] D. Press et al. "Ultrafast optical spin echo in a single quantum dot". *Nat. Photonics* 4.6 (2010), pp. 367–370.

[A4] M. Kroutvar et al. "Optically programmable electron spin memory using semiconductor quantum dots". *Nature* 432.7013 (2004), pp. 81–84.

[A5] N. V. Vitanov et al. "Laser-induced population transfer by adiabatic passage thechniques". *Annual Review of Physical Chemistry* 52.1 (2001), pp. 763–809.

[A6] A. André et al. "Quantum control of light using electromagnetically induced transparency". *J. Phys. B-At. Mol. Opt.* 38.9 (2005), S589.

[A7] V. Boyer A. M. Marino R. C. Pooser and P. D. Lett. "Tunable delay of Einstein–Podolsky–Rosen entanglement". *Nature* 457 (2009), pp. 859–862.

[A8] W. M. Itano et al. "Quantum projection noise: Population fluctuations in two-level systems". *Phys. Rev. A* 47.5 (1993), pp. 3554–3570.

[A9] Cronin, A. D. and Schmiedmayer, J. and Pritchard, D. E. "Optics and interferometry with atoms and molecules". *Rev. Mod. Phys.* 81 (2009), pp. 1051–1129.

[A10] M. Weidemüller and C. Zimmermann. *Cold Atoms and Molecules. A Testground for Fundamental Many Particle Physics*. WILEY-VCH Weinheim, 2009.

[A11] O. Mandel et al. "Coherent Transport of Neutral Atoms in Spin-Dependent Optical Lattice Potentials". *Phys. Rev. Lett* 91 (2003), p. 010407.

[A12] A. J. Daley et al. "Quantum Computing with Alkaline-Earth-Metal Atoms". *Phys. Rev. Lett.* 101 (2008), p. 170504.

[A13] T. D. Ladd et al. “Quantum computers”. *Nature* 464 (2010), p. 45.

[A14] M. Fleischhauer, A. Imamoglu, and J. P. Marangos. “Electromagnetically induced transparency: Optics in coherent media”. *Rev. Mod. Phys.* 77 (2005), pp. 633–641.

[A15] E. Knill. “Physics: Quantum computing”. *Nature* 463 (2010), p. 441.

[A16] B. T. Torosov and N. V. Vitanov. “Smooth composite pulses for high-fidelity quantum information processing”. *Phys. Rev. A* 83 (2011), p. 053420.

[A17] S. S. Ivanov and N. V. Vitanov. “High-fidelity local addressing of trapped ions and atoms by composite sequences of laser pulses”. *Opt. Lett.* 36 (2011), p. 1275.

[A18] Torosov, B. T. and Guerin, St. and N. V. Vitanov. “High-Fidelity Adiabatic Passage by Composite Sequences of Chirped Pulses”. *Phys. Rev. Lett.* 106 (2011), p. 233001.

[A19] David R. Lide, ed. *CRC Handbook of Chemistry and Physics, 84th Edition.* 84th. CRC Press, June 2003.

[A20] A. J. Murray and D. Cvejanovic. “Coplanar symmetric (e, 2e) measurements from calcium at low energy”. *J. Phys. B At. Mol. Opt. Phys.* 36.24 (2003), pp. 4875–4888.

[A21] C. E. Wieman and L. Hollberg. “Using diode lasers for atomic physics”. *Review of Scientific Instruments* 62.1 (1991), pp. 1–20.

[A22] K. C. Harvey and C. J. Myatt. “External-cavity diode laser using a grazing-incidence diffraction grating”. *Opt. Lett.* 16.12 (1991), pp. 910–912.

[A23] S. Lecomte et al. “Self-aligned extended-cavity diode laser stabilized by the Zeeman effect on the cesium D2 line”. *Appl. Opt.* 39.9 (2000), pp. 1426–1429.

[A24] M Merimaa et al. “Compact external-cavity diode laser with a novel transmission geometry”. *Optics Communications* 174.1–4 (2000), pp. 175–180.

[A25] T. Hieta et al. “External-cavity lasers based on a volume holographic grating at normal incidence for spectroscopy in the visible range”. *Optics Communications* 282.15 (2009), pp. 3119–3123.

[A26] M. Gilowski et al. “Narrow bandwidth interference filter-stabilized diode laser systems for the manipulation of neutral atoms”. *Optics Communications* 280.2 (2007), pp. 443–447.

[A27] X. Baillard et al. “Interference-filter-stabilized external-cavity diode lasers”. *Optics Communications* 266.2 (2006), pp. 609–613.

[A28] L. Ricci et al. “A compact grating-stabilized diode laser system for atomic physics”. *Optics Communications* 117.5–6 (1995), pp. 541–549.

[A29] Norman F. Ramsey. *Molecular Beams (International Series of Monographs on Physics).* Oxford University Press, 1990.

Part II

Frequency stability improvement of a caesium atomic fountain operating in quantum projection noise limited regime by employing an LVIS system

Chapter 3

Introduction

This part of the thesis is devoted to the improvements of the frequency stability of the Cs fountain primary frequency standard CSF2 [B1]. In CSF2 caesium atoms are cooled and accumulated in an optical molasses (OM). The captured atoms are subsequently launched in vertical direction to perform frequency measurements of the microwave clock transition between the $6^2S_{1/2}$ ground state hyperfine sublevels $|F = 3\rangle$ and $|F = 4\rangle$ [B2]. With the use of an optically-stabilized microwave signal [B3] the stability of the fountain was limited by quantum projection noise (QPN) over a wide range of atom numbers. As a result, the fountain frequency stability was improved with the square root of the detected atom number. The loaded and detected cold atom number was increased (and the corresponding QPN respectively reduced) by OM loading from a low-velocity intense source of cold atoms (LVIS, [B4]). The LVIS system was modified by adding a "dark" state pump laser which was used to reduce the velocity of the atoms in the slow beam. This resulted in another factor of two loading enhancement.

3.1 Motivation

The modern frequency metrology is perhaps the area where the coherent manipulation of quantum states has led to the most impressive results. Frequency measurements with up to 10^{-18} relative accuracy become possible because of the smart design of the interaction between the radiation field and the quantum system in an environment where the coherent time evolution of the quantum system can be maintained for sufficiently long periods of time and the residual interferences from the environment are controlled within a well defined range.

The caesium atomic clocks, although not as accurate and stable, as most of the optical clocks are still used for definition of the second in the international system of units. Their advantage over the optical clocks is the robust operation virtually without maintenance for very long periods of time. A lot of experimental work has been done worldwide to study the systematic shifts of the clock frequency under various effects and nowadays most of the atomic clocks work in a quantum-projection

noise limited regime. In this regime the frequency instability is directly related to the number of atoms involved in the Ramsey cycle. So the main motivation of this part of the thesis is to increase the number of atoms loaded in the optical molasses of the CSF2 caesium fountain in PTB, Germany, where the author has spent the last six months, working on the experimental part of this thesis.

The number of atoms in the fountain clock is increased by loading the optical molasses with a beam of slow caesium atoms. Among the many possibilities to form atomic beam we have chosen the LVIS because of its relative simplicity and the various possibilities to manipulates the quantum state of the atoms in the beam. In the present application of the LVIS this turned out to be very important because it was necessary to achieve not only an intense beam of slow Cs atoms, but optimal loading of the molasses and finally the maximum number of atoms participating in the Ramsey cycle.

3.2 Outline

The second part of the thesis is organized as follows:

Chapter 4 is devoted to the caesium atom and more specifically to its internal structure. The coupling among various angular momenta associated with the atom is examined since it leads to modification of the energy of the atomic states. The energy of the levels is also affected by the presence of external static electric and magnetic fields which lead to Stark and Zeeman shifts respectively. The latter is strongly related to the principle of operation of the magneto-optical trap in combination with a set of rules concerning the interaction of the atom with electromagnetic radiation. Almost every phenomenon discussed in the presented study is a result of the interaction between the caesium atoms with external fields.

Chapter 5 takes advantage of the developed theory in the previous chapter and shows several approaches which are utilized in the present experiment and allow for reduction of the kinetic energy of an ensemble of caesium atoms in the ground state using laser light.

Chapter 6 introduces the subject of precise frequency measurements with atomic clocks. First it sets the important terminology used in the field. Subsequently, the concept of frequency measurement in atomic clocks is described and how one could benefit from the possibility to cool atoms with light to realize an accurate atomic standard. Then it presents in details the construction of an atomic fountain, in particular CSF2, and focuses on the fountain performance limits in terms of accuracy and short-term stability, improvement of the latter being the main concern of this work. Lastly, it shows different approaches to reduce the influence of the limiting factors on the fountain stability and describes our choice of a working scheme. The reasons for employing an LVIS system to demonstrate frequency stability mainly governed by quantum projection noise are also discussed in this section.

Chapter 7 concentrates on the improvements made to the atomic beam source

whose experimental realization is described beforehand. An interesting scheme, which was used to control the the velocity of the atoms emerging from the LVIS, is proposed. Results from experimental investigation of the impact of the pump laser on the number of detected atoms in the fountain at the end of the Ramsey interaction are presented. A simple model involving Monte Carlo simulation was used to support the results qualitatively. Measurements for evaluation of the mean velocity and flux of the atoms in the slow beam are shown. Finally, the overall performance of the atomic fountain with enhanced loading (LVIS-CSF2) is presented. The quantum projection noise limited regime of fountain operation is demonstrated alongside with a measurement undoubtedly showing the improvement of the short-term stability of CSF2.

Chapter 8 summarises the results of the conducted experimental study and analyses the subsequent contributions to the field of metrology.

Chapter 4

The Caesium atom

The caesium atom has been extensively studied through the years. The substantial interest arises from theoretical and practical aspects as well. The relatively simple energetic structure allows for evaluation of the atomic properties through analytical models which later can be confirmed and refined in experimental studies. It has one naturally occurring isotope, ^{133}Cs and three long–lived radioisotopes. It has a low melting point of 28.4 °C and provides a substantial vapour pressure at easily accessible temperatures of a few hundred degrees °C. This makes it a rather suitable choice as a source of atoms in thermal beams. Additionally, the existence of a "closed" transition between components of the hyperfine structure in the ground and exited states turn it into an obvious candidate for applications of laser cooling and trapping techniques. The Cs ground state hyperfine transition was adopted for the definition of the second by the Conferérence Générale des Poids et Mesures (CGPM) in 1968 and remains so up to this day. Even today it is still in a position to attract the attention of the experimentalists in pursuit of better stability performance of the atomic clocks.

4.1 Hyperfine Structure

The caesium atom has one valence s electron. In this configuration the only contribution to the total angular momentum of the atom comes from this electron. Thereby, the orbital angular momentum $\boldsymbol{L}$ of the outer electron and the angular momentum associated with its spin $\boldsymbol{S}$ couple together to form the total angular momentum for all electrons $\boldsymbol{J}$, given by

$$\boldsymbol{J} = \boldsymbol{L} + \boldsymbol{S} \, . \tag{4.1}$$

The eigenvalues of $\boldsymbol{J}^2$ are $\hbar^2 \, J(J+1)$ and the quantum number J , which describes it, must lie in the range

$$|L - S| \leq J \leq L + S \, . \tag{4.2}$$

Different values of J lead to different energies of the states, since the spin-orbit interaction $H_{\rm so} = \frac{A}{r^3}\,\boldsymbol{L}\cdot\boldsymbol{S}$ depends on the mutual orientation of $\boldsymbol{S}$ and $\boldsymbol{L}$ (here A is the spin-orbit coupling constant). This splitting of the states, as a result of the spin -orbit interaction is called fine structure of the atom.

The electronic states of the alkali-metal atoms are fully specified in the Russell-Saunders notation as $n\,^{2S+1}L_J$, where n is the principal quantum number of the valence electron and L is substituted by a letter which refers to its value (i.e., S $\leftrightarrow L = 0$, P $\leftrightarrow L = 1$). For the ground state in caesium, $L = 0$ and $S = 1/2$, so $J = 1/2$; for the first excited state, $L = 1$ so $J = 1/2$ or $J = 3/2$. Hence the $L = 0 \rightarrow L = 1$ (D line) transition is split in two components, the D_1 line ($6\,^2S_{1/2} \rightarrow 6\,^2P_{1/2}$) and D_2 line ($6\,^2S_{1/2} \rightarrow 6\,^2P_{3/2}$), $\approx 16.6\,\mathrm{THz}$ apart from each other. In this study only the ground state of the atom and the D_2 line are manipulated by excitation of dipole transitions, and thereby collecting spectroscopic data.

If the interaction of the nuclear spin $\boldsymbol{I}$ with the total angular momentum of the electrons $\boldsymbol{J}$ is considered, then the electronic structure of the caesium atom becomes more complicated. Both momenta couple together to give the total angular momentum of the atom as

$$\boldsymbol{F} = \boldsymbol{I} + \boldsymbol{J}\ . \tag{4.3}$$

Again, for given J and I, the allowed values of the quantum number for the total angular momentum, F, are given by the coupling rules for two angular momenta [B5, p. 110]:

$$|J - I| \leq F \leq J + I\ . \tag{4.4}$$

The nuclear spin of the caesium atom is described by a quantum number $I = 7/2$. Then for the ground state $F = 3$ or $F = 4$ while for the excited state $6\,^2P_{3/2}$ F can take any of the values 2, 3, 4 or 5.

The new angular momentum eigenstates, in the presence of the hyperfine interaction, are given by the simultaneous eigenstates of the operators $\boldsymbol{F}^2$ and $\boldsymbol{F_z}$. Here $\boldsymbol{F_z}$ is the z-component of the total angular momentum $\boldsymbol{F}$ and its eigenvalues are $\hbar\, m_{_F}$. It can be shown that the correction to the atomic Hamiltonian as a result of the interaction between the nuclear spin and the electronic angular momentum is [B6]

$$H_{\rm hfs} = h\,A_{\rm hfs}\boldsymbol{I}\cdot\boldsymbol{J} + h\,B_{\rm hfs}\frac{3(\boldsymbol{I}\cdot\boldsymbol{J})^2 + \frac{3}{2}\boldsymbol{I}\cdot\boldsymbol{J} - I(I+1)J(J+1)}{2I(I-1)J(2J-1)}\ , \tag{4.5}$$

which leads to a shift of the energy levels

$$\Delta E_{\rm hfs} = \frac{1}{2}h\,A_{\rm hfs}K + h\,B_{\rm hfs}\frac{\frac{3}{2}\,K(K+1) - 2I(I+1)J(J+1)}{2I(2I-1)2J(2J-1)}\ , \tag{4.6}$$

where $K = F(F+1) - I(I+1) - J(J+1)$, h is Planck's constant and $A_{\rm hfs}$ is the magnetic dipole constant. The term with the electric quadrupole constant, $B_{\rm hfs}$,

applies only to the excited manifold of the D_2 line. For the caesium ground state $6\,^2S_{1/2}$ – $A_{\rm hfs} = 2.298\,157\,942\,5\,\text{GHz}$ [B6] is an exact value and for the excited state $6\,^2P_{3/2}$ the values for $A_{\rm hfs} = (50.275 \pm 0.003)\,\text{MHz}$ and $B_{\rm hfs} = (-0.53 \pm 0.02)\,\text{MHz}$ are taken from an experimental study [B7].

Therefore the atomic states described by different values of F for the same values of both J and I are split by the interaction. The resulting energy structure is called the hyperfine structure (hfs) and it is much smaller than the fine structure splitting. Fig.4.1 shows the level structure of the D_2 transition in caesium. From now on when quantum numbers are used in the text to label a particular atomic level the unprimed symbols will refer to the ground state and the primed to the excited state.

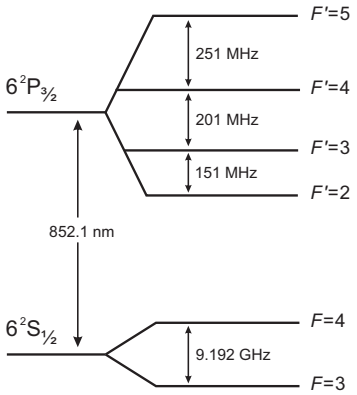

Figure 4.1 Hyperfine structure and frequency splittings between the hyperfine energy levels of the caesium D_2 transition.Graph not to scale.

4.2 Zeeman structure

The correction $H_{\rm hfs}$ (form Eq. 4.5) to the full atomic Hamiltonian shows no dependance on the quantum number m_F, whose value ranges from $-F$ to F with a step of unity

$$m_F = -F, (-F+1), ..., 0, ..., (F-1), F\ . \tag{4.7}$$

In other words, each particular state described by a certain value of F is $(2F+1)$-fold degenerate.

However, in the presence of static magnetic field $\boldsymbol{B}$ to the atom this degeneracy is lifted. The magnetic field interacts with the various magnetic moments present in the atom : the orbital and spin magnetic moments of the outer electron,

$$\boldsymbol{\mu_L} = -\frac{\mu_B}{\hbar}\, g_L\, \boldsymbol{L} \tag{4.8}$$

and

$$\boldsymbol{\mu_S} = -\frac{\mu_B}{\hbar}\, g_S\, \boldsymbol{S} \tag{4.9}$$

and the magnetic moment of the nucleus,

$$\boldsymbol{\mu_I} = \mu_N\, g_N\, \boldsymbol{I}\ . \tag{4.10}$$

In the above expressions the quantity $\mu_{\rm B} = \frac{e\,\hbar}{2m_{\rm e}}$ is the Bohr magneton and $\mu_{\rm N} = \frac{e\,\hbar}{2m_{\rm p}}$ is the nuclear magneton (e is the electron charge, $m_{\rm e}$ and $m_{\rm p}$ are the electron mass and the proton mass respectively). The numerical factors $g_{\mathbf{L}}$, $g_{\mathbf{S}}$ and $g_{\mathbf{I}}$ are respectively the electron orbital, electron spin and nuclear "g-factors". An additional term must be included to the Hamiltonian of the system which describes the interaction energy of the atom with the field $\boldsymbol{B}$. This correction can be written as

$$H_B = -\boldsymbol{\mu} \cdot \boldsymbol{B} = -(\boldsymbol{\mu}_{\mathbf{L}} + \boldsymbol{\mu}_{\mathbf{S}} + \boldsymbol{\mu}_{\mathbf{I}}) \cdot \boldsymbol{B} \; . \tag{4.11}$$

and leads to the Zeeman effect.

A very special case from the point of view of the techniques for laser cooling and trapping of atoms is the so called "anomalous Zeeman effect". In a situation of weak magnetic field, such that the induced energy shift is smaller than the hyperfine structure splitting, the Zeeman interaction does not disturb either the coupling of $\boldsymbol{L}$ and $\boldsymbol{S}$, nor the coupling of $\boldsymbol{J}$ and $\boldsymbol{I}$. Then F is a good quantum number and the Zeeman interaction Hamiltonian alternatively can be expressed as

$$H_B = -\boldsymbol{\mu}_{\mathbf{F}} \cdot \boldsymbol{B} = \frac{\mu_{\rm B}}{\hbar}\, g_{\mathbf{F}}\, \boldsymbol{F} \cdot \boldsymbol{B} \; , \tag{4.12}$$

where the hyperfine Landé g-factor is given by

$$g_{\mathbf{F}} \simeq g_{\mathbf{J}} \frac{F(F+1) + J(J+1) - I(I+1)}{2F(F+1)} \; , \tag{4.13}$$

and the expression for the Landé factor $g_{\mathbf{J}}$ is [B8, p.152]

$$g_{\mathbf{J}} \simeq 1 + \frac{J(J+1) + S(S+1) - L(L+1)}{2J(J+1)} \tag{4.14}$$

If the weak magnetic field $\boldsymbol{B} = (0, 0, B_z)$ is applied in the direction of the atomic quantization axis z, the Zeeman interaction perturbs the zero-field hyperfine energies of each particular atomic state $|F, m_F\rangle$ by an amount of

$$\Delta E_{Zeeman} = \mu_{\rm B}\, g_{\mathbf{F}}\, m_F\, B_z \; . \tag{4.15}$$

The above expression shows that a caesium atom moving through a region of space where a linear magnetic field gradient is preset would experience a linear change of the resonance frequency of any transition $|F, m_F\rangle \rightarrow |F', m_{F'}\rangle$ (except for the unperturbed states with $m_{F'} = 0$). This effect plays a crucial role in the laser cooling of atoms in particular in the magneto-optical trap, which will be discussed later.

4.3 Selection rules

The detailed knowledge of the energy level structure of the caesium atom is not sufficient to allow for a complete description of the observed spectrum. In addition, a certain set of selection rules that govern the transitions between the levels must

be considered. These rules arise from the conservation of angular momentum of the system during the transitions. Of course, the rules differ depending on the actual type of the interaction that causes the transition, i.e. the matrix element of which transition operator, calculated between the initial and the final state, is non-zero. Here the selection rules will be listed that are valid in the case of electric dipole transitions–E1, since they are the main subject of observation in this study. In the optical range their probability is $\sim 10^4$ [PR] higher than the probability for electric quadrupole or magnetic dipole transitions to occur.

The strength of the interaction between the caesium and nearly resonant optical radiation is characterized by the matrix elements $d_{fi} = \langle\psi_f|-e\boldsymbol{r}|\psi_i\rangle$ of the dipole moment operator $\boldsymbol{d} = -e\,\boldsymbol{r}$, which is of odd parity. Moreover, the parity of the atomic wavefunction, for a one-electron system, is determined by $(-1)^L$, so symmetry demands that ΔL is odd and the selection rule for one-photon excitation is

$$\Delta L = \pm 1\ . \tag{4.16}$$

The selection rule for the magnetic quantum number $m_{\scriptscriptstyle L}$ represents the conservation of angular momentum. The photon, being a boson particle, is characterized by a spin quantum number $S^{\mathsf{ph}} = 1$ and the projection of the photon spin on the direction of its wave vector S_k^{ph} has an expectation value of $\pm\hbar$. Nonetheless, the projection of this angular momentum on the atomic z-axis can take the values $0, \pm 1$ (in units of $\hbar$) []. The states with $S_z^{\mathsf{ph}} = 0$ correspond to light with polarization perpendicular to the atomic z-axis, the so called σ^+ and σ^- polarization. The states with $S_z^{\mathsf{ph}} = \pm 1$ correspond to light with polarization parallel to the atomic z-axis, the so called π polarization. Conservation of angular momentum requires that absorption of a photon is accompanied by a corresponding change of the projection of the angular momentum of the atom.

$$\Delta m_{\scriptscriptstyle L} = 0, \pm 1\ . \tag{4.17}$$

The last rule is in tight connection with the polarization state of the light field which causes the transition. $\Delta m = 0$ corresponds to linearly polarized π light while $\Delta m = \pm 1$ transitions are induced by right-handed (σ^+) and left-handed (σ^+) circularly polarized light. The linear polarization, perpendicular to the z axis can be presented as a superposition of σ^+ and σ^- components and in this case the selection rule will be $\Delta m = \pm 1$. In the case of fine and hyperfine interaction, the orbital angular momentum $\boldsymbol{L}$ can be replaced by the total angular momentum of the electron $\boldsymbol{J}$ or $\boldsymbol{F}$ of the atom, respectively. The same selection rules apply for $m_{\scriptscriptstyle J}$ and $m_{\scriptscriptstyle F}$.

The selection rules for J and F are

$$\Delta J = 0, \pm 1 \qquad J = 0 \nleftrightarrow J' = 0 \tag{4.18}$$

$$\Delta F = 0, \pm 1 \qquad F = 0 \nleftrightarrow F' = 0\ . \tag{4.19}$$

The laser cooling technique relies on scattering of a large number of photons in order to slow down an atom from thermal velocities down to near zero velocity. Therefore, the coupling strength between the levels involved in the cooling process has to be sufficiently high. In addition, the large number of cycles that the atoms have to undergo requires an effective ”closed“ system. In other words the decay from the excited to the ground state must be only to the state coupled by the light. Here the selection rules play a very important role to determine the available states, suitable for laser cooling. In systems like the caesium atom the cooling cycle is usually performed between the highest hyperfine components of the ground and excited states.

Chapter 5

Laser cooling and trapping of neutral atoms

By no means the discovery that the laser light can cool atoms is one of the greatest groundbreaking inventions of modern science which have triggered the rapid evolution of the atomic physics and have opened the doors for a variety of research fields in precision measurement [B9]. The possibility to cool and confine neutral atoms within a small region of space, for instance in a magneto-optical trap (MOT), has allowed the researchers to study atomic physics at extremely low temperatures where the interaction times with the atoms were significantly larger. Access to this ultra-cold atom regime has resulted in tremendous improvements in precision spectroscopy and atomic clock development.

To a great extent all of the experiments conducted through this part of the thesis rely on the techniques for laser cooling and trapping of atoms. In our fountain clock, for instance, both the optical molasses and the polarization gradient cooling techniques were employed to prepare an ensemble of cold Cs atoms. Furthermore, in the experiment, the production of a beam of slow Cs atoms was accomplished by utilizing a magneto-optical trapping in a modified scheme. Therefore, it is convenient to examine the basic working principles of these techniques first, and then to continue with more details about the performed study.

5.1 Optical molasses

The basic ideas behind laser cooling were first proposed independently by Hänsch and Schawlow [B10] and Wineland and Dehmelt [B11], both in 1975. At the heart of the cooling process lays the transfer of momentum between an atom and a resonant light field. The simplest picture of a two-level atom which is moving in an opposite direction with respect to an incoming laser beam is considered. Each time when the atom is excited by absorbtion of a photon with momentum $\boldsymbol{p}_{\mathrm{ph}} = \hbar\boldsymbol{k}$, where $\hbar$ is the reduced Planck constant, and $\boldsymbol{k}$ is the photon wave vector ($|\boldsymbol{k}| = 2\pi/\lambda$, λ is the photon wavelength), the momentum of the atom, $\boldsymbol{p}_{\mathrm{atom}}$, changes by the same amount

of $\hbar\boldsymbol{k}$. Then, after some period, the atom spontaneously emits a resonance photon, thereby giving away a momentum of $\hbar\boldsymbol{k}$. Since the emission is isotropic, in a random direction, after many cycles of absorption and subsequent spontaneous emission, the overall effect of the decay on the velocity of the atom averages to zero. Therefore, the continuous scattering of photons leads to a reduction of the atom momentum, and respectively its velocity decreases. The force exerted by the laser field on the atom depends on the photon momentum and on the scattering rate. This, so called scattering force, can be expressed as [B9]:

$$\boldsymbol{F}_{\text{scatt}} = \frac{\hbar\boldsymbol{k}\gamma}{2}\frac{I/I_{\text{s}}}{1 + I/I_{\text{s}} + 4(\delta - \boldsymbol{k}\cdot\boldsymbol{v})^2/\gamma^2}\,, \tag{5.1}$$

where $\hbar$ is the reduced Planck constant, $\boldsymbol{k}$ is the radiation field wave vector, I is the intensity of the light field, I_{s} is the saturation intensity ($I_{\text{s}} = \hbar c\, k^3\gamma/(12\pi)$), δ is the frequency detuning of the laser form resonance, γ is the natural linewidth of the transition, and $\boldsymbol{v}$ is the velocity of the atom. The term $\boldsymbol{k}\cdot\boldsymbol{v}$ accounts for the Dppler shift of the resonance induced by the motion of the atom. Therefore, the scattering rate of an atom, which propagates against the light source will be greater if the photons are red-detuned from resonance. From the above equation it is evident that increasing the intensity I of the laser does not increase the force to infinity, but it rather tends to a limiting value of $F_{\text{max}} = \hbar k\gamma/2$. Apparently, the efficiency of the technique is also restricted to a small range of atomic velocities. While slowing,the atom is shifted out of resonance due to the Doppler effect, the scattering rate considerably decreases and the cooling action ceases.

The addition of a second laser field, with the same frequency detuning, but propagating in the opposite direction with respect to the first one is referred to as 1D-optical molasses (OM) and the radiation pressure force acting on the atom is graphically represented in Fig. 5.1. If the atom travels through the common volume formed by the crossing of three orthogonal pairs of counterpropagating laser beams, a reduction of the atom velocity in three dimensions is achieved.

The random absorption of a photon from any direction by an atom at rest and the random emission direction of any emitted photons result in velocity fluctuations which effectively heat the atom. This heating competes with the mean cooling force, and the competition between the two yields the temperature to which the atomic sample can be cooled [B9]. The coldest temperatures are obtained with laser light red-detuned from the atomic resonance by one half the natural linewidth, γ. This Doppler-cooling temperature limit is:

$$T_{\text{D}} = \frac{\hbar\gamma}{2k_{\text{B}}}\,, \tag{5.2}$$

where k_{B} is the Boltzmann constant, and it gives the lowest temperature expected in the optical molasses technique. For Cs atom this temperature equals $T_{\text{D}} = 125\,\mu\text{K}$.

In 1985, for the first time, a group of scientists at Bell Laboratories observed three-dimensional optical molasses (OM) [B12]. The preliminary measurements of

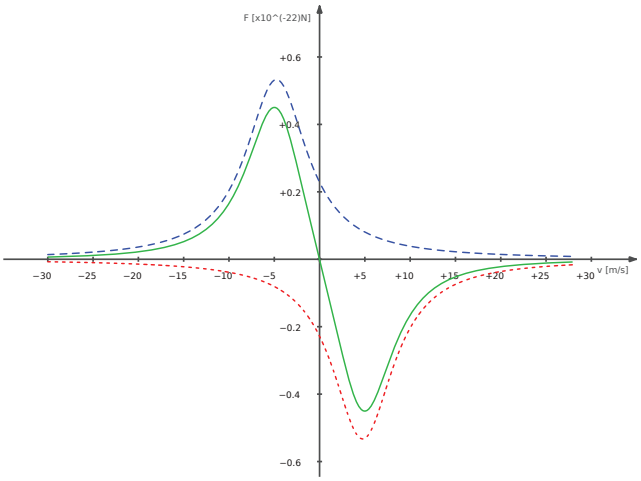

Figure 5.1 Cooling force in the 1D-optical molasses. The laser frequency is red-shifted to γ from the atomic resonance and $I = I_{\mathrm{S}}$. The dashed lines represent the force exerted on the atom from each of the counterpropagating laser beam separately and the solid line gives the resultant total action over the atom.

the average kinetic energy of the atoms were consistent with the theory of Doppler cooling of the two-level atom picture. Soon another group at the National Bureau of Standards (now NIST) had produced 3D OM. Along with that they developed more accurate method to measure the velocity distribution of the atoms in the OM [B13]. The estimated temperature of the cooled sodium atoms of $40 \pm 23\,\mu\mathrm{K}$ was 10 times lower than the expected Doppler limit of $T_{\mathrm{D}} = 240\,\mu\mathrm{K}$. This contradiction with the theory was a pure evidence that the understanding of the working principle of the Doppler cooling technique is not complete and can not be applied to a real atomic system. In later experiments on Cs [B14, B15] scientists noticed that the temperature depended on the polarization of the molasses beam and on the existence of external magnetic fields as well. Therefore, a new description of the mechanism was needed.

A reasonable explanation of the measurements of temperatures unexpectedly below T_{D} was given by two groups [B16, B17]. In their model they considered the multiplicity of the sublevels in the energy structure of a real atom (hyperfine structure and Zeeman sublevels) and the dynamics of optical pumping among these sublevels due to polarization gradients of the light field. This was the major difference from the previous treatment of the two-level picture.

If two linearly polarized light waves propagate against each other through the atoms in an OM, along the z axis, and their polarization vectors, $\hat{\mathbf{x}}$ and $\hat{\mathbf{y}}$, are also mutually orthogonal, the total field amplitude acting on the atoms is :

$$\begin{aligned} \boldsymbol{E} &= E_0\hat{\mathbf{x}}\cos(\omega_{_L}t - kz) + E_0\hat{\mathbf{y}}\cos(\omega_{_L}t + kz) \\ &= E_0\left[(\hat{\mathbf{x}} + \hat{\mathbf{y}})\cos(\omega_{_L}t)\cos(kz) + (\hat{\mathbf{x}} - \hat{\mathbf{y}})\sin(\omega_{_L}t)\sin(kz)\right] . \end{aligned} \tag{5.3}$$

It can be shown [B9] that the polarization of the resultant field has a strong z-

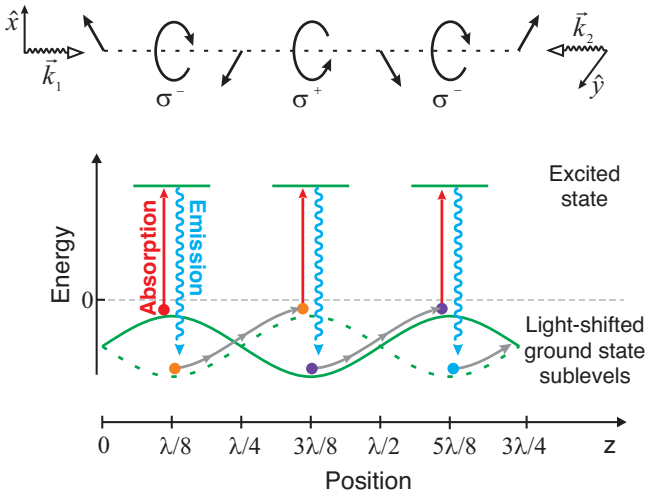

Figure 5.2 Polarization gradient cooling.

dependant elliptical polarization. At the origin, where $z = 0$, the field becomes linearly polarized but at an angle $-\pi/4$ to the x-axis (Fig. 5.2). Similarly, for $z = \lambda/4$, where $kz = \pi/2$, the field is also linearly polarized but at an angle $-\pi/4$ to the x-axis. In between these two points, at $z = \lambda/8$, where $kz = \pi/4$, the total field is

$$\boldsymbol{E} = E_0 \left[\hat{\mathbf{x}} \sin(\omega_L t + \pi/4) + \hat{\mathbf{y}} \cos(\omega_L t + \pi/4)\right] \ . \tag{5.4}$$

The last equation represents circularly polarized light rotating about the z-axis in the negative sense, because both components $\hat{\mathbf{x}}$ and $\hat{\mathbf{y}}$ have sine and cosine dependence and thus are out of phase by $\pi/2$. Similarly, at $z = 3\lambda/8$, where $kz = 3\pi/4$, the polarization is circular but in the positive sense. Fig. 5.2 illustrates how the polarization of the resulting field cycles from linear to circular to orthogonal linear to opposite circular in the space, within half a wavelength of light.

Depending on its position along z the atom interacts with a field with different polarization, and conditions for optical pumping between the atomic Zeeman sublevels are also changing periodically with the motion of the atom. On the other hand the electric field of the standing wave causes shift and broadening of the atomic Zeeman sublevels (ac Stark shift) which depends on the laser detuning, the saturation parameter, which in turn depends on on the polarization of the light and on the transition probability for the particular m_{F} sublevel that is being excited. Therefore, the energy shift of the ground state levels depends on z and follows the green curves (the solid one and the dashed one) shown in Fig. 5.2.

The key point to realize in this cooling scheme is that optical pumping between the sublevels takes a certain time, let's say τ. Then, an atom which starts at $z = \lambda/8$ and move to the right with such a velocity that it travels a distance of $\lambda/4$ for time τ. Then it always climbs a potential (the grey arrow in Fig. 5.2). However, when it reaches the $z = 3\lambda/8$, the conditions for optical pumping have changed and the atom is transferred to the lower potential, thereby emitting a photon with higher energy

than it has absorbed. Because the population density is larger in the minimum than in the maxima of the potentials, the atom climbs uphill more than downhill. It transfers part of its kinetic energy to photon energy and is therefore cooled.

A characteristic of the sub-Doppler cooling is that the final temperature depends on the laser intensity, while in the Doppler theory, it does not. The lower limit is given by the recoil temperature, which for ^{133}Cs is about 200 nK [B9].

5.2 Magneto-optical trap

In the previous section we have described the optical molasses arrangement and we have expressed the cooling force acting on the atoms. However, this force is only velocity dependant, δ and $\boldsymbol{k}$ are properties of the laser field. Therefore, although the atoms are being effectively cooled, after some time they will drift out of the optical molasses volume due to the continuous scattering of photons. In order to create a trapping action, one needs to provide a cooling force, which depends also on the position of the atoms. This is accomplished in the magneto-optical trap (MOT), where optical molasses are combined with an inhomogeneous magnetic quadrupole field [B18].

In Section 4.2 the induced energy shift of the magnetic sublevels of the atom in the presence of a magnetic field was examined. In the MOT this Zeeman shift plays a key role to the operation of the trap. The inhomogeneous field in the MOT is usually created by a pair of electromagnetic coils in anti-Helmholtz configuration. The working principle of the MOT is illustrated in Fig. 5.3 for the one-dimensional case of a two-level atom, placed in magnetic field with gradient along the z-direction. According to the chosen sign of the magnetic field on both sides of the trap center ($z = 0$ and $B_{z=0} = 0$) the atomic states will split as shown in Fig. 5.3. The ground state $|F = 0\rangle$ is not perturbed by the magnetic gradient. Nevertheless, the excited state $|F' = 1\rangle$ is split into three magnetic sublevels,$|F' = 1; m_{\text{F}'} = 0, \pm 1\rangle$. For a constant magnetic field gradient the magnetic field depends on the position coordinate z, and it can be written as $B(z) = A * z$, which gives as a result the depicted in Fig. 5.3 splitting of the atomic levels. For circularly polarized light the σ^- polarization will excite only the $|F = 0; m_{\text{F}} = 0\rangle \rightarrow |F' = 1; m_{\text{F}'} = -1\rangle$, while σ^+ - $|F = 0; m_{\text{F}} = 0\rangle \rightarrow |F' = 1; m_{\text{F}'} = +1\rangle$. An atom which travels in the region where $z \leq 0$, away from the trap center, scatters more photons from the σ^- beam and it is cooled and driven towards the MOT center. light

Similarly to the case of optical molasses, the force exerted on the atoms in MOT from two counterpropagating laser beams separately can be expressed as:

$$F_{\pm} = \hbar k \frac{\gamma}{2} \frac{I/I_{\text{s}}}{1 + I/I_{\text{s}} + 4(\delta_{\pm}/\gamma)^2} \,. \tag{5.5}$$

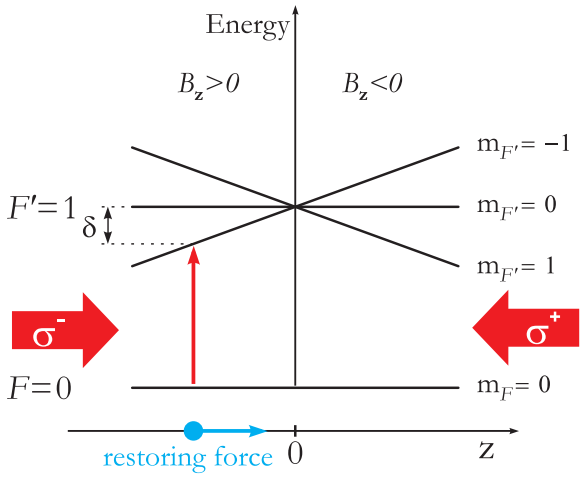

Figure 5.3 The mechanism of a magneto-optical trap illustrated for the case of an atom with a $|F = 0\rangle \rightarrow |F' = 1\rangle$ transition. In the magnetic field gradient the Zeeman splitting of the sub-levels depends on the atom's position. Two counter-propagating beams of circularly-polarized light illuminate the atom and the selection rules for transitions between the Zeeman states lead to an imbalance in the radiative force from the laser beams that pushes the atom back towards the centre of the trap.

The detunings for the two beams are

$$\delta_{\pm} = \delta_{\mathrm{L}} \mp k\, v \pm \frac{\mu' B}{\hbar}\,, \tag{5.6}$$

where δ_{L} is the laser detuning from resonance, and μ' is the magnetic dipole moment of the transition. It can be shown [B9] that for small velocities v and displacement from the trap center z the combination of the two forces from Eq. 5.5 gives a resultant force of the type:

$$F \approx -\beta\, v - \kappa\, z\,, \tag{5.7}$$

with the damping coefficient

$$\beta = -\frac{8\hbar\, k^2\, I/I_{\mathrm{s}}\delta_{\mathrm{L}}}{\gamma(1 + I/I_{\mathrm{s}} + 4\delta_{\mathrm{L}}^2/\gamma^2)}\,, \tag{5.8}$$

and the spring constant

$$\kappa = \frac{\mu' A}{\hbar\, k}\,. \tag{5.9}$$

For red detuning of the laser Eq. 5.7 describe a harmonic force with friction and thus result in both cooling and trapping of the atoms.

Chapter 6

Atomic fountain clocks

So far the main features of the energy structure of the caesium atoms and what follows from them in terms of interactions of the atom with electric and magnetic fields were presented. In this section the main terms concerning the atomic fountain as a frequency standards are discussed.

6.1 A short historical overview

The first experiments exploring this principle were performed by Zacharias [B19] in 1950s and later, in 1982, a refined proposal of the technique was made by de Marchi [B20]. The idea was to manipulate a group of slow atoms from a vertically directed thermal beam. Unfortunately, the number of atoms in the desired velocity group was not enough to obtain a sufficiently strong signal. The successful demonstration of the laser cooling techniques had changed the situation completely. It became possible to prepare ensembles of millions of cold atoms which have practically the same velocity. The first fountain for metrological use was developed at the Observatoire de Paris in France [B21]. Soon in other laboratories (PTB-CSF1[B22] at the Physikalisch Technische Bundesanstalt (PTB) in Germany, NIST-F1[B23] at National Institute of Standards and Technology (NIST) in the United States, IT-CsF1[B24] at the Instituto Elettrotecnico Nazionale (IEN) in Italy and NPL-CsF1[B25] at the National Physical Laboratory (NPL) in UK) were put into operation fountain setups with some variations in the design, mainly in the relative spatial arrangement of the cavities and the detection zone.

6.2 The atomic fountain clock CSF2 at PTB. Construction and operation.

In 2006 the second fountain clock PTB-CSF2 developed at PTB became operational [B26].

Figure 6.1 represents a simplified schematic drawing of the vacuum subsystem of the CSF2 fountain clock. An ion getter pump, attached to the bottom of the structure, reduces the residual gas pressure in the preparation zone to 8×10^{-6} Pa. There, the caesium atoms are cooled in optical molasses and a reservoir with ^{133}Cs, kept at room temperature, provides the atomic vapor which feeds the molasses. In the next stage of the fountain cycle, the cold atoms are launched vertically by the "moving molasses" technique. Immediately after that the ensemble is further cooled by exposing it to a process of polarization gradient cooling. Subsequently the atoms pass first through a state-selection cavity and then through a detection region, where the atomic ensemble is "purified" by laser light so only atoms in the $|F = 3, m_F = 0\rangle$ state are left to continue their travel towards the Ramsey cavity. The state-selection cavity is mounted 18.5 cm above the cooling zone. The detection region is located 30 cm above the cooling zone. It consists of two zones which are vertically separated by 2.3 cm. The two zones are used to separately detect the atoms in the $|F = 4\rangle$ (upper zone) and $|F = 3\rangle$ (lower zone) after the Ramsey interrogation cycle.

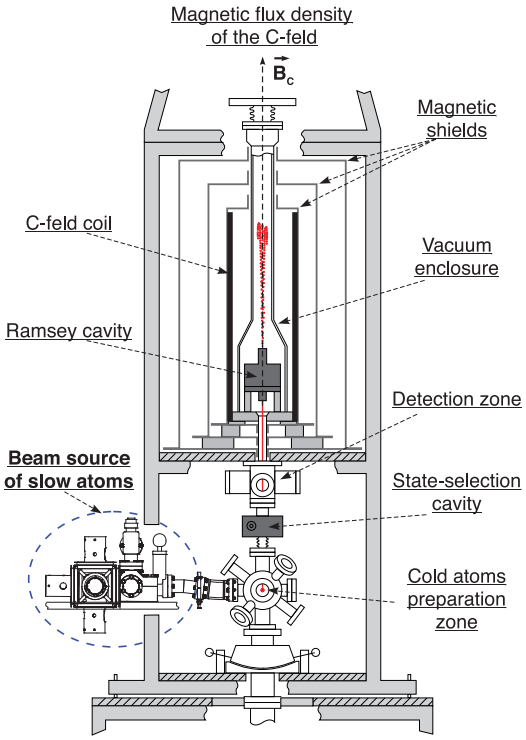

Figure 6.1 A schematic diagram of the CSF2 fountain clock.

The heart of the clock is the microwave cavity, where the Ramsey interaction occurs. A lot of effort has been put into the development and perfection of these devices. The atoms pass twice through the cavity and interact with the microwave field, once on their way up and again on their way down. This is an advantage of the fountain approach over the thermal beam clocks, since the end-to-end cavity phase shift [B27, p. 210] is eliminated. The cavity used in CSF2 is made from OFHC copper and has cylindrical geometry, with inner dimensions of 48.4 mm diameter and 28.5 mm height. The microwave field is fed through two slits at diametrically opposite positions of the cavity (Fig. 6.2). Additionally, two openings with diameter of 10 mm are made along the cylinder axis to allow for the atoms to pass through the cavity. Since the atomic cloud expands during its ballistic flight, generally, atoms will cross the microwave field at different positions on each pass trough the cavity. Thus the cavity is designed such that the microwave field excites the TE_{011} mode of the cavity and sustains low transverse phase variations of the microwave field across the 10 mm cavity openings [B28]. The Ramsey cavity is positioned 63.5 cm above the cooling

zone. The atoms are typically launched to 36.5 cm above the Ramsey cavity, resulting in Ramsey interaction time T_{R} of 0.54 s.

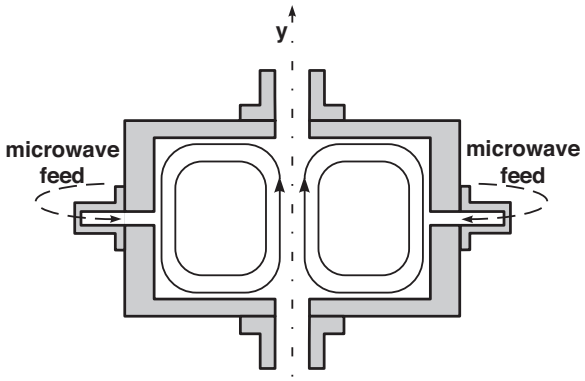

Figure 6.2 Sketch of the magnetic microwave field in the TE_{011} mode in the Ramsey cavity. The dotted-dashed line represents the axis of rotational symmetry of the cylindrical cavity and the atomic trajectory.

Diode lasers provide the light for cooling and probing of the atoms. Acousto-optical modulators (AOM) are used to achieve the various desired frequency detunings of the laser light for the cooling, launching, post-cooling and probing stages of the fountain cycle. The output frequency of the lasers is actively stabilized with a saturation spectroscopy setups, which results in linewidth of the lasers radiation ≤ 1 MHz. A Distributed Bragg Reflector (DBR) laser oscillates at a frequency which excites the center of the $|F = 3\rangle \rightarrow |F' = 4\rangle$ atomic transition. It is used for repumping in the OM and for probing the atoms in the detection zone of the fountain as well. An additional external-cavity diode laser, with frequency in the vicinity of the cycling atomic transition $|F = 4\rangle \rightarrow |F' = 5\rangle$, is used to deliver the light for cooling and detecting the atoms in the $|F = 4\rangle$ state .

The spatial orientation of the laser beams in the preparation zone of the fountain utilizes the so called "(1,1,1)" geometry. It can be imagined that the laser beams run along the six face normals of a cube, while its space diagonal fully overlaps with the fountain vertical axis. So three beams are pointing downwards, each at an angle of 54.4° with respect to the vertical and three beams are pointing upwards. This geometry allows for large diameters of the laser beams used for the optical molasses and leads to less stray light in the cavities and the drift region. The laser light is delivered to the preparation zone by six polarization-maintaining optical fibers. Collimator assemblies, which are attached to the fountain structure, are used to create collimated laser beams of 25 mm diameter ($1/e^2$ intensity level) in the OM zone. In the initial setup the cooling laser was co-propagating with the repumping laser light in all fibers but afterwards it was changed and the repumping light was introduced only along the fountain vertical axis as explained later in the experimental part. The polarization of the field in each pair of counterpropagating laser beams constitutes the lin$\perp$lin configuration, which was discussed earlier.

During the optical molasses loading, the frequency ν_L of the cooling laser is detuned $\sim 11\,\mathrm{MHz}$ below the cycling transition $|F=4\rangle \rightarrow |F'=5\rangle$. After the loading phase the frequency of the three laser beams pointing downwards is further red-detuned by an amount of $\delta\nu$ with respect to the cooling frequency ν_L. Simultaneously the frequency of the three beams pointing upwards is blue-detuned by the same amount of $\delta\nu$. Consequently, the phase front of the resulting field in the intersection volume of the laser beams will move upwards with a speed of $v = \lambda\delta\nu\sqrt{3}/2$. In the moving frame with velocity v the atoms will still be continuously cooled as they do not experience the change of the cooling frequency ν_L, while in the rest frame they will move with speed v in the direction of the fountain vertical axis. In CSF2 the atoms are launched by the moving molasses with speed of $\sim 4.4\,\mathrm{m/s}$. After the launch, the ensemble of atoms is further cooled by optimized process of polarization gradient cooling. In this post-cooling phase the optical frequency of all of the cooling laser beams is further detuned to about $\sim 68\,\mathrm{MHz}$ below the cycling transition and simultaneously the light intensity is extinguished. The repumping light is switched off several milliseconds after the cooling light allowing for the majority of the atoms to be transferred to the $|F=4\rangle$ ground state component. However, they are distributed among the $|F=4, m_F\rangle$ atomic substates, where $m_F = -4, -3, ..., 3, 4$. This marks the beginning of the ballistic flight of the atomic sample through the rest of the vacuum system.

Next, the atoms reach the state-selection cavity, where they interact with a microwave π-pulse. The frequency of the microwave field is tuned to the atomic microwave resonance and the magnetic field inside the cavity is oriented vertically. In these conditions the excitation probability is maximized for the $|F=4, m_F=0\rangle \rightarrow |F=3, m_F=0\rangle$ transition. Subsequently, the cloud reaches the upper detection zone where the atoms are irradiated by a near-resonant laser light. The frequency of the laser is tuned about $2\,\mathrm{MHz}$ above the cycling transition $|F=4\rangle \rightarrow |F'=5\rangle$. The light field transfers momentum to the atoms in the $|F=4, m_F\neq 0\rangle$ states in a running wave configuration so that they are effectively removed from the flying sample.

Above the detection zone, the atoms enter the interaction region of the fountain which is enclosed from the outside by three layers of magnetic shields. They are made from high permeability μ-metal. Additionally, a long precision-wound coil is placed between the drift tube of the fountain including the Ramsey cavity and the magnetic shields. The coil produces magnetic field with high homogeneity, the so called "C-field", along the interaction region, that spreads from the Ramsey cavity up to the apogee of the atomic ballistic flight. The purpose of the C-field is to define a quantization axis which is along that of the fountain and to remove the degeneracy of the atomic states for different values of the magnetic quantum number m_F.

The power of the microwave field inside the Ramsey cavity is chosen in such a way that on resonance a maximum number of atoms is transferred from the $|F=3, m_F=0\rangle$ to the $|F=4, m_F=0\rangle$ state. Such optimization results in a nominal π pulse area.

The final stage of the fountain cycle is the readout of the transition probability acquired by the Ramsey interaction. After the second pass through the Ramsey cavity

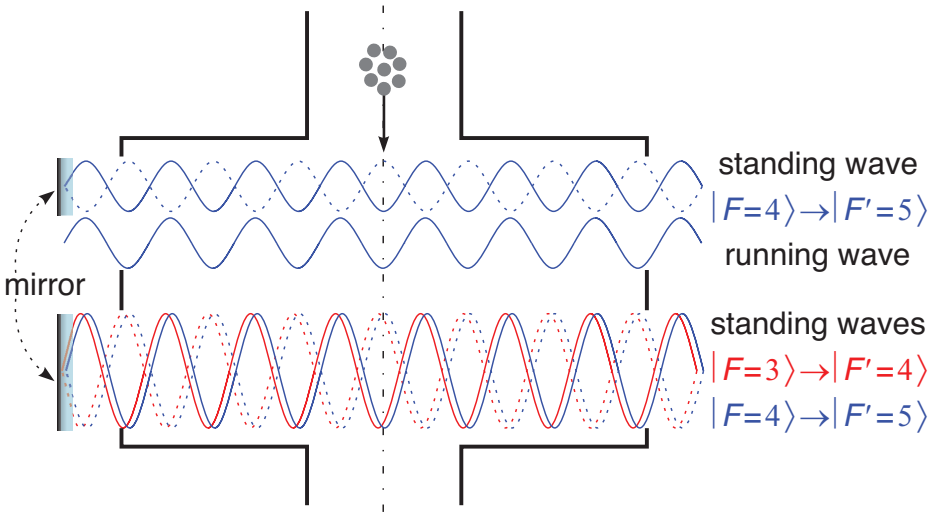

Figure 6.3 A schematic diagram of the detection region of the fountain. Light from a single laser is sent to both detection zones, perpendicularly to the atomic trajectory. The frequency of the field drives the cycling transition $|F = 4\rangle \rightarrow |F' = 5\rangle$. Both laser beams are retroreflected by a mirror to create standing waves in the detection zones. In the lower part of the upper zone the light is blocked before the mirror, thereby a running wave is created. A laser beam, delivered by a second laser with frequency driving the $|F = 3\rangle \rightarrow |F' = 4\rangle$ transition is sent only to the lower detection zone.

the atoms cross the detection region of the fountain, shown in Fig. 6.3. First, the atoms in the $|F = 4\rangle$ state are probed by the laser field of the standing wave in the upper detection zone. The scattered photons are imaged onto a photodiode by an optical system whose optical axis is orthogonal to the trajectory of the atoms and to the wave vector of the laser field. The time-integrated signal of the photodetector,N_4, is proportional to the number of atoms in the $|F = 4\rangle$ state. Subsequently, the falling sample passes through the running wave region of the upper zone, where the atoms in $|F = 4\rangle$ are pushed away from the cloud.

The atoms left in $|F = 3\rangle$ approach the lower detection zone, where they are first optically pumped to the $|F = 4\rangle$ state by the field of the $|F = 3\rangle \rightarrow |F' = 4\rangle$ standing wave and then are detected by their fluorescence on the $|F = 4\rangle \rightarrow |F' = 5\rangle$ transition. A second optical system, completely identical with the one in the upper detection zone, images the scattered by the atoms light onto another photodiode in opposite direction to the first one. This time the photodetector signal,N_3, is proportional to the number of atoms in the $|F = 3\rangle$ state.

The ratio $S = N_4/(N_3 + N_4)$ is used to determine the transition probability due to the Ramsey interaction. This ratio S is independent of the shot-to-shot fluctuations in atom number and is used as an input signal to the microwave frequency servo loop. A typical Ramsey fringe pattern is given in Figure 6.4.

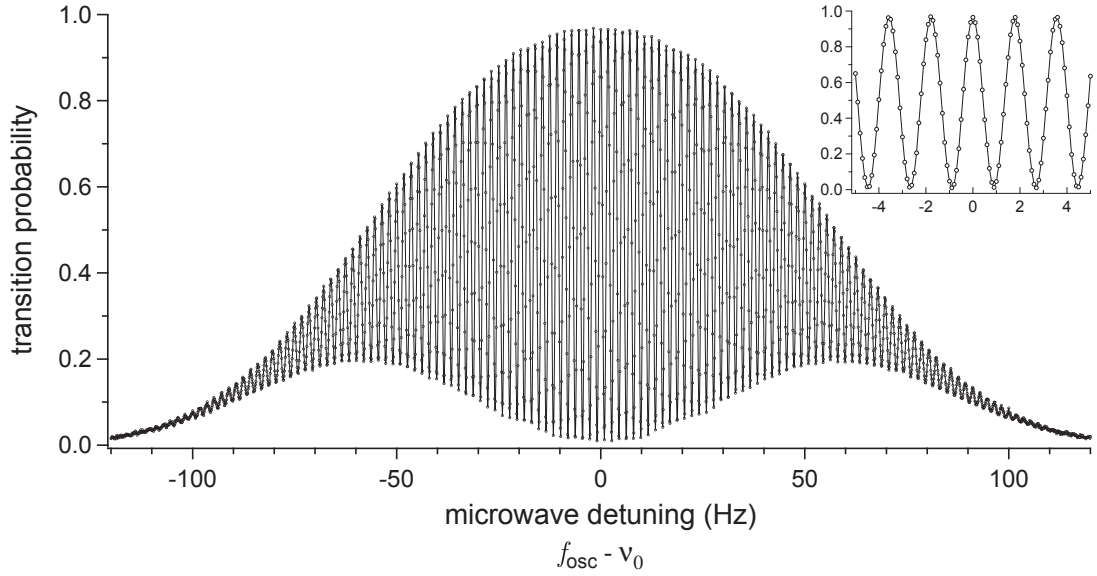

Figure 6.4 Measured Ramsey fringe pattern for CSF2 fountain clock (dots). Inset: the central part enlarged. The central fringe has a contrast of 95% and a width of 0.9 Hz. The solid lines are to guide the eye.

6.3 Absolute frequency measurements with a fountain clock

The fountain system on its own is not a clock. It can be thought of as a passive frequency standard since one needs an interrogation signal which provides information about the atomic transition frequency. Thus an electronic system must be associated with the fountain to produce a signal whose frequency is locked to the atomic resonance. Several different configurations are used for the synthesis of the microwave signal for the state-selection cavity and for the Ramsey interaction [B22, B29, B30, B31].

For example a low-noise BVA (Boîtier à Vieillissement Amélioré, Enclosure with Improved Aging) voltage-controlled quartz-crystal oscillator (VCO) generates a signal at 5 MHz. The interrogation microwave signal at 9192 MHz is obtained by frequency synthesis. For example the output frequency of the voltage-controlled oscillator is upconverted to 9200 GHz by means of frequency multiplication. This signal is mixed with the 7.36 MHz output of a radio-frequency synthesizer and the generated signal, at frequency 9192.63 MHz feeds the cavity for probing the atomic transition. The frequency synthesizer is also referenced to the 5 MHz output of the crystal oscillator. In order to lock the frequency, $f_{\rm osc}$, of the interrogating microwave signal to the frequency, ν_0, of the atomic resonance, the maximum of the central Ramsey fringe, the output frequency of the synthesizer is square-wave modulated at a low rate. The depth of modulation is set to about half of the width of the central fringe $\Delta\nu/2$

(Figure 6.5).

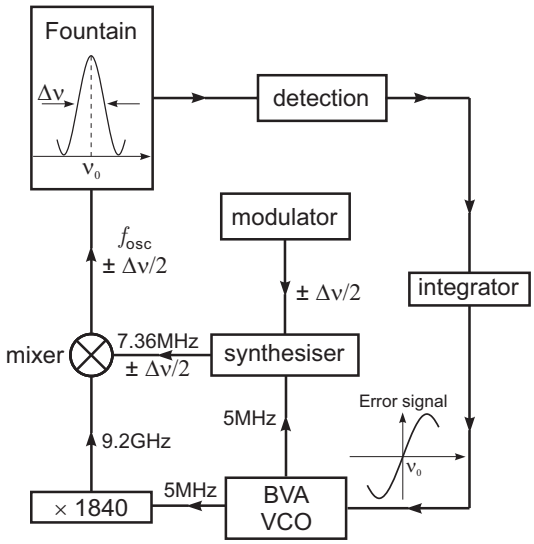

Figure 6.5 Block diagram of the frequency control of a quartz oscillator using the atomic hyperfine transition.

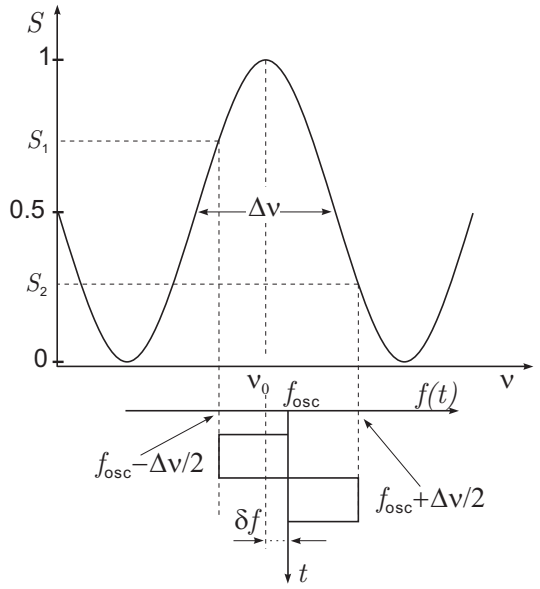

Figure 6.6 Schematic diagram of the response of the atomic fountain, in terms of measured transition probability S, to a square-wave frequency modulation of the interrogating microwave field $f_{\rm osc}$. The modulation amplitude is set to a half of the width of the central Ramsey fringe.

In general $f_{\rm osc}$ defers from ν_0 by some amount δf. The frequency of the interrogating microwave field is continuously altered on both sides of the central fringe. Within one fountain cycle the frequency is set at $(f_{\rm osc} + \delta f - \Delta\nu/2)$ while during the next cycle it is switched to $(f_{\rm osc} + \delta f + \Delta\nu/2)$. At the end of each fountain cycle the normalized number of atoms (the ratio S) having made the transition is measured, as explained earlier. The difference in the two transition probabilities, S_1 and S_2 in Figure 6.6, is a measure for the agreement of $f_{\rm osc}$ with the maximum of the Ramsey fringe. The process is repeated and the obtained signal is integrated by digital processing over several fountain cycles in order to construct an error signal as a function of $f_{\rm osc}$. This error signal is then used to lock the interrogating frequency to the maximum of the central Ramsey fringe, making the detuning δf virtually zero, by applying a correction voltage to the VCO. In this case the output frequency of the VCO represents the atomic resonance frequency ν_0.

Unfortunately, the measured frequency, where the maximum of the central Ramsey fringe is positioned, differs from the frequency of the unperturbed atomic hyperfine transition $\nu_{\rm HFS} = 9\,192\,631\,770\,\text{Hz}$. Typically this difference is of the order of 1 mHz and it is governed by the clock parameters stability and accuracy. The accuracy of the frequency measurement is discussed in the next paragraph.

6.4 Frequency accuracy. Frequency shifts and their uncertainties in CSF2.

Although the procedure for measuring the frequency of the atomic hyperfine transition looks straightforward the measured frequency ν_0 is subject to frequency biases and differs from the unperturbed frequency ν_{HFS}. The presence of certain physical phenomena causes frequency shifts and the realization of a clock as a primary standard requires their precise evaluation. Finally, the output frequency of the standard must be corrected for the corresponding offsets. Usually it is assumed that these processes are not correlated and the uncertainties in the evaluation of the magnitude of each individual shift add up in quadrature to give the overall uncertainty of the corrected frequency of the standard.

Some of the effects which cause frequency shift from the unperturbed clock frequency and have the largest uncertainty in their evaluation in the case of CSF2 fountain, are briefly described in the following. A complete analysis and extensive explanation of all known physical phenomena which are sources of frequency biases of the clock frequency can be found in the book by Vanier and Audoin [B32].

Quadratic Zeeman effect.

Between the Ramsey interactions, the atoms in the drift tube of the fountain travel in a region of weak nonzero magnetic field. The C-field, used to remove the degeneracy of the m_F Zeeman components, causes a second-order Zeeman shift of the clock transition frequency. Then the measured frequency ν of the clock transition is given by the equation [B32, Volume 1, Table 1.1.7]:

$$\nu = \nu_{\text{HFS}} + \nu_{\text{C}} = \nu_{\text{HFS}} + 427.45 \times 10^8 B_{\text{C}}^2 \,, \tag{6.1}$$

where

ν_{HFS} is the unperturbed hyperfine frequency defined as 9 192 631 770 Hz

ν_{C} is the second-order Zeeman shift

B_{C} is the applied magnetic field induction in Tesla.

This is the most important shift in the frequency standard and must be determined with an accuracy corresponding to the accuracy desired in the final evaluation. Furthermore, field fluctuations must be minimized for reasons of frequency stability. This constraint forces the use of efficient magnetic shielding around the Ramsey cavity. A practical way to determine the magnitude of the magnetic flux density is to measure the frequency shift $\nu_Z = 700.84 \times 10^7 \, m_F \, B_{\text{C}}$ of a first-order field-sensitive transition, usually the $|F = 4, m_F = -1\rangle \rightarrow |F = 3, m_F = -1\rangle$. The fountain arrangement allows for different heights h of launching of the atomic cloud. The technique is used for mapping the magnetic flux density in the drift tube and gives access to the homogeneity of the C-field along the atomic trajectory. The calculated value for $B_{\text{C}}(h)$ at different positions above the Ramsey cavity is used to determine the average value $\langle B_{\text{C}} \rangle = 147.12\,\text{nT}$ of the magnetic induction. The corresponding rela-

tive frequency correction of the clock transition due to the second-order Zeeman shift is $\nu_{\rm C}/\nu_{\rm HFS} = -1006.43 \times 10^{-16}$ [B33]. The uncertainty of the shift due to magnetic field inhomogeneity is estimated to be on the order of 2×10^{-19}. Observation of the magnetic field instability over a period of months shows monthly variation of ν_z of less than 0.3 Hz. Such variation corresponds to an uncertainty of the second-order Zeeman shift correction on the order of 0.59×10^{-16}.

Black-body radiation shift.

The thermal radiation of the vacuum enclosure of the fountain causes ac Stark shift of the output frequency of the standard. If this radiation gives rise to a spectral power density which is equivalent to that of a black body, according to [B34, B35], the clock transition frequency is shifted by

$$\nu_{\rm BB} = k_0 \, E_{300\rm K}^2 \left(\frac{T}{300\,\rm K}\right)^4 \times \left[1 + \epsilon \left(\frac{T}{300\,\rm K}\right)^2\right] , \tag{6.2}$$

where

$k_0 = -2.282(4) \times 10^{-10}\,\rm Hz/(V/m)^2$ is the scalar dc polarizability of the clock transition [B36]

$E_{300\rm K} = 831.9\,\rm V/m$ is the rms electric field of the black body radiation at $T_0 = 300\,\rm K$ from Stefan-Boltzman's law [B34]

T is the temperature of the vacuum enclosure in Kelvin

ϵ is a constant that has a value of 0.013(1) [B37].

In CSF2 four PT100 sensors are located along the drift tube of the fountain. They are used to determine the average value of the temperature T with measurement uncertainty of 0.2 K. The relative frequency correction of the clock transition due to the black-body radiation is calculated to be $(164.54 \pm 0.76) \times 10^{-16}$ [B33].

Collisional shift.

The collisions among the cold atoms in the cloud constitute another major source of uncertainty; they also induce a frequency shift in the output of the fountain [B38]. The magnitude of the shift depends on the rate of the collisions, which in turn is a function of the atomic cloud density, the relative speed of the atoms (temperature) and the collisional cross-section [B39].

The design of CSF2, in particular the large-beam molasses and the (1,1,1) geometry, allow for the preparation of less dense cold sample with more uniform density distribution. Therefore CSF2 has some advantages over the fountains using MOT for cooling the atoms instead, which produce more dense and smaller size samples. For the same number of Ramsey interrogated atoms, the collisional shift will be smaller in CSF2. A 1D temperature of the cloud of $T \approx 600\,\rm nK$ is inferred by measuring the change of the spatial distribution of the atoms during their ballistic flight in between the two Ramsey interactions. Time-of-flight measurements in the detection zone of

the fountain are used to determine the expansion of the cloud during its ascent and descent [B1].

The traditional approach in evaluation of the collisional shift is to measure the clock's output frequency for two or more effective densities of the atomic cloud and then extrapolate to zero density. Because the frequency shift is linear in effective atom density, one can extrapolate by using a linear regression. This is the method currently employed by all primary fountain clocks. Since the actual density of the cloud is not readily accessible in the experiment, one substitutes the number of detected atoms N_{at} instead. This, of course, assumes that there is a strict proportionality between N_{at} and effective density. A collisional shift slope is derived from the frequency difference and the detected atom numbers corresponding to high and low density. The collisional shift value and uncertainty are obtained by multiplying the slope factor and its uncertainty by the detected atom number, respectively. However the alteration of the density of the atomic cloud in the conventional methods, such as a $\pi/2$ microwave pulse interaction in the state-selection cavity, is usually accompanied by a change of the velocity of the atoms in the cloud and its distribution. This inevitably leads to an inaccurate extrapolation to zero density. It has been demonstrated [B40] that the use of this method could not provide accuracy in the determination of the collisional shift better than 10%–20%.

Alternatively a rapid adiabatic passage (RAP) technique for precise alternation of the cloud density is utilized in CSF2 [B41]. This method relies on the fact that the population of state $|F = 4, m_F = 0\rangle$ can be transferred with 100% efficiency into state $|F = 3, m_F = 0\rangle$ if the frequency of the microwave radiation inside the selection cavity is subjected to a linear sweep in a well-controlled manner. One has to ensure that the rate of change of the microwave frequency is much lower at all times than the square of the Rabi frequency (which is proportional to microwave power). When the pulse is switched off abruptly exactly at zero detuning the atoms are left in an exactly equal superposition of both states. The important feature of the rapid adiabatic passage is that this happens independently of the actual Rabi frequency an atom sees, i.e., it does not depend on where an atom passes through the field inside the cavity (the field amplitude decreases across the aperture when going away from the center). The pushing beam in the detection zone therefore removes exactly half of all atoms, without changing the density distribution, temperature, or velocity of the cloud—in contrast to the other methods where such changes cannot be excluded.

The employed RAP method sets the systematic uncertainty below 1% of the determined value of the collisional shift. Typically, an overall collisional shift uncertainty of 2.6×10^{-16} is obtained [B41], dominated by the statistical uncertainty of the slope factor. To improve the collisional shift uncertainty for fixed measurement times, operation with increased atom numbers is necessary. The resulting improved instability will reduce the statistical uncertainty of frequency measurements and the slope factor statistical uncertainty at the same time.

A number of schemes have been devised to reduce the collisional shift or at least its contribution to the uncertainty budget of the caesium fountain clock, for instance

by lowering the density of the atomic cloud and therefore the collision rate. A reduced number of atoms, however, reduces the detected signal and therefore the signal-to-noise ratio and the short-term stability. An extensive overview of the techniques used to decrease the collisional shift is given in [B2].

Other sources of frequency shifts such as *Light shift, Majorana transitions* [B1], *Rabi and Ramsey pulling* [B42], *Distributed cavity phase (DCP) and Microwave lensing* [B33] are evaluated with uncertainties which lie well below the 10^{-16} range. Comprehensive information on their evaluation can be found in the assigned references.

6.5 Frequency (in)stability of a fountain clock

The experimental study presented in this part of the thesis targets directly the question of the achievable short-term stability of the frequency measurements performed with an atomic fountain. Accordingly, it naturally follows that the physical processes and effects which determine and limit the fountain stability must be considered, before an approach to handle with them is described.

The information about the coincidence of the frequency of the interrogating microwave field with the atomic resonance frequency is gathered by detection of fluorescence photons. It follows, therefore, that the frequency stability is limited by the presence of random fluctuations in the number of photons arriving at the detector, or noise, as seen by the detection system. Moreover, the stability of the fountain output frequency depends on the time behaviour of various biases that affect the frequency of the resonance. The origin of these biases and the uncertainties associated with their evaluation will be described later.

The relative frequency instability of a fountain clock expressed by the Allan standard deviation can be written as [B43]

$$\sigma_y(\tau) = \frac{1}{\pi\, Q_{\mathrm{at}}} \sqrt{\frac{T_c}{\tau}} \left(\frac{1}{N_{\mathrm{at}}} + \frac{1}{N_{\mathrm{at}} n_d} + \frac{2\,\sigma_{\delta N}^2}{N_{\mathrm{at}}^2} + \gamma \right)^{1/2} \tag{6.3}$$

where

- τ is the measurement (or averaging) time in seconds
- T_c is the duration of a cycle of the measurement. It includes the time necessary for cooling and preparation of atomic sample, state selection and Ramsey interrogation and detection.
- $Q_{\mathrm{at}} = \nu_{\mathrm{HFS}}/\Delta\nu$ is the atomic quality factor with $\Delta\nu$ the width of the central Ramsey fringe, and ν_{HFS} is the hyperfine splitting of the clock transition.

Equation 6.3 contains the main noise components being identified, which degrade the signal observed and affect the fountain frequency stability. But before looking in more details at their individual origin it is still possible to extract an important essence out of it. As can be seen several terms appear in the brackets in the equation

above and three of them depend explicitly on the number of detected atom, N_{at}, after the microwave interrogation and only the first depends purely on it. In one particular situation, which is relevant to the presented study, the influence of the last three terms can be brought down to such a level that only the first term dominates and determines the stability of the fountain. This special regime of fountain operation is called quantum projection noise limited regime [B43] and thereby the Allan standard deviation of the relative frequency measurements will decrease if N_{at} is enhanced. This will be demonstrated in section 7.5 of the thesis. Of course there are some limitations to that avenue and they will be mentioned as well.

The first term in Equation 6.3 is a direct reflection of the probabilistic nature of quantum mechanical processes. Again the two level atom is a wonderful example to begin with. Suppose that the atom is prepared in a linear superposition of both pure states $|g\rangle$ and $|e\rangle$. Then the system can be described by a single quantum state vector of the form $|\Psi\rangle = \alpha\,|g\rangle + \beta\,|e\rangle$ and the coefficients α and β are normalized such that $|\alpha|^2 + |\beta|^2 = 1$ holds. Generally, any measurement performed over the system which indicates whether it is in state $|g\rangle$ or state $|e\rangle$ would result in probabilistic distribution of the results. Except for the trivial case when α or $\beta = 0$ the outcome of the measurement cannot be predicted with certainty and the probability to find the system in state $|g\rangle$ is simply $p_{_g} = |\alpha|^2$. Respectively the chance for the system to occur in state $|g\rangle$ is given with probability $p_{_e} = |\beta|^2$. The analog with the fountain clock, where caesium atoms in the cold sample are interrogated by a microwave field, is complete. For each fountain cycle the frequency of the microwave field is set off of the maximum of the central Ramsey fringe by about one half linewidth. This means that the ensemble is left in equal superposition of both hyperfine components,$|F = 3\rangle$ and $|F = 4\rangle$. So noise in the detection arises from this unpredictability of the emission process.

The effect was named *quantum projection noise* and has been experimentally observed by Itano *et al.* [B44]. They have measured the populations of the energy levels in two different quantum systems – a single $^{199}\mathrm{Hg}^{+}$ ion in a linear rf trap and multiple (up to 400) $^{9}\mathrm{Be}^{+}$ ions in a Penning trap. Ramsey's method of separated fields was used in both experiments to prepare the system in a particular superposition of the pure ionic states and the readout of the final population was done by detecting a signal from laser-induced fluorescence. In the single-particle experiment the ion was successively prepared under identical conditions and the results were obtained by averaging the outcomes of the subsequent measurements in order to simulate an ensemble behaviour. It has been demonstrated that for a system containing N_{at} uncorrelated particles the fluctuations or the variance of the atoms which have made the transition due to quantum projection noise is $(\Delta N_{\mathrm{QN}})^2 = N_{\mathrm{at}}\,p_{_e}(1 - p_{_e})$. Finally, the quantum noise effect must be taken into account when a frequency measurement as in the case of a fountain clock is realized. The uncertainty in the number of detected atoms is reflected in fluctuations in the number of photons as observed at the detector and thus influences the stability of the frequency measurement. The standard deviation of frequency fluctuations scales as $N_{\mathrm{at}}^{-1/2}$.

The information about the sate of the probed atoms comes from detecting fluorescence photons which result from a random process, spontaneous emission. This implies that the measured resonance frequency is subject to additional noise, generally called shot-noise. The second term in Equation 6.3, which also depends on the number of detected atoms N_{at}, accounts for the photon shot-noise. The parameter n_d corresponds to the real detected photons scattered by a single atom. An expression for it can be given in the following form

$$n_d = n_{ph}\,\varepsilon_c\,\varepsilon_d \tag{6.4}$$

where

$n_{\boldsymbol{ph}}$ is the number of fluorescence photons emitted per atom
$\varepsilon_{\boldsymbol{c}}$ is the efficiency of the collection of the photons at the detector
$\varepsilon_{\boldsymbol{d}}$ is the efficiency of the detector.

The two optical systems used in CSF2, for detection of the atoms in the $|F = 3, m_F = 0\rangle$ and the $|F = 4, m_F = 0\rangle$ atomic states, image the corresponding fluorescence volumes on large-area ($1\,\mathrm{cm}^2$) photodiodes. As a result, photon detection efficiencies, the quantity $\varepsilon_c\,\varepsilon_d$, of several percent have been achieved. Furthermore, the high number of scattered photons ($\sim 10^4$) per atom ensures that the atom detection efficiency is close to 100 %.

It is worth mentioning that noise can be generated in the electronics of the detection system (e.g. transimpedance amplifiers), as well and thus degrades the fountain stability. Generally in well-designed systems this electronic noise is made negligible by means of proper choice of components.

The caesium atoms, which are interrogated during each clock cycle, have been cooled in an optical molasses before they are launched vertically. Therefore, fluctuations in the number of launched, and respectively detected atoms from shot-to-shot are very likely to occur. This also induces fluctuations $\delta N_{ph}(t_{\mathrm{k}})$ in the detected photons in each clock cycle. Here t_{k} denotes the time at which the measurement has been taken. The series $\{\delta N_{ph}(t_{\mathrm{k}})\}$ of the fluctuations $\delta N_{ph}(t_{\mathrm{k}})$ is a sequence of random variables which has the properties of a white noise process with zero mean and variance $\sigma^2_{\delta N_{ph}}$ [B45]. However, what is more easily accessible to measurement, after the atomic line has been probed on both sides, is the quantity $\delta N(t_{\mathrm{k}}) = \delta N_{ph}(t_{\mathrm{k}}) - \delta N_{ph}(t_{\mathrm{k-1}})$, and its variance is $\sigma^2_{\delta N} = 2\sigma^2_{\delta N_{ph}}$. The influence of this type of noise on the clock stability is accounted by the third term in Equation 6.3, and it can be also neglected in our experiment due to the large number, on the order of 10^6, of detected atoms.

In contrast to the more traditional atomic resonators, in the atomic fountain the atoms are interrogated periodically. The process of cooling the atoms and preparing them in a desired quantum state requires some time, and the frequency of the quartz oscillator is not continuously controlled by the atomic resonance signal. This, so called "dead" time in the clock cycle, results in a degradation of the fountain frequency stability, caused by the frequency noise of the local oscillator. The effect has been firstly described by G. John Dick [B46],hence its name "Dick" effect. The last term,

γ, in Equation 6.3 accounts for noise contributions from the local oscillator and it represents one of the hardest for overcoming barriers which limit the stability of the fountain clocks. This subject has been addressed and extensively studied in several other papers [B47, B48, B45].

The issue is that even with the state-of-the-art VCOs used today the fountain posses short-term fractional instability limited to about $10^{-13}\,(\tau/\mathrm{s})^{1/2}$ [B47]. Hence it is possible to go beyond that value either by decreasing the "dead" time between the measurements or by using a microwave source with better noise characteristics than the VCO's.

6.6 Limiting the local oscillator noise

Several experimental techniques have been suggested in order to reduce the Dick effect in the fountain clocks. In one of them a scheme for realization of the apparatus of a continuous fountain is proposed [B49], which in practice would function without any "dead" time between the measurements. In a theoretical study performed by Joyet *et al.* [B50] the benefits of using a continuously operated Ramsey resonator are explained. It is shown that no frequency instability due to aliasing is induced if the period of modulation of the phase of the interrogating microwave field equals twice the Ramsey interaction time. Later, the operation of such a fountain has been experimentally demonstrated, where the quantum noise limited regime is reached and fractional frequency stability of $6 \times 10^{-14}\,(\tau/\mathrm{s})^{1/2}$ is measured [B51].

Another approach to reduce the Dick effect in a pulsed atomic fountain has been demonstrated by Santarelli *et al.* [B43]. In their experiment they have made use of the superior short-term stability (below 10^{-14} up to 10 s) and phase noise properties of a cryogenic sapphire oscillator (SCO) as a local oscilator. The frequency measurements, being limited only by the quantum projection noise, showed fractional frequency stability of $6 \times 10^{-14}\,(\tau/\mathrm{s})^{1/2}$ when the number of interrogated atoms was $N_{\mathrm{at}} = 2.7 \times 10^6$. In 2004 Bize *et al.* [B52] has reported measured fractional frequency stability of $1.6 \times 10^{-14}\,(\tau/\mathrm{s})^{1/2}$ by employing a beam source of decelerated atoms [B53] to increase the number of atoms in the fountain cycle up to $N_{\mathrm{at}} = 10^7$.

Although the above methods are effective in reducing the contribution of the Dick, certain pitfalls exists in their practical application. The realization of a continuous fountain setup involves numerous of technical and experimental challenges to be addressed. For instance, no stray laser light must be present in the Ramsey interaction region – need for a "light trap" [B54]; a special microwave cavity must be designed due to the parabolic path of the atoms during their free flight between the interactions [B55]. Furthermore, the expenses associated with maintenance and cooling of the CSO oscillator to a cryogenic temperature makes this method also not preferable in long-term operation. Alternatively, an optically stabilized microwave source for synthesis of the 9.192 MHz microwave signal can be used [B56].

In the last decade a considerable advances in frequency stabilization techniques

of diode lasers have been made [B57, B58]. Locking the output frequency of such a laser to an environmentally isolated cavity with high-finesse provides optical frequency sources with relative instabilities of $\sigma_y(1\,\mathrm{s}) = 2 \times 10^{-15}$ [B59]. In addition, the invention and development of mode-locked lasers allow for transferring this stability to a source in the microwave range of the frequency spectrum which is superior to the noise characteristics of all available crystal oscillators in that range [B60, B61].

In Figure 6.7 is presented a block diagram of the frequency synthesis chain used in our experiment. The output frequency, $\nu_{\mathrm{L}} \approx 344\,\mathrm{THz}$, of a 871 nm extended cavity diode laser (ECDL) is stabilized to a high-finesse cavity made of ultra-low expansion glass (ULE cavity). A laser linewidth of less than 1 Hz and relative frequency instability of $\sigma_y(\tau) \leq 2 \times 10^{-15}$ is obtained for averaging times $0.3\,\mathrm{s} \leq \tau \leq 30\,\mathrm{s}$[B62]. A commercial erbium-doped fiber-based optical frequency comb (FOFC) is used as a transfer oscillator of the ECDL stability to a dielectric resonator oscillator (DRO). The used FOFC emits in the wavelength range around 1550 nm and the DRO output frequency is $\nu_{\mathrm{DRO}} = 9.6\,\mathrm{GHz}$, which is used to provide interrogation signal for the fountain. Here only the concept of the method will be briefly described without going into details of the practical implementation of the technique. More information can be found in Ref.[B61]. The idea is by proper mixing of the frequencies ν_{L}, ν_{DRO} and one of the spectral components of the FOFC to derive a transfer signal ν_{t} which is a function of ν_{L} and ν_{DRO} only and does not depend on the comb parameters such as pulse repetition rate f_{rep} and the carrier-envelope offset frequency f_{CEO}. This transfer signal is further used to phase-lock the output frequency of the DRO.

The optical frequency of each spectral component at the output of the mode-locked laser is fully characterized by the pulse repetition rate, f_{rep}, and the carrier-envelope offset frequency f_{CEO} and can be expressed as

$$\nu_{\mathrm{m}} = \mathrm{m} f_{\mathrm{rep}} + f_{\mathrm{CEO}} \ , \tag{6.5}$$

where m is an integer number which represents the $\mathrm{m}^{-\mathrm{th}}$ teeth of the comb. We assume that f_{rep} and f_{CEO} are known and that they are accessible to the experiment. First, one of the spectral components of the mode-locked laser at 1740 nm must be frequency doubled. Let's say the second harmonic is at frequency $2\nu_{\mathrm{m}}$. Then one wants to produce a beat signal between ν_{L} and $2\nu_{\mathrm{m}}$. The the low-frequency component of this signal is at frequency

$$\nu_{\mathrm{x}} = \nu_{\mathrm{L}} - 2\mathrm{m} f_{\mathrm{rep}} - 2 f_{\mathrm{CEO}} \tag{6.6}$$

Next, this frequency is divided by 2, then it is mixed with signal at f_{CEO} to produce a new signal whose frequency is further divided by a constant factor c. One obtains a signal with frequency

$$\nu_1 = \frac{1}{\mathrm{c}} \left(\frac{\nu_{\mathrm{x}}}{2} + f_{\mathrm{CEO}} \right) = \frac{\nu_{\mathrm{L}}}{2\mathrm{c}} - \frac{\mathrm{m} f_{\mathrm{rep}}}{\mathrm{c}} \ . \tag{6.7}$$

Similarly, a signal from the DRO at frequency ν_{DRO} is mixed with signal with frequency at the $\mathrm{a}^{-\mathrm{th}}$ harmonic of the pulse repetition rate as detected by a photodiode.

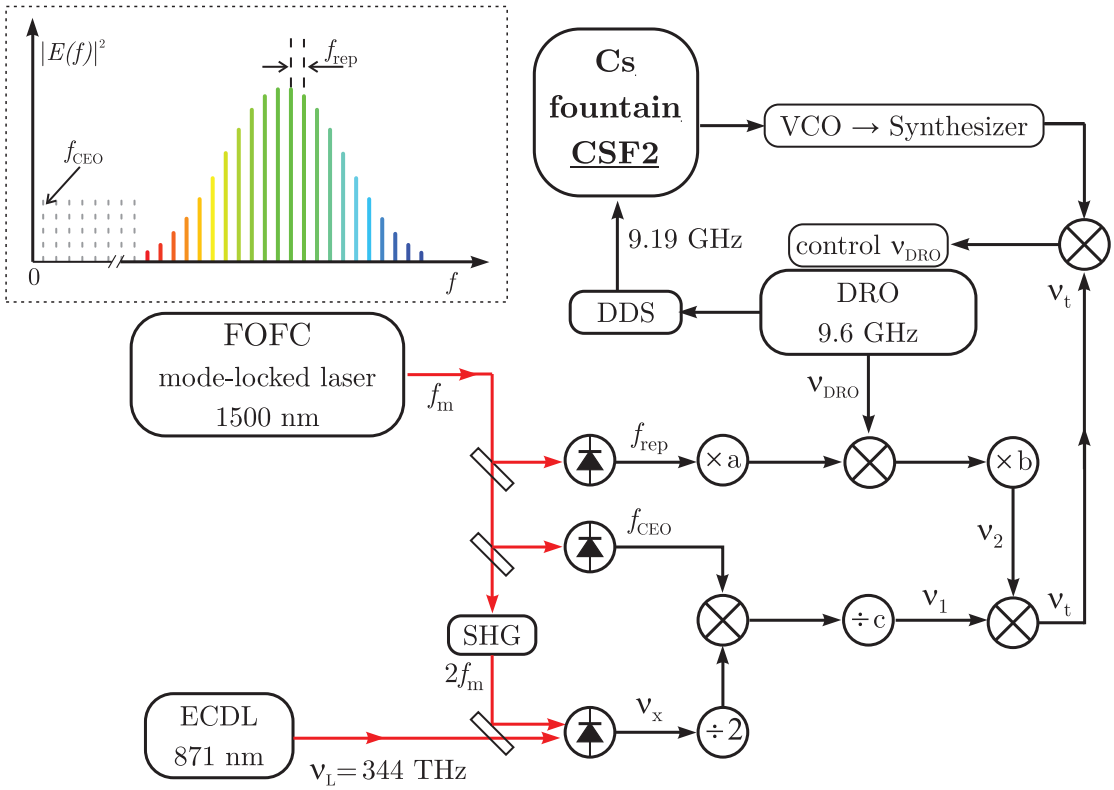

Figure 6.7 Schematic diagram of the frequency synthesis chain used in our experiment. The interrogation signal for CSF2 is delivered by a dielectric resonator oscillator (DRO), which is phase-locked to an ultra-stable ECDL laser via frequency comb (FOFC). In this scheme the frequency comb plays a role of a transfer oscillator of the stability of a source in the optical domain down to another source with output frequency in the microwave region. The insert in the top left corner represent the output spectrum of a FOFC with its characteristic parameters f_{rep} and f_{CEO}.

The frequency of the resulted signal is further multiplied by a constant factor b and one yields a signal with frequency

$$\nu_2 = \mathrm{b}\,(\nu_{\mathrm{DRO}} - \mathrm{a} f_{\mathrm{rep}}) \ . \tag{6.8}$$

The multiplication factors used above are chosen such that $\mathrm{m} = \mathrm{a} \times \mathrm{b} \times \mathrm{c}$, where a and b are integers and c is a rational number. Both signals at frequencies ν_1 and ν_2 are mixed together to obtain the signal at the transfer frequency

$$\nu_{\mathrm{t}} = \nu_1 - \nu_2 = \frac{\nu_{\mathrm{L}}}{2\mathrm{c}} - \mathrm{b}\nu_{\mathrm{DRO}} \ . \tag{6.9}$$

It is clearly seen that the signal at frequency ν_{t} is independent of the noise properties of the FOFC. This signal is used to phase lock the DRO to the ECDL laser. The 9.6 GHz output of the DRO is also shifted by another frequency synthesizer circuit (DDS) to provide microwave signal at 9192.6 MHz for interrogating the Cs atoms in

the fountain. With the describes scheme on board it is possible to overcome some of the limitations even of the state-of-the-art quartz crystal and to use instead an optically-stabilized microwave source as a LO for the fountain, and the Dick effect would be significantly reduced. So the last step towards improving the clock stability is to increase N_{at}.

6.7 Fountain clock with an increased number of atoms

The most obvious way to increase the number of atoms, N_{at}, which take part in the Ramsey cycle is to increase the amount of launched atoms. One way to acquire more cold atoms is to let the optical molasses to load from the background thermal vapour for a longer period. However, this would inevitably increase the dead time of the frequency measurement and the fountain stability would be deteriorated due to the Dick effect. Alternatively, one might be tempted to increase the partial pressure of the caesium in the OM zone, for example, by rising the temperature of the Cs reservoir. It certainly would result in a gain in terms of OM loading rate but surely it would also lead to an increase in the rate of background gas collisions. Therefore, another approach to control the number of cold atoms must be applied, and the production of a beam of slow atoms appears as the most feasible avenue.

6.7.1 Cold atomic beams and their place in atomic clocks

Certainly the discovery of the laser cooling technique has given the biggest push towards the development of various approaches for producing intense beams of slow atoms find. Today, such cold beams are used in many applications: atom interferometry, lithography, atom optics, and frequency standards. Generally speaking, a beam of slow atoms can be formed either by decelerating atoms directly from a thermal beam or by extracting atoms which have been pre-cooled in an optical molasses or in a magneto-optical trap.

Starting with a thermal beam, atoms possessing velocity of several hundreds of m/s can be slowed down by continuous scattering of resonance photons from a laser beam, which illuminates the atoms against their direction of motion, thereby a mean velocity in the range of a few m/s can be achieved. However, while decelerating, the Doppler effect shifts the atomic transition out of resonance with the laser field. In order to compensate for the Doppler effect, some brilliant solutions have been devised. In one of them the atoms are slowed while moving through a region of space where an inhomogeneous magnetic field is created. The magnetic field provides continuous Zeeman tuning of the atomic resonance such that the atoms are always in resonance with the cooling laser. This apparatus is the so called Zeeman slower [B63]. In another technique, the atoms are cooled by a laser whose output frequency is chirped [B64]. Although these techniques are able to provide high flux of slow atoms (10^10 atoms/s [B65]), they seem not appropriate for use to load the OM of the fountain. The need

of an intense slowing laser along the atomic beam axis and the requirement of a relatively high magnetic field, in the case of the Zeeman slower, would make their practical application to the fountain system unnecessarily complicated.

An alternative approach to forming a beam of slow atoms is to extract pre-cooled atoms from a magneto-optical trap. One experimental arrangement relies on the magneto-optical trap demonstrated by Lee *et al.*[B66] who have achieved laser cooling of rubidium atoms in a MOT of a very neat design. They have utilized a single laser beam in order to create two variations of the trap within a hollow mirror of either pyramidal or conical shape. By producing a small hole in the apex of the mirror it is possible to generate a beam of cold atoms as it has been demonstrated later in a pyramidal MOT [B67] (pulsed atomic beam) and [B68] (continuous atomic beam), and in a conical mirror funnel [B69] (pulsed atomic beam). These experimental realizations are able to provide a flux of cold atoms on the order of $\approx 10^9$–10^{10}atoms/s [B67, B69].

Another method to create an intense beam of slow atoms relies on the the 2D-MOT and the 2D$^+$-MOT arrangements. In the first case a 2D quadrupole magnetic field is used with transverse optical cooling in along the two axes orthogonal to the atomic beam. In experiment with such type of source it has been demonstrated a high flux of 6×10^10 atoms/s, with a mean velocity of 50 m/s was obtained [B70]. In the 2D$^+$-MOT configuration the two-dimensional magneto-optical trapping is complemented with a pair of laser beams which provide optical molasses cooling in axial direction. The production of a beam of cold atoms with flux of 9×10^9 atoms/s at a mean velocity of 8 m/s, employing a 2D$^+$-MOT has been demonstrated by Dieckmann *et al.*[B71].

It is also possible to continuously extract cold atoms by utilizing the moving molasses technique [B72, B73], which was described earlier.

It is clear now that the existent concepts for production of slow atomic beams are quite diverse, and all of them have certain advantages and disadvantages if applied to achieve our goal. To increase the loading rate of the OM it is not sufficient to provide only a highly intensive beam of slow atoms. The CSF2 fountain is a readily working scientific apparatus, and its design and construction, as well as the working conditions of the supplementary devices, such as laser intensities and frequencies, have been already optimized for the best performance of the clock. In that sense, we were eager to accommodate a source which implies the least disturbance of the fountain operation. Additionally, since we were going to load an optical molasses and not a trap, it was mandatory that the linear velocity of the incoming atoms fall in the range of a few m/s. This way they linear velocity could be reduced sufficiently within the common volume of the OM lasers, and not fly through it. Having in mind this considerations, it was decided that the so called LVIS (low-velocity intense source) system [B4] is the best candidate for the purpose.

The LVIS arrangement is very similar to the classical 3D magneto-optical trap (MOT) scheme [B9] for atom cooling with a single distinctive detail. In the LVIS scheme one of the six cooling laser beams has a significantly reduced field intensity in

a small central region of its spatial profile. This feature perturbs the MOT trapping potential and creates a leak channel (extraction column) for the trapped cold atoms. Atoms from this region become subject to acceleration by the counterpropagating laser beam, also called "forcing beam" or "accelerating beam", and get pushed out of the trap resulting in a cold particle beam.

During my work on the experiment it was discovered that the arrangement of the present laser fields inside the original LVIS scheme [B4] could be modified in a clever way, which provides control over the quantum state of the atoms in the beam and their velocity. This is described in details in Chapter 7 of the thesis.

Chapter 7

Experiment

This chapter is devoted to the description of the improved stability performance of CSF2 working in the quantum projection noise limited regime. The number of cold atoms in the molasses zone of the fountain was dramatically increased by using a modified low-velocity intense source of atoms. First, the physical realization of the source in our lab is described. Then, the findings obtained from the insertion of a dark state pump laser are presented and explained. As a final step in the characterization of the LVIS, measurements and evaluations of the mean flux and velocity of the atoms are shown. Lastly, the improved stability of CSF2 by evaluating a real frequency measurement result is demonstrated.

7.1 Slow beam apparatus

The LVIS trapping zone was constructed around a standard DN35CF six–way cube. Optical access was provided by five AR-coated windows with diameter of 38 mm. The free end of the cube was attached to the OM chamber of the fountain vacuum system through a six-way cross and a flexible metal bellows. The distance between both trap centers was approximately 53 cm and the LVIS cube was positioned 11 mm higher than the OM center in order to compensate the height difference acquired by the atoms along their ballistic flight. Figure 7.1 represents a simplified overview of the experimental apparatus.

Two identical coaxial coils, arranged in anti-Helmholtz configuration created the quadrupole magnetic field for the trap operation. The line passing through the coil centers defined the trap symmetry axis z (see Fig. 7.2). Diode lasers provided the trapping light. It was introduced into the LVIS trough five individual single-mode polarization maintaining fibers with collimators (Schäfter&Kirchhoff Fiber Collimator 60FC-T-4-M100-37) at the fiber ends. The collimators come with integrated quarter-wave plate and provided circularly polarized, collimated laser light having a gaussian profile with 21 mm beam diameter (at $1/e^2$ intensity level). Along the z axis, only one fiber collimator was mounted, while on the opposite side of the MOT center, at a distance of 18 mm, the output coupler of the LVIS system was positioned. It consisted

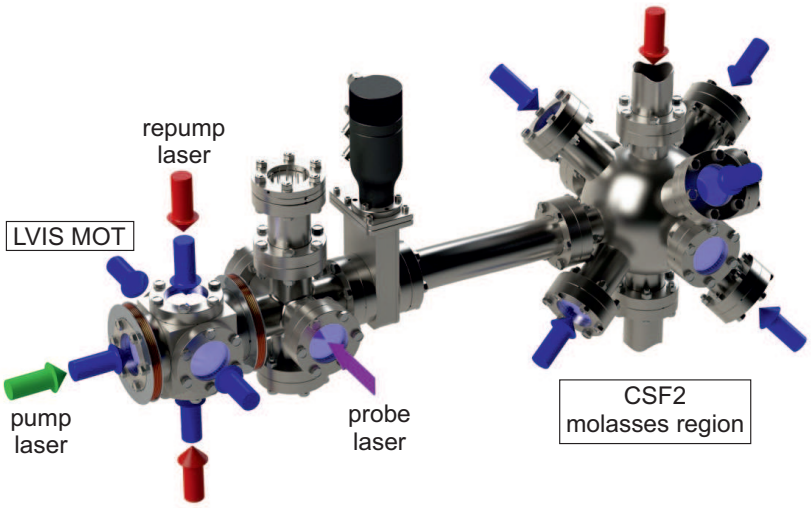

Figure 7.1 Illustration of the experimental apparatus. Here for simplicity only the molasses region of CSF2 is shown, while the fountain detection zone, the state selection cavity and the Ramsey interrogation zone are not depicted. The existent trapping laser light fields are displayed as blue (for cooling) and red (for repumping) solid arrows.

of a pierced quarter-wave plate, with an 0.5 mm diameter aperture in the center and with a high-reflection coating deposited on the back side. The output coupler produced a retro-reflected laser beam which had opposite circular polarization with respect to the incident beam, which was a necessary condition for the MOT operation. The aperture in the output coupler formed the desired extraction column in the LVIS. No additional collimation of the atomic beam was performed.

7.2 Initial optimization and preliminary results

Here are described in more details the LVIS MOT dynamics in order to point out the essential parameters of the LVIS system. A special care was taken to ensure that they have been optimized and reflected the maximum OM loading efficiency, which could be achieved in our setup.

Background gas atoms from the low-velocity tail of the thermal distribution were constantly cooled and pushed towards the confinement region of the trap. The opening in the output coupler defined a cylindrical region around the trap symmetry axis z, where an imbalance between the confining forces arose on both sides of the trap center. Therefore, an atom which ended up in the extraction column experienced a net spontaneous force pointing towards the LVIS output coupler. The atoms from the resulting atom beam were continuously confined within the extraction column by the transverse laser beams (cooling and repumping). Those that diverged from the central column were recycled back into the trap. Too large beam divergency, which is a measure for the atoms transverse velocity, would compromise the loading efficiency of the OM. Due to technical reasons, a direct measurement of the atomic beam diver-

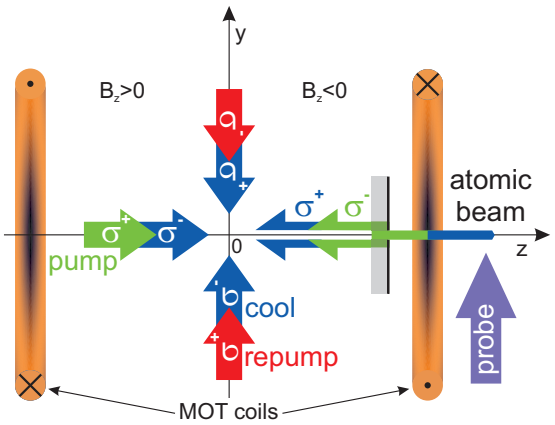

Figure 7.2 Schematic drawing of the enhanced low velocity intense source system.

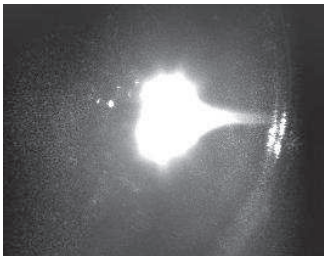

Figure 7.3 A snapshot of the LVIS MOT region made with a CCD camera. The bright central spot is the fluorescence from the trapped caesium atoms, and the tail emerging from it is due to scattered photons from atoms which leave the trap and form the cold atom beam. The conditions at which the picture is taken are 18 mW cooling laser optical power on each beam, 0.79 mT/cm axial and 0.39 mT/cm radial magnetic field gradients.

gency was not possible in our experimental setup. Instead, we relied on observations and evaluations from previous studies carried out by Lu [B4] and Park [B74]. It was found that a pure geometrical factor could well describe the measured beam size and the divergence of the atomic beam scaled as $\theta = d/x$, where d is the diameter of the aperture in the LVIS output coupler and x is the distance between the aperture and the LVIS trap center. In our case that would result in an atomic beam diameter of 15 mm at the OM trap center, where the OM cooling laser beams had a diameter of 25 mm ($1/e^2$).

Additionally, the number of cold atoms loaded in the OM zone of the fountain depended on the atomic beam flux and losses during the atom capture process in the OM. The atomic beam flux was determined mainly by the LVIS trap capture rate [B4]. Parameters relevant to the capture rate were the value of the atomic vapour background pressure, magnetic field gradient, cooling laser power, frequency detuning, intensity profile and distribution among the cooling laser beams, as well as repumping laser parameters. An additional factor was the size of the aperture in the LVIS output coupler. The complexity of the system LVIS – OM did not allow to fully separate the individual impact of all these factors on the loading process. The performance of the overall system was assessed and optimized by observing the total number N_{at} of detected cold atoms at the end of the fountain interrogation cycle.

Initially, the formation of an ensemble of cold atoms in the LVIS MOT was accomplished by distributing the power of the cooling laser equally among the three trap axes. The needed polarization state of each individual beam was defined by

the magnetic field orientation of the MOT. The fluorescence emitted by the trapped atoms in the LVIS MOT is shown in Fig. 7.3. The asymmetric shape of the cold atom cloud resulted from the imbalanced radiation pressure force along the z axis. Fluorescence from atoms which form the atom beam and leave the MOT central region appears as a tail on the right hand side of the main cooled ensemble. Already without any further optimizations a noticeable change in N_{at} was encountered which indicated an enhanced loading of atoms in the OM zone of the fountain. An advantage of using the above described source of cold atoms is that the small aperture size in the LVIS output coupler provides a differential pumping mechanism between both trap chambers. This allowed us to increase the caesium partial pressure in the LVIS MOT zone and at the same time to preserve the rest of the fountain vacuum system from unfavourable rise of the local background pressure. This in turn would increase the OM loss rate, and the rate of collisions of the interrogated cold atoms with the hot background Cs atoms during the free propagation time.

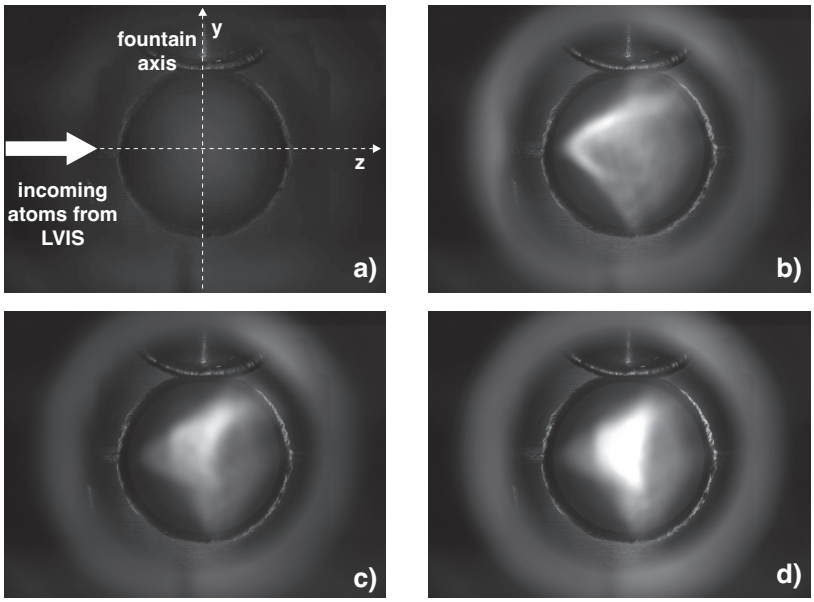

Figure 7.4 Snapshots of the cold ensemble of atoms in the fountain OM zone. Each picture is taken for different regime of OM loading as follows: **(a)** background gas loading without LVIS; **(b)** loading with LVIS and molasses repumping laser is collinear with the cooling laser beams; **(c)** loading with LVIS but with a single repumping laser beam along the fountain axis (vertically); **(d)**; enhanced OM loading with additional pump laser in the LVIS and vertical repumping laser beam in the OM;

However, during the first test some asymmetries in the spatial distribution of the cold atoms in the OM zone were observed (Fig. 7.4). At the beginning the cooling and repumping laser beams in the OM zone of the fountain were sharing the same optical fibers. Thus the effective 3D cooling of the beam atoms started immediately after the first of them approached the common volume of the molasses laser beams. As a consequence the main part of the incoming atoms "froze" slightly off-center from the

fountain vertical axis Fig. 7.4b). This was a major problem in our setup since after the launching stage of the fountain the biggest part of the atoms were obstructed by the physical dimensions of the 1 cm openings in the Ramsey resonator. This issue was resolved by introducing the repumping light in the OM zone only from the top end of the main fountain chamber along the fountain vertical axis. The achieved better centering of the atom cloud instantly reflected into higher number of detected atoms at the end of the fountain cycle Fig. 7.4c) and d).

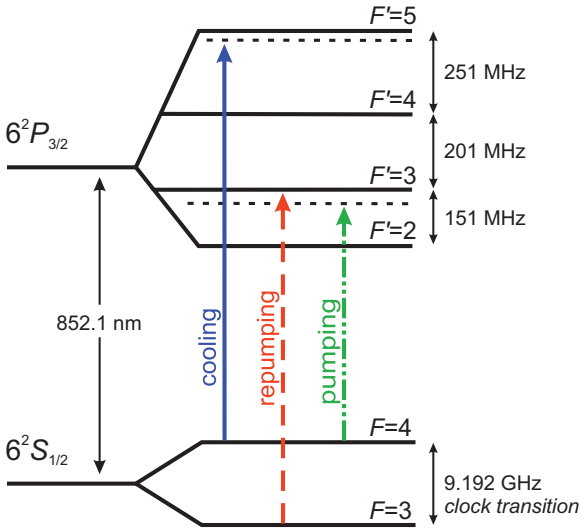

Figure 7.5 The caesium D_2 line and the frequency splitting between the hyperfine components of the $6^2S_{1/2}$ ground and $6^2P_{3/2}$ excited states (not to scale). The transitions driven by the various laser fields, present in our LVIS trap, are shown as well.

A Fabry-Perot laser diode (JDSU 5430) at 852 nm served as the LVIS cooling laser. Its frequency was stabilized through an injection locking technique to the frequency of the master laser of CSF2. An acousto-optic modulator was used to tune the laser absolute frequency about 2Γ to the red of the $|F = 4\rangle \rightarrow |F' = 5\rangle$ cycling transition ($\Gamma = 5.2$ MHz is the natural linewidth of the transition). In total, the cooling laser delivered 90 mW optical power to the LVIS trap. The trap center was aligned with the extraction column by suitably distributing the laser power between the transverse laser beams.In Fig. 7.5 the level structure of the D_2 spectral line of the caesium is recalled again, where the transitions driven by the various laser fields used in the LVIS trap are shown.

The intensity of the accelerating beam was a crucial parameter, concerning the efficiency of the OM loading process. In our experimental arrangement the optimum value for the power of the accelerating beam was found to be 10 mW. Also the optimum value of the quadrupole magnetic field gradient was close to the one for optimum MOT capture rate. Beside laser parameters the value of the magnetic field gradient defined the rate of absorption-emission cycles that an accelerated atom experienced and thus the final atom beam velocity. In our experiment, the anti-Helmholtz coils

were driven with a current of 2.7 A, creating 0.71 mT/cm and 0.35 mT/cm magnetic field gradients in axial and radial directions, respectively. An additional distributed Bragg reflector (DBR) laser diode (Photodigm PH852DBR120) was used as a repump laser to bring the atoms which have decayed to the $|F = 3\rangle$ state back to the cooling cycle. The DBR laser diode delivered a total optical power of 6.2 mW into the LVIS MOT and its output frequency was stabilized by saturated absorption spectroscopy. This laser was sharing the same optical fibers with the cooling laser depending on the chosen configuration.

7.3 Modification. Pump Laser.

With the traditional LVIS setup [B4] and using transverse repumping, nearly 20 times more caesium atoms were detected at the end of the fountain interrogation cycle in comparison with background gas OM loading. In both cases the loading time constant was about 1 s. The efficiency of the LVIS–OM system was sensitive to the velocity of the beam atoms, because of the limited velocity capture range of the OM. However, the traditional LVIS system described so far did not provide enough flexibility to control the velocity of the atoms. The atoms in the extraction column were accelerated (and heated) by the accelerating beam until the Doppler shift brought the atomic transition out of resonance [B75]. To stop the acceleration at a certain moment, it was found expedient to shelve the atoms in a "dark" state [B76], for which the $|F = 3\rangle$ component of the caesium ground state was a convenient choice.

The only way for an atom in the extraction column to escape the cycling transition $|F = 4\rangle \rightarrow |F' = 5\rangle$ and to occur in the $|F = 3\rangle$ state is by off-resonant excitation of the $|F' = 4\rangle$ state. Since the frequency splitting between $|F' = 4\rangle$ and $|F' = 5\rangle$ is relatively large (~ 251 MHz), this process has low probability. Therefore, an additional laser beam , called "pump" laser, was brought into action and it was intended to drive either the $|F = 4\rangle \rightarrow |F' = 3\rangle$ or $|F = 4\rangle \rightarrow |F' = 4\rangle$ transitions. While this laser granted a very efficient optical pumping to the $|F = 3\rangle$ state, the presence of opposing repumping light along the z axis supported continuous transfer of atoms back from the $|F = 3\rangle$ to the $|F = 4\rangle$ state during their flight to the OM zone. To avoid this scenario the repumping light was removed from the atomic beam path and was left only to be present in the vertically aligned LVIS MOT laser beams.

Fig. 7.2 illustrates the present laser fields in our LVIS trap and their orientation. We have chosen the sign of the B_z component of the magnetic field on both sides of the trap center ($z = 0$) as shown in this figure. We define the quantization axis to be coincident with the z axis and therefore the cooling laser light coming out of the fiber and having a wave vector pointing towards the LVIS output coupler must be σ^- circularly polarized. The pump laser beam was spatially overlapped with the accelerating beam as they propagated in the same optical fiber, but it possessed opposite σ^+ circular polarization. Since beam atoms with positive displacement along z ($B_z < 0$)

and outside the transverse laser region were shelved in the $|F = 4, m_F = -4\rangle$ state by the on-axis σ^- polarized cooling laser, only σ^+ polarized pump light was able to promote optical pumping to the $|F = 3\rangle$ component according to the transition selection rules. As a result of the complementary laser pump field, the loaded number of atoms in the OM region was significantly increased.

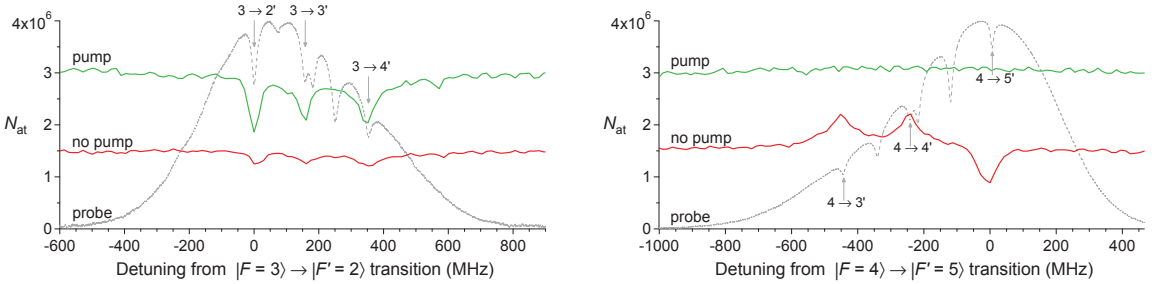

(a) **(b)**

Figure 7.6 The detected atom number N_{at}, resulting from fountain OM loading by means of the LVIS system, as a function of the probe laser frequency detuning from: (a) the $|F = 3\rangle \rightarrow |F'\rangle$ and (b) the $|F = 4\rangle \rightarrow |F'\rangle$ transition. Results, with and without pump laser present, are shown by a green (top) and a red (bottom) trace, respectively. The pump laser is operated on the $|F = 4\rangle \rightarrow |F' = 3\rangle$ transition with an optical power of 0.01 mW. With grey dashed line in the background is given a signal from saturation spectroscopy as a reference to the instantaneous frequency of the probe laser. At exact resonance frequencies, the transitions are indicated by the quantum numbers $F \rightarrow F'$, while the crossover resonances in between are not denoted.

For verifying the internal state of the atoms after they left the LVIS trap, a probe laser was applied perpendicular to the path of the atoms, 11 cm away from the trap center. The probe laser was intended to transfer momentum to the atoms in a given $|F\rangle$ component in a direction transverse to that of propagation or to cause optical pumping. Both effects depend on the probe laser frequency detuning, polarization, intensity, and on the given static magnetic field. A rectangular aperture was used to produce a thin sheet of light from this laser with 2 mm thickness and 10 mm height, perpendicular to the atomic beam direction. In this way it was guaranteed that the resulting probe light with 30 mW optical power interacted with most of the passing atoms. In Fig. 7.6 the detected atom number N_{at} is shown, when the frequency of the probe laser is scanned in the vicinity of both, the $|F = 3\rangle \rightarrow |F' = 2\rangle$ (Fig. 7.6a and the $|F = 4\rangle \rightarrow |F' = 5\rangle$ (Fig. 7.6b transitions. In each sub-figure two modes of OM loading with the LVIS are shown. The top green and bottom red traces represent the situation with and without pump laser, respectively. In the following the results of Fig. 7.6 are discussed only for a qualitative illustration of the most general features of the probe laser influence on the atom loading process, and do not attempt a quantitative explanation.

Without the pump laser (red traces in Fig. 7.6), there were atoms in both states $|F = 3\rangle$ and $|F = 4\rangle$, and their interaction with the probe laser tuned close to the

$|F\rangle \rightarrow |F'\rangle$ resonances leaded either to a decrease or an increase in the detected atom number N_{at}. The atom number N_{at} was decreased, when either the probe laser were pushing away beam atoms ($|F = 3\rangle \rightarrow |F'\rangle$ (Fig. 7.6a or $|F = 4\rangle \rightarrow |F'\rangle$ (Fig. 7.6b transitions), or it pumped beam atoms from $|F = 3\rangle$ to $|F = 4\rangle$ ($|F = 3\rangle \rightarrow |F' = 3, 4\rangle$ transitions, Fig. 7.6a), so that they were subsequently detrimentally accelerated and heated by the cooling laser light. On the other hand the detected atom number increased, when the beam atoms were pumped by the probe laser from $|F = 4\rangle$ to $|F = 3\rangle$ ($|F = 4\rangle \rightarrow |F' = 3, 4\rangle$ transitions, Fig. 7.6b, avoiding damaging acceleration and heating, and providing thus more efficient capturing in the fountain OM.

With the pump laser (green traces in Fig. 7.6), the atoms were transferred to the state $|F = 3\rangle$, so that they did not interact with the probe laser tuned around $|F = 4\rangle \rightarrow |F' = 5\rangle$ (Fig. 7.6b, while probe laser tuning close to the resonances $|F = 3\rangle \rightarrow |F'\rangle$ (Fig. 7.6a resulted in either pushing the atoms away by light scattering, or pumping them to $|F = 4\rangle$ with subsequent detrimental acceleration by the cooling laser light.

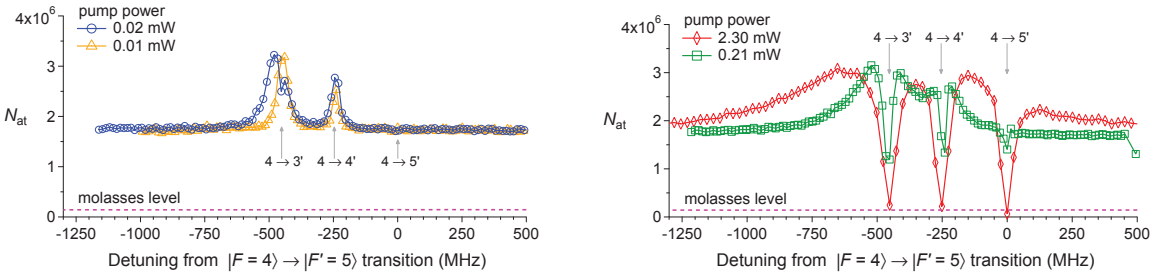

Figure 7.7 Plot of the detected atom number N_{at} as a function of the pump laser frequency at four different laser powers. For comparison, the dashed magenta trace represents N_{at} obtained in the standard mode of fountain operation (background gas OM loading).

In a next step the effects of the pump laser properties were investigated. Fig. 7.7a and Fig. 7.7b illustrate the dependence of N_{at} on the pump laser frequency for several different values of its optical power. The laser frequency was continuously tuned through the $|F = 4\rangle \rightarrow |F'\rangle$ resonances. For frequencies far-detuned from resonance, N_{at} stayed stable at a level corresponding to the value of detected atoms without utilizing the pump laser. Once the frequency of the pump laser matched a transition, the process of optical pumping of atoms to the dark state started to compete with the MOT loading rate. At low power (Fig. 7.7b this laser efficiently transfered the atoms from the beam to the $|F = 3\rangle$ component without significant heating so that most of them stayed confined within the extraction column, and later on, traveled unaffected towards the OM region. As a result, sharp peaks were observed at frequencies matching the $|F = 4\rangle \rightarrow |F' = 3, 4\rangle$ transitions (orange triangle symbols in Fig. 7.7a. These peaks indicated the increased number of atoms which take part in the CSF2 measurement cycle. The difference in the transfer efficiency to the "dark"

state noticed around the $|F = 4\rangle \rightarrow |F' = 3\rangle$ and $|F = 4\rangle \rightarrow |F' = 4\rangle$ resonances (Fig. 7.7b can be explained by referring to the Clebsch-Gordan coefficients of the corresponding transitions [B9]. Because the pump laser beam had a very low optical power compared to the power of the repumping and cooling laser beams (which were about three orders of magnitude higher), it did not significantly disturb the cooling process in the LVIS MOT.

When the power of the pump laser was increased, the cooling process became more disturbed, and a drop in N_{at} was observed. In the curves in Figs. 7.7a (only $|F = 4\rangle \rightarrow |F' = 3\rangle$ at $\approx -450\,\mathrm{MHz}$ detuning, blue circles) and 7.7b (green squares and red rhomboids) this appeared as a formation of dips for frequencies close to the resonances. The dips widths broadened gradually when the power of the pump beam was increased, since, even off-resonance, the disturbance of the LVIS MOT became more and more effective. At the same time, broad maxima of N_{at} developed (Figs. 7.7b), more and more shifted to lower frequencies with respect to the $|F = 4\rangle \rightarrow |F' = 3\rangle$ and $|F = 4\rangle \rightarrow |F' = 4\rangle$ transitions. For sufficiently high pump optical power it was even observed a complete loss of the LVIS MOT fluorescence and the number of detected atoms in CSF2 as well. With the pump laser beam in a direction transverse to the LVIS symmetry axis there was no enhancement of N_{at}. The observed dips in the spectrum close to the resonance frequencies were similar to the dips in Fig. 7.7b, caused by the same mechanisms of MOT disturbance. Such experiment also demonstrated that the optical pumping of the atoms to the $|F = 3\rangle$ state mainly occured after they leave the LVIS transverse laser beams. On the other hand, with the pump laser beam along the LVIS symmetry axis but with an opposite circular polarization σ^+ (the same as the cooling laser) also no increase of N_{at} was observed, as no optical pumping could take place according to transition selection rules.

At the moderate pump optical powers (0.2 mW to 2 mW, see Fig. 7.7b the maximum obtainable value of N_{at} was only 4% lower compared to the maximum obtainable N_{at} at low pump optical powers (0.01 mW to 0.02 mW, see Fig. 7.7a. However, for moderate pump optical powers the loading process became less sensitive to the pump laser detuning. In our setup the peak value of the detected atom number reached saturation at pump beam intensities of about $3.6\,\mu\mathrm{W/cm^2}$ (50 µW power). For the frequency instability measurements (see Section 7.5) the power of the pump beam was 0.45 mW with a red frequency detuning of $10\,\Gamma$ from the $|F = 4\rangle \rightarrow |F' = 3\rangle$ transition.

It is worth mentioning that scanning the pump laser through the $|F = 3\rangle \rightarrow |F'\rangle$ resonances showed no significant effect on N_{at} compared to the case of LVIS–OM loading without the pump laser - the pump laser effect on the atoms in the LVIS was similar to the effect of a repump laser along the z-axis.

The properties of the LVIS repumping laser also affected the loading process of the OM with the atomic beam. Fig. 7.8 illustrates the impact of both, operating frequency and orientation of the LVIS repumping laser, on N_{at}. Changing the repumping laser tuning from the more efficient repumping transition $|F = 3\rangle \rightarrow |F' = 4\rangle$ to the less efficient repumping transition $|F = 3\rangle \rightarrow |F' = 3\rangle$ resulted in a higher number of cold

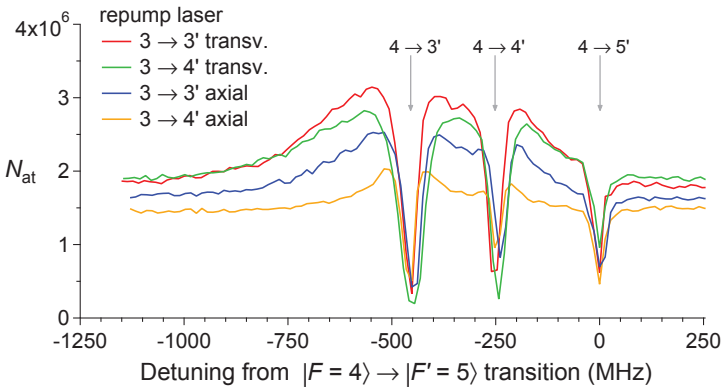

Figure 7.8 Plot of the detected atom number N_{at} vs. the frequency of the pump laser for different LVIS repumping laser configurations. Each configuration is characterized by the operating frequency of the repumping laser (driving either the $|F = 3\rangle \rightarrow |F' = 3\rangle$ transition or the $|F = 3\rangle \rightarrow |F' = 4\rangle$ transition) and by the particular spatial orientation of the repumping light in the LVIS trap (either the repumping light is available along the z axis (atomic beam axis) or it is applied only transversely to the z axis). For all four cases the LVIS repumping laser optical power was kept the same and the delivered power by the pump laser was 0.45 mW.

atoms loaded into the OM of CSF2 (Fig. 7.8). This finding was probably the result of two competing effects and depended on the particular repumping laser intensities and geometry of our LVIS setup: While the utilization of the $|F = 3\rangle \rightarrow |F' = 4\rangle$ repumping transition was beneficial for the LVIS MOT operation, stray light from the repumping laser at this transition interacting with the $|F = 3\rangle$ atoms in the beam was more efficient in pumping the atoms to the $|F = 4\rangle$ state (resulting in the described detrimental acceleration effect) than stray light from the $|F = 3\rangle \rightarrow |F' = 3\rangle$ repumping transition. In our setup, with the given experimental parameters (pump laser power 0.45 mW and a red frequency detuning of $10\,\Gamma$ from the $|F = 4\rangle \rightarrow |F' = 3\rangle$ transition), the latter repumping transition was the better of the two choices, resulting in a factor of 40 increase of N_{at} compared to operation of CSF2 with OM loading from background gas.

7.4 Slow beam parameters

7.4.1 Atom velocity

The first step in the atom velocity measurement was to allow the atomic beam to reach a steady state after the LVIS lasers were turned on. The probe laser was also turned on and tuned to the $|F = 3\rangle \rightarrow |F' = 2\rangle$ transition. Its intensity was increased to efficiently heat the cold beam atoms prepared in $|F = 3\rangle$ state by the pump laser, and effectively prevent them from reaching the molasses zone. As a second step, after the atom beam flux reached a steady state (0.5 s after the LVIS lasers were turned on),

the probe laser was turned off and the molasses beams were simultaneously turned on for 1.1 s. In Fig.7.9a the pulse waveforms represent the time sequence in which the above described processes took place. Along with them, the blue solid line shows the time evolution of the fluorescence in the OM, observed by a photodiode.

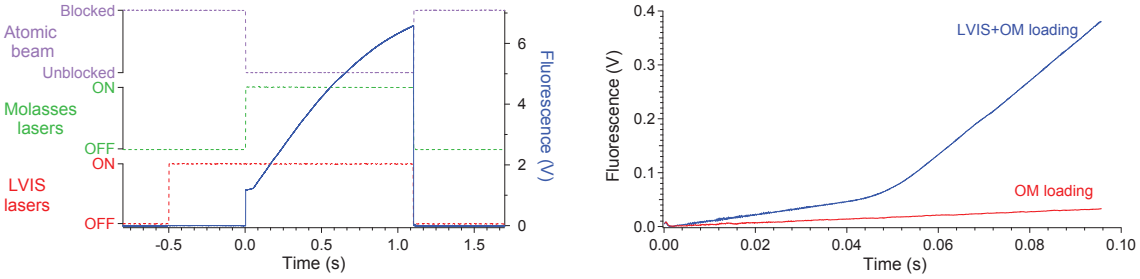

Figure 7.9 (a) Build-up of the fluorescence signal in the optical molasses zone for OM loading time of about 1.1 s (blue trace). After probe laser is turned off the atoms emerging from the LVIS are free to access the OM zone. The pulsed waveforms represent the time sequence in which the various laser fields are present during this experiment; (b) Fluorescence signal from the OM zone shortly after the probe laser is turned off. Comparison of the rates of change of the fluorescence, when the OM are loaded either only from the background gas (red trace) or by the LVIS system (blue trace), reveals that the probe laser does not effectively block all of the atom leaking from the LVIS. Therefore, the effect must be considered by the model, which is used to estimate the velocity of the beam atoms.

The atoms from the beam were allowed to propagate undisturbed towards the molasses zone in the absence of the probe laser. Subsequently, a change in the molasses loading rate occurred as the first atoms reached the molasses zone. The delay between releasing the atom beam at time $\tau_0 = 0$ and the observed sudden increase in the molasses fluorescence was used to calculate the atom velocity. The blue trace in Fig.7.9b shows the behaviour of the fluorescence signal shortly after the moment τ_0. The initial jump of the fluorescence signal at τ_0 observed in Fig.7.9a, which is due to stray light from the background atoms and the walls of the vacuum chamber, was corrected here.

However, the observed rather gradual change of the growth rate of the fluorescence signal (approximately 50 ms after the probe laser was turned off), instead of a sudden change, implied a velocity distribution of the incoming atoms. A very simplified method was used to interpret the recorded data. It was focused on the assumption that the velocity of the atoms is a normally distributed variable described by a probability density function of the following form:

$$G(v|\bar{v},\sigma_v) = \frac{1}{\sigma_v\sqrt{2\pi}}\exp\left(-\frac{(v-\bar{v})^2}{2\sigma_v^2}\right), \tag{7.1}$$

where $\bar{v}$ is the mean velocity of the atoms and σ_v is the standard deviation of the distribution. The probe beam interacted with the atom beam at a distance $L = 0.42$ m

apart from the OM center. Let's suppose that the pulse duration which sets the probe laser off is infinitesimally short. Then for a given observation time interval $\Delta\tau = \tau - \tau_0$ all atoms with velocity $v > \frac{L}{\Delta\tau}$ would reach the OM and the number of atoms $n(t)$ can be expressed by the integral

$$n(t) = \int_{\frac{L}{\Delta\tau}}^{+\infty} G(v)\,\mathrm{d}v. \tag{7.2}$$

Since at the moment τ_0 the atom beam has reached a steady state, the total number of atoms that have arrived at the OM and give rise to the fluorescence signal is:

$$N^{\mathrm{b}}(t) = b \int_{\tau_0}^{\tau} n(t)\,\mathrm{d}t, \tag{7.3}$$

where b is a scale constant.

In order to investigate only the effect of the beam atoms on the OM loading rate it was necessary to compensate the detected signal for the one that resulted from optical molasses loading from the background atoms in the absence of the LVIS (red colored trace in Fig.7.9b). Both signals were compared to one another and it turned out that the initial slope in the blue trace could not simply be explained by the OM loading from the background gas. Apparently, there is an additional contribution which resulted from the probe laser not blocking effectively all the atoms in $|F = 3\rangle$. It is also possible that some amount of atoms from the beam were left in $|F = 4\rangle$ state hence they were not sensitive to the probe laser. Again it was assumed that the atoms which passed through the probe laser have normally distributed velocity with the same mean $\bar{v}$ and standard deviation σ_v. At the time τ_0 a certain amount of atoms that have managed to pass through the probe laser are distributed along the distance L. The part of them which have arrived in the OM until some later moment in time τ can be expressed by

$$N^{\mathrm{a}}(t) = a \int_{\tau_0}^{\tau} \int_{-\infty}^{\frac{L}{\Delta\tau}} G(v)\,\mathrm{d}v\,\mathrm{d}t, \tag{7.4}$$

where a is a scale parameter. Combining both equations 7.3 and 7.4 gives the total number of atoms as :

$$N(t) = N^{\mathrm{a}}(t) + N^{\mathrm{b}}(t) = \int_{\tau_0}^{\tau} \left(a \int_{-\infty}^{\frac{L}{\Delta\tau}} G(v)\,\mathrm{d}v + b \int_{\frac{L}{\Delta\tau}}^{+\infty} G(v)\,\mathrm{d}v \right) \mathrm{d}t\,, \tag{7.5}$$

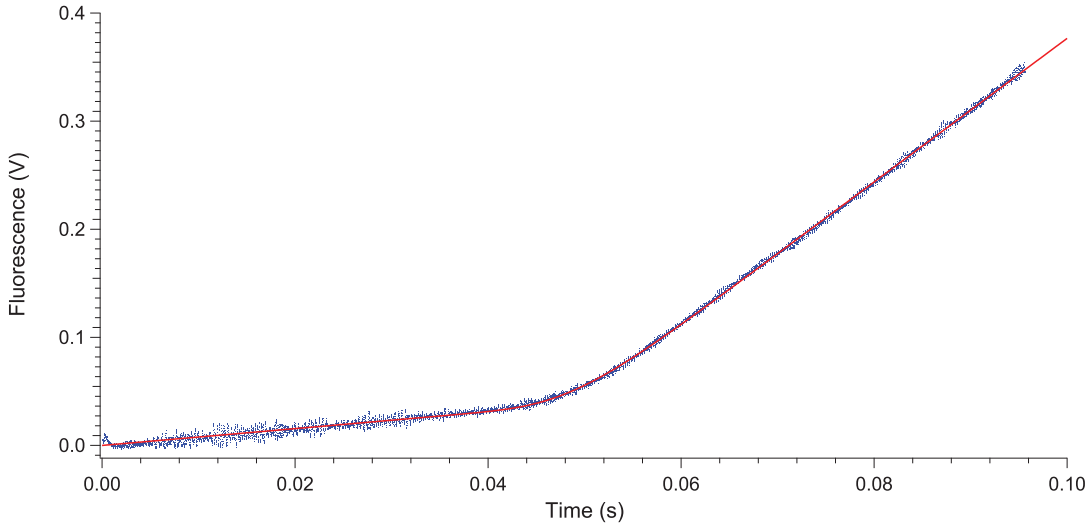

Figure 7.10 Non-linear least squares fit (red solid line) performed over the experimental data (blue dots).

The Equation 7.5 was used to construct a non-linear least-squares fit, and the experimental data were processed by using the symbolic mathematical computation program "Mathematica" and more specific it's *"NonlinearFitModel"* fitting function. In fact, the collected experimental data did not represent directly the number of atoms which were captured in the optical molasses, but rather a voltage signal which is proportional to this number. Therefore, the scale parameters a and b are introduced in the above equations and in the model function. In more general form the model to be fitted can be written as $N = N(t; \bar{v}, \sigma_v, a, b)$. In order to evaluate the parameters, which best describe the experimental data, the merit function, expressed as a sum of the squared residuals:

$$\chi^2(\bar{v}, \sigma_v, a, b) = \sum_{i=1}^{m} (N_i - \hat{N}(t_i; \bar{v}, \sigma_v, a, b))^2 \,,$$

is minimized; here N_i is the $i^{-\text{th}}$ measured data point, $\hat{N}$ is the fitted or predicted value, t_i are predictor variables and m is the number of data points.

	Estimate	Standard Error
$\bar{v}$ [m/s]	8.682	0.004
σ_v [m/s]	1.00	0.01
a [arb]	0.778	0.002
b [arb]	6.643	0.005

Table 7.1 Fit parameters table

$$C = \begin{pmatrix} 1 & 0.105 & -0.669 & -0.529 \\ 0.105 & 1 & -0.462 & 0.639 \\ -0.669 & -0.462 & 1 & -0.152 \\ -0.529 & 0.639 & -0.152 & 1 \end{pmatrix}$$

Table 7.2 Correlation matrix

In Fig. 7.10 one can see the result of the fit performed over the experimental data, and the estimated values of the fit parameters are given in Table 7.1 alongside with the correlation matrix C, represented in Table 7.2. At first glance it is difficult to judge on the validity of the results, or more generally on our assumptions made to construct the model function i.e. that the velocity of the atoms in the beam obeys normal distribution. Moreover, the variance of the measurement is not known and it was set equal to 1 in the fit. Nevertheless, the obtained results of 8.682 m/s for the mean velocity of the atoms and the FWHM=$2\sqrt{2\ln 2} = 2.35$ m/s of the distribution are in a good agreement with result obtained in experiments with similar sources of slow atoms [B77, B74, B4, B78]. A plot of the residuals acquired from the fit are presented in Fig. 7.11.

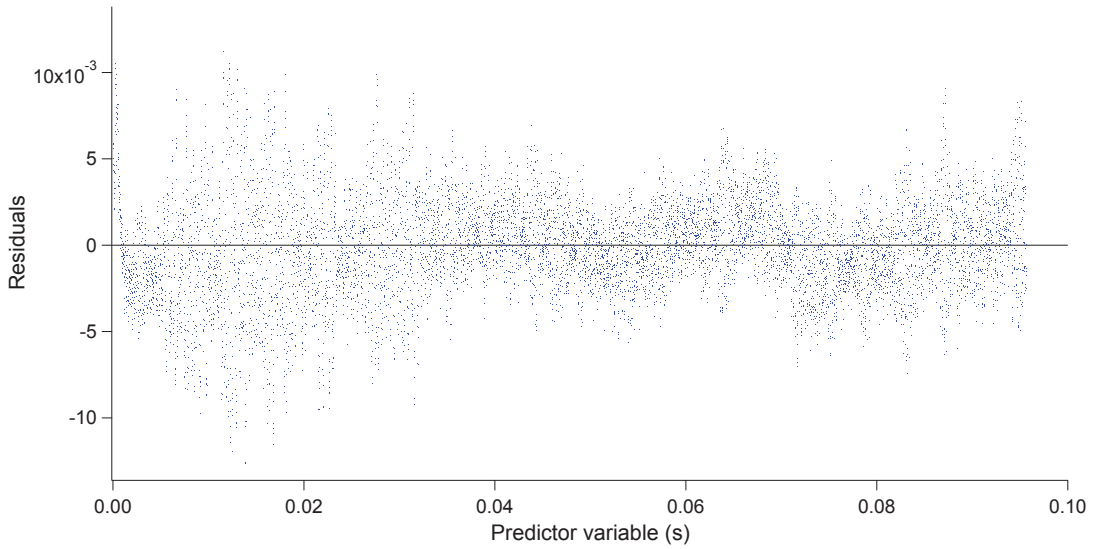

Figure 7.11 Residuals

7.4.2 Atom beam flux

The atom flux was estimated by performing a measurement of the cloud absorption in the molasses zone. For this measurement, the molasses and LVIS lasers were operated simultaneously for 1 s. At the end of this period all lasers were turned off and the probe beam was turned on, preventing additional arrival of cold atoms in the molasses zone. After 10 ms, a weak absorption laser beam, resonant with the $|F = 4\rangle \rightarrow |F' = 5\rangle$ transition was introduced along the direction of one of the molasses beams. It propagated in the molasses fiber, and had the same Gaussian intensity profile and direction as the corresponding molasses beam. Its polarization was linear and orthogonal to that of the corresponding molasses beam. The beam could pass the input polarizer after the polarization in the optical fiber was slightly misaligned from the fiber/polarizer axis. After passing the molasses zone, the absorption beam was

detected at the exit port of the opposite molasses beam polarizer with a high-gain photodetector.

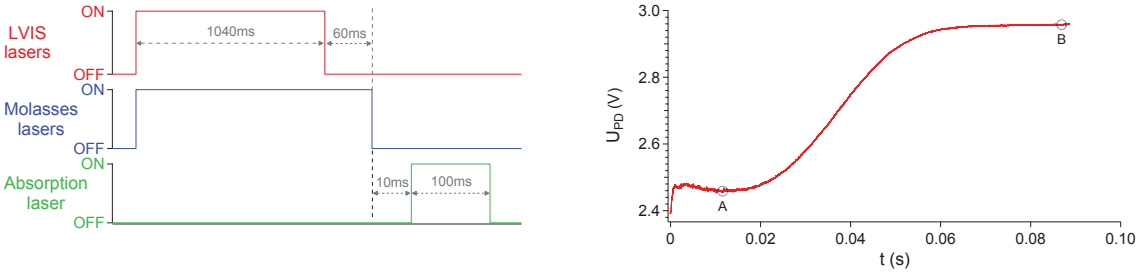

(a) **(b)**

Figure 7.12 Estimation of the number of loaded atoms in the OM zone: Graph (a) represents the state (ON/OFF) of the different laser fields during the absorption measurement. Graph (b) shows the detected by the photodiode signal. After the cooling laser beams of the molasses are turned off, the amount of absorbing particles, probed by the absorption laser, decreases and more light reaches the detector, thus an increase of the detected signal is observed.

The absorption beam was kept on for 100 ms. During this measurement time, the absorption changed in accordance with the molasses loss rate due to gravity. In Fig.7.12b is shown the evolution of the absorption signal in time, where the absorption beam is switched on at the moment $t = 0$. The detection was done with an opto–electronic integrated circuit type OPT301. It contains a photodiode and transimpedance amplifier on a single chip. The photodiode spectral response at wavelength $\lambda = 852\,\mathrm{nm}$ is $S_{\mathrm{PD}} = 0.45\,\mathrm{A/W}$. The transimpedance amplifier gain was set to $G_{\mathrm{PD}} = 9.1 \times 10^7\,\mathrm{V/A}$. These two quantities give the connection between the measured absorption signal U_{PD} and the instantaneous power P of the laser beam through the expression

$$P = \frac{U_{\mathrm{PD}}}{S_{\mathrm{PD}}\, G_{\mathrm{PD}}}\,. \tag{7.6}$$

The two regions marked as "A" and "B" on the signal curve in Fig.7.12b correspond to the maximum and minimum detected absorption respectively. The measured signal $U^{\mathrm{B}}_{\mathrm{PD}} = 2.96\,\mathrm{V}$ allowed for derivation of the power of the laser beam as $P^{\mathrm{B}} = 73\,\mathrm{nW}$. The radius of the laser beam was estimated to be $w = 12.5\,\mathrm{mm}$ ($1/\mathrm{e}^2$ intensity level) and the on-axis intensity I_0 can be expressed as [B79, p. 671]:

$$I_0 = \frac{2P}{\pi\, w^2} = 29.8\,\mathrm{nW/cm^2}\,. \tag{7.7}$$

The Beer's law of linear absorption was used to calculate the number of atoms in the molasses zone:

$$I = I_0 \exp\left(-\frac{N^{\mathrm{OM}}_{\mathrm{at}}\,\sigma_0\, l}{V}\right)\,. \tag{7.8}$$

In the above equation l stands for the optical length which is probed by the laser and V is the volume of the interaction region. The ratio of the transmitted intensity through the atom cloud I to the incident intensity I_0 is simply $I/I_0 = U^{\mathrm{A}}_{\mathrm{PD}}/U^{\mathrm{B}}_{\mathrm{PD}} = 0.83$. The on–resonance scattering cross section σ_0 for the $|F = 4\rangle \rightarrow |F' = 5\rangle$ transition generally depends on the polarization of the absorption laser and the atomic alignment. Its value is on the order of a few $10^{-9}\,\mathrm{cm}^2$ which yields a value for the number of atoms $N^{\mathrm{OM}}_{\mathrm{at}}$ on the order of a few 10^8 atoms and respectively a flux of the atom beam on the order of 10^8 atoms/s (for 1 s loading time).

A rough estimate can be done on the validity of this result. The transition rate from the lower hyperfine level $|F = 4\rangle$ to the upper hyperfine level $|F' = 5\rangle$ can be expressed in terms of Einstein coefficients A and B. The inverse of the natural lifetime of the transition τ_{sp} gives the spontaneous decay rate Γ, respectively the coefficient $A = \Gamma = 3.28 \times 10^7\,\mathrm{s}^{-1}$. The connection between the coefficients A and B is given by:

$$B_{45'} = A_{5'4}\frac{\lambda^3}{8\pi\, h} = 1.22 \times 10^{21}\,\mathrm{m}^3/(\mathrm{J\,s}^2)\,, \tag{7.9}$$

where $\lambda = 852\,\mathrm{nm}$ is the transition wavelength and $h = 6.63 \times 10^{-34}\,\mathrm{J\,s}$ is the Planck's constant. Then the average time at which a stimulated excitation occurs is

$$t_{\mathrm{st}} = \frac{1}{B_{45'}\,\rho(\nu)} = \frac{c\,\delta\nu_{\mathrm{L}}}{B_{45'}\,I_0} = 0.83\,\mathrm{ms}\,, \tag{7.10}$$

where $\rho(\nu)$ is the spectral power density of the laser field, $\delta\nu_{\mathrm{L}} \approx 1\,\mathrm{MHz}$ is the spectral width of the laser and c is the speed of light. Compared to the value of $\tau_{\mathrm{sp}} \approx 30\,\mathrm{ns}$ it is $\approx 3 \times 10^4$ times larger and effects of optical stimulated emission due to the interaction of the absorption laser with the atoms in the molasses can be neglected. Additionally, as a typical value of the average velocity of the caesium atoms in optical molasses can be used 2.5 cm/s (at temperature of 10 µK). Then the maximum average time that a caesium atom spends within the range of the absorption laser is $\approx 73\,\mathrm{ms}$ (considering the Earth's acceleration due to gravity as the main source of atom losses). Hence the atom will experience ≈ 90 absorption-emission cycles before it leaves the interaction region.

7.5 CSF2 operation with LVIS loading

So far the presented work was focused on the examination of the properties of the new pump laser, which was introduced into the LVIS, and the parameters of the whole system have been optimized such that the maximum number of atoms participate in the clock cycle. In the following section the performance of the fountain with the LVIS on board is described.

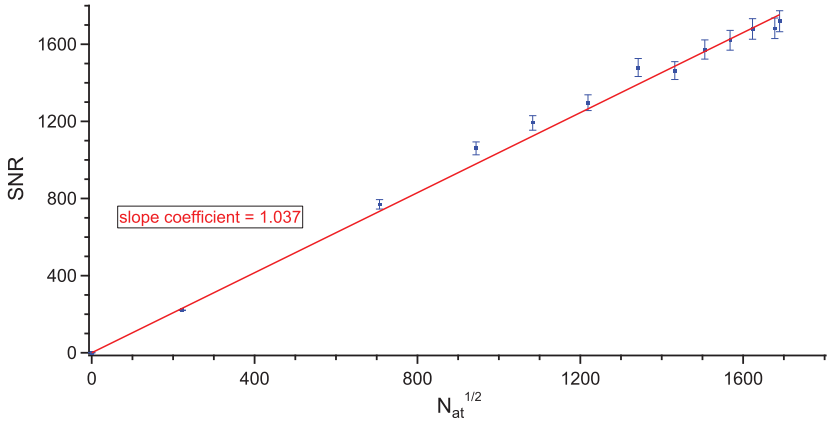

Figure 7.13 Quantum projection noise-limited operation of CSF2. The slope coefficient given by the performed linear regression fit (red line) over the experimental data (blue dots) is in a good agreement with the expected linear dependance of the measured signal-to-noise ratio on the square root of the number of interrogated atoms.

The frequency instability of a fountain frequency standard, alternatively to Equation 6.3, can be expressed by the Allan deviation as:

$$\sigma_y(\tau) = \frac{1}{\pi}\frac{\Delta\nu}{\nu_0}\frac{1}{\mathrm{SNR}}\sqrt{\frac{T_c}{\tau}}, \tag{7.11}$$

where $\Delta\nu$ is the FWHM of the central Ramsey fringe, $\nu_0 = 9\,192\,631\,770\,\mathrm{Hz}$ is the clock transition frequency, SNR is the signal-to-noise ratio of the measured signal, T_c is the cycle time, and τ the measurement time. In the case of quantum projection noise-limited operation, $\mathrm{SNR} = \sqrt{N_{\mathrm{at}}}$, with N_{at} the total number of detected atoms in the $F = 3$ and $F = 4$ hyperfine components of the Cs ground state.

The SNR was measured directly by operating the fountain CSF2 in a regime where the noise of the local oscillator did not contribute to the instability [B43]. The variation of the loaded number of atoms was achieved by altering loading period of the OM. For each particular loading time the fountain was left to perform a set of 1000 measurements (shots) of the atomic resonance, and the experimental data from each set (transition probability - $P(t_{\mathrm{k}})$ and detected atom number N_{at} in relative units) are stored on by the fountain control software on a computer. Here (t_{k}) is the time at which the measurement was taken and it can be incremented with integer numbers of T_c. For each set of measurements the series $\{P(t_{\mathrm{k}})\}$ were used to calculate the Allan variance, expressed as:

$$\sigma^2_{\mathrm{Allan}} = \frac{1}{2}\sum_{k=1}^{999}\frac{(P(t_{\mathrm{k}}) - P(t_{\mathrm{k}}+1))^2}{999},$$

and the signal-to-noise ratio, expressed as:

$$\mathrm{SNR} = \frac{\langle\{P(t_{\mathrm{k}})\}\rangle}{\sigma_{\mathrm{Allan}}}.$$

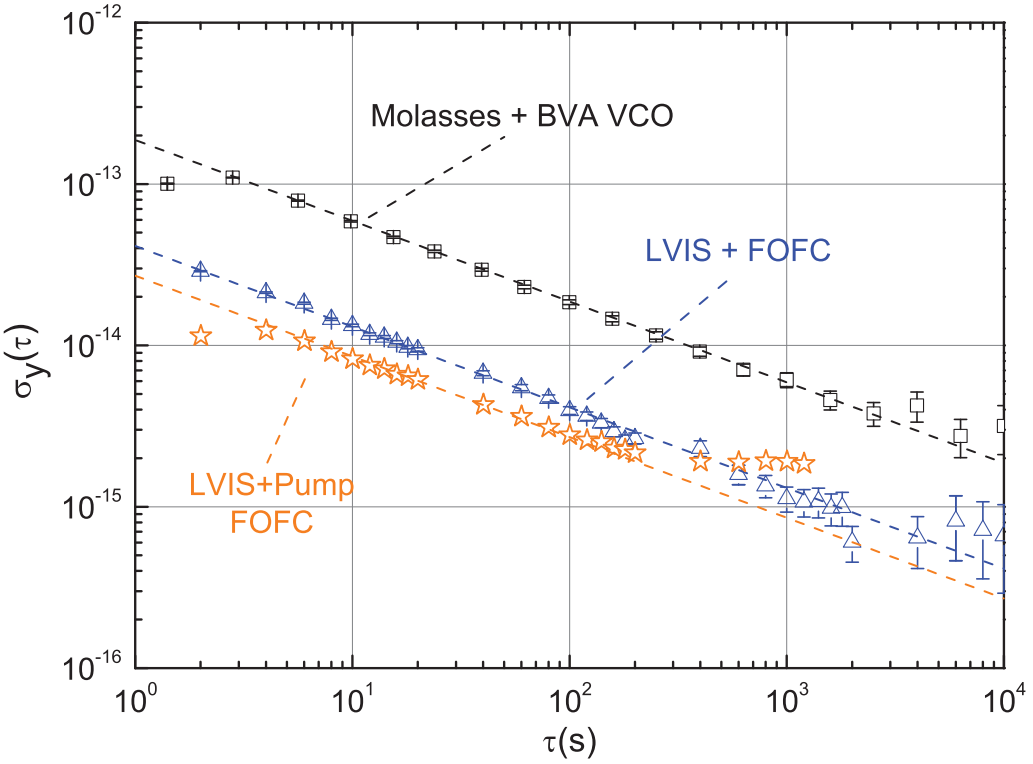

Figure 7.14 Allan deviation of the CSF2 frequency measured: black square symbols - OM loading from background gas, LO used - BVA VCO; blue triangles - OM loading with cold atom beam from the original LVIS setup, LO - DRO referenced to an optical cavity via FOFC; orange stars - OM loading from the LVIS setup operating with the pump laser, LO - DRO referenced to an optical cavity via FOFC; In the last case a fountain frequency instability of $\sigma_y(\tau) = 2.7 \times 10^{-14}\tau^{-1/2}$ is achieved - shown with a dashed orange line.

The measured SNR increased linearly as a function of $\sqrt{N_{\mathrm{at}}}$ (measured in relative units) and reached values larger than 1700. The linear dependence between SNR and $\sqrt{N_{\mathrm{at}}}$ allowed for calibration of N_{at} in terms of the absolute number of detected atoms (see Fig. 7.13).The expected CSF2 instability, calculated from Eq. 7.11 for $\Delta\nu = 0.9\,\mathrm{Hz}$, $T_c = 2\,\mathrm{s}$, SNR = 1680 and $N_{\mathrm{at}} = 2.9 \times 10^6$ was $\sigma_y(1\mathrm{s}) = 2.6 \times 10^{-14}$.

To experimentally confirm this value, the fountain was operated in a regime where the dominant contribution to its instability was the quantum projection noise. To reach this regime, an optically-stabilized 9.6 GHz microwave signal was generated using a frequency comb (FOFC) as a transfer oscillator, and it was used for the frequency synthesis of CSF2. This approach was described in Section 6.6. The frequency comb was referenced to a laser locked to an ultra-stable optical cavity, transferring the stability of the laser to a 9.6 GHz dielectric resonator oscillator (DRO). After removing the linear drift of the DRO frequency caused by the drift of the optical cavity, the measured Allan deviation $\sigma_y(\tau)$ showed a $\tau^{-1/2}$ dependence for measurement times up to 100 s (Fig. 7.14).

The measured fountain instability $\sigma_y\,(1\mathrm{s}) = 2.7 \times 10^{-14}$ was in a good agreement with the value of 2.6×10^{-14} inferred from the SNR measurements. It is also close to the best measured instability of $\sigma_y\,(1\mathrm{s}) = 1.6 \times 10^{-14}$ in a primary fountain clock, where the atoms were loaded from a decelerated Cs atomic beam [B53].

Chapter 8

Conclusion

As a result of the work on this part of the thesis, a new and more flexible modification of the existing source of slow caesium atoms LVIS was constructed [B81] and the optimization of the LVIS for loading the optical molasses of the PTB-CSF2 fountain clock was presented. The optimization needs a deep understanding of the operation of the clock and therefore its working principle is described in details in Chapter 6 of the thesis. Loss mechanisms of cold atoms during their flight between the LVIS apparatus and the loading zone have been identified and investigated. It could be demonstrated that such loss mechanisms are based on continued atom acceleration and heating due to light scattering. A pump laser, directed along the atom beam path, was introduced, which reduced atom losses. It allowed to selectively prepare the Cs atoms in the beam in a desired hyperfine ground state component and also to adjust their longitudinal velocity for optimal loading of the molasses.

Beams of slow atoms have a widespread importance in fields such as atom interferometry, atom optics, quantum gases, and atom lithography. The demonstrated optimization of the LVIS system can make it the preferable choice over other sources of slow atoms such as two-dimensional MOTs [B71].

In the PTB-CSF2 fountain clock, the atoms were additionally loaded in a volume in the proximity of the fountain axis by using a repumping laser beam propagating only along the fountain axis, which further increased the number of detected atoms and potentially it would also lead to a reduced contribution of the distributed cavity phase to the frequency uncertainty of the fountain [B33]. The achieved detected atom number was a factor of 40 above the one used in normal operation of CSF2. The LVIS atom flux and velocity were characterized through fluorescence and absorption measurements. With the LVIS in operation and using an optically stabilized microwave signal, the fountain frequency instability was quantum projection noise-limited and a value for it of $\sigma_y(\tau) = 2.7 \times 10^{-14}\tau^{-1/2}$ was measured. With such instability, the statistical uncertainty of the fountain reaches the level of its present systematic uncertainty in 10^4 s. The improved stability of the PTB-CSF2 clock ranks it among the best primary frequency standards in the world.

References for Part II

[B1] V. Gerginov et al. "Uncertainty evaluation of the caesium fountain clock PTB-CSF2". *Metrologia* 47.1 (2010), p. 65.

[B2] R. Wynands and S. Weyers. "Atomic fountain clocks". *Metrologia* 42.3 (2005), S64–S79.

[B3] S. Weyers, B. Lipphardt, and H. Schnatz. "Reaching the quantum limit in a fountain clock using a microwave oscillator phase locked to an ultrastable laser". *Phys. Rev. A - At. Mol. Opt. Phys.* 79.3 (2009), pp. 1–4.

[B4] Z. T. Lu et al. *Phys. Rev. Lett* 77 (1996), pp. 3331–3334.

[B5] Claude Cohen-Tannoudji, Bernard Diu, and Frank Laloë. *Quantum Mechanics (Volume 2)*. Volume 2. Wiley, New York, 1977.

[B6] E. Arimondo, M. Inguscio, and P. Violino. "Experimental determinations of the hyperfine structure in the alkali atoms". *Reviews of Modern Physics* 49.1 (1977), pp. 31–75.

[B7] Carol E. Tanner and Carl Wieman. "Precision measurement of the hyperfine structure of the ^{133}Cs $6P_{3/2}$ state". *Phys. Rev. A* 38 (3 1988), pp. 1616–1617.

[B8] Peter F. Bernath. *Spectra of Atoms and Molecules*. 2nd ed. Oxford University Press, 2005.

[B9] Harold. J. Metcalf and Peter van der Starten. *Laser cooling and trapping*. Springer-Verlag, New York, 1999.

[B10] T.W. Hänsch and A.L. Schawlow. "Cooling of gases by laser radiation". *Opt. Commun.* 13.1 (1975), pp. 68–69.

[B11] D. Wineland and H. Dehmelt. "" *Bull. Am. Phys. Soc.* 20 (1975), p. 637.

[B12] Steven Chu et al. "Three-dimensional viscous confinement and cooling of atoms by resonance radiation pressure". *Phys. Rev. Lett.* 55.1 (1985), pp. 48–51.

[B13] Paul D Lett et al. "Observation of Atoms Laser Cooled below the Doppler Limit". *Phys. Rev. Lett.* 61.2 (1988), pp. 169–172.

[B14] C Salomon et al. “Laser Cooling of Cesium Atoms Below 3µK”. *Europhysics Lett.* 12.8 (1990), p. 683.

[B15] M Drewsen et al. “Investigation of sub-Doppler cooling effects in a cesium magneto-optical trap”. *Appl. Phys. B* 59.3 (1994), pp. 283–298.

[B16] J Dalibard and C Cohen-Tannoudji. “Laser cooling below the Doppler limit by polarization gradients: simple theoretical models”. *J. Opt. Soc. Am. ˜B* 6.11 (1989), pp. 2023–2045.

[B17] David S. Weiss et al. “Optical molasses and multilevel atoms: theory”. *J. Opt. Soc. Am. B* 6.11 (1989), p. 2072.

[B18] E. L. Raab et al. “Trapping of Neutral Sodium Atoms with Radiation Pressure”. *Phys. Rev. Lett.* 59.23 (1987), pp. 2631–2634.

[B19] Norman F. Ramsey. *Molecular Beams (International Series of Monographs on Physics)*. Oxford University Press, 2005.

[B20] Andrea de Marchi. “The Optically Pumped Caesium Fountain: 10 -15 Frequency Accuracy?” *Metrologia* 18.3 (1982), p. 103.

[B21] a Clairon et al. “Ramsey Resonance in a Zacharias Fountain”. *Europhys. Lett.* 16.2 (1991), pp. 165–170.

[B22] S. Weyers et al. “First performance results of PTB’s atomic caesium fountain and a study of contributions to its frequency instability”. *Ultrasonics, Ferroelectrics, and Frequency Control, IEEE Transactions on* 47.2 (2000), pp. 432–437.

[B23] S.R. Jefferts et al. “Preliminary accuracy evaluation of a cesium fountain primary frequency standard at NIST”. *Frequency and Time Forum, 1999 and the IEEE International Frequency Control Symposium, 1999., Proceedings of the 1999 Joint Meeting of the European*. Vol. 1. 1999, 12–15 vol.1.

[B24] F. Levi et al. “IEN-CsF1 accuracy evaluation and two-way frequency comparison”. *Ultrasonics, Ferroelectrics, and Frequency Control, IEEE Transactions on* 51.10 (2004), pp. 1216–1224.

[B25] K. Szymaniec et al. “Evaluation of the primary frequency standard NPL-CsF1”. *Metrologia* 42.1 (2005), p. 49.

[B26] R. Wynands et al. “Current status of PTB’s new caesium fountain clock CSF2”. *Frequency and Time Forum (EFTF), 2006 20th European*. 2006, pp. 200–202.

[B27] Fritz Riehle. *Frequency Standards: Basics and Applications*. 1st ed. Wiley-VCH, 2005.

[B28] R. Schroder, U. Hubner, and D. Griebsch. “Design and realization of the microwave cavity in the PTB caesium atomic fountain clock CSF1”. *Ultrasonics, Ferroelectrics, and Frequency Control, IEEE Transactions on* 49.3 (2002), pp. 383–392.

[B29] A. Sen Gupta et al. "A new 9-GHz synthesis chain for atomic fountain clocks". *Proc. IEEE Int. Freq. Control Symp. Expo.* (2007), pp. 234–237.

[B30] M Kumagai et al. "Evaluation of caesium atomic fountain NICT-CsF1". *Metrologia* 45.2 (2008), pp. 139–148.

[B31] Krzysztof Szymaniec et al. "First accuracy evaluation of the NPL-CsF2 primary frequency standard". *Metrologia* 47.4 (2010), p. 363.

[B32] Jacques Vanier and Claude Audoin. *The Quantum Physics of Atomic Frequency Standards*. 1st. Adam Hilger, 1989.

[B33] S Weyers et al. "Distributed cavity phase frequency shifts of the caesium fountain PTB-CSF2". *Metrologia* 49.1 (2012), p. 82.

[B34] Wayne M. Itano, L. L. Lewis, and D. J. Wineland. "Shift of $^2S_{1/2}$ hyperfine splittings due to blackbody radiation". *Phys. Rev. A* 25.2 (1982), pp. 1233–1235.

[B35] E Simon, P Laurent, and A Clairon. "Measurement of the Stark shift of the Cs hyperfine splitting in an atomic fountain". *Phys. Rev. A* 57.1 (1998), pp. 436–439.

[B36] Peter Rosenbusch, Shougang Zhang, and Andre Clairon. "Blackbody radiation shift in primary frequency standards". *Proc. 2007 Ieee Int. Freq. Control Symp. With 21St Eur. Freq. Time Forum, Vols 1-4* 3 (2007), pp. 1060–1063.

[B37] E. J. Angstmann, V. A. Dzuba, and V. V. Flambaum. "Frequency shift of hyperfine transitions due to blackbody radiation". *Phys. Rev. A - At. Mol. Opt. Phys.* 74.2 (2006), pp. 1–8.

[B38] E. Tiesinga et al. "Spin-exchange frequency shift in a cesium atomic fountain". *Phys. Rev. A* 45.5 (1992), pp. 2671–2673.

[B39] Paul J. Leo et al. "Collisional frequency shifts in 133Cs fountain clocks". *Phys. Rev. Lett.* 86.17 (2001), pp. 3743–3746.

[B40] F. Pereira Dos Santos et al. "Controlling the cold collision shift in high precision atomic interferometry." *Phys. Rev. Lett.* 89.23 (2002), p. 233004.

[B41] M. Kazda et al. "Investigation of Rapid Adiabatic Passage for Controlling Collisional Frequency Shifts in a Caesium Fountain Clock". *Instrumentation and Measurement, IEEE Transactions on* 62.10 (2013), pp. 2812–2819.

[B42] Vladislav Gerginov, Nils Nemitz, and Stefan Weyers. "Initial atomic coherences and Ramsey frequency pulling in fountain clocks". *Phys. Rev. A - At. Mol. Opt. Phys.* 90.3 (2014), pp. 1–12.

[B43] C Santarelli et al. "Quantum projection noise in an atomic fountain: A high stability cesium frequency standard". *Phys. Rev. Lett.* 82.23 (1999), pp. 4619–4622.

[B44] W. M. Itano et al. "Quantum projection noise: Population fluctuations in two-level systems". *Phys. Rev. A* 47.5 (1993), pp. 3554–3570.

[B45] Claude Audoin et al. *IEEE Trans. Ultrason. Ferroelectr. Freq. Control* 45.4 (1998), pp. 877–886.

[B46] G John Dick. "Local oscillator induced instabilities in trapped ion frequency standards". *19th PTTI Appl. Plan. Mtg.* (1987), pp. 133–147.

[B47] Giorgio Santarelli et al. "Frequency stability degradation of an oscillator slaved to a periodically interrogated atomic resonator". *IEEE Trans. Ultrason. Ferroelectr. Freq. Control* 45.4 (1998), pp. 887–894.

[B48] C.A. Greenhall. "A derivation of the long-term degradation of a pulsed atomic frequency standard from a control-loop model". *IEEE Trans. Ultrason. Ferroelectr. Freq. Control* 45.4 (1998), pp. 895–898.

[B49] Patrick Berthoud et al. "Toward a primary frequency standard based on a continuous fountain of laser-cooled cesium atoms". *IEEE Trans. Instrum. Meas.* 48.2 (1999), pp. 516–519.

[B50] Alain Joyet et al. "Theoretical study of the dick effect in a continuously operated Ramsey resonator". *IEEE Trans. Instrum. Meas.* 50.1 (2001), pp. 150–156.

[B51] Laurent Devenoges et al. "Improvement of the frequency stability below the dick limit with a continuous atomic fountain clock". *IEEE Trans. Ultrason. Ferroelectr. Freq. Control* 59.2 (2012), pp. 211–216.

[B52] Sebastien Bize et al. "Advances in atomic fountains". *Comptes Rendus Phys.* 5.8 SPEC.ISS. (2004), pp. 829–846.

[B53] C. Vian et al. "BNM-SYRTE Fountains: Recent Results". *IEEE Trans. Instrum. Meas.* 54.2 (2005), pp. 833–836.

[B54] F. Füzesi et al. "An electrostatic glass actuator for ultrahigh vacuum: A rotating light trap for continuous beams of laser-cooled atoms". *Rev. Sci. Instrum.* 78.10 (2007), p. 103109.

[B55] L. Devenoges et al. "Design and realization of a low phase gradient microwave cavity for a continuous atomic fountain clock". *2013 Jt. Eur. Freq. Time Forum Int. Freq. Control Symp. EFTF/IFC 2013* (2013), pp. 235–238.

[B56] J. Millo et al. "Ultralow noise microwave generation with fiber-based optical frequency comb and application to atomic fountain clock". *Appl. Phys. Lett.* 94.14 (2009), pp. 12–15.

[B57] T. Nazarova, F. Riehle, and U. Sterr. "Vibration-insensitive reference cavity for an ultra-narrow-linewidth laser". *Appl. Phys. B Lasers Opt.* 83.4 (2006), pp. 531–536.

[B58] S A Webster et al. "Thermal-noise-limited optical cavity". *Phys. Rev. A* 77 (2008), pp. 1–6.

[B59] I. Sherstov et al. "Diode-laser system for high-resolution spectroscopy of the $^2S_{1/2} \rightarrow {}^2F_{7/2}$ octupole transition in $^{171}Yb^+$". *Phys. Rev. A - At. Mol. Opt. Phys.* 81.2 (2010), pp. 2–5.

[B60] A. Bartels et al. "Femtosecond-laser-based synthesis of ultrastable microwave signals from optical frequency references". *Opt. Lett.* 30.6 (2005), pp. 667–669.

[B61] Burghard Lipphardt et al. "The stability of an optical clock laser transferred to the interrogation oscillator for a Cs fountain". *IEEE Trans. Instrum. Meas.* 58.4 (2009), pp. 1258–1262.

[B62] C. Tamm et al. "Cs-based optical frequency measurement using cross-linked optical and microwave oscillators". *Phys. Rev. A - At. Mol. Opt. Phys.* 89.2 (2014), pp. 1–8.

[B63] W. D. Phillips and H. Metcalf. "Laser Deceleration of an Atomic Beam". *Phys. Rev. Lett.* 48.9 (1982), pp. 596–599.

[B64] W. Ertmer et al. "Laser Manipulation of Atomic Beam Velocities: Demonstration of Stopped Atoms and Velocity Reversal". *Phys. Rev. Lett.* 54.10 (1985), pp. 996–999.

[B65] R. N. Watts and C. E. Wieman. "Manipulating atomic velocities using diode lasers". *Opt. Lett.* 11.5 (1986), p. 291.

[B66] K I Lee et al. "Single-beam atom trap in a pyramidal and conical hollow mirror". *Opt. Lett.* 21.15 (1996), p. 1177.

[B67] J. J. Arlt et al. "A pyramidal magneto-optical trap as a source of slow atoms". *Opt. Commun.* 157.1-6 (1998), pp. 303–309.

[B68] R. Williamson et al. "A magneto-optical trap loaded from a pyramidal funnel". *Opt. Express* 3.3 (1998), p. 111.

[B69] K. Kim et al. "Cold atomic beam produced by a conical mirror funnel". *Phys. Rev. A* 64.1 (2001), pp. 1–5.

[B70] J. Schoser et al. "Intense source of cold Rb atoms from a pure two-dimensional magneto-optical trap". *Phys. Rev. A* 66.2 (2002), p. 023410.

[B71] K. Dieckmann et al. "Two-dimensional magneto-optical trap as a source of slow atoms". *Phys. Rev. A* 58.5 (1998), pp. 3891–3895.

[B72] S. Weyers et al. "A continuous beam of cold cesium atoms extracted from a two-dimensional magneto-optical trap". *Opt. Commun.* 143.1-3 (1997), pp. 30–34.

[B73] P. Berthoud, E. Fretel, and P. Thomann. "Bright, slow, and continuous beam of laser-cooled cesium atoms". *Phys. Rev. A* 60.6 (1999), R4241–R4244.

[B74] Ch. Y. Park, M. S. Jun, and D. Cho. *J. Opt. Soc. Am. B* 16.6 (1999), pp. 994–997.

[B75] He Wang and W. F. Buell. *J. Opt. Soc. Am. B* 20.10 (2003), pp. 2025–2030.

[B76] B K Teo, T Cubel, and G Raithel. "A slow and dark atomic beam". *Opt. Commun.* 212.4-6 (2002), pp. 307–315.

[B77] H. Wang and G. Iyanu. "MOT-based continuous cold Cs-beam atomic clock". *2010 IEEE International Frequency Control Symposium*. 2010, pp. 454–458.

[B78] J. Fang et al. "Compact high-flux cold cesium beam source based on a modified two-dimensional magneto-optical trap". *J. Opt. Soc. Am. B* 32.5 (2015), B61–B66.

[B79] Antony. E. Siegman. *Lasers*. University Science Books, New York, 1986, p. 671.

[B80] B. Lipphardt et al. (). to be published.

[B81] G. Dobrev, V. Gerginov, and S. Weyers. "Loading a fountain clock with an enhanced low-velocity intense source of atoms". *Physical Review A*. 93 (2016), p. 043423.

Part III

Experimental investigation of transition metal hydride radicals FeH and NiH

Chapter 9

Introduction

9.1 High resolution studies of FeH

Some of the first-row transition metal monohydrides seen in sunspots and in the spectra of cool stars have been noted as possible probes of magnetic field, particularly for cool stellar objects. FeH, cited for example by Afram et al.[C1], seems particularly promising in this respect, because of its strong Zeeman response in the near infrared (NIR) where molecular features dominate in cool star spectra. Laboratory spectra are required to supply reliable parameters for spectropolarimetric analysis of remote objects, but producing parameters appropriate for the equilibrium temperatures of cool stellar objects - usually more than 3000K and greatly in excess of temperatures accessible in the laboratory - is non-trivial. Forming such species at near-ambient temperatures has the advantage of reducing Doppler widths, and making it possible to resolve (at least partially) Zeeman structure within rotational lines. High-sensitivity spectroscopy is an asset in this context. Another major challenge is to model available data so that extrapolations to hotter conditions are plausible.

The near-infrared spectrum of FeH continues to interest astrophysicists studying cool stellar systems and molecular physicists. The former see the possibility to use FeH as possible probes of magnetic field. The latter are trying to unravel the complexity of the electronic structure of this small radical. On the experimental side the high resolution data are limited, which makes FeH an interesting challenge both for theoretical chemistry and for laboratory spectroscopy.

Stellar signatures of the $F^4\Delta$–$X^4\Delta$ electronic system of FeH were first recognized in the 1960s and reported by Wing and co-workers on M- and S-type dwarfs [C4]. Simple molecules survive in cool solar or stellar environments. Those with the strongest electronic transition dipole moments and greatest abundances are observed in absorption as band spectra. Of special interest are molecules with permanent magnetic moment, because their spectra can be used to assess magnetic fields (strength and direction) in such objects. This may be possible if the magnetic response of these species is known through reliable models (not available for FeH) or by laboratory work. Two molecular bands of FeH F-X system give rise to now well-established signatures in the

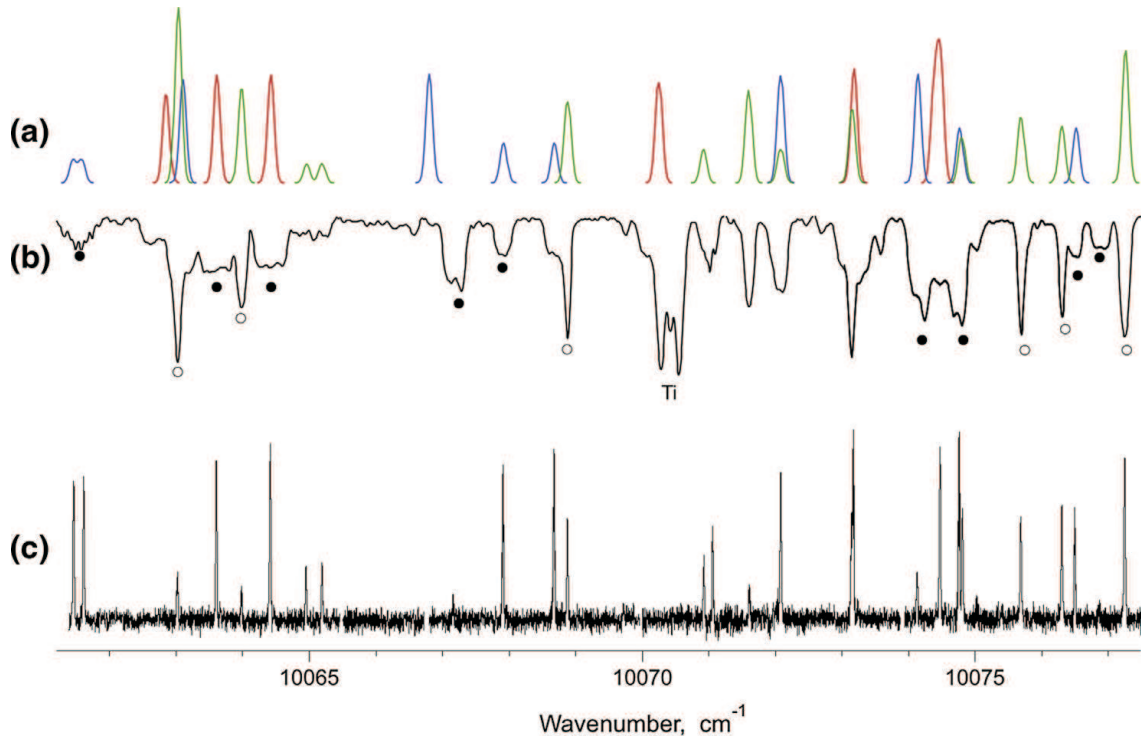

Figure 9.1 Comparison between zero field and sunspot spectra in the Wing-Ford band of FeH. FeH spectrum recorded within this study (trace c) at zero field, and corresponding solar umbral absorption (trace b) taken from the solar atlas of Wallace et al. [C2]. The upper trace gives relative intensities predicted from the FeH Atlas [C3] at 3300 K, assuming FWHM = $0.12\,\mathrm{cm}^{-1}$ for all contributions (no Zeeman broadening). Transitions between the F_1 components are drawn with thick (red) solid lines, F_2 with thinner (blue) ones, and F_3 transitions as (green) lines. Magnetically active or inactive lines are indicated by filled or empty circles respectively.

spectra of cool stellar surfaces, such as sunspots [C5, C6] or brown dwarf stars [C1]: the 1-0 band at 869.2 nm, and the so called Wing-Ford 0-0 band at 989.6 nm. Thus considerable effort has been made in the laboratory to supply the astronomers with accurate line positions, line strength factors [C7], and magnetic response parameters [C8, C9, C10].

The presence of FeH in cool stars is explained by reaction of H and Fe (the most abundant metal produced by stellar nucleosynthesis). The dissociation energy of FeH is estimated to be $D_{00} = 1.86$ eV [C11] so once formed, the radicals can survive at (cool stellar surface) equilibrium temperatures of several thousand Kelvin. The sunspot umbral absorption atlas of Wallace and co-workers [C2] identifies numerous lines of the F-X system of FeH in the near infrared. Many of these profiles can be seen to be Zeeman-broadened when compared with a laboratory absorption spectrum taken at zero field, as shown in Fig. 9.1. It is perhaps surprising, given the interest of these particular bands (located in a relatively uncluttered region of the solar spectrum, where Zeeman splittings start to be significant relative to Doppler broadening) that laboratory data are lacking. But it has proved difficult to provide extensive benchmark measurements in well-controlled conditions. The King furnace source is not readily compatible with a large and homogeneous magnetic field, and other methods of production used in laser spectroscopic work (laser ablation [C12], discharge in iron pentacarbonyl [C13, C14, C15, C16] or sputter sources [C17]), while offering higher spectral resolution, have fallen seriously short in terms of thermal distribution. The Wing-Ford band in particular happens to lie in an optically awkward region (1 μm), at the very edge of currently available tuneable Ti:sapphire lasers, and well away from the peak sensitivity of Si and InGaAs detectors used in the near infrared. The fact that laser-induced fluorescence from the Wing-Ford band happens to be quasi-resonant complicates the detection issue a little further, as laser scatter cannot be attenuated with optical filters. Thus for many of the lines, the best estimates of Landé factors available in the literature are still those extracted from the profiles of sunspot data, for example by Harrison and Brown [C5], or Afram and coworkers [C1].

The Doppler-limited zero-field thermal emission spectrum recorded using a King furnace near 2000 K recorded and analysed by Phillips and co-workers [C18], has provided an extensive collection of rotational data of the F-X system, involving all four spin-orbit components of both electronic states, and covering seven vibrational bands. Dulick et al. [C3] took the analysis of these data some steps further, and produced an Atlas designed to assess molecular opacities; their model predicted parity splittings that were unresolved in the original spectrum, as well as positions of many unobserved lines.

Laboratory measurements of Landé factors have emerged gradually in the literature. Accurate g_J Landé factors for several rotational levels of the ground X $^4\Delta_\Omega$ state were determined by laser magnetic resonance spectroscopy (LMR), first with a variable magnetic field tuning pure rotational transitions into resonance with methanol lines pumped by a CO_2 laser in work performed at NIST, Boulder [C13], in 1988.

The range of rotational levels was gradually extended, and when shorter-wavelength laser lines became available, fine-structure transitions were also measured [C14]. The paper from Brown et al. [C14] became a reference for ground state energies for the lowest rotational levels, giving proton hyperfine parameters and effective Landé factors for ^{56}FeH that have provided the basis for deducing F$^4\Delta$ state Landé factors in subsequent laboratory work on optical spectra. The first high-resolution investigation of the Zeeman effect in the F-X system of FeH was reported by Harrison et al., who formed the radical in a laser ablation source, and used a supersonic expansion to work at rotational temperatures < 20 K [C12]. Only transitions in the 1-0 band, from the lowest rotational level of the ground state, were recorded, but Zeeman broadening was obvious at fields < 600 Gauss. Two Landé factors were extracted for the F $^4\Delta_{7/2}$ state, for $v = 1$, $J = 7/2$ and $9/2$. Given this key information as a starting point, Harrison and Brown went on to model the profiles of some of the FeH lines identified in the sunspot atlas [C2], with upper state Landé factors being the parameters to be determined [C5]. A lower spectral resolution and some uncertainty in the effective magnetic field in the umbral regions complicated the task, but this approach remains the only option to study transitions originating from thermally excited lower levels. In a similar vein, Afram and co-workers [C1] fitted the profiles of selected magnetically sensitive lines of FeH in data from the sunspot atlas, plus polarimetric data taken by Ruedi et al. [C19] to determine effective Landé factors for more levels. They then parameterised the trend of the Landé factors in order to extrapolate to high J, motivated by the need for this information if FeH features were to be used as a probe for magnetic fields in L-type stars. Even if the extrapolation parametrisation is not entirely convincing, the match in line profiles was close enough to conclude that this system of FeH was indeed a good choice for magnetic field diagnostics. At about the same time, Shulyak and co-workers were faced with a similar need for reliable Landé factors, as they tried to understand the molecular Zeeman spectra observed in M-dwarf stars [C20], where FeH lines (notably in the Wing-Ford band) are particularly pronounced. They calculated effective g_J factors from considerations of molecular angular momentum, testing different empirical descriptions to describe the appropriate "intermediate" between the limiting Hund's case (a) and (b) coupling regimes. They likewise relied on comparison with solar umbral spectra to adjust their parameters, and mentioned the inadequacies of such a model to accurately represent the electronic structure of this species. It seems useful then to extend the range of laboratory benchmark measurements.

9.2 Goals

The present experimental study is motivated by the need of accurate laboratory data for interpretation of the astrophysical observations of FeH. These data include zero-magnetic field transition frequencies, relative line intensities and effective g-factors.

9.2.1 Design of a New coaxial discharge source : validation on NiH

As already discussed, one of the main challenges in the laboratory studies of metal hydrides is their production in conditions which allow precision spectroscopy and measurements in well defined magnetic fields. In the Lyon experiment FeH is formed in a sputter source, at rotational temperatures around 500 K, and probed with a laser between permanent magnets, generating well-defined magnetic fields of the order of 3000 Gauss (comparable with sunspot field strengths). This is sufficient to partially resolve the Zeeman patterns associated with the first rotational lines in the 0-0 and 1-0 bands of the F-X system, from which we aim to define effective g_{eff} Landé factors to 1% accuracy. This source produces MH like NiH and FeH at high concentrations and proved to be very efficient for high resolution studies including Fourier-Transform-Spectroscopy (FTS) [C21]. A disadvantage of this source is that the absorption length is not well defined and therefore it is difficult to determine absorption cross-sections. Additionally, the region where molecules are excited for LIF-FTS studies is very close to the discharge region, whose emission cannot be filtered out and enters the FT-spectrometer, producing a background of atomic lines (mostly Ar).

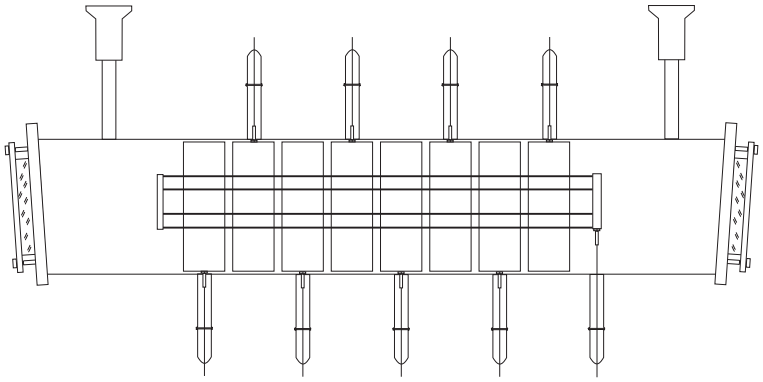

Figure 9.2 Scheme of the coaxial discharge tube from [C22]

In Sofia, a new type of discharge source was designed [C22]. The cathode consists of eight separate nickel rings, forming a cylinder with a total length of 250 mm. The anode is formed by six stainless steel rods laid equidistantly on a cylindrical surface (coaxial with the cathode) with a diameter of approximately 30 mm. When run with H_2 gas at pressures above 2 Torr and with currents between 100-200 mA, it was demonstrated that the discharge is contained between the anode and the cathodes and no emission comes from the central part of the tube. This design of source for MH offers a well defined absorption path length and possibly better conditions for LIF experiments. Part of my thesis was intended to find a way to overcome some of the problems discovered in [C22] and to construct a new coaxial source, suitable for measurements also in magnetic fields. Details are given in chapter 11.

9.2.2 High resolution studies of MH with a hollow cathode source : FeH, NiD

The spectroscopic part of this work is devoted to systematic high resolution study of the first vibrational levels ($v' = 0$ and $v'' = 1$) of the $^4\Delta_{7/2}$ and $^4\Delta_{5/2}$ components of the F state in FeH. Experiments were carried out both in zero magnetic field and in magnetic fields up to 5000 Gauss.

This information was collected by laser absorption spectroscopy of the F-X electronic system in FeH. The data on the $X^4\Delta$ state [C14] was used to reduce the measured transition frequencies to energy level positions of the F state.

For each of the investigated rovibrational levels of the F state, experiments in a static magnetic field were conducted in order to determine the Landé g-factors. The experimental values were compared with the theoretical calculations for the pure Hund's cases(a) and (b).

In the course of this study it turned out that the thermal population of rotational levels with $J > 10.5$ in the used sources is very low and the associated lines are very weak. Since high J levels are particularly interesting in astrophysics, it is necessary to ensure sufficient signal-to-noise ratio for the lines split in magnetic fields. Several possible solution are discussed in this thesis. One of them is a Cavity ring-down spectroscopy (CRDS) setup employed in combination with the current discharge sources.

Chapter 10

Diatomic Molecules : metal hydrides

In this chapter a brief theoretical description of the diatomic molecules is presented. The metal monohydrides are molecules of rather complicated electronic structure and it is necessary to discuss it before one can speak about the Zeeman effect in molecules.

10.1 Born-Oppenheimer approximation. Hund's cases.

The theoretical description of diatomic molecules is based on two basic assumptions: the Born-Oppenheimer approximation and the Hund's cases.

The Born-Oppenheimer (BO) approximation assumes that the electron motion is much faster than the nuclear, therefore one can describe the electronic motion by fixed nuclei. Of course, the electronic wave function $\Psi_{\rm el}$ depends on the distance between the two nuclei R. Quantum mechanically, the Born-Oppenheimer approximation can be written as [C23]:

$$\frac{\partial \Psi_{\rm el}}{\partial R} \approx 0 \ ,$$

for all R, consequently the second derivative $\partial^2 \Psi_{\rm el}/\partial R^2$ is also approximately zero for all R. Given the BO approximation, the total wave function of the molecule can be written as a product of the electronic wave function $\Psi_{\rm el}(\vec{\mathbf{r}}, \vec{\mathbf{R}})$ and the nuclear wave function $\Psi_{\rm nuc}(\vec{\mathbf{R}})$, where $\vec{\mathbf{r}}$ are the electronic coordinates and $\vec{\mathbf{R}}$ – the nuclear coordinates. The electronic wave function is the eigenfunction of the electronic part of the total Hamiltonian:

$$\mathbf{H}_{el} \Psi_{{\rm el},i}(\vec{\mathbf{r}}, \vec{\mathbf{R}}) = U_i(R) \Psi_{{\rm el},i}(\vec{\mathbf{r}}, \vec{\mathbf{R}}). \tag{10.1}$$

The nuclear wave function is the eigenfunction of the nuclear part of the total Hamiltonian:

$$\left[\mathbf{H}_{nuc} + U_i(R)\right] \Psi_{{\rm nuc},ij}(\vec{\mathbf{R}}) = E_{ij} \Psi_{{\rm nuc},ij}(\vec{\mathbf{R}}). \tag{10.2}$$

The R-dependent eigenenergies, $U_i(R)$, of the electronic Hamiltonian play the role of potential energy curves in the nuclear equation (10.2). The electronic equation cannot be solved exactly even for the lightest molecules, therefore the potential curves can be obtained only numerically and their accuracy is usually much lower than the accuracy of the experimental observations [1]. Nevertheless, the potential curve is a useful concept which helps to classify the experimental observations and to develop methods for description of the energy levels structure of the molecule within the experimental uncertainty.

Each solution of the electronic equation corresponds to an electronic state. The i-index consists of a series of quantum numbers. They correspond to electronic operators, which commute with the total molecular Hamiltonian. Strictly speaking such operators are only the total angular momentum of the molecule and its projection on a chosen molecular symmetry axis. Fortunately, there are other operators, which to a good approximation also commute with the total Hamiltonian. The particular set of such operators depends on the molecule. Moreover, the set may change by going from one electronic state to the other.

The angular momenta in a diatomic molecule are summarized in the following table:

Single particle angular momenta:	
spin of nucleus A or B	$\vec{\mathbf{i}}_A$, $\vec{\mathbf{i}}_B$
orbital angular momentum of the i^{th} electron	$\vec{\mathbf{l}}_i$
spin of the i^{th} electron	$\vec{\mathbf{s}}_i$
angular momentum of the nuclear framework	$\vec{\mathfrak{R}}$
Single particle angular momenta can couple to:	
total nuclear spin	$\vec{\mathbf{I}} = \vec{\mathbf{i}}_A + \vec{\mathbf{i}}_B$
total electronic angular momentum	$\vec{\mathbf{L}} = \sum_i \vec{\mathbf{l}}_i$
total electron spin	$\vec{\mathbf{S}} = \sum_i \vec{\mathbf{s}}_i$
total angular momentum excluding $\vec{\mathbf{I}}$	$\vec{\mathbf{J}} = \vec{\mathfrak{R}} + \vec{\mathbf{S}} + \vec{\mathbf{L}}$
total angular momentum	$\vec{\mathbf{F}} = \vec{\mathfrak{R}} + \vec{\mathbf{L}} + \vec{\mathbf{S}} + \vec{\mathbf{I}}$
total angular momentum excluding $\vec{\mathbf{S}}$ and $\vec{\mathbf{I}}$	$\vec{\mathbf{N}} = \vec{\mathbf{J}} - \vec{\mathbf{S}} = \vec{\mathfrak{R}} + \vec{\mathbf{L}}$
total electronic angular momentum	$\vec{\mathbf{J}}_a = \vec{\mathbf{S}} + \vec{\mathbf{L}}$
Projections of angular momenta:	
$\vec{\mathbf{L}}$ projected on the molecular axis	L_z
$\vec{\mathbf{S}}$ projected on the molecular axis	S_z
$\vec{\mathbf{J}}$ projected on the molecular axis	J_z

The choice of the good quantum numbers depends on the particular coupling of the various angular momenta in the molecule. Some idealized coupling schemes, called Hund's coupling cases, are presented in Fig. 10.1.

[1] except for the lightest molecules like H_2, Li_2

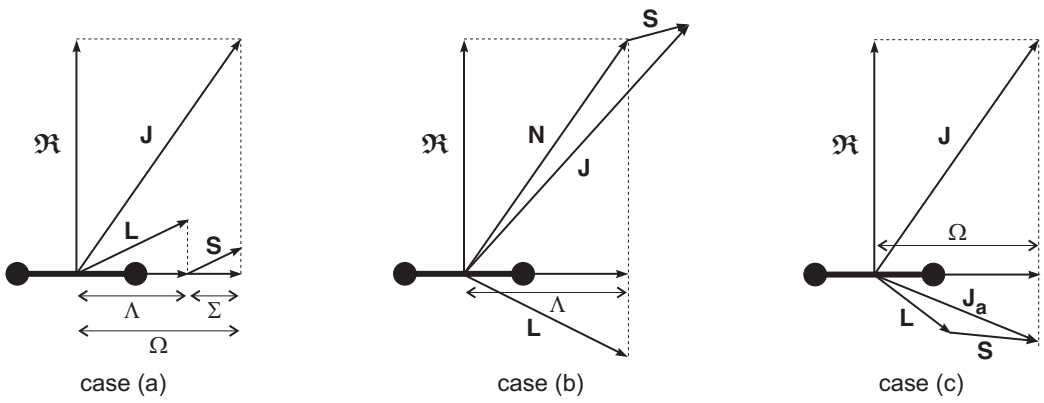

Figure 10.1 Coupling schemes of the angular momenta for Hund's cases (a), (b) and (c)

In Hund's case (a) there is a strong electric field along the internuclear axis, and $\vec{\mathbf{L}}$ is therefore coupled to the internuclear axis. Similarly to the Stark effect in atoms, its projection L_z is quantized as $\Lambda\hbar$ and Λ becomes a good quantum number. The total electronic spin cannot couple directly to the electrostatic field along the internuclear axis, but once $\vec{\mathbf{L}}$ is coupled, the associated magnetic field couples $\vec{\mathbf{S}}$ and the quantum number Σ, describing the projection S_z also becomes a good quantum number. The sum of Λ and Σ is Ω, and this is also a good quantum number. The total angular momentum $\vec{\mathbf{J}}$ is a sum of the nuclear rotation $\vec{\mathfrak{R}}$ and the projections L_z and S_z. Obviously, Ω is associated with the projection of $\vec{\mathbf{J}}$ on the intermolecular axis. Hund's case (a) is a good approximation for molecules with strong electric field along the intermolecular axis. However, even for such molecules, when the projection of $\vec{\mathbf{L}}$ is zero ($\Lambda = 0$), the spin cannot couple to z-axis and case (a) fails to be a good approximation. Hund's case (a) also fails when the magnetic field produced by the rotation of the nuclear frame is stronger than that produced by L_z. This may happen in very light molecules, containing at least one hydrogen atom.

The case when $\vec{\mathbf{S}}$ does not couple to the internuclear axis is called Hund's case (b) [C23]. Here $\vec{\mathfrak{R}}$ and L_z couple to form the intermediate angular momentum $\vec{\mathbf{N}}$. Λ is still a good quantum number. The electronic spin couples to the weak magnetic field produced by $\vec{\mathbf{N}}$ and the total angular momentum $\vec{\mathbf{J}} = \vec{\mathbf{N}} + \vec{\mathbf{S}}$. Since S_z is not coupled to the internuclear axis, Σ is no longer a good quantum number.

In both Hund's cases (a) and (b) the relativistic effects (spin-orbit and spin-spin interactions) are neglected. For heavier molecules, however, this is no longer a reasonable approximation. Hund's case (c) considers molecules where the spin-orbit interaction plays a dominant role in the coupling scheme. $\vec{\mathbf{L}}$ couples with $\vec{\mathbf{S}}$ and the intermediate angular moment $\vec{\mathbf{J}}_\mathbf{a}$ is formed. The total angular momentum $\vec{\mathbf{J}} = \vec{\mathfrak{R}} + \vec{\mathbf{J}}_\mathbf{a}$. Neither Σ, nor Λ are good quantum numbers, but Ω, describing the projection of $\vec{\mathbf{J}}_\mathbf{a}$ still is.

The good quantum numbers in each Hund's case are used to label the electronic wave function (resp. the electronic state). For example in Hund's case (a) the electronic states are designated as:

$$^{2S+1}\Lambda_{\Omega} \ ,$$

where $2S+1$ is called spin multiplicity. For example, when the total electronic spin is described by a quantum number $S = 0$, the multiplicity is 1 and the electronic states are called singlets. When $S = 1/2$ the states are called doublets and so on. The states with $\Lambda = 0$ are called Σ states [1], with $\Lambda = 1$ – Π states, with $\Lambda = 2$ – Δ states and so on.

In Hund's case (b) the electronic states are labelled as:

$$^{2S+1}\Lambda \ .$$

In Hund's case (c) the electronic states are labelled simply as:

$$\Omega \ ,$$

since S, Λ, Σ are no longer good quantum numbers.

10.2 Radial Schrödinger equation

The nuclear equation (10.2) can be further simplified if one takes into account the Hund's coupling schemes.

The nuclear part of the Hamiltonian consisting of the kinetic energy of the nuclei [2] can be split into two parts [C23]:

$$\mathbf{H}_{\mathrm{nuc}} = \mathbf{H}_{\mathrm{v}ib} + \mathbf{H}_{\mathrm{r}ot} \tag{10.3}$$

by changing the coordinate system from Cartesian (x, y, z) to spherical coordinates (R, θ, ϕ). Then

$$\mathbf{H}_{\mathrm{v}ib} = \frac{-\hbar^2}{2\mu R^2}\frac{\partial}{\partial R}\left(R^2\frac{\partial}{\partial R}\right), \tag{10.4}$$

and

$$\mathbf{H}_{\mathrm{r}ot} = \frac{-\hbar^2}{2\mu R^2}\left(\frac{1}{\sin\theta}\frac{\partial}{\partial\theta}\left(\sin\theta\frac{\partial}{\partial\theta}\right) + \frac{1}{\sin^2\theta}\frac{\partial^2}{\partial\phi^2}\right) = \frac{-\hbar^2\vec{\mathfrak{R}}^2}{2\mu R^2}., \tag{10.5}$$

where $\vec{\mathfrak{R}}$ is the angular momentum of the nuclei. One should be careful not to confuse this operator with the internuclear distance R!

[1] not to be confused with quantum number for the projection of the electronic spin!

[2] the operator of the Coulomb repulsion between the nuclei is included for convenience in the electronic part of the Hamiltonian

$\vec{\mathfrak{R}}^2$ does not commute with the total Hamiltonian, but for particular Hund's case it can be approximated as a combination of angular momenta, which commute. For example for Hund's case (a) [C23]:

$$\vec{\mathfrak{R}}^2 = \left[(\vec{\mathbf{J}}^2 - J_z^2) + (\vec{\mathbf{L}}^2 - L_z^2) + (\vec{\mathbf{S}}^2 - S_z^2) + L^{\pm}S^{\mp} - J^{\pm}S^{\mp} - J^{\pm}L^{\mp}\right]. \qquad (10.6)$$

Here the operators of the type $L^{\pm}S^{\mp}$ denote $L^+S^- + L^-S^+$, where $L^{\pm} = L_x \pm iL_y$ and $S^{\pm} = S_x \pm iS_y$. These operators are neglected in the Hund's case (a).
The expectation value of these operators is calculated with the electronic wave function. $\vec{\mathbf{L}}^2$ does not commute with the total Hamiltonian, therefore the R-dependent expectation value:

$$\frac{-\hbar^2}{2\mu R^2} \langle \Psi_{\mathrm{el},i} | \vec{\mathbf{L}}^2 - L_z^2 | \Psi_{\mathrm{el},i} \rangle$$

may be added to the potential energy curve, which is usually done in the literature.

Finally one obtains:

$$\langle \Psi_{\mathrm{el},i} | \vec{\mathfrak{R}}^2 | \Psi_{\mathrm{el},i} \rangle \approx J(J+1) - \Omega^2 + S(S+1) - \Sigma^2 \ .$$

For Hund's case (b) [C23]:

$$\vec{\mathfrak{R}} = \vec{\mathbf{N}} - \vec{\mathbf{L}}$$

and after some manipulations:

$$\vec{\mathfrak{R}}^2 = \vec{\mathbf{N}}^2 - N_z^2 + \vec{\mathbf{L}}^2 - L_z^2 - N^{\pm}L^{\mp} \ .$$

Again, the $N^{\pm}L^{\mp}$ term is neglected and the expectation value of $\vec{\mathbf{L}}^2 - L_z^2$ is added to the potential energy. Since the projection of $\vec{\mathbf{N}}$ coincides with L_z ($\vec{\mathfrak{R}}$ is perpendicular to the internuclear axis) $N_z = L_z$. Finally for a particular electronic state one obtains:

$$\langle \Psi_{\mathrm{el},i} | \vec{\mathfrak{R}}^2 | \Psi_{\mathrm{el},i} \rangle \approx N(N+1) - \Lambda^2 \ .$$

For Hund's case (c) [C23]:

$$\vec{\mathfrak{R}} = \vec{\mathbf{J}} - \vec{\mathbf{J}_\mathbf{a}}$$

and after some manipulations:

$$\vec{\mathbf{J}_\mathbf{a}}^2 - \vec{\mathbf{J}_\mathbf{az}}^2 = \vec{\mathbf{J}}^2 - \vec{\mathbf{J}_\mathbf{z}}^2 + \vec{\mathbf{J}_\mathbf{a}}^2 - \vec{\mathbf{J}_\mathbf{az}}^2 + J^{\pm}J_a^{\mp} \ ,$$

In case (c) $J^{\pm}J_a^{\mp}$ is neglected and the expectation value of $\vec{\mathbf{J}_\mathbf{a}}^2 - \vec{\mathbf{J}_\mathbf{az}}^2$ (multiplied by $\hbar^2/2\mu R$) is added to the potential energy.

For a particular electronic state the expectation value of $\vec{\mathfrak{R}}$ is:

$$\langle \Psi_{\mathrm{el},i} | \vec{\mathfrak{R}}^2 | \Psi_{\mathrm{el},i} \rangle \approx J(J+1) - \Omega^2 \ .$$

Finally the nuclear equation is reduced to:

$$\left[\mathbf{H}_{\mathrm{vib}} + \frac{\hbar^2}{2\mu R^2} X + U_i(R) \right] \xi_{ivJ}(R) = E^{BO}_{ivJ} \xi_{ivJ}(R), \tag{10.7}$$

where

$$X = \begin{cases} J(J+1) - \Omega^2 + S(S+1) - \Sigma^2 & \text{for Hund's case (a)}, \\ N(N+1) - \Lambda^2 & \text{for Hund's case (b)}, \\ J(J+1) - \Omega^2 & \text{for Hund's case (c)}. \end{cases} \tag{10.8}$$

10.3 Symmetry properties of the wave functions

Following the Born-Oppenheimer approximation and the Hund's cases, the total wave function for diatomic molecule can be written as a product of the electronic, vibrational and the rotational wave functions:

$$\Psi(\vec{\mathbf{r}}, R) = \Psi_{\mathrm{el}}(\vec{\mathbf{r}}, R)\} \xi_{ivJ}(R) \Phi_{\mathrm{rot}}(\theta, \phi)$$

The symmetry properties of the wave functions, along with the good quantum numbers, can be used for the classification of the states of a diatomic molecule.

The first type of symmetry, is the result from a reflection of spatial and spin coordinates of all electrons and nuclei, through a plane containing the internuclear axis. Even wave functions remain unchanged after such reflection, but odd wave functions change their sign. It can be shown [C24] that for states with $\Lambda = 0$ the parity changes as:

$$(-1)^{(J-2\Sigma+S)}$$

and these electronic states are called Σ^+ states, or alternatively as

$$-(-1)^{(J-2\Sigma+S)}$$

and these states are called Σ^- states.

So, for Σ electronic states, the parity of the successive rotational states (or levels) changes with J. The energy pattern is shown in Figure 10.2.

In states with $\Lambda \neq 0$ the wave function can be built as a symmetric or antisymmetric combination of functions, like $\Psi_{\mathrm{el},\Lambda} \pm \Psi_{\mathrm{el},-\Lambda}$, since for particular value of Λ the wave function is neither symmetric, nor antisymmetric. Therefore, for $\Lambda \neq 0$ states, two levels of different symmetries correspond to each v and J.

Sometimes a J-independent parity label e/f is used to mark the levels. For e levels, the total parity alters as $+(-1)^J$ and respectively – $-(-1)^J$ for f levels. If

J is half integer the parity of the e levels changes as $+(-1)^{J-1/2}$ and the f levels as $-(-1)^{J-1/2}$.

The energy patterns of selected electronic states are shown in Figure 10.2. For $^1\Sigma^+$ states $\Lambda = 0$ and $S = 0$. The energy levels are the eigenvalues of the radial Schrödinger equation with a single potential energy curve. For given value of v, there is a single ladder of rotational levels, which parity alters as $(-1)^J$, so they are all e-parity levels.

For $^1\Pi$ states $\Lambda = 1$, so the lowest rotational level has $J = 1$ (since in this case Λ corresponds to the projection of $\vec{\mathbf{J}}$ on the intermolecular axis). Each rovibrational level is twofold degenerate (due to $\Lambda \neq 0$) with components having different "+", "−" parity (one e and one f-parity level).

The $^3\Sigma^+$ states always correspond to Hund's coupling scheme (b). The total electronic spin is $S = 1$ but it is not coupled to the internuclear axis. The natural rotational quantum number is N and it is this quantum number that determines the $\pm$ parity of the levels. For each rotational level described by N, following the rules for coupling of angular momenta, three values of J are possible $N - 1$, N, $N + 1$ – see Figure 10.3.

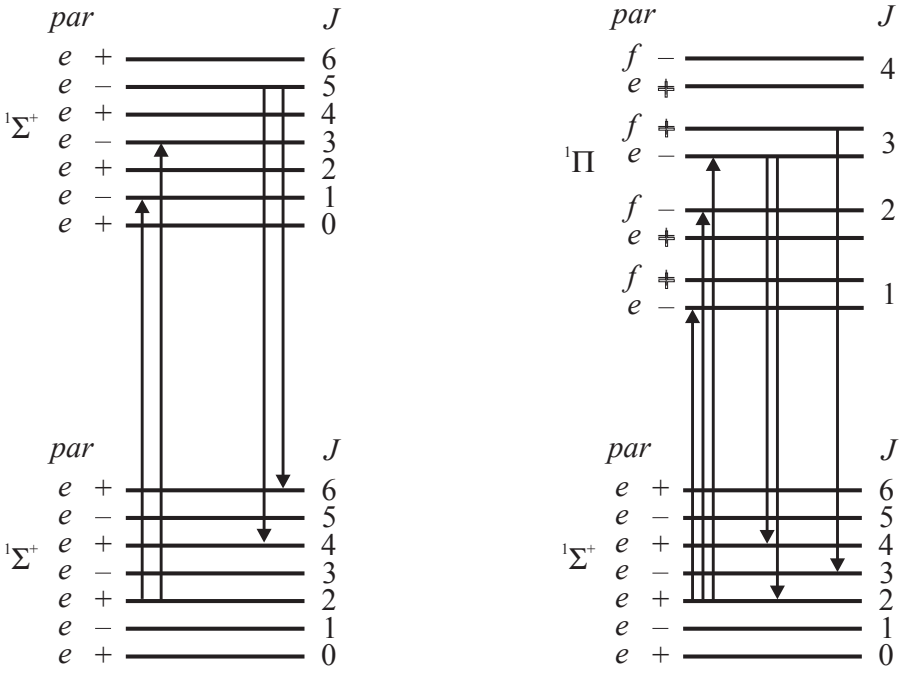

Figure 10.2 Energy levels pattern and possible transitions for $^1\Sigma^+$ and $^1\Pi$ selected electronic states.

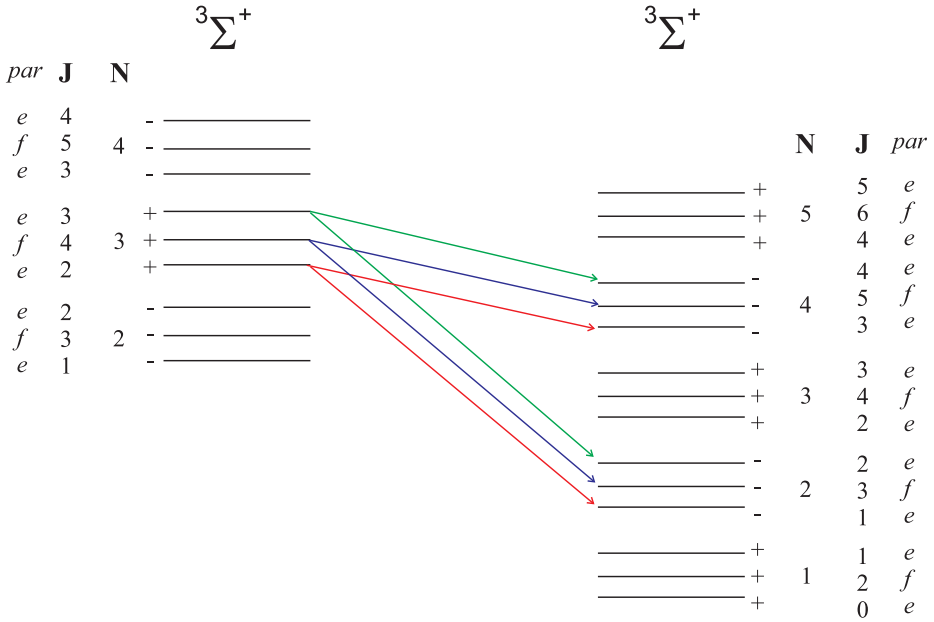

Figure 10.3 Energy levels pattern and possible transitions between $^3\Sigma^+$ electronic states.

10.4 Selection rules for electric dipole transitions

By electric dipole transitions one can define selection rules which say for which pairs of molecular states, the matrix elements of the electric dipole operator $H_{\text{el.dip}}$ [C23, C24]:

$$\langle \Psi_{\Lambda,\Sigma,\Omega,S,v,J} | H_{\text{el.dip}} | \Psi_{\Lambda,\Sigma,\Omega,S,v,J} \rangle \tag{10.9}$$

are nonzero. Here, for example, the matrix elements are calculated with the Hund's case(a) basis functions.

The selection rules can be distinguished as general, which are independent of the approximation of the Hamiltonian H and as those which hold for certain Hund's case.

General selection rules:

For any systems the selection rules for the J are [C23]:

$\Delta J = 0, \pm 1$ with the exception $J = 0 \nleftrightarrow J = 0$, $(\Delta J = J' - J'')$

Usually, transitions with $\Delta J = -1$ are called P-transitions, with $\Delta J = 0$ are called Q-transitions and$\Delta J = 1$ are called R-transitions.

The symmetry selection rules also hold strictly:

$+ \leftrightarrow -$, $+ \nleftrightarrow +$, $- \nleftrightarrow -$

The same rule in terms of e/f parity is:

$e \leftrightarrow f$ for $\Delta J = 0$; $e \leftrightarrow e$ $f \leftrightarrow f$ for $\Delta J = \pm 1$

Selection rules for Hund's coupling case (a)

Here the rules are the same as for case (b) with some additional restrictions [C23]. The component of the total spin of the electrons along the internuclear axis Σ is defined (if the interaction between the spin and orbital angular momentum is not too large):

$\Delta\Sigma = 0$

The selection rule for Ω:

$\Delta\Omega = 0, \pm 1$

seems redundant for case (a), because it follows from the rules for Λ and Σ. However it holds even for strong interactions of spin and orbital angular momentum (as in case(c)), when the rules for Λ and Σ are not valid.

If $\Omega = 0$ for both electronic states the following restriction holds:

$\Delta J = 0$ is forbidden for $\Omega = 0 \rightarrow \Omega = 0$.

Selection rules for Hund's coupling case (b)

In case (b) Λ is a good quantum number for which:

$\Delta\Lambda = 0, \pm 1$

For Σ electronic states the rules are:

$\Sigma^+ \leftrightarrow \Sigma^+$, $\Sigma^- \leftrightarrow \Sigma^-$, $\Sigma^+ \nleftrightarrow \Sigma^-$

Both selection rules may became less rigorous for high values of J.

The rule for S is:

$\Delta S = 0$.

For heavy molecules this rule is violated by the action of the H^{SO} operator.

Selection rules for Hund's coupling case (c)

Good quantum numbers for case (c) are J and Ω. The selection rules for these quantum numbers are the same as already defined for case (a). Σ and S are not defined in case (c), so the selection rules for them are not relevant.

Selection rules for M

The quantum number M describes the projection of the total angular momentum $\vec{\mathbf{J}}$ on the laboratory z-axis. For electric dipole transitions the selection rules for M are

$$\Delta M = 0, \pm 1$$

and they depend on the projection of the electric field $\mathfrak{E}$ on the z axis. If the polarization of the light is such, that the electric field is orthogonal to the quantization axis $\Delta M = \pm 1$, when $\mathfrak{E}$ is parallel to the z-axis $\Delta M = 0$.

10.5 Transition probability and line intensity

The transition probability W_{ij} between rovibrational levels (v', J') and (v'', J'') of two electronic states i and j coupled by light with electrical vector $\vec{\mathfrak{E}}$ can be written as:

$$W_{ij} = \langle i, v'J'M'|\vec{\mathfrak{E}}\,\vec{\mathbf{d}}|j, v''J''M''\rangle^2\,, \tag{10.10}$$

where $\vec{\mathbf{d}}$ is the dipole moment of the molecule, defined as a sum over the product of the coordinates of all charged particles in the molecule (electrons and the nuclei) and their charge:

$$\vec{\mathbf{d}} = \vec{\mathbf{d_e}} + \vec{\mathbf{d_N}} = \sum_k e\vec{\mathbf{r}} + Z_A e\vec{\mathbf{R_A}} + Z_B e\vec{\mathbf{R_B}}.$$

It can be shown [C23] that $\langle i, v'J'M'|\vec{\mathfrak{E}}\vec{\mathbf{d_N}}|j, v''J''M''\rangle$ is zero for electronic transitions $(i \neq j)$ and $\langle i, v'J'M'|\vec{\mathfrak{E}}\vec{\mathbf{d_e}}|i, v''J''M''\rangle = 0$ for transitions between the rovibrational levels of the same electronic state. The non-zero matrix element of $\vec{\mathbf{d}}_{\mathrm{N}}$ occur only for heteronuclear molecules and are responsible for rotational and vibrational transitions within the same electronic state. Further on only electronic transitions will be considered.

The variation of the electric field with $\vec{\mathbf{r}}$ can be neglected and thus

$$\langle i, v'J'M'|\vec{\mathfrak{E}}\vec{\mathbf{d_e}}|j, v''J''M''\rangle = \vec{\mathfrak{E}}\,\langle i, v'J'M'|\vec{\mathbf{d_e}}|j, v''J''M''\rangle\ .$$

By calculating this matrix element one should keep in mind, that the dipole moment is defined in the laboratory fixed coordinate system, whereas the wave functions – in the molecule fixed system. Thus the appropriate transformation should be carried out (see for example [C23]).

The evaluation of the transition probability is more straightforward when for the electric field and the electronic dipole moment spherical basis is used instead of the laboratory fixed cartesian basis. For example, the transformation for the dipole moment is:

$$d_0 = d_z$$

$$d_{\pm 1} = \mp\frac{1}{\sqrt{2}}(d_x \pm i d_y)$$

and similarly for other vectors. In this basis $\mathfrak{E}_0$ corresponds to linearly polarized light with electrical vector along the laboratory z axis. $\mathfrak{E}_{\pm 1}$ correspond to right and left circularly polarized light with electrical vector perpendicular to z. Assuming only one component of the electrical field $\mathfrak{E}_p$ and partitioning of the molecular wave function to electronic, vibrational and rotational part, one obtains [C23] :

$$\langle i, v'J'M'|\vec{\mathfrak{E}}\vec{\mathbf{d}}|j, v''J''M''\rangle = \\ = \sum_q (-1)^q \mathfrak{E}_{-p} \sqrt{2J'+1}\sqrt{2J''+1} \\ \begin{pmatrix} J' & 1 & J'' \\ -\Omega' & q & \Omega'' \end{pmatrix} \begin{pmatrix} J' & 1 & J'' \\ -M' & p & M'' \end{pmatrix} \\ \langle \Psi_{\mathrm{el}i}\xi_{iv''}|d_q|\Psi_{\mathrm{el}i}\xi_{jv'}\rangle \ ,$$

where $\Psi_{\mathrm{el}i}$ represents the electronic wavefunction, and $\xi_{jv'}$ represents the vibrational wavefunction.

Here d_q are the coordinates of the electric dipole moment in the molecular fixed coordinate system. For a given pair of electronic states q can be either 0 ($\Omega' = \Omega''$) or ± 1 for $\Omega' - \Omega'' = \pm 1$, so $q = \Omega' - \Omega''$, otherwise the corresponding 3-j symbol is zero. For a particular choice of p and q, the square of the transition dipole moment is equal to:

$$\langle i, v'J'M'|\vec{\mathfrak{E}}\vec{\mathbf{d}}|j, v''J''M''\rangle^2 = \\ = \mathfrak{E}^2_{-p}(2J'+1)(2J''+1) \\ \begin{pmatrix} J' & 1 & J'' \\ -\Omega' & \Omega' - \Omega'' & \Omega'' \end{pmatrix}^2 \begin{pmatrix} J' & 1 & J'' \\ -M' & p & M'' \end{pmatrix}^2 \\ \langle \Psi_{\mathrm{el}i}\xi_{v''}|d_q|\Psi_{\mathrm{el}i}\xi_{v''}\rangle^2$$

The 3-j symbol

$$\begin{pmatrix} J' & 1 & J'' \\ -M' & p & M'' \end{pmatrix}$$

is zero unless $M' - M'' = p$, i.e. $\Delta M = 0$ for linear polarization and $\Delta M = \pm 1$ for circular polarization.

By excitation with unpolarized light the square of matrix element of the electric dipole operator should be summed over all M' and M'' quantum numbers [C23]. Since

$$\sum_{M,M'} \begin{pmatrix} J' & 1 & J'' \\ -M' & p & M'' \end{pmatrix}^2 = \frac{1}{3}$$

for every polarization, the sum of the squares of the matrix element of the electric dipole operator (called line strength $S_{iv'J',jv''J''}$) can be written as a product of three factors [C25]:

$$S_{iv'J',jv''J''} = \sum_{M'M''} \langle i, v'J'M'|\vec{\mathbf{d}}_{\mathbf{q}}|i, v''J''M''\rangle^2 = \mu^{ij} f^{ij}_{v''v'} S^{\Omega'\Omega''}_{J'J''}$$

The first factor is the μ^{ij} is the square of the matrix element of the electronic dipole moment, calculated with the electronic wave functions of the states (i) and (j):

$$\mu^{ij} = \left[\int \Psi_{\mathrm{el},i} \vec{\mathbf{d}}_{\mathbf{q}} \Psi_{\mathrm{el},j} \right]^2 .$$

The second factor is the Frank-Condon factor:

$$f^{ij}_{v'v''} = \left[\int R^2 \xi^*_{iv'J'} \xi_{jv''J''} dR \right]^2 , \tag{10.11}$$

which is the square of the overlap integral of the vibrational wave functions of the two states.

The last factor is $S^{\Omega'\Omega''}_{JJ'}$ the so-called Hönl-London factor[1] [C25]:

$$S^{\Omega'\Omega''}_{J'J''} = (2J'+1)(2J''+1) \begin{pmatrix} J' & 1 & J'' \\ -\Omega' & \Omega' - \Omega'' & \Omega'' \end{pmatrix}^2 . \tag{10.12}$$

Given the matrix elements of the electric dipole operator and assuming that the radiation density ρ is constant within the bandwidth of the molecular transition, one may write the Einstein coefficient A as[2] [C23, C25]:

$$A_{ij} = \frac{8\pi^2 \nu^3_{ij}}{3\epsilon_0 \hbar (2J''+1)} \mu^{ij} f^{ij}_{v''v'} S^{\Omega'\Omega''}_{J'J''}$$

The line intensities are connected with the population of the initial molecular level $(i, v'J')$ and the transition probability. In absorption, the transmitted light intensity is given by Beer's law [C23, C24]:

$$I = I_0 \mathrm{e}^{-\sigma(n_i - n_j)l} , \tag{10.13}$$

where n_i and n_j are the populations of the ground state and the excited state levels, l is the absorption length and σ is the absorption cross section, which is directly connected to the transition probability.

Depending on the excitation (broadband or narrowband) and the definition of I (the light intensity integrated over the line profile or the intensity at the central frequency of the line profile) different expressions can be derived connecting the cross-section σ and the Einstein A_{ij} coefficient. For more details see Ref. [C24, C23].

[1] The $(2J'+1)(2J''+1)$ factor is missing in the corresponding definition in [C23]

[2] This formula agrees both with Eq.(6.1.6a) from [C23] and Eq.(5) from [C25], when the missing $(2J'+1)(2J''+1)$ factor in [C23] is taken into account.

10.6 Molecular spectra

The appearance of the molecular spectra depends strongly on the experimental conditions.

Usually the molecules are in the lowest electronic state and their distribution over the rovibrational levels follows the Maxwell-Boltzmann distribution:

$$n_{vJ} \sim (2J+1)\exp(-E_{vJ}/kT) \ ,$$

where n_{vJ} is the molecular density for molecules with energy E_{vJ} and T is the molecular temperature. The factor $(2J+1)$ takes into account the degeneracy of the rotational levels.

If a molecular sample is illuminated with a broadband source and one records the spectrum of the transmitted light, the corresponding spectrum is called absorption spectrum. It consists of all allowed transitions from the thermally populated ground state levels. The line intensity depends on the transition probability, but also on the population of the ground state level. Therefore absorption spectrum of the same molecule can differ with the gas temperature.

If the molecules are excited (for example by electric discharge, by a broadband light source or by a laser) and one observes the light emitted by the molecules, the associated spectra are called emission spectra. Their appearance depends strongly on the excitation. By broadband excitation, the emission corresponds to allowed transition from all populated rovibrational levels of the excited state. The line frequencies of the emission and the absorption lines are of course the same (defined by the energy difference), but the intensity distribution can be very different. In absorption the line intensities depend only on the population of the lower state (usually the ground state) levels, whereas in emission the population of the excited state levels should also be taken into account.

The absorption and emission spectra by broadband excitation can be very complex even for simple diatomic molecules due to overlapping lines. Significant simplification can be achieved by employing resonant laser (narrow band) excitation. The emission spectra following a laser excitation will consist of a lines progression from a single excited level – the so called Laser-Induced-Fluorescence (LIF). The simplification of the absorption spectra is less straightforward, but can be achieved by labelling a preselected ground state level with one laser source and then observing only transitions from this levels when a second laser is scanned. This is realized in a series of double-resonance techniques, one example being Polarization Labeling Spectroscopy [C26].

If the line density is low enough and the absorption lines do not overlap, by employing a scanning laser source instead of a broadband source can bring some advantages – there is no need for a high resolution spectrometer and the resolution is usually limited by the Doppler width of the spectral lines. Moreover, several techniques can enhance the sensitivity of the laser absorption, for example Cavity ring-down spectroscopy.

As an example, relevant for this thesis, the energy level structure and the corresponding transitions in the $F^4\Delta$-$X^4\Delta$ system of FeH will be presented. The associated electronic states may be described either in Hund's case (a) or (b).

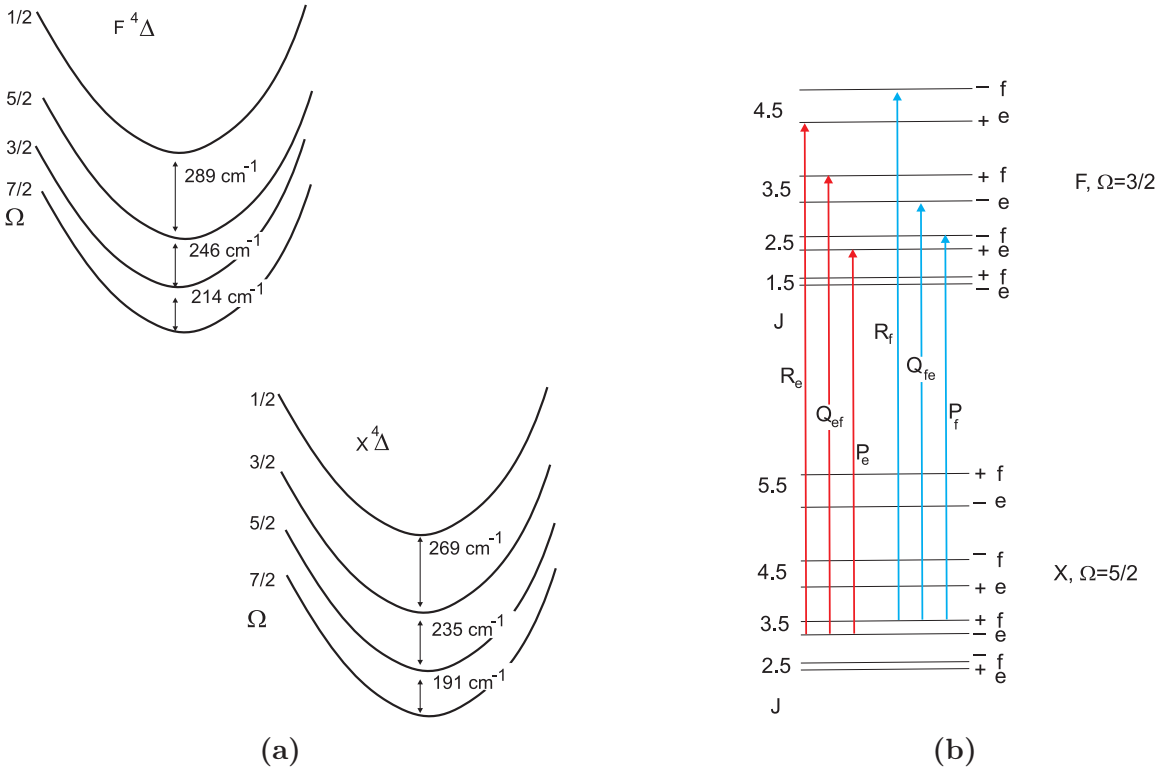

Figure 10.4 Schematic diagram of the relative positions of the Ω components of the X $^4\Delta$ and F $^4\Delta$ states in FeH (Splitting between Ω components taken from [C18]). Energy level pattern and possible transitions for the $\Omega = 5/2 \rightarrow \Omega = 3/2$ system.

In Hund's case (a) the total electronic spin is defined, $S = 3/2$. $\Lambda = 2$, which means that four values of Ω are possible: $\Omega = 1/2, 3/2, 5/2$ and $7/2$. Without spin-orbit interaction the electronic states, corresponding to different values of Ω will have the same potential energy curves and therefore – the same energy levels scheme. The presence of spin-orbit interaction, however, results in four separate potential energy curves, one for each of the Ω components (see fig 10.4). By weak spin-orbit interaction the potential curves are again almost identical and just shifted with respect to each other. The splitting between the potential curves is taken from Table 6 of Ref. [C18]. For each vibrational level of these potentials, the lowest value of J is limited by its projection of the internuclear axis Ω. For example for $\Omega = 1/2$ the lowest $J = 0.5$, while for $\Omega = 7/2$, $J \geq 3.5$. Each rotational level is two fold degenerate (due to $\Lambda \neq 0$) and these two levels, e and f, have different parity. Parity selection rules,$+ \leftrightarrow -$,mean that R and P transitions involve upper and lower levels of either e or f symmetry. They are often indicated simply by R_e or R_f. For Q transitions, if the upper state is e parity, the lower level will be of f parity, and the line is labelled

Q_{ef}. If the upper state takes an f parity label, the line will be labelled Q_{fe}.

The rotational constant B_e of the X and the F states is about 6 cm^{-1} [C18]. By $J \geq 7$ the rotational energy ($B_e J(J+1)$) is comparable with the splitting between the Ω components, and therefore the states are not pure Hund's (a) states, but rather an intermediate case between Hund's cases (a) and (b).

The level structure of the $^4\Delta$ states in Hund's case (b) is shown in Figure 10.5. In this case the natural rotational quantum number is N and each rotation level is two fold degenerate (due to $\Lambda \neq 0$) and then four fold degenerate due to the four possible couplings between $\vec{\mathbf{N}}$ and $\vec{\mathbf{S}}$. The higher the rotational quantum number, the stronger is the interaction between the magnetic field produced by $\vec{\mathbf{N}}$ and the electronic spin $\vec{\mathbf{S}}$ (the so-called spin-rotation interaction). It lifts the degeneracy in S and each N level splits into four components designated as F_1 for $J = N + 1.5$, F_2 for $J = N + 0.5$, F_4 for $J = N - 0.5$ and F_4 for $J = N - 1.5$. In Figure 10.5 they are shown with different colors.

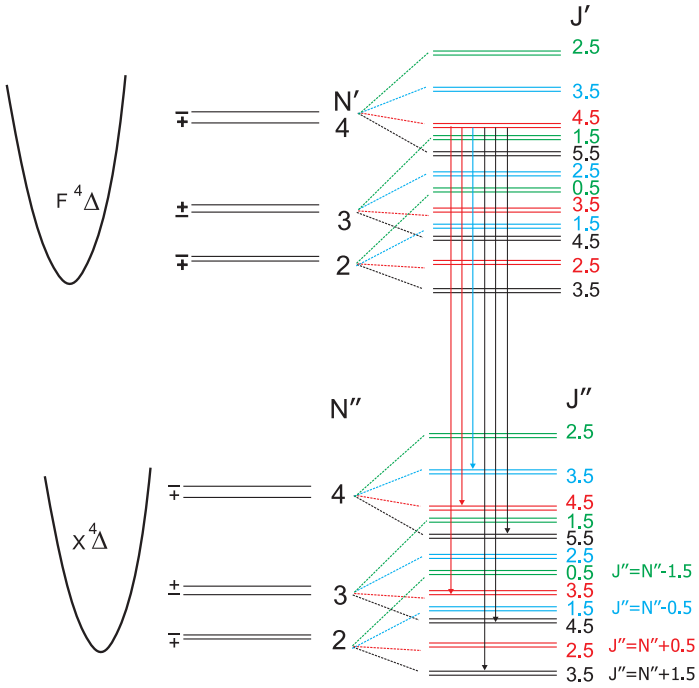

Figure 10.5 Schematic diagram of the X $^4\Delta$ and F $^4\Delta$ states in FeH and the rotational structure in the Hund's case (b). Possible transitions are shown from a single ($N' = 4$, $J' = 4.5$, e) level of the F state.

The energy structure of the X $^4\Delta$ and F $^4\Delta$ states, of course, is independent on the Hund's case approximation. The real states are neither (a) nor (b) case states, but depending on the coupling on the angular momenta one or the other case may be closer to the experimentally observed structure. It should be underlined, that in both cases one expects the same number of rovibrational levels. For example the F_1 components (shown in black in Fig.10.5) may be thought to form the manifold of the

$\Omega = 7/2$ state, the F_2 components (shown in red in Fig.10.5) – the manifold of the $\Omega = 5/2$ state and so on.

10.6.1 Perturbations in molecular spectra

The Born-Oppenheimer and the Hund's coupling schemes are approximations of the total molecular Hamiltonian. Deviations of the experimental observations from the energy pattern predicted by these approximate Hamiltonian are called perturbations. An operator, neglected in the approximate total Hamiltonian, may have diagonal and off-diagonal matrix elements, calculated with the approximate wave functions. The diagonal elements lead to shifts in the energy levels, whereas the off-diagonal couple molecular states.

Very often the perturbations create energy shifts that are below the experimental uncertainty and then the approximate total Hamiltonian can be used for description of the experimental data. When the states coupled by a neglected operator lie sufficiently far from each other, the perturbation can be treated by the second-order perturbation theory, which leads to effective corrections to the zero-order energy levels. When the energy distance between the interacting states is comparable with the matrix elements of the perturbing operators, the single-channel radial Schrödinger equation does not hold anymore and one should solve systems of coupled radial Schrödinger equations.

An example of operator, neglected in the Hund's case (a) coupling scheme is the L-uncoupling operator [C23], $\mathbf{H_{LJ}} = -(1/2\mu R^2)\mathbf{J}^{\pm}\mathbf{L}^{\mp}$. It only has off-diagonal matrix elements between electronic states with $\Delta\Omega = \Delta\Lambda = 1$ and $\Delta S = 0$. Examples of such interactions are those between $^1\Sigma^{\pm}$ and $^1\Pi$, $^2\Sigma^{\pm}$ and $^2\Pi_{3/2}$, $^4\Delta$ and $^4\Phi$ and so on. This operator will have non-zero off-diagonal elements only between the wave functions of the same parity. For the case of the $^1\Sigma^+$ and $^1\Pi$ states, the result is that only the e-parity levels of both states are coupled, while the f-parity levels of the $^1\Pi$ state remain unaffected.

If the two interacting states are sufficiently separated in energy one can take into account the influence of the $\mathbf{H_{LJ}}$ operator on the energy levels by means of second order perturbation theory. For the e-parity levels of a $^1\Pi$ state [C23]:

$$\delta E^{\Pi}_{vJ} = q_e(v)J(J+1), \tag{10.14}$$

where:

$$q_e(v) = \sum_{v'} \frac{\langle iv|\mathbf{H_{LJ}}|jv'\rangle}{E^{\Pi}_{vJ} - E^{\Sigma}_{v'J}} \tag{10.15}$$

In the $^1\Pi$ state the correction (10.14) leads to splitting between the e/f components of each J energy level (the so called Λ-doubling). In fact formula (10.14) may include the joint effect of all far $^1\Sigma^{\pm}$ states on the $^1\Pi$ state under consideration. This results in different corrections, $q_e(v)$ and $q_f(v)$ for e- and f-parity levels. Experimentally only the difference between $q_e(v)$ and $q_f(v)$ can be determined, but not their

actual values. In practice often, the v dependence of $q_e(v)$ and $q_f(v)$ can be neglected and they may be fixed as constants q_e and q_f.

In FeH, it is the L-uncoupling operator that causes the splitting between the e and the f parity levels for a given rotational levels of the X $^4\Delta$ and the F $^4\Delta$ states.

The second operator relevant for this study is describing the spin-orbit interaction, which is neglected both in Hund's cases (a) and (b). It has the general form of

$$\mathbf{H_{SO}} = A(\vec{\mathbf{R}}, \vec{\mathbf{r}})\mathbf{LS}.$$

This operator has both diagonal and off-diagonal elements. For given Hund's case (a) electronic state the diagonal elements lead to Ω dependent energy shifts which lift the correspondent degeneracy. For example the energies of a $^2\Pi_{1/2}$ and a $^2\Pi_{3/2}$ states are split by $\langle vJ|A(\vec{\mathbf{R}}, \vec{\mathbf{r}})|vJ\rangle\, \Lambda\Sigma$ [C23]. It is the diagonal elements of $\mathbf{H_{SO}}$, which cause the splitting of the $\Omega = 1/2, 3/2, 5/2$ and $7/2$ components of the $X^4\Delta$ and $F^4\Delta$ states in FeH (Figure 10.4). The off-diagonal elements mix electronic states for which ($\Delta\Lambda = -\Delta\Sigma$) or ($\Delta\Lambda = \Delta\Sigma = 0$, $\Lambda \neq 0$ and $\Sigma \neq 0$). Always, however, $\Delta\Omega = 0$. These matrix elements are responsible for transition from Hund's case (a) to Hund's case (c). In Hund's case (a) the matrix elements of $\mathbf{H_{SO}}$ are non-zero only if $\Delta J = 0$.

In Hund's case (b) the matrix elements of $\mathbf{H_{SO}}$ are more elaborate (see [C23]) and they are non-zero for $\Delta N = 0, \pm 1$. It means that this operator mixes the neighboring rotational levels of the same electronic state with $\Lambda \neq 0$ and $S \neq 0$! The off-diagonal elements, like for the Hund's case (a) lead to transition to Hund's case (c).

Another operator, neglected in Hund's case (b) is the spin-rotation operator $\mathbf{H_{SR}} = \gamma\mathbf{NS}$ [C23]. This operator is responsible for splitting each N rotational level into $2S + 1$ components. It is easy to show, that $\mathbf{NS} = \mathbf{1/2}(\mathbf{J^2} - \mathbf{N^2} - \mathbf{S^2})$, so the expectation value of $\mathbf{H_{SR}}$ is [C23]:

$$< \mathbf{H_{SR}} >= -\frac{\gamma}{2}(J(J+1) - N(N+1) - S(S+1)\ .$$

For the case of quartet state ($S = 1.5$) the splitting of each N level is:

$$\Delta E_{F1} = 3/2\gamma N \text{ for the } F_1 \text{ component},$$
$$\Delta E_{F2} = 1/2\gamma(N-3) \text{ for the } F_2 \text{ component},$$
$$\Delta E_{F3} = -1/2\gamma(N+4) \text{ for the } F_3 \text{ component},$$
$$\Delta E_{F4} = -3/2\gamma(N+1) \text{ for the } F_4 \text{ component}.$$

The L-uncoupling operator [C23] in Hund's case (b) has the form

$$\mathbf{H_{LN}} = -(1/2\mu R^2)\mathbf{N}^{\pm}\mathbf{L}^{\mp}$$

and has similar effect on the rotational levels as the corresponding operator in the Hund's case (a) – it causes the splitting of the e and f components of each N level.

The effect of $\mathbf{H_{SR}}$ and $\mathbf{H_{LN}}$ cannot be neglected in FeH since both the X $^4\Delta$ and the F $^4\Delta$ states are intermediate between Hund's cases (a) and (b).

10.6.2 Zeeman effect

In the presence of static magnetic field $\mathfrak{B}$, the energy structure of a diatomic molecule is influenced by interaction of this field with the internal angular momenta. The corresponding operator may be written as [C24]:

$$\mathbf{H_M} = -\vec{\mu} \cdot \vec{\mathfrak{B}}$$

where $\vec{\mu}$ is the magnetic dipole operator of the molecule. $\vec{\mu}$ is sum over the magnetic dipole moments associated with each of the angular momenta. For example the magnetic dipole moment due to $\vec{\mathbf{L}}$ is:

$$\vec{\mu}_L = -\frac{\mu_B}{\hbar}\vec{\mathbf{L}} \ ,$$

where μ_B is the Bohr magneton. The total electronic spin leads to:

$$\vec{\mu}_S = -g_e\frac{\mu_B}{\hbar}\vec{\mathbf{S}} \ ,$$

where g_e is the Landé-g factor of the electron, which is $g_e \approx 2.0023$. Due to this factor, the total magnetic moment of the electrons

$$\vec{\mu} = -\frac{\mu_B}{\hbar}(\vec{\mathbf{L}} + g_e\vec{\mathbf{S}})$$

is not collinear with the total angular momentum of the electrons. For sufficiently weak magnetic fields, the couplings between the internal angular momenta is not changed and one can express $\vec{\mu}$ as [C24]:

$$\vec{\mu} = -g\frac{\mu_B}{\hbar}\vec{\mathbf{J}} \ ,$$

where g is the molecular g-factor, which depends not only on the molecular electronic state (i.e. on Λ, Ω etc.), but also on J and v. For some simple molecules g can be calculated theoretically, as for simple atoms. For example, for pure Hund's case (a) molecular states and weak magnetic fields, g can be written as:

$$g = \frac{\Omega}{J(J+1)}(\Lambda + g_s\Sigma) \tag{10.16}$$

When molecular rotation couples with $\vec{\mathbf{L}}$ and $\vec{\mathbf{S}}$, Λ and Σ cease to be good quantum numbers and formula 10.16 fails. It can be only measured experimentally. Now g can be expressed as an effective electronic Landé factor g_{eff}:

$$g = \frac{\Omega}{J(J+1)}g_{eff}. \tag{10.17}$$

For calculation of the matrix elements of the $\mathbf{H_M}$ operator it is convenient to set the z laboratory axis along the magnetic field. Then $\mathbf{H_M}$ reduces to:

$$\mathbf{H_M} = g\frac{\mu_B}{\hbar} J_z \mathfrak{B}_z \ .$$

Written in this form, $\mathbf{H_M}$ commutes with the total Hamiltonian and its matrix elements are:

$$\Delta E_M = < \Psi_{\Lambda,\Sigma,\Omega,S,v,J,M} | \mathbf{H_M} | \Psi_{\Lambda,\Sigma,\Omega,S,v,J,M} > = g\mu_B M \mathfrak{B}_z \tag{10.18}$$

So, the Zeeman effect lifts the degeneracy of the rotational levels. Each level with rotational quantum number J splits into $2J+1$ equally spaced components, separated by $-g\mu_B\mathfrak{B}$ in the weak field limit.

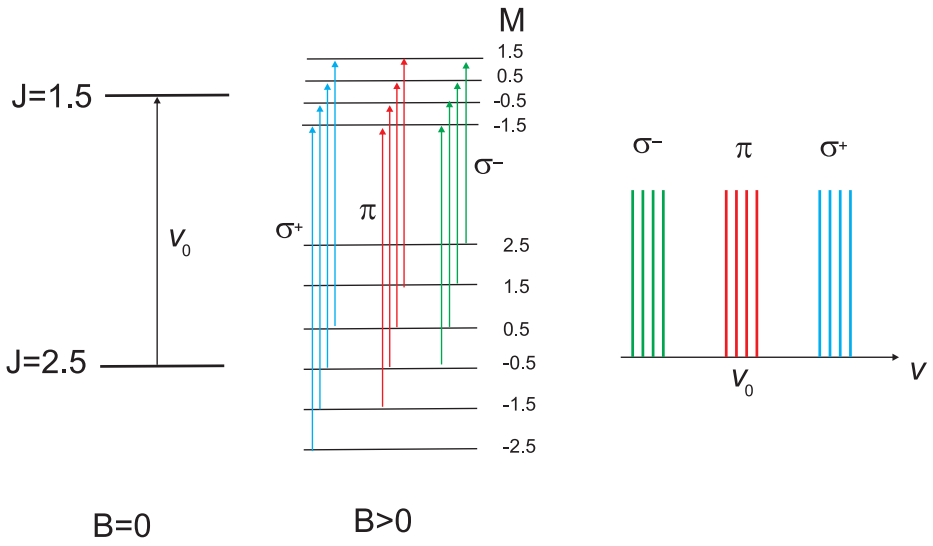

Figure 10.6 Example of the Zeeman splitting of levels with $J = 1.5$ and $J = 2.5$ and possible transitions between them.

An example of the Zeeman splitting of levels with $J' = 1.5$ and $J'' = 2.5$ is presented in Figure 10.6. In the presence of a magnetic field these levels split into 4 and 6 M-components respectively. From the splitting one can see that the g-factor for the upper levels is smaller. Following the selection rules for M, the σ^+ polarized light can induce $M'' \to M' = M'' + 1$ transitions, σ^- – $M'' \to M' = M'' - 1$ transitions and π polarized light can induce $M'' \to M' = M''$ transitions. The frequencies of these transitions are shown schematically in Figure 10.6. One can see that due to the magnetic field the absorption of σ^+ light is shifted to higher frequencies, whereas for σ^- light – to lower frequencies.

Analyses of the shifts between the Zeeman components can be used for experimental determination of the g factors.

Chapter 11

Coaxial discharge source

This chapter is devoted to the development of a new plasma source for efficient production of MH radicals.

This work is a natural extension of the experimental study performed by Bozhinova et al. [C22], where the advances towards successful production and detection of NiH molecule in a discharge source with coaxial geometry were demonstrated. They investigated the optimum conditions at which the highest concentration of radicals was achieved by varying the gas pressure in the source, the gas mixture (different concentration of Ar and H_2), and the discharge current. One of their findings was that the production rate of NiH molecules significantly drops with an increase of the temperature of the cathodes, so the efficiency of the source diminishes with long-term operation. They concluded that the lack of cooling mechanism for the cathode, and the fact that the source can not be easily adapted for spectroscopic studies in magnetic field were the major drawbacks of their particular design. The construction of a more flexible discharge source where the above considerations can be applied became my task and provided me with an introduction into this research topic.

The work on building a new discharge source started in Sofia, where preliminary tests of the source were performed and the absorption spectrum of NiH molecule was observed. Subsequently the source was transferred to Lyon, where it was possible to further investigate the source performance. The continuous wave (CW) dye laser available there allowed the absorption of NiH to be monitored over a wide frequency range. Additionally, adequate water cooling of the source cathode was provided and the source was equipped with magnetic coils so that the Zeeman response of NiH was measured in absorption, as well. Fig.11.1 shows a diagram of the NiH electronic structure derived from ab initio calculations. The absorption spectra observed in this study resulted from excitation of rovibronic transitions in the $B\,^2\Delta - X\,^2\Delta$ system of NiH.

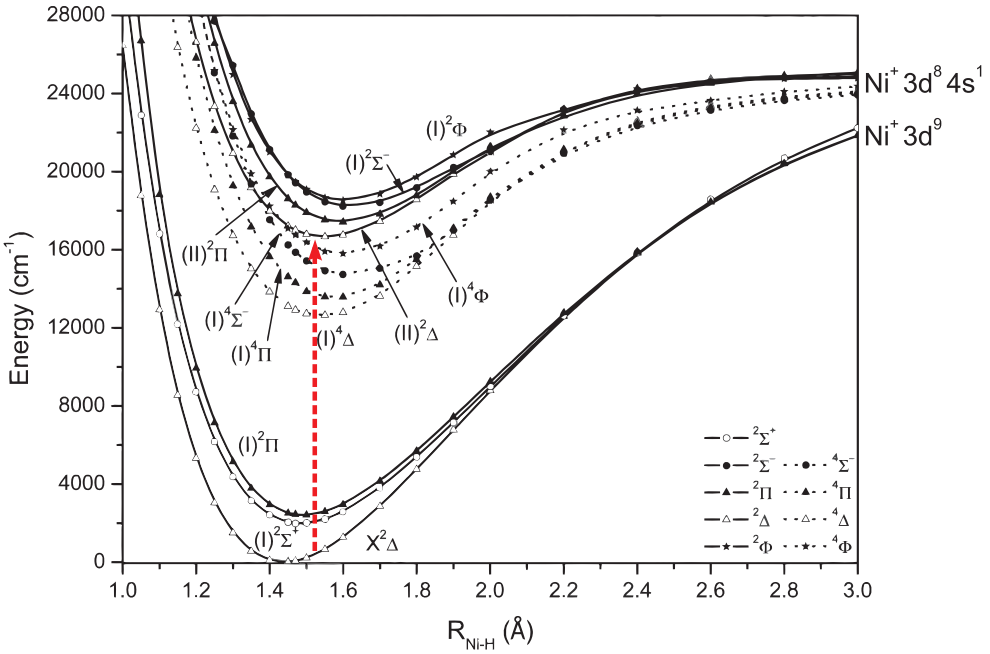

Figure 11.1 NiH electronic structure from ab initio calculations. Picture taken from Ref. [C27]. The red arrow denotes the electronic transition of interest in my work - $X\,^2\Delta$–$B\,^2\Delta$.

11.1 Hardware design

The developed source consisted of two aluminum tubes with dimensions of ∅40 × 130 mm terminated with standard DN40KF vacuum flanges. The two tubes were joined together with a fast clamp mechanism through a Viton® o-ring for sealing the assembly. The free ends of the tube assembly were used to fit additional vacuum elements such as gas inlet ports, connections for attachment of a vacuum pump and a pressure gauge, vacuum-proof feedthrough for electrical wiring of the anode section and last but not least, the viewports of the source, which resulted in overall length of the source of 360 mm. Fig. 11.2 shows a schematic drawing of the assembled source.

Unlike the source from [C22] with multiple cathode rings, this source relied upon a single cathode. The cathode was produced from nickel foil, which was first rolled and then plugged inside the tube assembly. When the roll was released the springback effect (elastic recovery) caused the foil to adhere to the internal wall of the aluminum tubes. The cathode was kept at "virtual" ground potential and the electrical link was realised by connecting the tube assembly to the ground lead of the laboratory power line. The coaxial geometry of the source was achieved by installing the anode section concentrically to the cathode. The anode section was connected electrically to the positive potential output of a benchtop dc power supply.

Another advantage of the physical contact between the Ni foil and the aluminum tubes was that the temperature of the cathode could be effectively controlled by

directly cooling the tubes. Fig. 11.3 shows a photograph of the designed water-cooling units, which were entirely made from aluminum. In each unit, vertical and horizontal channels were produced such that they formed a U-shaped path for water flow . The cooling units were installed at both ends of the discharge tube.

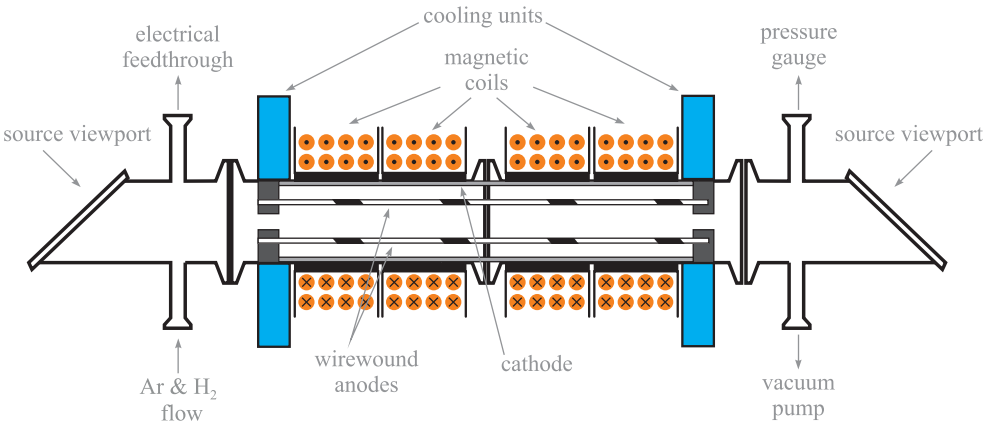

Figure 11.2 Schematic drawing of the source with wirewound anodes.

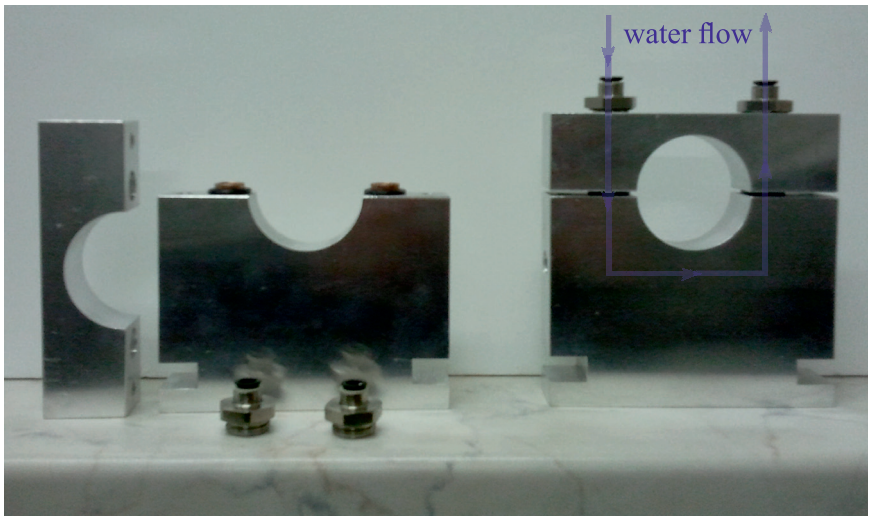

Figure 11.3 Photo of the units used to cool the cathode in the plasma source. The water flow inside the unit is drawn with blue arrows.

In the course of work several modifications of anode arrangement, shown in Fig. 11.4, were tested because some of them resulted in unstable burning of the discharge, as discussed in the next section.

The model drawing in Fig. 11.4a represents the initial design of the anode assembly. It consisted of eight aluminum rings with a central opening of diameter 10 mm. In addition, two diametrically opposite openings at a distance of 9 mm from the ring center were produced on each ring, so that the rings could be strung on two glass

tubes with length of 250 mm and external diameter of 4.5 mm. The outermost rings were secured to the ends of the glass tubes to form the supporting structure of the anode assembly. The external diameter of these two rings was approximately 39 mm. The six remaining interior rings, with external diameter of 26 mm, were evenly spaced along the supporting glass tubes. They were individually wired and connected via separate ballast resistors to the power supply to serve as "sectioned" anode. In the assembled source the anode-cathode distance was 7 mm.

In the second anode configuration tested, the six anode rings were replaced by two pieces of iron wire (∅0.5 mm) directly wound around the glass tubes as shown in Fig. 11.4b. This resulted in a distance between the anode and the cathode of 8 mm. The two anodes were also connected to the power source via separate ballast resistors.

Finally, the third modification applied to the anode section of the source was to produce supporting rings for the anode assembly from PTFE[1] in order to replace the aluminum ones. The anode consisted of twelve iron rods, ∅2 mm, arranged on a cylindrical surface of 24 mm diameter as shown in Fig. 11.4c. In this case the anode-cathode distance was 7 mm.

11.2 Observation of molecular absorption of NiH

It is difficult to judge the significance of NiH molecule for astronomical studies and its probable application as a magnetic field probe for cold stellar environments such as sunspots and brown dwarfs. Although Ni is estimated to be the second, after Fe, most abundant transition metal in these environments, the most recent studies which reported on the identification of NiH molecule in spectra of sunspots umbrae are more than 40 years old[C28, C29], and these remain unconfirmed.

However, our intentions were to use nickel cathodes as a proof-of-concept for the robustness and reliability of the developed source. Moreover, assuming an equal production rate of FeH and NiH molecules the absorbtion in the latter was expected to be stronger, and observation of relative absorption below 0.1% requires considerable sensitivity of the detection scheme. In addition one can benefit from the substantial amount of laboratory data for the electronic structure of NiH molecule obtained with various experimental methods, for instance, via intracavity laser spectroscopy [C30] and via detection of Fourier-transform resolved fluorescence [C21, C31]. The presence of molecular transitions around 632 nm and the availability of laser diodes in that range also determined the choice of nickel as a starting point.

The tests of the new source using the multi-ring sectioned anode, shown in Fig. 11.4a, were performed in Sofia. Molecular absorption spectrum of NiH was successfully observed. A single-mode CW diode laser was used to excite the P(6.5),(0-0) line of the $B\,^2\Delta_{5/2} - X\,^2\Delta_{5/2}$ transition at 15 804.03 cm^{-1}[C30]. The absorption signal was obtained in discharge medium containing only H_2 gas. The detection was done in a differential scheme with two photodiodes similar to the one described later in this

[1]PTFE - Polytetrafluoroethylene (Teflon)

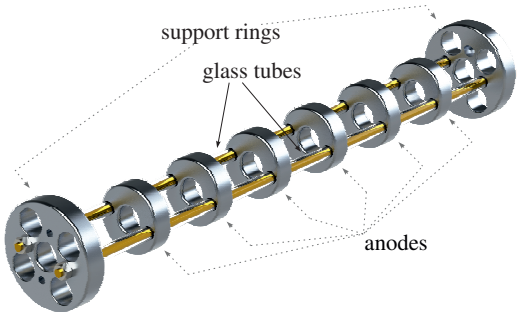

(a) Six aluminum rings serve as anodes. Each anode is connected via a separate load resistor to the output of the power supply source - six-sectioned anode.

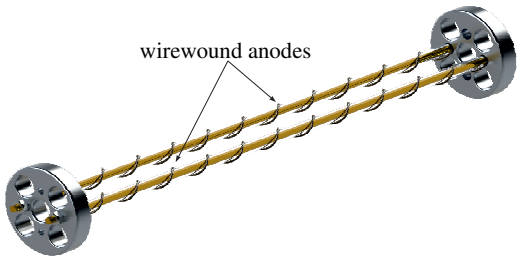

(b) The aluminum anodes are replaced by two separate iron wires wound around the support glass tubes - two-sectioned anode.

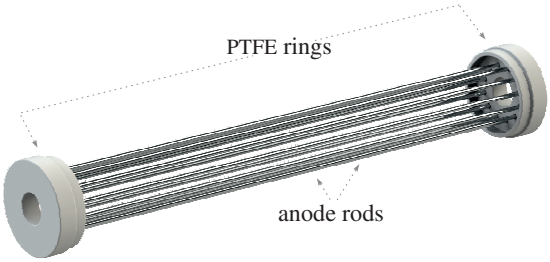

(c) PTFE support rings for better confinement of the discharge. The twelve iron rods are connected in short circuit to serve as a single anode.

Figure 11.4 Model drawings of different configurations of anode arrangement used in the coaxial discharge source.

section. Without going into any further in details on the detection I would like to emphasise the important conclusions drawn from the tests.

First and foremost the amplitude of the acquired signals were approximately three times weaker than signals obtained in the same conditions using the source from study [C22]. Obviously the conditions for production of radicals were different in the new source, although the discharge had again coaxial geometry. The most distinguishing mark observed with the new design was that at high discharge current, where an increase of the sputtering rate of cathode material was expected to produce greater absorption, the plasma column in the source became unstable. Instead of being confined within the region between the anode and the cathode the discharge glow was concentrated near the outermost, support, rings. This could explain the big difference in production rates for both sources. The source was disassembled and the support rings were wrapped with an isolation band (PTFE tape) in order to avoid electrical connection of the support rings with the aluminum tubes, and respectively with the cathode. At first iteration this modification improved the behaviour of the plasma inside the source.

Subsequently, the source was transferred to Lyon where the study was continued. Unfortunately after some time of operation the problem reappeared. It was found that the sputtering of Ni metal was so intense that the leads of the individual anode rings were covered with conductive layer and the anode sectioning was compromised. This implied the replacement of the anode design with the one shown in Fig. 11.4b.

In Fig. 11.5 is presented a schematic drawing of the experimental setup used in the tests of the modified source.

The laser system consisted of a single-mode ring dye laser[1]. The laser was operated with Rhodamine 6G dye, pumped at 532 nm by a frequency-doubled CW Nd:YAG laser[2]. Coarse tuning of the dye laser frequency was achieved by manual rotation of the birefringent filter, an intracavity frequency-selective element. Furthermore, the control electronics of the laser provided continuous single-mode tuning range of about 30 GHz and linewidth of the output radiation of about 1 MHz. The dye laser was able to deliver more than 300 mW optical power, far in excess of requirement for absorption spectroscopy in the discharge source.

The output laser beam was transmitted sequentially through two glass wedge beam splitters(BS). The reflected beams from the first beam splitter (BS_1) were used for differential measurement of absorption in the source. One of the light beams was directed to traverse the discharge tube and then it was detected by a silicon photodiode[3]. The other beam served as a reference and it was directly detected by a second photodiode of the same type. The output signal of each photodiode was fed to a pre-amplifier stage with a variable gain, from 0 to 5. This way the amplitude of the signals delivered by the photodiodes were equalized electronically in order to compensate for differences in the intensity of the reference and the absorption light

[1]SP380D by Spectra-Physics
[2]Millennia Pro by Spectra-Physics
[3]VTB8440BH

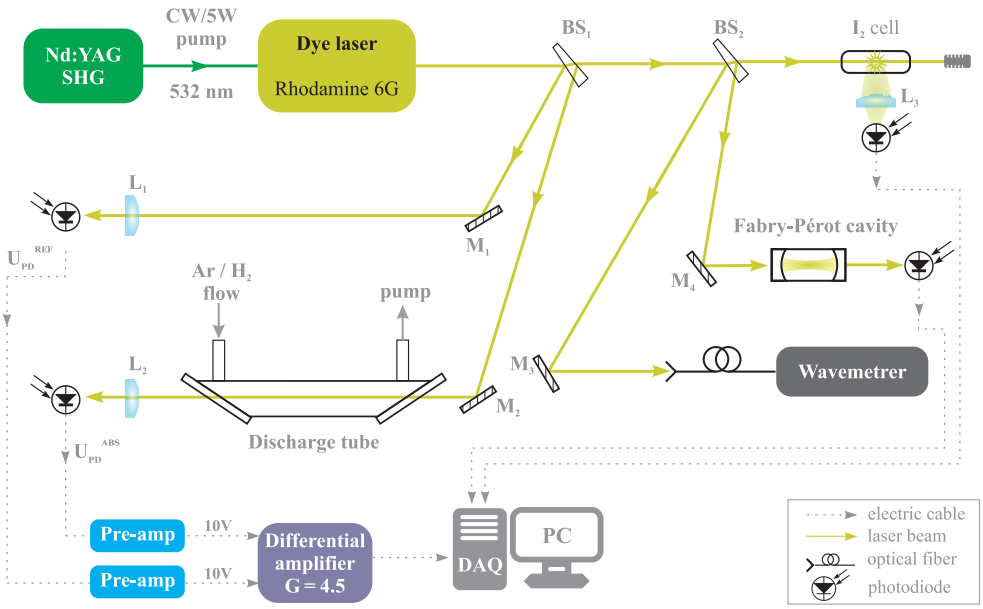

Figure 11.5 Schematic drawing of the experimental setup for detection of differential absorption in NiH molecule. The optical signals are detected with photodiodes. The output signals from the detectors are directed to a Data Acquisition (DAQ) board and are stored on a personal computer (PC) for further data processing. The symbols in the drawing indicate optical elements as follows: L-lens; BS-glass wedge beam splitter, M-mirror.

beams. Subsequently, the equalised signals were fed to the inputs of a differential amplifier with output gain of 4.5. The output of the differential amplifier was directed to a data acquisition (DAQ) board which stored the experimental data on a computer. In Fig. 11.5 the photodiode signals are indicated as $U_{\mathrm{PD}}^{\mathrm{REF}}$ for the reference beam and $U_{\mathrm{PD}}^{\mathrm{ABS}}$ for the absorption beam.

Additionally, part of the laser light was coupled to the optical fiber input of a commercial wavelength meter[1], which allowed for measurement of the laser frequency with absolute accuracy of ± 0.2 ppm. The laser was also coupled to a Fabry-Pérot (FPI) cavity with Free Spectral Range (FSR) of 1.5 GHz and the cavity response was recorded on a photodiode. The main part of the output laser light was directed through a glass cell containing iodine vapour and the absorption spectrum of the I_2 molecule was detected with another photodiode, which observed the integrated fluorescence in the cell. The FPI response and the I_2 molecular absorption spectrum were also recorded on the computer via the DAQ board, to provide spectral callibration.

For evacuation of the source volume a rotary vane pump was attached to the tube assembly. The obtained pressure in the source was below 1 mTorr as indicated by a capacitance gauge. Furthermore, the discharge tube was equipped with two identical

[1]Burleigh WA-1500

commercial mass flow meters[1] each one controlled by a digital driver[2]. They allowed for the source to be filled either with gas mixture of 10%H_2 in Ar, pure H_2 gas or both. The conditions for optimal production of molecular NiH were investigated for a wide range of discharge currents, from 0 to 200 mA, both in gas flow and cell regime.

The top black trace in Fig. 11.6 presents an absorption spectrum of NiH. The signal was acquired at the best conditions (maximum absorption signal) for production of radicals in the particular source determined as follows: 150 mA discharge current, 320 mTorr pressure obtained at flow rate of pure H_2 gas of 25.5 sccm . The laser frequency was continuously tuned by ± 0.42 cm^{-1}around 17 462.6 cm^{-1}in the vicinity of the transition $(v'' = 0, J'' = 2.5) \rightarrow (v' = 1, J' = 2.5)$ of the electronic states $B\,^2\Delta_{5/2} - X\,^2\Delta_{5/2}$. This allowed for several NiH absorption lines (associated with different isotopes of Ni) to be observed in a single scan.

The optical power of the laser beam transmitted through the source tube was measured to be 3 mW, and after the pre-amplifier stage the signal fed to the differential amplifier had an amplitude of 10 V. Accounting for the differential amplifier output gain of 4.5 we estimated relative absorption of $\Delta I/I_0 = \left(U_{\mathrm{PD}}^{\mathrm{REF}} - U_{\mathrm{PD}}^{\mathrm{ABS}}\right)/U_{\mathrm{PD}}^{\mathrm{REF}} = 0.11\%$ and signal-to-noise ratio (SNR) of 20 for this Q(2.5) line ^{58}NiH. The absorption spectrum shown in Fig. 11.6 resulted from averaging of the recorded differential absorption signal over 128 successive frequency scans of the laser. The total recording time was about 2 min.

Following [C26] the Doppler width of the spectral line, $\delta\nu_{\mathrm{D}}$ measured in Hz, is connected with the temperature of the absorbing particles, T expressed in Kelvin, via the equation

$$\delta\nu_{\mathrm{D}} = 7.16 \times 10^{-7}\,\nu_0 \sqrt{\frac{T}{M}}\,,$$

where ν_0 is the transition frequency in Hz, and M denotes the molar mass of the molecule, which for NiH radical equals approximately 60. Thus the estimated Doppler width of the observed transition of 0.96 GHz corresponds to a molecular gas temperature of NiH of about 393 K.

A rough estimate for the concentration of NiH molecules in the source, N_J was made by using Beer's law for linear absorption (for laser intensities bellow saturation of the observed transition) rewritten in the following form:

$$\frac{\Delta I}{I_0} = \sigma(\nu_0)\, N_J\, L\,, \tag{11.1}$$

where L stands for the length of the absorption path (in our case it is the overall length of the discharge tube 360 mm) and $\sigma(\nu_0)$ is the absorption cross. At the central frequency of the transition the absorption cross section is given by [C24]

$$\sigma(\nu_0) = \frac{2\lambda^2\, A_{10}}{8\pi\,\delta\nu_{\mathrm{D}}} \sqrt{\frac{\ln 2}{\pi}}\,. \tag{11.2}$$

[1] 179A Mass Flow Meter by MKS Instruments
[2] PR4000 Flow Meter Digital Driver by MKS Instruments

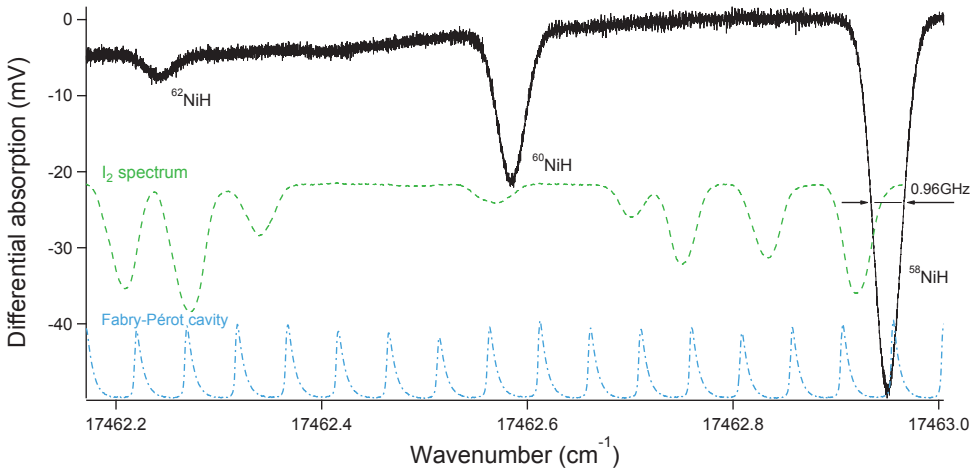

Figure 11.6 Differential absorption spectrum of NiH molecule obtained by laser excitation of the Q(2.5) transition from the (1-0) band between the $B\,^2\Delta_{5/2} - X\,^2\Delta_{5/2}$ electronic states (top black trace). The three resolved lines correspond to molecules formed by hydrogen and different isotopes of nickel. The spectrum was obtained by continuous tuning of the frequency of a dye laser. The supplementary traces on the graph represent: LIF spectrum of the iodine molecule denoted with green dot-dash trace and the response of a Fabry-Pérot cavity (FSR=1.5 GHz) given with blue dashed trace.

In the above equation λ stands for the transition wavelength, and A_{10} is the Einstein coefficient for spontaneous emission of the excited state. Moreover, the lifetime of the ro-vibrational levels with $v' = 1$ of the $B\,^2\Delta_{5/2}$ state is known to be about 1 µs(see Ref. [C32]). With the estimated $\sigma(\nu_0) \approx 1.27 \times 10^{-13}\,\mathrm{cm}^2$ we calculated the concentration of molecules in the state $v'' = 0, J'' = 2.3$ to be $N_{J''=2.5} \approx 0.2 \times 10^9\,\mathrm{molecules/cm}^3$. If we assume that the molecules in the source are at thermodynamic equilibrium, Boltzmann distribution over all ro-vibrational levels at a temperature of $T = 393\,\mathrm{K}$, then it can be shown that the concentration of the molecules in $J'' = 2.5, v'' = 0$ is approximately 14% of the total number of molecules in the $v'' = 0$ level. If we assume that the only vibrational level in the ground state which is thermally populated is the $v'' = 0$ state, then the total number density of molecules in the source can be estimated as

$$N_J^{\mathrm{TOT}} \approx N_{J''=2.5}/0.14 \approx 1.4 \times 10^9\,\mathrm{molecules/cm}^3\ .$$

This number appears almost an order of magnitude smaller than the value reported in Ref. [C32] and it could be explained by a lower sputtering rate in our source due to lower current density (current per unit cathode area). In addition, in the same work a weak magnetic field of about 0.04 Tesla was used to stabilize the discharge and to enhance the sputtering rate in the source.

The experimental study of the source was extended with observations of absorption in magnetic field.

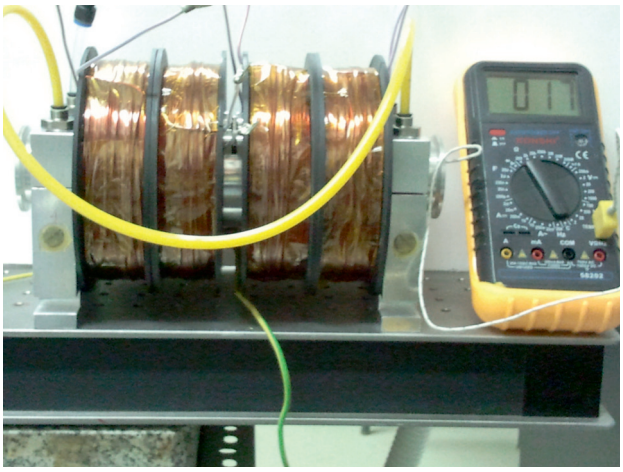

Figure 11.7 Photo of the discharge source with the installed coils. The two cooling units are also visible at both ends of the tube assembly. The windows of the source are not attached to the tube.

11.3 Zeeman response of NiH molecule

The magnetic field was created by four identical coils which were installed around the source tube as shown in Fig. 11.7. The coils were connected in series in order to provide a homogenous axial field in the region of the discharge. Each coil consisted of a plastic spool with 500 turns of copper wire with diameter of 1.5 mm, which resulted in a resistance of 1.65 Ω per coil. Each spool had length of 43 mm, inner and outer diameters of 56 mm and 138 mm respectively. The supply current for the coils was delivered by a benchtop dc power supply with variable output.

Two independent procedures were applied for estimation of the magnetic flux density created by the coils. First, the magnetic field inside the source volume was measured with a commercial gaussmeter[1] with an accuracy of 1% and a resolution of 1 mT. The probe of the gaussmeter was mounted on a 3-axis mechanical translation stage with micrometer screws, which allowed for measurement of the field both along the source length and across the tube cross section. However, such a measurement was possible only in a source with dismounted windows. Furthermore, the field was estimated at a certain positions inside source volume and at several different values for the supply current of the coils. Thus an alternative method for evaluating the field profile was needed. For this purpose we provided a numerical simulation program which accounted for the real geometry of the setup. The code of the program was written to be used with Wolfram Mathematica software.

The achieved correspondence between the calculated and the measured values was within the accuracy of the magnetic probe and can be seen in Fig. 11.8. The presented data points do not cover the whole length of the source because probe was shorter than the distance between the supporting rings of the anode structure. An

[1] Hirst GM07

alternative approach could be to repeat the measurement by staring at the opposite side of the source, although it would be difficult to ensure that the measurement is done on the same axis. Instead we relied on the symmetry of the field with respect to the mid-point of the tube assembly, suggested by the numerical calculations.

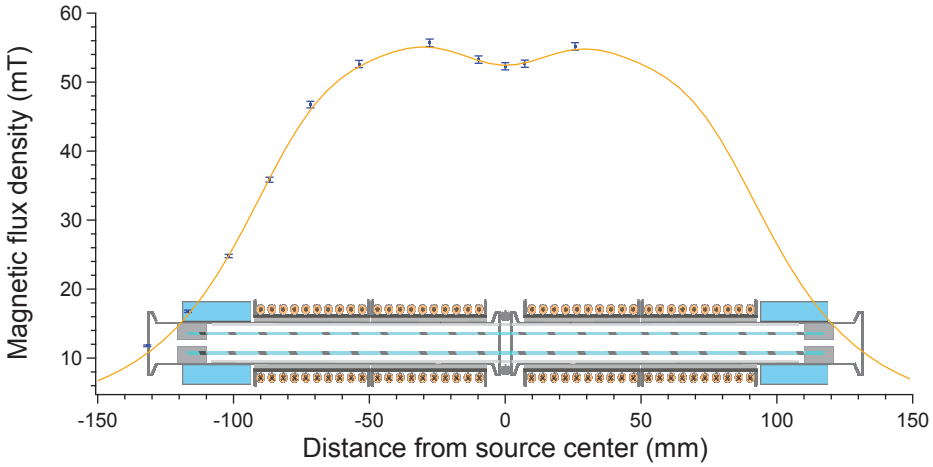

Figure 11.8 Axial profile of the magnetic flux density inside the source at a current of 4.55 A flowing through all four coils. The orange thick trace represents numerical calculation and the blue dots denote measured values. The error bars in the experimental data are ±1% of the measured value. The shaded insert in the graph is a model drawing of the corresponding part of the source where the field was probed. The available data points were limited by the length of the probe.

The addition of a magnetic field changed the optimum conditions for production of NiH. Unlike the case without any magnetic field, when the highest concentration of NiH was observed in a flow regime with pure H_2 gas, now it was desirable to add some amount of Ar gas. It is difficult to explain the exact role of the argon gas in the production of radicals but it was observed that the plasma column inside the source became unstable when the discharge was produced in hydrogen gas only. Regardless of whether the source was operated in cell or flow regime the brightness of the discharge significantly decreased and it was not possible to observe absorption signal from NiH at the conditions used before, without magnetic field. At a higher discharge current the plasma was no longer confined within the source volume and it was seen to "escape" through the openings of the outermost rings of the anode assembly and became uncontrollable. However, feeding some amount of Ar gas to the discharge medium stabilized the plasma causing it to be constrained in the region between the anode and the cathode.

The absorption spectrum shown in Fig. 11.9 presents the Zeeman response of the NiH molecule. The discharge source was operated at a current of 150 mA, in a regime with 6 sccm gas flow rate of 10%H_2 mixture in Ar and additional 15 sccm gas flow rate of H_2. The created pressure in the source was 222 mTorr as indicated by the pressure gauge. The current of 9.1 A fed to the coils was at the limit of the power source.

In these conditions the magnitude of the magnetic field along the source axis was calculated to be 0.11 T at its maximum. During this experiment both the detection scheme and the probed transition were the same as in the previous measurement without magnetic field.

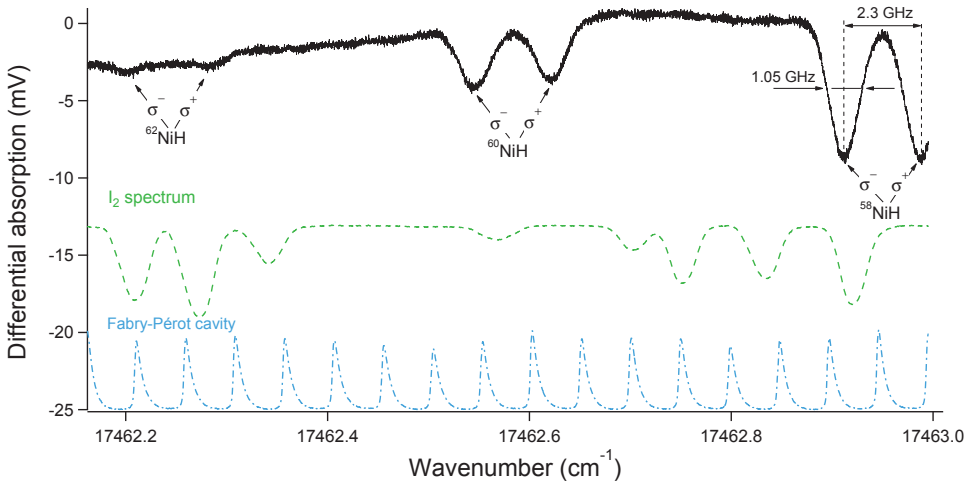

Figure 11.9 Partially resolved Zeeman structure obtained by detection of differential absorption spectrum of NiH molecule - top black trace. The transition of interest is the same as in Fig. 11.6 (Q(2.5), (1-0) band, $B\,^2\Delta_{5/2} - X\,^2\Delta_{5/2}$). The spectrum was recorded at axial magnetic field in the source of 0.1 T. The exciting laser beam traverses the plasma medium along the direction of the magnetic field, which resulted in the appearance of σ^+ and σ^- Zeeman components in the observed spectrum. Supplementary traces in the graph:absorption spectrum of the iodine molecule - green dot-dash trace and the spectral response of a Fabry-Pérot cavity (FSR=1.5 GHz) - blue dashed trace.

In the recorded spectrum in Fig. 11.9 the absorption lines associated with different isotopomers of NiH molecule can be clearly recognized. Each spectral line appears to be split in two components which are shifted in frequency with opposite signs with respect to the frequency of the zero-field transitions. Since the magnetic field inside the source was oriented along the direction of propagation of the laser beam, σ^+ and σ^- transitions were simultaneously excited by the light field. For the transition of interest, Q(2.5), the rotational quantum number for the ground and the excited state are equal, $J'' = J' = 2.5$. In magnetic field each rotational level splits into $2J + 1$ magnetic components, which are shifted in frequency. One would expect to observe five spectral lines which correspond to σ^+ transitions and five lines which correspond to σ^- transitions. However, in our case the magnetic field was not sufficient to completely resolve the different Zeeman components. As a result the observed spectral profiles appeared as a convolution of the lines associated with transitions between the individual M-states.

11.4 Discussion

The validation of new discharge source indicated the possible options to ensure better performance of the source. The experiments demonstrated that the implemented system for cooling of the cathode met our expectations, and the operation time of the source was considerably increased without affecting the production efficiency of the molecules. We were able to operate the source without interrupting the discharge for more than 20 min. After more than 30 hours of operation the cathode was without any noticeable traces of a wear and during the experiments it was never replaced. The conditions, in terms of discharge current, gas pressure, and gas mixture (Ar/H_2), which lead to the highest concentration of NiH molecules were evaluated. Additionally, differential absorption spectra of molecular NiH were obtained, both in zero field and in magnetic fields up to 0.1 T.

The experiment suggested that for achieving a magnetic field, high enough to observe a well resolved Zeeman spectra, a different approach must be used; for instance, a specially designed magnetic circuit with rare-earth magnets, as it was done in the other sputtering source that is described next, in section 12.1. Although the coils allow for the magnetic field to be easily varied by adjusting the supply current the amount of current needed to induce fields on the order of 0.5 T is related to a lot higher power dissipation in the windings wire which in turn would require additional cooling of the coils.

Moreover the obtained signal-to-noise ratio for the Q(2.5) line (see Fig. 11.6) in combination with the estimated gas temperature, on the order of ≈ 400 K, did not allow for observation of differential absorption for transitions between states with rotational quantum number higher than $J'' = 8.5$. One possibility to improve on that would be to reduce the surface area of the cathode by making the discharge tube shorter in a future work. Assuming operation at a similar magnitude of the discharge current this would result in a greater current density, and in a higher sputtering rate respectively.

At this stage the experimental study of the new discharge source was deferred and our efforts completely focused on a study of magnetic response of molecular FeH that was in progress at the same time, working with the sputter source previously developed in Lyon, and used primarily for emission spectroscopy.

Chapter 12

High-resolution spectroscopy on the Zeeman effect in FeH molecule

The present study aimed to provide experimental data concerning accurate transition frequencies and Landé factors for the first vibrational levels ($v' = 0$ and $v' = 1$) of the excited electronic state $F\,^4\Delta$ of FeH radical. The magnetic response of the $X\,^4\Delta$ state has already been studied by laser magnetic resonance (LMR) [C14]. Fig. 12.1 represents a diagram of the FeH energy levels obtained by MRCI calculations [C33].

The molecules were formed via discharge sputtering of material from a cathode made of pure iron, while the discharge burned in a mixture of Ar and H_2 gas. The plasma torch flowed downwards through a small volume below the source anode where the molecules were probed by a single mode Ti:sapphire laser. The optical signal from laser-induced fluorescence was detected by an avalanche photodetector, whose output was then recorded via a digital acquisition system (DAQ) on a computer. Continuous tuning of the laser frequency through the resonances of the (0-0) and (1-0) bands

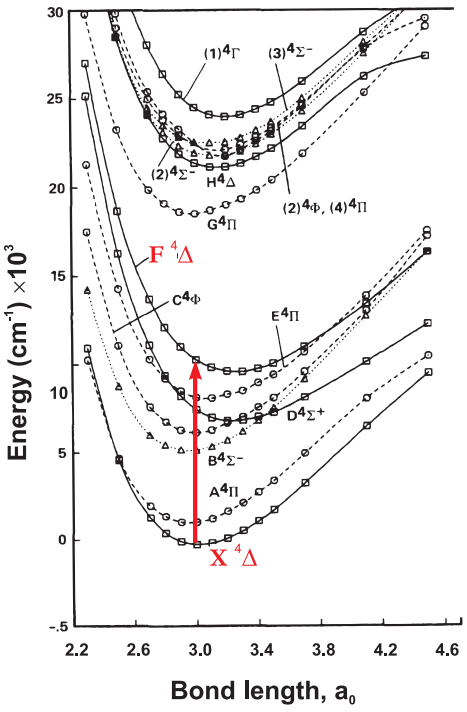

Figure 12.1 FeH electronic structure from MRCI calculations. Picture taken from Ref. [C33]. The red arrow denotes the electronic transition of interest in my work - $F\,^4\Delta - X\,^4\Delta$.

of the $F\,^4\Delta - X\,^4\Delta$ electronic system of FeH resulted in an absorption spectrum. The latter was further processed for calibration of the absolute frequency of the observed transitions, using written for the purpose routines in the program language of Igor Pro software.

In order to obtain experimental values for the Landé factors of the $F\,^4\Delta$ state levels the study was repeated in magnetic field (up to 0.5 T) as well. Having established the profile of the magnetic field within the probed region of the plasma torch, from well-resolved argon atomic lines, another fitting procedure, also written in Igor Pro, was applied to the recorded Zeeman spectra. The fit, which also considered the transition frequencies that were evaluated in zero field, was able to reproduce the Zeeman spectra, and thereby provided estimates for line centers of different M_J components where the Zeeman patterns were not completely resolved. This was notably the case for higher J lines in the P and Q branches. Transition wavenumbers extracted from this fit at several magnetic field strangths could then be included in a global linear least squares fit to determine effective Landé factors.

12.1 Hollow-cathode sputtering source

The source employed in the present study of FeH was already available in the lab in Lyon. It has been previously utilized for spectroscopic investigation of NiH radical [C21, C34]. The first validation of the source and its design are described in detail in Ref. [C35, C17]. Here its main features are discussed.

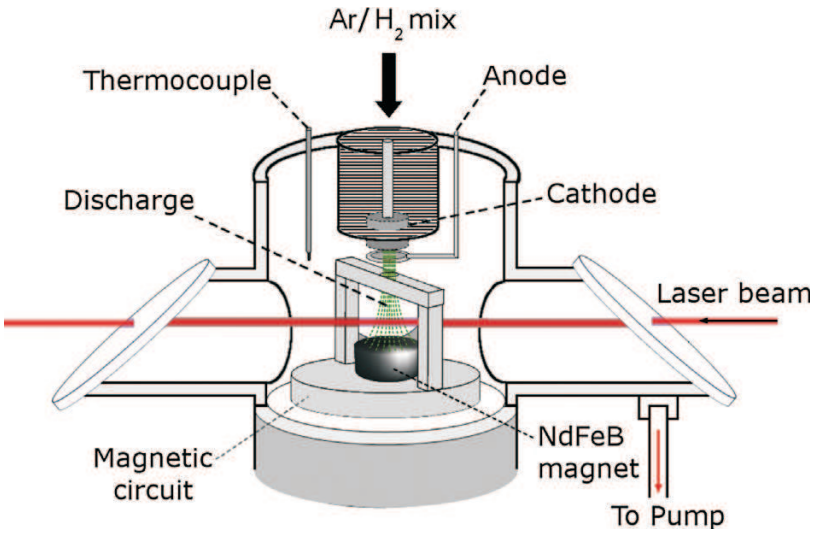

Figure 12.2 Scheme of the hollow cathode discharge source (the picture is taken from Ref. [C17]).

A cylindrical cathode 10 mm in length and 12 mm in diameter is machined from an Fe rod, and pierced with an 1.2 mm central channel. The cathode is tightly fitted inside a slot specially formed along the symmetry axis of a double-walled copper

cylinder with dimensions of $\approx \varnothing 100 \times 100$mm, as shown in Fig. 12.2. A continuous flow of water is established in the compartment between the two walls in order to provide efficient cooling of the cathode during operation. Moreover, an axial channel is also produced in the copper cylinder such that it appears as an extension of the cathode channel. The source assembly is attached to the flange of a vacuum chamber.

In the present experiment the chamber was kept at a pressure maintained close to 1 Torr as a mixture of Ar with 10% H_2 flowed through the cathode cental opening at a rate of about 60 µmol/s, then through an annular anode (copper) located a few mm below the cathode outlet. A DC discharge established between the electrodes produced a stream of FeH molecules which were probed by a laser beam below the anode. Additionally, in the interaction region a homogenous magnetic field was produced by a permanent magnet enclosed in a ferromagnetic circuit, so that the induced field was orthogonal to the direction of propagation of the probing laser. A closer view of the magnetic circuit is shown in Fig. 12.3.

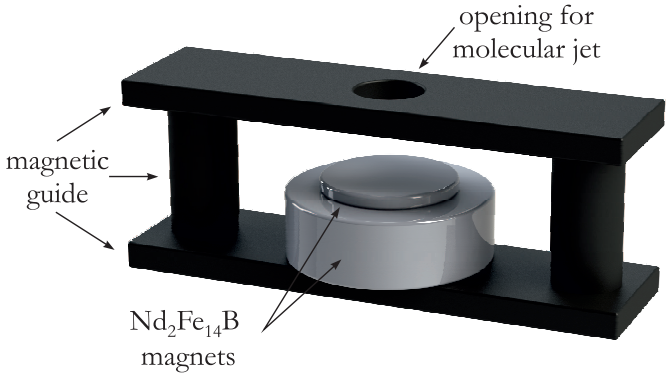

Figure 12.3 Closer look at the ferromagnetic circuit. The magnetic field is provided by Neodymium-based magnets ($Nd_2Fe_{14}B$) placed in a magnetic guide made of iron. A $\varnothing 10$ mm central opening is produced in the top iron bar to allow for the molecules to penetrate the interaction region with the laser. The magnetic field $\approx$ 10 mm above the surface of the magnet is around 0.5 T.

12.2 Experimental setup

The experimental arrangement used here is shown in Fig. 12.4. The employed Ti:sapphire laser[1], was able to scan continuously up to 2 cm^{-1} single mode between 850 and 1000 nm. Its typical RMS linewidth is 0.08 MHz, with an output power up to 2W (well in excess of our requirements here) with 10W pump at 532 nm. A linearly polarised beam from the laser probed the molecular flux in the near IR absorption bands (869–1000 nm). Laser-induced fluorescence was observed through a side-window of the vacuum chamber, and focused on to low-noise avalanche detectors: InGaAs [2] when

[1]Sirah Matisse TS
[2]Thorlabs APD 110CM

exciting the 0-0 band close to 1 µm, and Si [1] for fluorescence from 1-0 excitation transitions.

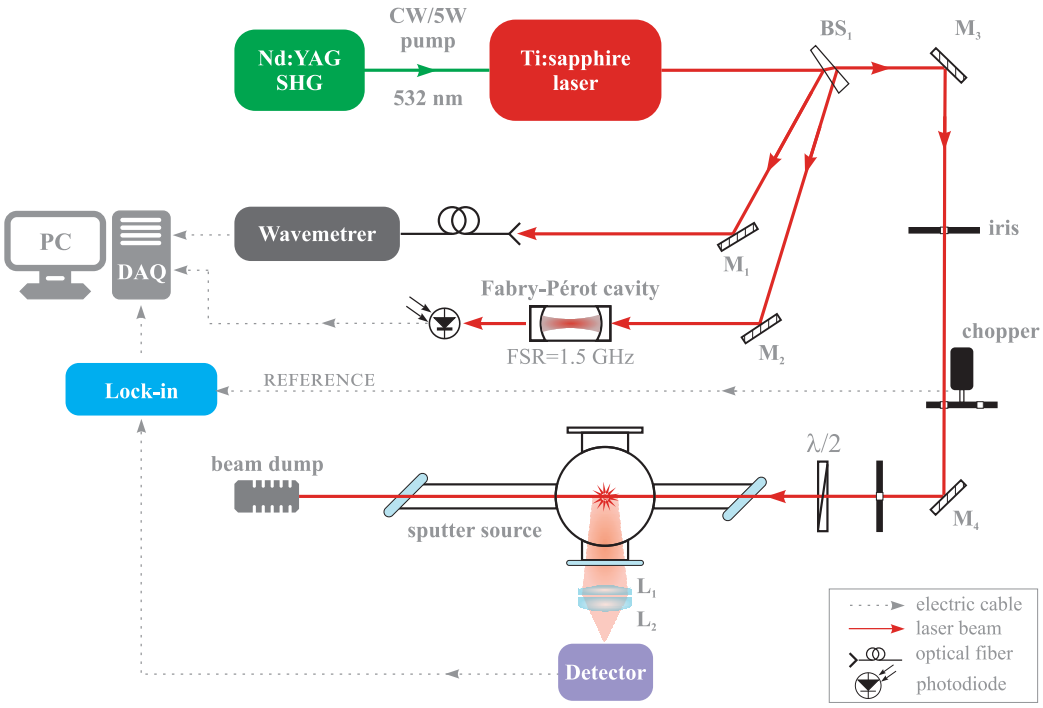

Figure 12.4 Schematic drawing of the experimental setup: M - mirror, L - lens, BS - beam splitter, $\lambda/2$ - half-wave plate.

However, scattered light from the discharge produced a significant background signal at the detector, usually several orders of magnitude larger than the observed fluorescence from molecular FeH, so a phase-sensitive detection was applied to filter out most of this background (it nevertheless limited the sensitivity of detection). Before traversing the vacuum system the intensity of the laser beam was modulated by a mechanical chopper ($f_{\mathrm{MOD}} \approx 800\,\mathrm{Hz}$), and subsequently the detector signal was directed to a digital lock-in amplifier[2]. The laser was scanned slowly (50–100 MHz/s) because the signals were weak in many cases, requiring longer integration time (typically 30 ms). Several irises were introduced along the beam path to reduce the amount of scattered laser light from the optical elements in the setup reaching the detector.

The experiment relied on accurate calibration of both the laser frequency and the magnetic field. Therefore part of the laser was directed to an additional setup consisting of a wavemeter[3] and a confocal Fabry–Pérot interferometer[4] for tracking the laser wavelength during frequency scans. Reasonably accurate absolute calibration came from the wavemeter readings, and the interferometer, with a 1.5 GHz FSR and

[1] Hamamatsu-C5460
[2] SR830 Stanford Research Systems
[3] Burleigh WA1500 wavemeter
[4] Eagle-Eye by Sirah/Newport-SpectraPhysics

a typical finesse of 250, provided a more strict control on relative calibration (since Zeeman spacings were the features of primary interest).

The response of the interferometer was monitored by a photodiode, and its output signal was fed to a data acquisition (DAQ) board which stored the data on a computer. The wavemeter provided electrical output signal which represents the instantaneous frequency of laser. Similarly, this signal, together with the lock-in output signal were also fed to the DAQ board via a GPIB interface. Finally, the whole data acquisition was controlled by a routine written in the Labview software.

Magnetic field calibration turned out to be very straightforward, as transitions between excited states of Ar I fall in the same spectral region, and their magnetic response is well documented [C36]. It was also possible to investigate a range of magnetic fields by adjusting the height of the probe beam from the magnet (the entire source was mounted on a lab-jack, and could be raised or lowered by $\approx$1 cm with respect to the incoming laser beam). Magnetic field strength was greater close to the magnet, but the density of radicals decreased as the laser beam was moved further from the cathode, so fluorescence signals (detected orthogonally to the laser) became smaller.

In situ calibration of the magnetic field relied on profile fits, or resolved peak position fits, of transitions excited from metastable atomic levels of argon atoms produced in the discharge.

Table 12.1 Reference frequencies for Ar I lines from the NIST data base [C36], used to calibrate the magnetic field.

Transition (cm^{-1})	E'' (cm^{-1})	E' (cm^{-1})	Terms	$J''-J'$	$g''-g'$
10 351.5012	93 750.5978	104 102.0990	$^2[3/2]^o - {}^2[1/2]$	1 – 1	1.404 – 1.985
10 837.7242	95 399.8276	106 237.5518	$^2[1/2]^o - {}^2[3/2]$	1 – 2	1.102 – 1.305
10 958.3390	93 143.7600	104 102.0990	$^2[3/2]^o - {}^2[1/2]$	2 – 1	1.506 – 1.985

Table 12.1 lists the three argon lines that were used to calibrate the magnetic field flux in this way, and Fig. 12.5 shows assignments for the peaks obtained for the strongest of these. Fitting either peak positions, or the entire profile, allows an average value for the magnetic field (between 0.2 T and 0.5 T) to be determined to within 3 mT. An argon line spectrum was measured before and after each series of measurements on FeH, with the laser beam polarisation tuned to excite $\Delta M_J = 0, \pm 1$ transitions together (see Fig.12.5). Because no modification (other than laser wavelength) was required when changing from FeH transitions to argon transitions, the magnetic field was assumed to be known to 0.5% accuracy in the subsequent FeH measurements.

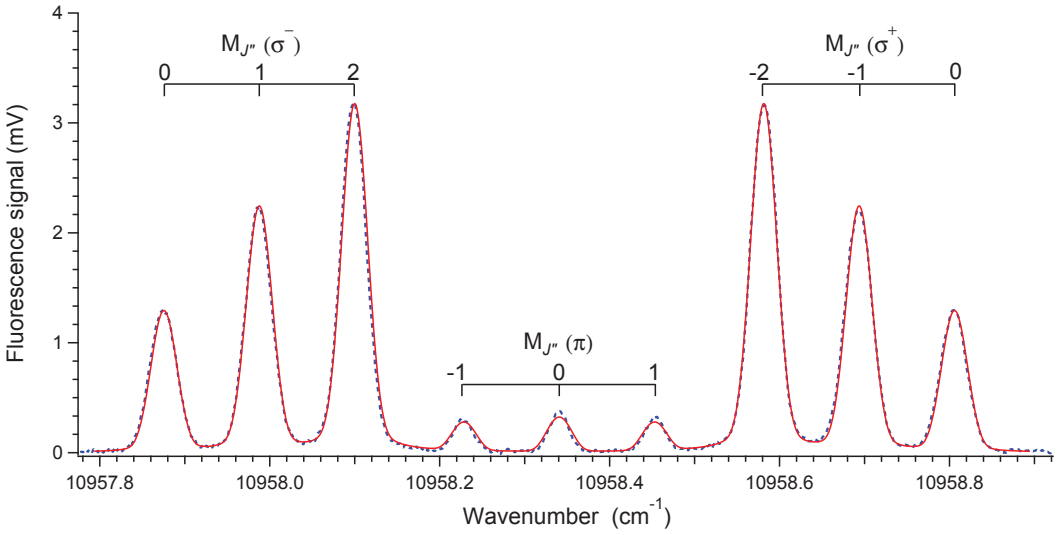

Figure 12.5 Typical LIF Zeeman spectrum from Ar I transition $^2[1/2]_1$ – $^2[3/2]^o_2$ with laser polarisation arbitrarily chosen to enhance $\Delta M_J = \pm 1$ transitions. The magnetic field of B = 0.502(2)T is deduced from performing a curve fitting (continuous (red) plot) on the recorded spectrum (broken (blue) line). $M_{J''}$ numbers are indicated.

12.3 Spectroscopic measurements

The iron hydride molecules were produced at rotational temperature $T_{\rm rot} \approx 500\,{\rm K}$, allowing us to detect $J < 11.5$ in X $^4\Delta_{7/2}$ and $J < 8.5$ in X $^4\Delta_{5/2}$.

The laser frequency was scanned successively through the low J lines of the 0-0 and 1-0 bands of the F–X system of FeH, first at zero field, to determine the parity splittings for the low-J lines, where they were unresolved in the high temperature spectrum of Phillips et al. [C18] because of the increased Doppler width. Fig 12.6 shows the Q-head region of the F $^4\Delta_{7/2}$ – X $^4\Delta_{7/2}$ 1-0 band in ^{56}FeH. Parity splittings broaden the second Q line (Q(4.5)); $Q_{\rm fe}$ and $Q_{\rm ef}(5.5)$ are partially resolved.

The experiment was then repeated with the magnet and the magnetic circuit in place. The laser polarisation was adjusted either parallel or perpendicular to the magnetic field direction to select cleanly either $\Delta M_J = 0$ (π) or $\Delta M_J = \pm 1$ (σ) transitions, and scanned through the Zeeman profile, while recording simultaneously Fabry Pérot fringes and resonant fluorescence signal from FeH. Around 200 wavemeter readings were also recorded during each of those 1–2 cm^{-1}scans, controlled by a Labview interface. The Zeeman patterns were better resolved in the R lines than in the stronger Q branches; this is explained by a smaller difference between upper state and lower state Landé factors for Q lines, making consecutive Zeeman components more difficult to resolve. Consequently, most information comes from R(J) transitions, recorded under different magnetic field conditions. An example for the R(8.5) line is given Fig. 12.7. Unblended lines had Gaussian profiles, with full-width-at-half maximum 0.02 cm^{-1}. Zeeman structures started to be resolved with $B > 0.2\,{\rm T}$. Spec-

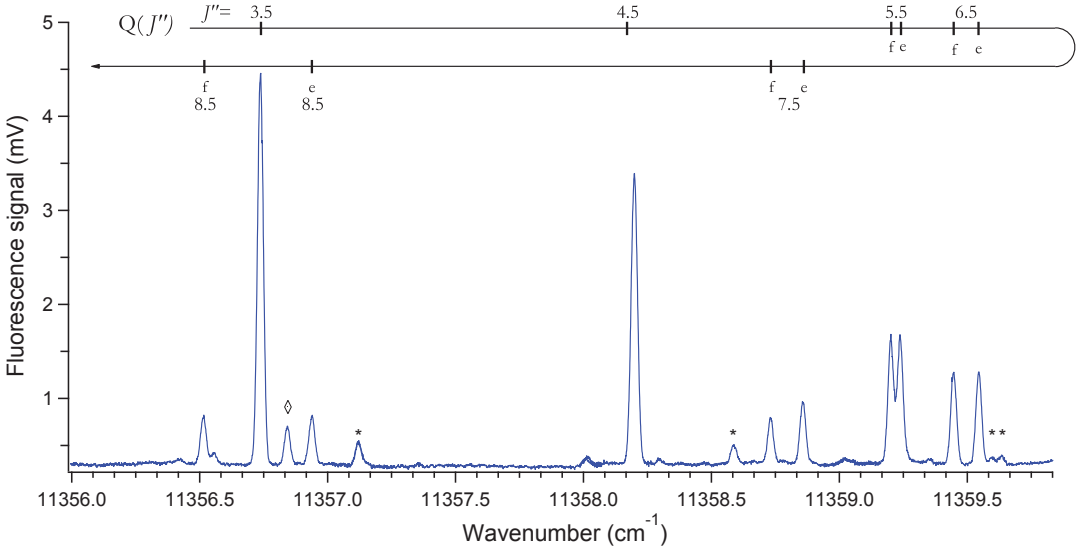

Figure 12.6 Q head of the F $^4\Delta_{7/2}$ – X $^4\Delta_{7/2}$ 1-0 band in ^{56}FeH. Asterisks indicate lines from the less abundant ^{54}FeH, and diamond symbol the $P_f(5.5)$ transition of the F_3 ($\Omega' = 3/2$ - $\Omega'' = 3/2$) sub-band. Experimental parameters: discharge current = 300 mA, pressure = 1.06 Torr, Ar/H_2 (50/50 mix) flow rate = 60 µmol/s, laser power =130 mW (laser beam unfocused). Lock-in detection: modulation frequency =1.7 kHz, time constant =30 ms.

tra were deceptively strong and simple when the Zeeman splitting happened to allow transitions from e and f parity components to overlap, and as J increased, this was sometimes the best way to obtain an exploitable spectrum.

However, in certain cases it occurred that magnetic components of several different lines overlap within the explored spectral region and contribute together to the observed Zeeman spectra, and thus making it rather complex. An example of such a spectrum is the one shown in Fig. 12.8. It represents part of the spectrum depicted in Fig. 12.6 but this time acquired in magnetic field of about 0.502 T. 174 Zeeman components of four Q lines, Q(4.5), Q(5.5),Q(6.5),Q(7.5) and the corresponding parity components, contribute to the observed spectral profile. A stick spectrum of Zeeman components is plotted in Fig. 12.9.

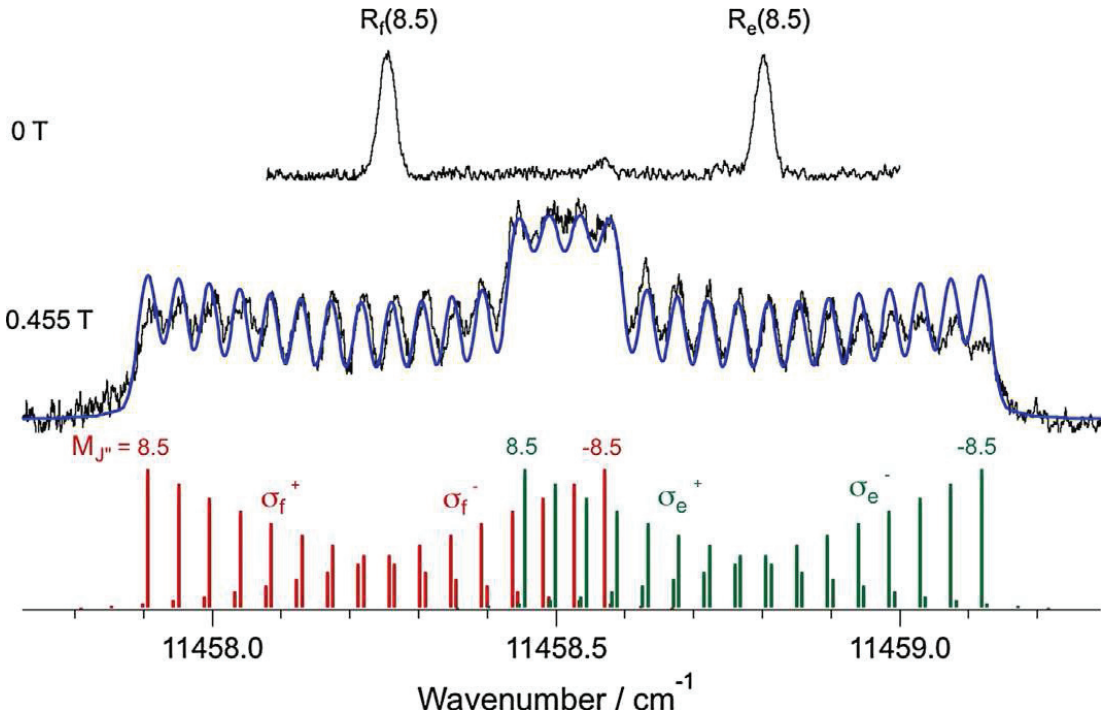

Figure 12.7 Examples of partially resolved $\sigma^{\pm}$ ($\Delta M = \pm 1$) Zeeman structures in the 1-0 band of ^{56}FeH. The $R_1(8.5)$ line shows that Λ-doubling compounded with Zeeman splittings can result in complex envelopes for some transitions. Upper trace, zero-field spectrum. Middle trace recorded at 0.455 T, with the blue line indicating a simulated spectrum calculated from the individual Zeeman f (red) and e (green) parity components, shown in the stick spectrum of the lowest trace, convoluted with Doppler linewidth.

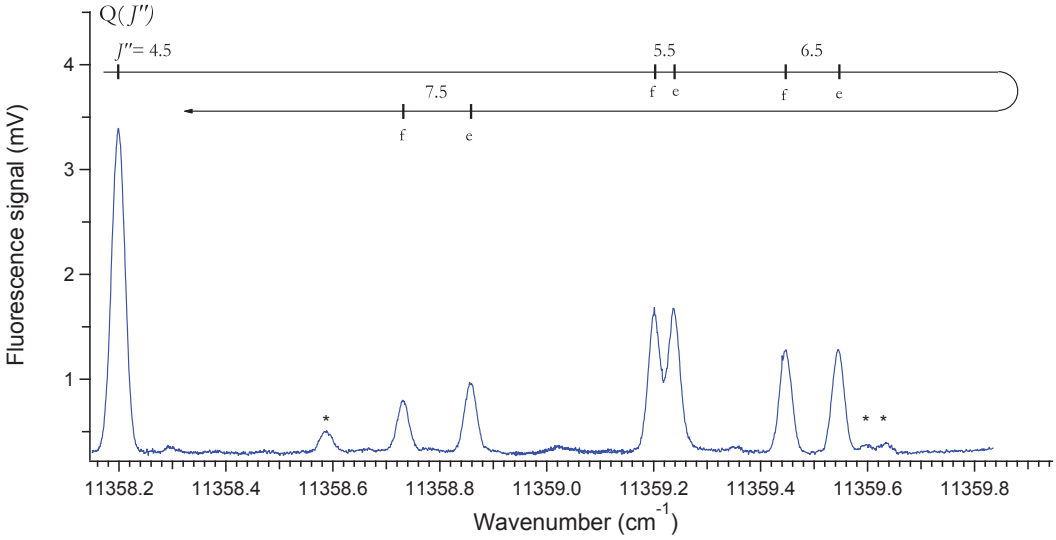

(a) Part of the Q head of the F $^4\Delta_{7/2}$ – X $^4\Delta_{7/2}$ 1-0 band in ^{56}FeH acquired in zero magnetic field, previously shown in Fig. 12.6, that is relevant to the fitted waveform from Fig. 12.8b acquired in magnetic field of about 0.5 T.

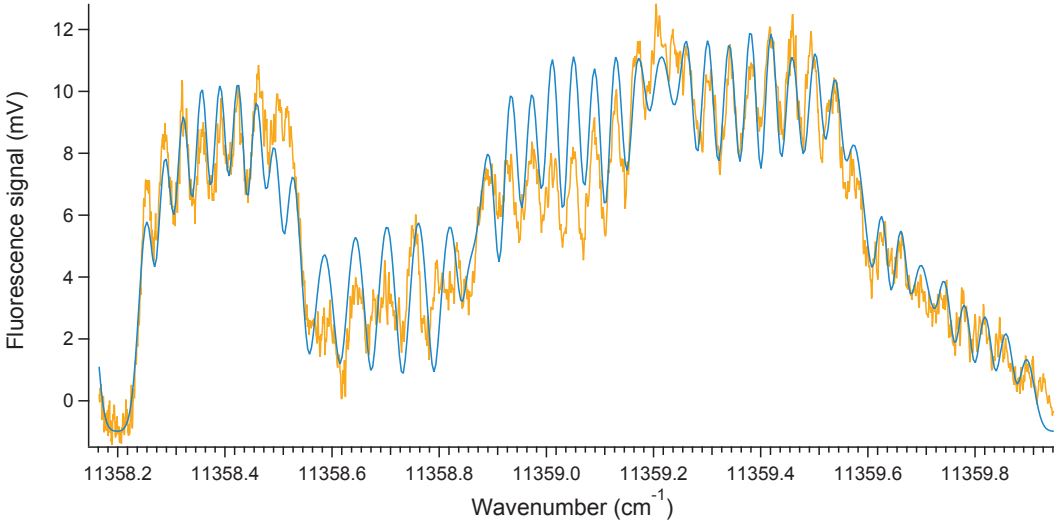

(b) Partially resolved $\sigma^{\pm}$ ($\Delta M = \pm 1$) Zeeman structures in the 1-0 band of ^{56}FeH. The trace in orange represents acquired experimental data and blue trace represents the output of the performed fitting procedure.

Figure 12.8

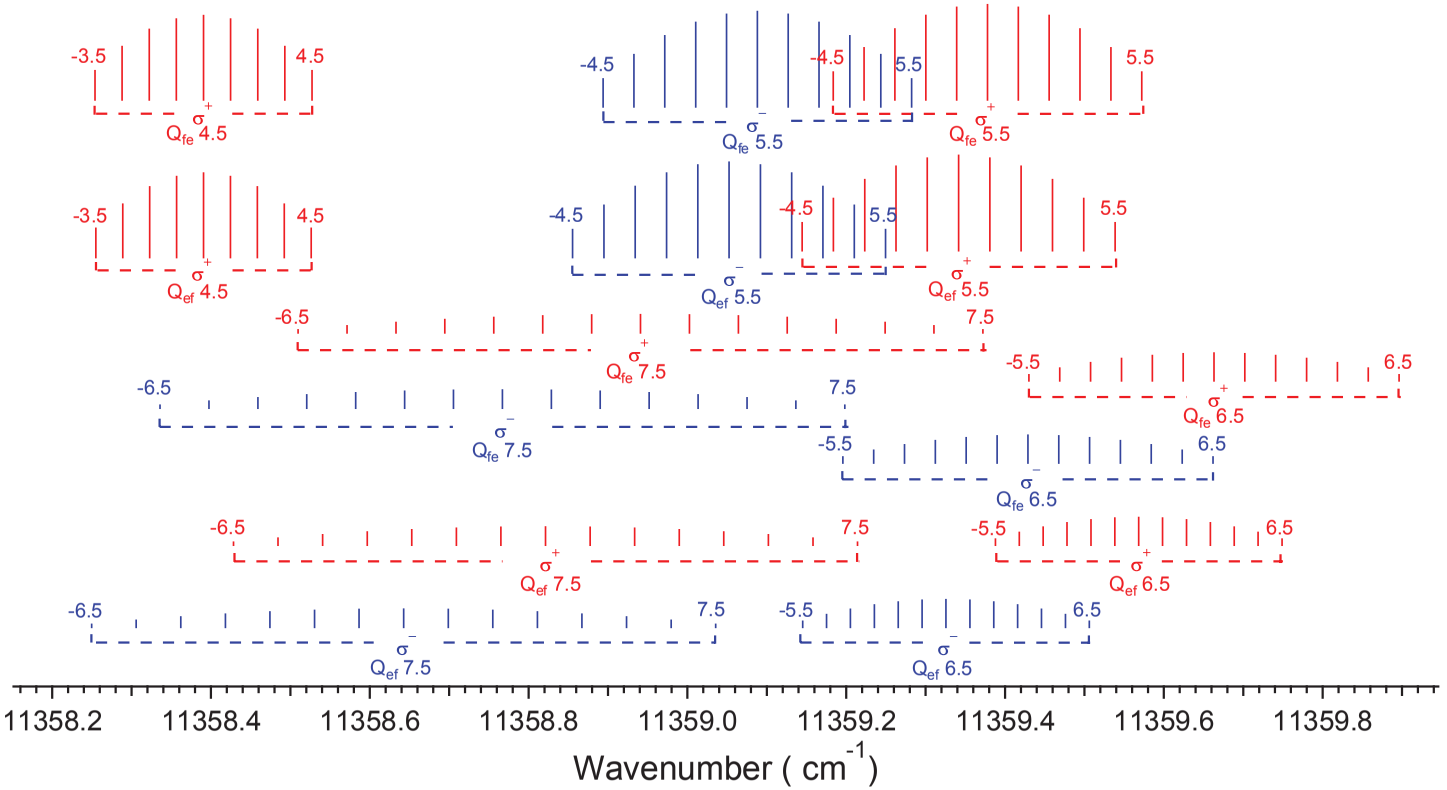

Figure 12.9 Stick spectrum of the Zeeman components which are present in the frequency range of the observed in Fig. 12.8 spectral profile. σ^+ and σ^- transitions are plotted in red and in blue color respectively. Beneath each set of sticks the corresponding Q line relevant to the observed transitions is also labeled. The height of the sticks represents the strength of the transitions between the Zeeman sublevels normalized in such a way that their sum over all Zeeman transitions for the given J' and J'' is unity[C37]. Beneath each set the associated Q line is labeled as well.

12.4 Analysis of the spectra

As in earlier work on NiH [C34], a term value fit of all transitions was performed, yielding a term energy and effective Landé factor g_J for each rovibrational level observed. In the same way for FeH, the lines recorded in zero field (wavenumber ν_0) established an energy scale with respect to the lowest energy level $v'' = 0$, $J'' = 5/2$ in the ground state $\mathrm{X}\,^4\Delta_{7/2}$. Wavenumbers of resolved Zeeman structures were expressed as

$$\nu = \nu_0 + (g_{J'}\, M_{J'} - g_{J''}\, M_{J''})\mu_{\mathrm{B}}\, B \ ,$$

where g_J, are upper and lower state Landé factors, μ_{B} is the Bohr magneton and B is the magnetic flux (determined from the Zeeman effect observed in argon). This simple expression does not take into account second-order effects due to nearby rotational levels, established to be a negligible effect in this case [C5]. Ground state energies and $g_{J''}$ are known for most $v'' = 0$, $\mathrm{X}\,^4\Delta_{7/2,5/2}$, levels observed here, and have been constrained in the fits to values given by far IR laser magnetic resonance measurements [C14]. A linear least-squares fit produced the upper state Landé factors given in Table 12.2, where upper state energies, g_J and also reduced Landé factors, $g_{J_{elec}}$ given by $g_J \times J(J+1)/\Omega$ are given. The latter quantity gives a direct indication to the extent with which the angular momentum coupling deviates from the Hund's case (a) limit, whereupon $g_{J_{elec}} = \Lambda + 2\Sigma$. Table 12.2 2 also indicates the magnitudes of parity splittings when resolved. Taken in combination with the e/f separations in the electronic ground state, Λ-doubling effects can be significant (see Fig. 12.6), and should also be taken into account when constructing line profiles for comparison with solar or stellar observation (it has sometimes been assumed otherwise [C37]), particularly since this work confirms that there is sufficient configuration mixing to result in different Zeeman responses for the parity components of a given level.

This has already been noted by Harrison et al. [C12] in their higher resolution investigation of the profiles of the Q(3.5) and R(3.5) lines of the 1-0 band using an ablation source. They reported distinct values for g_J(3.5 e,f), differing by 0.0025 (see Table 12.2). The value obtained here is slightly larger than both of theirs, just outside quoted uncertainties. In the present work the parity splittings for these transitions were not resolved, but the $\mathrm{F}\,^4\Delta_{7/2}$, $v = 1$, $J = 3.5$ level was probed through Q(3.5) and P(4.5) lines. Furthermore, it was possible to obtain a fully resolved the Zeeman structure of the P(4.5) line (whereas it was reported to be "only broadened" in Ref. [C12]). So our upper state Landé factors should be reliable. Ref. [C12] also reports $g_J = 0.785$ for $\mathrm{F}\,^4\Delta_{7/2}$, $v = 1$, $J = 4.5$ level (no distinction between parity levels) based on profile matches. Again, with fully resolved Zeeman structures, this time from R(3.5), we believe the new value to be more reliable. In most cases, however, the Zeeman structures are not completely resolved, and it became pertinent to use curve-fitting routines instead of the simpler peak-fitting approach. This entailed matching laser excitation signals with profiles calculated assuming a Gaussian (Doppler) lineshape (ignoring ^{1}H hyperfine structure) and admitting proportionality between the total fluorescence power signal (spontaneous emission reaching a Si detec-

tor with photoelectric sensitivity $\eta_{\rm PE} = 1.5 \times 10^6\,{\rm V/W}$) and absorption line strength. This can be expressed as

$$V(\nu) = \eta_{\rm PE}\, P_{\rm W}(\nu) \approx \eta_{\rm PE}\, \delta(N_1\, \sigma_{12}\, x) P_{\rm LAS}\ ,$$

where N_1 is the molecule density in the gas sample region of length x, δ is the efficiency of the collection optics, σ_{12} is the absorption cross-section for the transition and $P_{\rm LAS}$ is the incident laser power. Assuming that the signals are not saturated, this gives $V(\nu) \propto \sigma_{12}(\nu)\, P_{\rm LAS}(\nu)$. In practice, these signals are quite weak. As an order-of-magnitude indication, absorption of a 100 mW laser beam through a sample 1 cm in length, with the absorption coefficient $k = 10^{-4}{\rm cm}^{-1}$(taking a value typical for NiH, for which Li et al. have given a direct measurement of absorption coefficient [C32]) would produce a signal of 5 mV on the detector, which is roughly 5× the detection limit of the APD C5460. The absorption cross-section between electronic states α' , α'' is given by:

$$\sigma_{12}(\nu) = B_{12}(\nu_0)\, g(\nu - \nu_0)\, h\, \nu_0/c\ ,$$

where

$$B_{12}(\nu_0) = 1/(6\epsilon\hbar^2)\, \langle \alpha', v', J', M' | \mu_{12} | \alpha'', v'', J'', M'' \rangle^2$$

and $g(\nu - \nu_0)$ is a normalized Gaussian function. The intensity profile

$$V(m) = g(\nu - \nu_0)\, P_{\rm LAS}(\nu)\, \langle \alpha', v', J', M' | \mu_{12} | \alpha'', v'', J'', M'' \rangle^2$$

was introduced in the profile fitting routine of Igor Pro. The matrix elements for the transition dipole moment were taken as normalized Wigner $3j$ factors [C38], with corresponding formulae for transitions between M_J sublevels (with selection rules imposed by the orientation of the linearly polarised pump laser) taken from Berdyugina and Solanki [C37]. Profile fitting was very sensitive to any baseline irregularity, to contributions from weaker transitions in the same spectral region, and to strong correlation between parameters. In most cases, it was helpful to constrain ν_0 and – when possible – the ground state Landé factors, since the signal/noise ratio was typically < 10. Recalculation of spectral profiles did sometimes highlight unexpected differences in relative intensities (for two parity components of a given line, for example); this sort of information is important in developing a set of reference lines for use of FeH as a magnetic probe.

12.5 Discussion

Perhaps the major challenge for laboratory work of this ilk was the restricted range of ro-vibrational levels that were probed from thermally populated levels of the ground state, since the strongest lines in solar umbral spectra, or from cool low-mass stars, are associated with rotational quantum numbers typically higher than $J = 10.5$. Wanting some estimate of such Landé factors with which to interpret the Stokes I and Stokes V profiles of magnetically sensitive lines of FeH recorded in the cooler

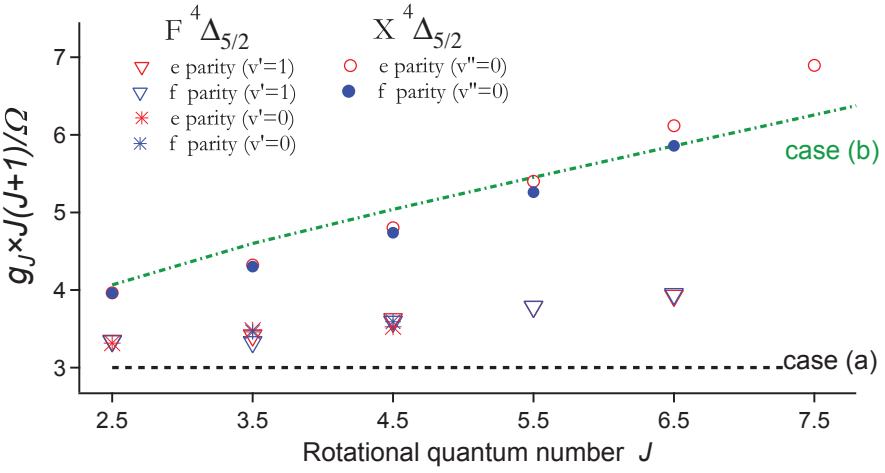

(a)

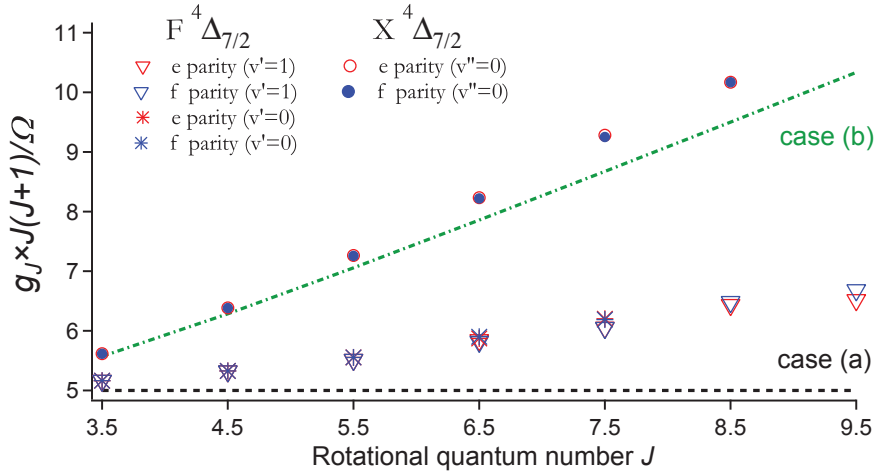

(b)

Figure 12.10 Plot of reduced Landé factors for rotational levels belonging to $\Omega = 7/2$ and $\Omega = 5/2$ components of the X $^4\Delta$ and F $^4\Delta$ states. Circles indicate measurements for the X $^4\Delta$ components; crosses and triangles - for the F $^4\Delta$ components. Parities e and f are respectively indicated by red and blue. Dashed lines indicate limiting values corresponding to pure Hund's case (a) and Hund's case (b) coupling.

parts of sunspot umbrae, or cool dwarf stars, Afram et al. [C1] focused on the diagnostic potential of selected lines of FeH. They first calculated g_J factors from the effective Hamiltonian analysis of Dulick et al. [C3], and compared these values with the quantities they deduced from a selection of FeH lines with sunspot profiles. Finding that the effective Hamiltonian of Ref. [C3] generated workable Landé factors for many lines, but failed for example for higher J values in the P branch of the 0-0 band of the F–X system, they proposed some new estimates of effective Landé factors for the 'perturbed' lines, and in modelling these, found that the magnetic response of the molecule might be interpreted as a lesser degree of spin uncoupling in the lower state, and a greater one in the upper state, than predicted from the Hamiltonian of Ref. [C3]. Afram and co-workers gave an empirical expression fitting their results, which are used to generate the last column of Table 12.2, to give some comparisons. It can be seen that as J increases, the new laboratory values are systematically higher than those estimated from the solar spectra. Line profiles are more sensitive to the differences between upper and lower state magnetic response than to the absolute values of $g_{J''}$ and $g_{J'}$, and the differences are in fact less pronounced. Few of our spectra are totally resolved, actually allowing upper and lower state Landé factors to be determined independently with confidence; but for the first R lines, our results clearly agree (with larger uncertainties) with the LMR results. We therefore accepted the numbers proposed in [C14], and admit that our results for the F $^4\Delta$ state will be totally correlated to those values. The idea of following the trend of degree of spin uncoupling, as the rotating molecule moves between the limiting Hund's case (a) and Hund's case (b) situations is appealing, however. The observed trend is illustrated in Fig. 12.10, where all available laboratory determinations of the reduced Landé factors, $g_{J_{elec}} = g_J \times J(J+1)/\Omega$, for the F $^4\Delta$ state are plotted as a function of J, with ground state $v = 0$ values indicated for comparison. For a molecule following pure Hund's case (a), this function will be invariant, given by $\Lambda + |g_s\Sigma|$, where g_s is the electron spin g-factor$= -2.00232$. For a molecule in pure Hund's case (b), the quantity increases with J. The values determined here for the F state lie somewhere between the two. Empirically, it is possible to make an 'educated guess' for the values for the next few rotational levels. However, the influence of other low-lying electronic states (notably $^4\Pi$ and $^6\Delta$, within one vibrational quantum spacing from $v = 0$ of the ground state) means that Λ is unlikely to remain a 'good' quantum number anyway, and that for immediate purposes, it is preferable to use weaker transitions for which direct measurements have been made, rather than rely on unsure extrapolations for the stronger lines involving higher rotational levels. Observing transitions from the next higher (thermally populated) rotational levels remains difficult with the signal/noise we have at present.

12.6 Perspectives

During the year spent in Lyon (French government Eiffel scholarship), I took part in experiments that gave access to new rotational data (up to $J = 10.5$) concerning the vibrational levels 0 and 1 of the $F^4\Delta$ state of ^{56}FeH, both at zero field and for magnetic fields up to 0.5 T. Later, I worked on the routines to simulate and fit the complex line profiles in the more crowded region of the spectra. This supplied the best available estimate for Zeeman components of high J lines, that could then be included in the global fits performed by other members of the Lyon group.

New information, including line frequencies, parity doubling and Landé factors, was obtained. As with NiH, signal to noise ratios limited the range of rotational levels that could be explored, and future work will have to overcome contributions from discharge fluctuations (more pronounced than in NiH as higher currents were used) and background. Possible improvements which were considered included moving to intracavity techniques, detecting either laser induced fluorescence, or absorption with femtosecond frequency comb sources. The latter would combine the advantages of absolute frequency calibration and wide spectral coverage. A sub-Doppler spectroscopy, for example via polarization labelling to resolve particularly crowded Zeeman profiles, was also envisaged. The main focus for future work in Lyon will be to improve and extend laboratory spectroscopy measurements and modeling of the electronic spectra of FeH and CrH to provide reference data for spectropolarimetric observation at telescopes. The instrument SPIROU, which should be commissioned at the Canada–France–Hawaii Telescope (CFHT) before the decade is out, will offer simultaneous full-Stokes coverage of the 0.98–2.45 μm region, at a resolving power of 75000. Amongst its many scientific goals, SPIROU will study very-low mass stars, so a reliable characterisation of the optical transitions from species which are signature of magnetic activity in such objects will be required.

Table 12.2 Landé factors g_J and reduced Landé factors $g_{J_{elec}}$ for F $^4\Delta_{7/2,5/2}$ levels observed in this work. Ground state parameters are from LMR experiment [C14], or (a) extrapolated from lower J'' of [C14]. Given in the last column, for comparison, values deduced from analysis of solar umbral spectra [C1] or (b) from measurements made in a laser ablation experiment [C12].

J	parity	E (cm^{-1})	1 SD (cm^{-1})	$g_{J_{elec}}$	1 SD	g_J	1 SD	g_J[C1]
F $^4\Delta\,\Omega_{7/2}$, $v=0$								
3.5	ef	9934.950	(0.003)	5.163	(0.032)	1.1473	(0.007)	1.151
4.5	ef	9985.190	(0.001)	5.328	(0.009)	0.7535	(0.001)	0.760
5.5	ef	10046.540	(0.001)	5.554	(0.010)	0.5437	(0.001)	0.540
6.5	e	10119.005	(0.001)	5.872	(0.022)	0.4216	(0.002)	0.405
6.5	f	10118.995	(0.000)	5.900	(0.033)	0.4236	(0.002)	
7.5	e	10202.505	(0.002)	6.202	(0.029)	0.3405	(0.002)	0.317
7.5	f	10202.508	(0.002)	6.189	(0.028)	0.3398	(0.002)	
F $^4\Delta\,\Omega_{5/2}$, $v=0$								
2.5	e	10185.784	(0.002)	3.316	(0.023)	0.9474	(0.007)	
3.5	e	10225.558	(0.003)	3.481	(0.037)	0.5525	(0.006)	0.549
3.5	f	10225.429	(0.003)	3.461	(0.037)	0.5493	(0.006)	
4.5	e	10276.689	(0.002)	3.527	(0.038)	0.3562	(0.004)	0.357
4.5	f	10276.045		3.592	(0.041)	0.3628	(0.004)	
F $^4\Delta\,\Omega_{7/2}$, $v=1$								
3.5	ef	11356.721	(0.001)	5.164	(0.011)	1.1475	(0.002)	e: 1.1449(12)[b]
								f: 1.1425(11)[b]
4.5	ef	11405.266	(0.001)	5.322	(0.007)	0.7526	(0.001)	0.785[b]
5.5	ef	11464.526	(0.001)	5.515	(0.011)	0.5399	(0.001)	
6.5	e	11534.511	(0.001)	5.844	(0.018)	0.4196	(0.001)	
6.5	f	11534.497	(0.001)	5.817	(0.018)	0.4176	(0.001)	
7.5	e	11615.181	(0.002)	6.055	(0.034)	0.3324	(0.002)	
7.5	f	11615.137	(0.001)	6.049	(0.027)	0.3321	(0.002)	
8.5	e	11706.396	(0.002)	6.434	(0.045)	0.2789	(0.002)	
8.5	f	11706.373	(0.002)	6.485	(0.039)	0.2811	(0.002)	
9.5	e	11808.227	(0.001)	6.516	(0.030)	0.2286	(0.001)	
9.5	f	11808.131	(0.001)	6.683	(0.028)	0.2345	(0.001)	
F $^4\Delta\,\Omega_{5/2}$, $v=1$								
2.5	e	11613.844	(0.001)	3.347	(0.012)	0.9563	(0.003)	
2.5	f	11613.923	(0.001)	3.341	(0.011)	0.9547	(0.003)	
3.5	e	11652.489	(0.001)	3.417	(0.025)	0.5423	(0.004)	
3.5	f	11652.140	(0.001)	3.329	(0.023)	0.5284	(0.004)	
4.5	e	11701.832	(0.002)	3.625	(0.042)	0.3661	(0.004)	
4.5	f	11701.764	(0.001)	3.593	(0.027)	0.3629	(0.003)	
5.5	e	11762.112	(0.001)	3.785	(0.024)	0.2647	(0.002)	
5.5	f	11761.919	(0.001)	3.785	(0.024)	0.2647	(0.002)	
6.5	e	11833.306	(0.001)	3.927	(0.042)	0.2014	(0.002)	
6.5	f	11833.005	(0.002)	3.949	(0.056)	0.2025	(0.003)	
X $^4\Delta\,\Omega_{7/2}$, $v=0$								
3.5	ef	0.0000		5.616		1.2480		1.148
4.5	e	47.069		6.384		0.9028		0.841
4.5	f	47.079		6.383		0.9026		0.841
5.5	e	105.303		7.263		0.7111		0.647
5.5	f	105.341		7.258		0.7105		0.647
6.5	e	174.964		8.233		0.5911		0.521
6.5	f	175.069		8.220		0.5902		0.521
7.5	e	256.280		9.281		0.5095		0.435
7.5	f	256.514		9.251		0.5079		0.435
8.5	e	349.433		10.17		0.441[a]		0.374
8.5	f	349.884		10.17		0.441[a]		0.374
X $^4\Delta\,\Omega_{5/2}$, $v=0$								
2.5	e	163.955		3.964		1.1325		0.936
2.5	f	163.979		3.959		1.1311		0.936
3.5	e	208.013		4.322		0.6861		0.625
3.5	f	208.146		4.302		0.6829		0.625
4.5	e	264.414		4.802		0.4851		0.443
4.5	f	264.828		4.739		0.4786		0.443
5.5	e	333.047		5.401		0.3777		0.334
5.5	f	334.013		5.260		0.3679		0.334

Chapter 13

New prospects for magnetic probes. Chromium hydride.

Like the FeH radical, the chromium hydride molecule, CrH, is of significant astrophysical importance. Nowadays absorption spectra in the (0-0) and (1-0) bands of the $A^6\Sigma^+$–$X^6\Sigma^+$ transition of molecular CrH, respectively at 861 and 764 nm, are used as markers for low-temperature stars, like L-type brown-dwarfs (surface temperature= $1400 - 2000$ K) [C39]. In addition molecular rotational lines arising from the infrared band systems of CrH and CrD molecules have been identified in sunspot umbral spectra [C40]. CrD is also a candidate for the "deuterium test" applied to distinguish between cold stellar objects (fusion reactions occur) and planets (no fusion).

Despite the interest no experimental measurement of the magnetic response has been performed for a broad range of rotational quantum numbers on this molecule. So far only the very first N values had been probed in a molecular beam [C41]. Given the context, the CrH molecule appears as a possible candidate for future laboratory studies on the subject.

In the described sputtering source switching to production of other MH molecules rather than FeH is relatively easy. By simply replacing the iron cathode with one that was made of iron-chromium alloy[2] it was possible to observe molecular absorption of CrH. In Fig. 13.1 a typical LIF spectrum of ^{52}CrH is shown. The acquired spectrum was obtained with the same experimental setup, that was used for the study of FeH radical at zero magnetic field.

Within this study several scans of the laser frequency in different spectral regions of the (0-0) band of the $A^6\Sigma^+$–$X^6\Sigma^+$ states of ^{52}CrH were performed. This allowed for observation of molecular absorption of CrH, where eighteen spectral lines were identified. These are listed in Table 13.1. The set of labels used to describe each transition, given in the first two columns, is explained in the following.

Since both electronic states are sextets for each rotational state described by the rotational quantum number N six values of J are possible: $J = N + 5/2,\ N +$

[2]Fecralloy®- Iron/Chromium (Fe72.8/Cr22/Al 5/Y 0.1/Zr 0.1)

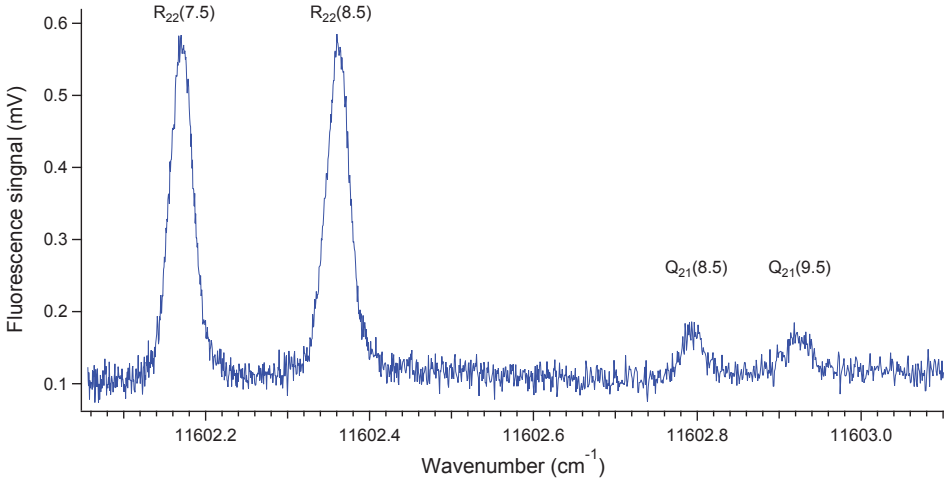

Figure 13.1 Absorption spectrum of (0-0) band of the $A^6\Sigma^+$–$X^6\Sigma^+$ system of ^{52}CrH.

$3/2,\ N+1/2,\ N-1/2,\ N-3/2,\ N-5/2$, and the corresponding energy levels are designated as $F_1, F_2, F_3, F_4, F_5, F_6$ respectively. In order to label each particular transition observed in addition to the branch label (P, Q, R) a pair of lower indices is used which indicate the spin components of the excited and the ground states between which the transition occurs.

The evaluated transition frequencies of the observed spectral lines were compared with values from the work by Burrows et al.[C42]. This theoretical work uses ab initio calculations to extrapolate from available experimental data. Almost half of the frequencies we measured agreed well within the experimental error with the predicted by the model values, but it was also noticed that for some transitions they differed by more than several times the measurement error. It is due to the fact that the model can give also results for measured lines, and being from ab initio molecular constants on d-electron species, it can be not accurate, especially for high J. Our data were also compared with transition frequencies obtained via Fourier transform emission spectroscopy in an experiment performed by Ram et al.[C43]. Here the agreement with our data was complete for all of the observed transitions.

So it is tempting to acquire a well calibrated spectrum of CrH in a broad frequency range at zero field, in order to make a comparison with the line list form Ref.[C42], and hopefully to improve it providing accurate transition frequencies and relative line intensities as well.

The knowledge acquired during the present work should pave the way to a much more complete characterisation of the $A^6\Sigma^+$–$X^6\Sigma^+$ (0,0) and (1,0) bands, under magnetic fields from 0 to 0.6 Tesla. This case (b) radical follows the Paschen-Back regime even at moderate values of the magnetic flux [C44]. Therefore, performing a laboratory study of the generalized Landé factors is needed in order to deduce the magnetic field from spectropolarimetric measurements on cold stellar objects like L-stars.

Table 13.1 Observed rotational lines of the $0-0$ band of the $A^6\Sigma^+$–$X^6\Sigma^+$ system of ^{52}CrH.

Transition			Wavenumber (cm^{-1})		
branch	J''	parity	calculated [C42]	measured (this work)	difference
P_{11}	3.5	e	11 538.707	11 538.708	+0.001
R_{55}	9.5	e	11 538.571	11 538.595	+0.024
Q_{54}	6.5	f	11 567.406	11 567.404	−0.002
Q_{21}	2.5	e	11 567.791	11 567.793	+0.002
R_{22}	14.5	e	11 568.032	11 567.957	+0.075
R_{44}	7.5	f	11 577.083	11 577.079	−0.004
Q_{21}	3.5	e	11 577.290	11 567.295	+0.005
R_{11}	4.5	e	11 585.126	11 585.137	+0.011
Q_{21}	4.5	e	11 585.572	11 585.573	+0.001
R_{22}	11.5	f	11 592.705	11 592.552	+0.153
Q_{32}	6.5	f	11 592.625	11 592.635	+0.010
R_{33}	5.5	e	11 592.736	11 592.747	+0.011
Q_{21}	6.5	e	11 597.498	11 597.496	−0.002
Q_{21}	7.5	e	11 600.990	11 600.987	−0.003
R_{22}	7.5	f	11 602.170	11 602.171	+0.001
R_{22}	8.5	f	11 602.346	11 602.363	+0.017
Q_{21}	8.5	e	11 602.795	11 602.793	−0.002
Q_{21}	9.5	e	11 602.906	11 602.922	+0.016

Chapter 14

A CRDS sputter-source experiment to study MH radicals

14.1 Introduction

Laboratory spectra of metal-hydride molecules are typically acquired at temperatures far lower than that of a cool star, and thus probe lower energy levels than those thermally populated in the stellar atmosphere. Dispersed fluorescence, and non-equilibrium sources (such as the high-enthalpy source developed recently in Rennes to study hot bands in continuous wave Cavity ring-down (cw-CRDS) spectroscopy [C45]) probe vibrationally or even electronically excited states, but rotational distributions are still rather restricted to the lower rotational levels. In this part of the thesis an approach of improving the sensitivity of the measurement is adopted in order to extract information from the high-J tail of a warm Boltzmann distribution. A cw-CRDS experiment is arranged around the hollow cathode discharge source that produces MH species at temperatures around 350 K. The long interaction path between laser light and the MH molecules in the ring-down cavity provides the sensitivity enhancement that we need to extend measurements to more highly excited rotational levels. In this chapter the approach to cw-CRDS will be described, which features improvements to the stability of the cavity in the presence of the discharge, optical fibre to make the injection of laser light into the cavity more reliable, and an active tracking scheme to keep the laser wavelength centred on a mode of the cavity. The system has been applied to NiH and NiD molecules, which are readily produced in the discharge source. Cavity-based measurement techniques have proven successful in obtaining spectra of NiH and NiD with high sensitivity, because high-reflectance mirrors produce a very long equivalent pathlength for absorption, but the cavity alignment requires very careful control.

14.2 Experiment

14.2.1 The molecular source and optical cavity

The cw-CRDS system was built around a pair of 0.8"-diameter mirrors with 99.995 % nominal reflectivity at the peak of their 615-665 nm bandpass (Los Gatos Research, Inc., now CRD Optics, Inc.). Optical rovibronic transitions in the $B^2\Delta_{5/2} - X^2\Delta_{5/2}$ (0-0) bands of NiH and NiD near 633 nm were chosen for study since they were a good match to the mirror bandpass. The aim was to design and build a functional cw-CRDS experiment in the visible to examine transitions in molecules that we can readily create in our sputtering source, as a preparation for studying molecules like FeH and CrH that are of more immediate interest to the astrophysical community, for which transitions lie in the infrared where alignment and setup will be more difficult.

The hollow-cathode sputter source has been previously described in chapter 12. It was outfitted with KF standard connections along the path through which the laser beam passes, spaced by about 15 cm, to which side-arms that allow for an overall separation L=66.6 cm between the cavity mirrors were added. The mirrors were mounted in commercial holders[1] that could make a vacuum-tight connection to the side-arms, and which permitted three-point adjustment of the mirrors for alignment. A reactant gas mixture of 10% H_2 or 5% D_2 in argon flowed at about 40 sccm through the pierced Ni cathode (aperture 1 mm) during operation, with a small part of the gas directed to the front of each mirror to protect the coatings. A primary vacuum pump limited pressures in the cell to about 1 Torr were recorded under typical operating conditions. When the anode-to-cathode potential difference was set to 250 V, currents of 50-100 mA excited the mixture of sputtered nickel, hydrogen/deuterium and argon to produce a green plume that emerged through the anode loop. The cathode was positioned so that the laser beam crossed the flux of excited products about 2 cm below the anode. Two hollow tubes, concentric with the laser beam, were sometimes placed to either side of the centre of the plume to more clearly define the length l of the interaction region between the beam and the discharge products. This is important since the filling factor l/L is required to quantify the absorption of the laser light by the molecules.

14.2.2 The laser system and beam injection into the optical cavity

The single-longitudinal-mode ring-dye laser[2] was operated with Kiton Red laser dye, tuneable over the 590-650 nm range. Since it was run without any external optical reference, its frequency jitter was appreciable (45 MHz over 100 ms). The output beam of 100-200 mW was directed with folding mirrors onto a beam-splitter, and the resulting reflected 4% pick-off beam was used for frequency diagnostics via a

[1] Los Gatos, Inc/CRD Optics, Inc

[2] Spectra Physics SP380

wavemeter, Fabry-Perot interferometer, and iodine cell. The transmitted primary beam was run through an optical isolator to prevent feedback into the laser from reflections from the CRDS cavity mirrors, and suitably attenuated so that 10-15 mW were available to inject into a single-mode optical fibre with a transmission of $> 50\%$. The fibre[1] minimizes the influence of day-to-day changes in the laser beam direction since its output is firmly mounted to the optical table; once proper injection into the fibre is achieved the output beam path remains constant. The beam exiting the fibre is directed into an acousto-optic modulator[2] (AOM), which produces diffracted spots at orders $m = 0, \pm 1$ when activated. The $m = +1$ beam then passes through mode-matching optics designed to excite only the TEM00 mode of the optical cavity, and into the high-finesse cavity itself. A Si-avalanche photodetector (APD) converts the photons leaking out of the cavity into a low-voltage signal (< 1 V from a typical 2 mW beam injected into the cavity). Deactivation of the AOM cuts off the beam over a time of 200 µs to initiate a ring-down event. The experimental arrangement is illustrated in Figure 14.1.

14.3 Data acquisition

Spectra were recorded on a personal computer running a Labview program that controlled three instruments: a lock-in amplifier[3] (via a USB2 – GPIB interface), a wavemeter[4] (via an RS232 communications port) and a 12-bit analog sampling card[5] mounted into a peripheral slot in the computer. The 16-bit D/A output port of the lock-in provided a control voltage that adjusted the laser galvoplates to scan the laser beam frequency. The scan steps applied to the galvoplates were set to approximately match the free spectral range (FSR) of the cavity (225 MHz). A 200 Hz modulation signal was added to the laser control voltage, with its amplitude adjusted to keep the modulation depth within the cavity FSR. A suitable tracking strategy (detailed in the following paragraph) controlled the voltage of the scan step, and guaranteed that the ring-down event always happened at the centre of the laser frequency modulation. Once a scan step was set, two beam frequency diagnostics were recorded through the 16-bit A/D converters on the lock-in: fringes from a Fabry-Pérot etalon (read on photodiode PD1) and fluorescence from an iodine cell (PD2). Additionally, the wavemeter reading was recorded, but only for every third step, since obtaining the reading takes some time, and makes the data collection cycle unacceptably slow if taken at every step.

When the laser beam frequency became resonant with the cavity, the build up of power inside led to readily measurable leakage of light through the back mirror. This light was measured on the APD, and the voltage signal from it was used to trigger

[1] Thorlabs SM600
[2] OptoElectronic MT200/A0.5-ir
[3] SR830 Stanford Research System
[4] Coherent Wavemaster
[5] PCI 9812-20 MHz

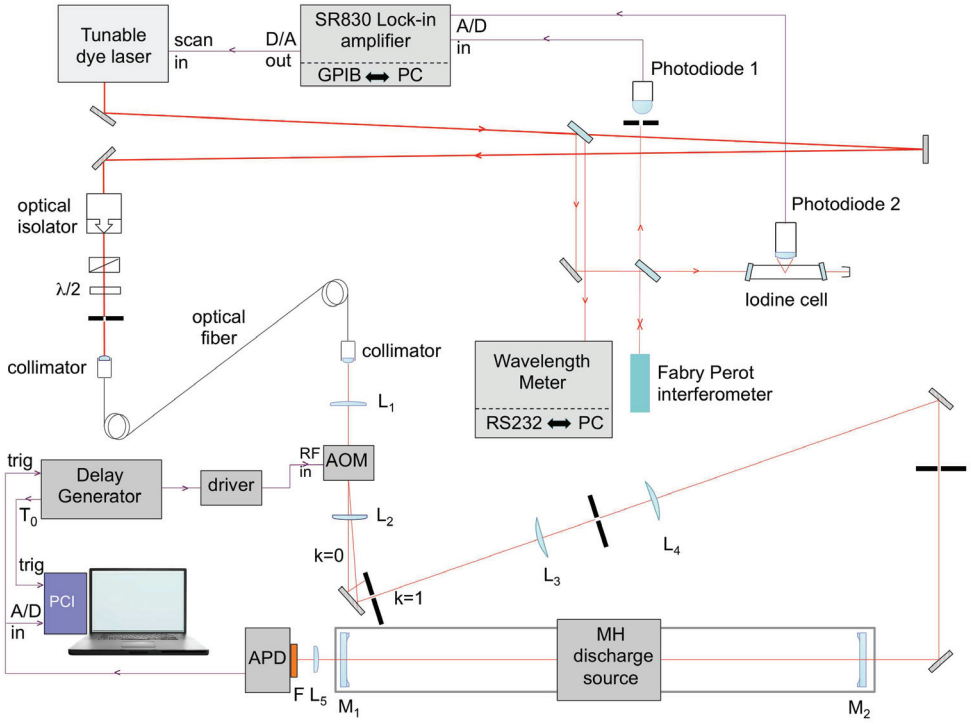

Figure 14.1 Outline of the CRDS experimental setup (tracking circuit not included). Dye laser : Spectra Physics SP380; single mode fiber : Thorlabs SM600 ; Focusing lenses : L_1, f=250 mm, L_2 f=200 mm, L_5 f=20 mm; Mode-matching lenses L_3, L_4 (f_3=200 mm, f_4=60 mm) ; Cavity mirrors M_1, M_2 : reflectivity =99.995% near 633 nm, R=6 m, ϕ=20.3 mm, ϵ=1/4"; AOM : acousto-optic modulator OptoElectronic MT200/A0.5-ir); Wavelength Meter : Wavemaster from Coherent Inc.; Fabry Perot : 1 GHz glass etalon ; Delay Generator : delay/pulse generator SRS DG535; PCI : fast acquisition board (PCI 9812) ; APD : silicon avalanche photodetector (Hamamatsu C5460) ; F : λ<650 nm low-pass filter.

a digital delay generator[1] once the increasing voltage crossed a pre-set level. The generator then sent a TTL signal to the AOM to switch off the $m = +1$ diffracted beam. The switching signal's duration was 200 μs, about 5 times the ring-down time τ_0 of the empty cavity. After a pause of 100 ns to ensure that the beam-switching event (estimated to be 12 ns) had finished, the ring-down decay curve was measured with the analogue sampling card for the remainder of the 200 μs window. Figure 14.2 schematically illustrates the laser-control scheme.

A Labview subroutine performed real-time exponential decay fits to extract the ring-down time. A typical decay trace is shown in Figure 14.2, together with the fitted curve whose flat residual verifies the single-mode excitation of the cavity. The Labview acquisition program allowed a chosen number N of ring-down times τ to be averaged (usually N=50) at each wavelength step. Although we achieved mode-matching to the TEM00 mode at a few-percent level, some non-TEM00 modes still coupled into

[1]SR535

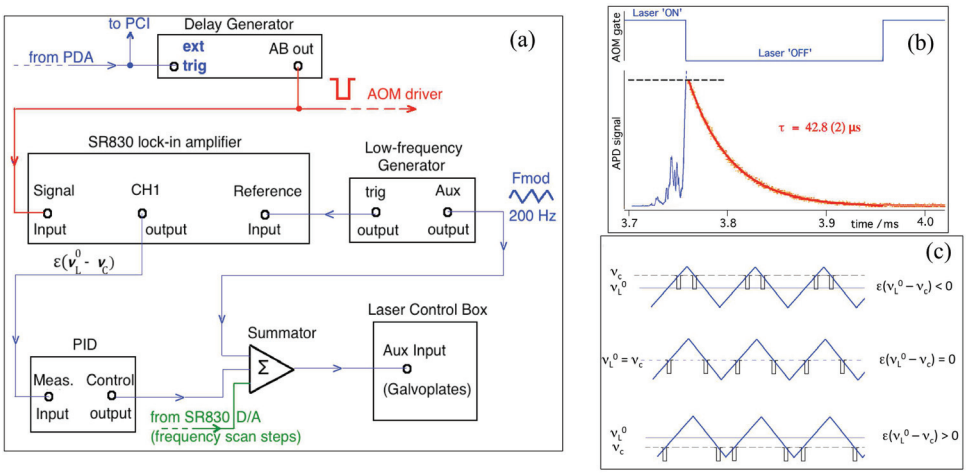

Figure 14.2 Laser frequency control schematics for the CRDS experiment. 2a : Laser frequency modulation and tracking servo-loop. 2b : signal detected from avalanche photodiode APD. Build-up (blue trace) is followed by decay (red trace), measured only when the AOM has blocked the input laser. 2c : series of TTL pulses and error signal ϵ generated by laser modulation, in the cases where the laser modulation centre ν_L^0 is a little lower (upper trace), matching, or a little higher (lower trace) than a chosen cavity mode ν_c.

the optical cavity, and contributed to the total signal. This was unavoidable, due to the low threshold value set on the digital delay generator (required to obtain ring-down events in case of relatively strong absorption), and due to the frequency noise inherent in our laser (which can sometimes produce large signals, even if the spatial coupling is low for transverse modes [C46]). It was possible to manage this situation by rejecting some ring-down events with software. During acquisition of ring-down values at a given laser wavelength, any ring-down time $\tau(n)$ that lay outside the range $[0.9\tau(n-1),\ 1.1\tau(n-1)]$, was rejected. When N acceptable ring-down times had been averaged, the wavelength step was incremented, and the process was repeated until the entire spectrum was accumulated.

14.3.1 Laser tracking

To keep the laser frequency's modulation range centred on a mode of the CRDS cavity, an active tracking strategy had to be devised to compensate for slow drifts of the cavity length and laser frequency, and to account for the nonlinearity of the galvoplates' response. To this end, the lock-in amplifier was employed to provide an error signal that drove a PID circuit. The lock-in was referenced to the 200-Hz laser modulation frequency, and detected the TTL signal that activated the AOM on/off switch. If the laser modulation range was centred on a cavity mode (see the middle graph of Figure 14.2(c), then two AOM events evenly spaced in time occurred per modulation cycle, and the fundamental Fourier component of the AOM signal occurred at 400 Hz, so no 200 Hz component was detected, resulting in a zero

error signal. As the modulation centre frequency drifted away from the cavity mode, corresponding to the situation shown in the top and bottom graphs of Figure 14.2(c), a fundamental Fourier component occurred at 200 Hz, and became stronger as the frequency at the ends of the modulation excursions drifted toward that of a cavity mode. The lock-in passed this signal, which was provided to the PID loop to effect the frequency control. With a wavelength modulation frequency $f_0 = 200$ Hz and a square-pulse relative duration $f_0\Delta t = 0.04$, a lock-in time constant of 300 ms was sufficient to maintain symmetric modulation of the laser frequency around the closest cavity mode until the required number of measurements had been averaged. This tracking minimized the acquisition time, so that 20 GHz were scanned in 78 s.

14.3.2 Laser frequency calibration and extraction of the absorption spectrum

Frequency calibration was performed in a 2-step process, using graphical procedures written in the Igor Pro (Wavemetrics Inc.) programming environment. In the first step, the etalon trace was plotted as a function of point number x in the scan, and was fit to the equation:

$$y(x) = y_0 + A\cos(2\pi(x - x_0)/T) \tag{14.1}$$

to extract the etalon's y-offset (y_0), amplitude (A), period T in points, and an offset (x_0) between a peak in the etalon trace and first point in the scan. The position of the peaks of the etalon trace could now be determined in points, by taking the first and second derivatives of equation 14.1 with respect to x, and finding the x values at which the first derivative was zero, and the second negative for the set of parameters determined by the fit. The peak positions were then used to convert the laser-frequency axis from points to fringe numbers of the etalon. In the second step, the iodine trace, plotted as a function of fringe number, was fit directly to the iodine FT spectrum given in a reference atlas [C47], effectively 'morphing' the frequency scale to best match the position, amplitude and width of the iodine trace to the reference spectrum. This second fit provided a conversion from fringe number to wavenumber to complete the calibration. Ideally, each feature of the unknown spectrum would lie between well-defined I_2 transitions. The calibrated I_2 transitions were compared visually to the atlas to check the calibration; generally, differences were $< 5.10^{-3}$ cm^{-1}.

Finally, absorption spectra $\alpha(\nu)$ can be deduced for the species of interest (NiH or NiD), using the relationship:

$$\frac{1}{c\tau} = \frac{1}{c\tau_0} + \alpha(\nu)\frac{l}{L} \tag{14.2}$$

where $1/\tau_0$ represents the baseline (no absorber inside the cavity) and l/L is the filling factor of the gas sample relative to the cavity length L. Eq. 14.2 is an approximation

that implicitly assumes the radical number density to be invariant across our discharge source. This is not the case, but we cannot quantify the spatial distribution of MH formed in the experiment. Visually, laser-induced fluorescence appears homogeneous over ≤ 2 cm, and then drops gradually. Note we also use ν rather than the wavenumber in the equations describing linestrengths and cross-sections (SI units), following [C48].

14.3.3 Performance

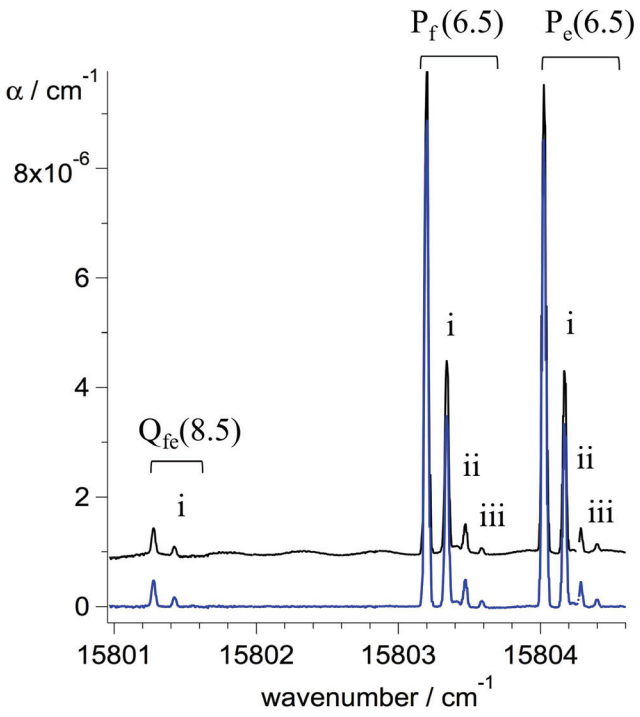

Figure 14.3 Effect of baseline removal around the P(6.5) NiH B–X (0-0) lines, recorded as a concatenation of 6 CRDS scans. The black spectrum shows the raw $1/c\tau$ signal. The lower (blue) trace shows the spectrum after software removal of the baseline, corresponding to $\alpha(\nu(l/L) = 1/c\tau - 1/c\tau_0$. Recording conditions: discharge current 100 mA, gas flow rate [10% H2 in Ar]=45 sccm, pressure=0.8 Torr; laser power=1.4 mW (cavity input). Each of the 100 points of a laser scan is recorded by averaging 50 filtered ring-down events τ_0 (see the text).

The NiH and NiD $B^2\Delta_{5/2}$ – $X^2\Delta_{5/2}$ (0-0) bands match the range of the cavity supermirrors. The transitions are already known [C49, C30], so the laser was actually scanned only in the regions where transitions were expected, rather than across the full range of the mirrors. Figure 3 shows the cavity ring-down spectrum around the ^{58}NiH B-X (0-0) P(6.5) lines. The upper trace shows oscillation in the baseline, originating in etalon effects. The baseline oscillation FSR (0.52 cm^{-1}) is compatible with the 1/4”

glass substrates of our high reflectance cavity mirrors (not wedged, but with a large (6 m) radius of curvature). The lower trace shows the spectrum after applying the sine-wave baseline removal routine provided in the Igor Pro package. The Doppler-limited resolution is significantly better than the spectrometer used in the intracavity laser absorption work of ref. [C30], so that the narrow peaks from the even-mass isotopes of Ni are now completely resolved. The sensitivity is just sufficient to discern a very weak contribution from hyperfine-broadened ^{61}NiH, with 1.1 % natural abundance. Quantitatively, the noise level of this spectrum sets a threshold for detection for our system at $\alpha_{min} = 7 \times 10^{-7}$ cm^{-1}, using the small-signal limit of expression 14.2:

$$\alpha_{min} = \frac{\delta\tau_{noise}}{\tau_0^2}.$$

This takes into account the filling factor of 0.015 for our cavity, when the laser-shield tubes are set so that NiH radicals are probed in just 1 cm of the discharge plume, which is a small fraction of the 66.6 cm optical cavity length. The effective pathlength for absorption is of the order of 200 m.

14.3.4 Scan reproducibility

Figure 14.4 illustrates another critical feature of our CRDS spectra: scan reproducibility. The measured absorption coefficients $\alpha(\nu)$ ought be invariant for given discharge conditions. Some are easy to control (gas flow rate, discharge current, pressure defining sample length, for example) but others, influencing the production of MH radicals, are not (sputtering rate, cathode channel diameter). Figure 14.4, comparing successive scans of the same region, indicates that in the short term, uneven sputtering seems not to degrade the reproducibility of the spectra. But Figure 14.5, which is a composite of spectra recorded over several days, tells a different story. $\alpha(\nu)$ values for the P(6.5) and P(7.5) lines are clearly lower than one would expect for a Boltzmann population distribution, so intensities of transitions recorded over a longer timespan should be used with caution.

14.3.5 Gas sample concentration

So far, we have been concerned with relative intensity distributions, which are the product of linestrength and concentration $N_{J''}$, assuming the validity of Beer's law. The concentration $N_{J''}$ of radicals in the level J'' is deduced from the absorption coefficient measurement $\alpha(\nu)$ at resonance (obtained from ring-down time measurements via eq. 14.2 by applying:

$$\alpha(\nu_0) = N_{J''}\sigma_{12}(\nu_0) \tag{14.3}$$

where $\sigma_{12}(\nu_0)$ is the absorption cross-section for the current rotational line. Stimulated emission is neglected. Following [C31], the absorption cross-section profile is expressed as

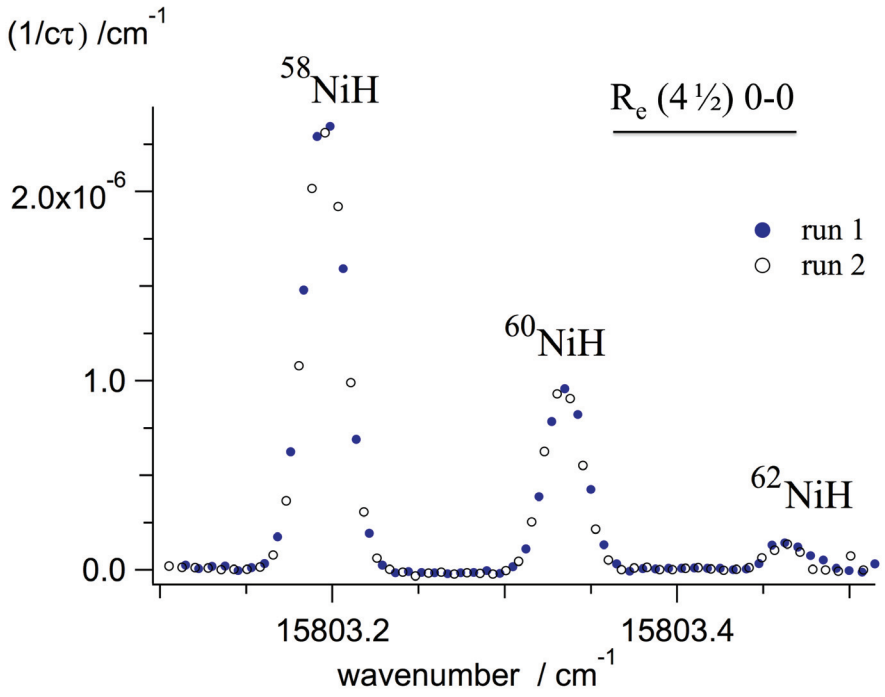

Figure 14.4 Successive scans (filled and open circles) of the NiH B - X (0-0) $R_e(4.5)$ lines indicate the short-term reproducibility of the experiment in peak intensity. Each scan took 102 seconds, probing 10 mm of the plasma flux. Note that successive scans do not always give such a good match in frequency calibration; shifts up to 0.006 cm^{-1} are not uncommon.

$$\sigma_{12}(\nu) = \frac{\lambda^2}{8\pi\tau_{sp}} \frac{2J'+1}{2J''+1} g_D(\nu - \nu_0)$$

.

The radiative lifetime τ_{sp} for the excited state has been measured for several rotational levels of $v = 0$ in the $B^2\Delta_{5/2}$ state of NiH [C48], giving $\tau_{sp} \approx 1\mu s$. The normalized Doppler-profile maximum $g_D(0)$ is given by $g_D(0) = \frac{2}{\Delta\nu_D}\sqrt{\ln 2/\pi}$. The measured full-width-half-maximum width of our absorption peaks is $\Delta\nu_D = 0.839$ GHz, yielding $\sigma_{12}(\nu_0) = 1.53 \times 10^{-13}$ cm^2. Using the ^{58}NiH $P_f(6.5)$ line shown in Figure 14.3, recorded with a filling factor of 0.015, the measured ring-down time gives $\alpha(\nu_0) \times l/L = 2.06 \times 10^{-6}$ cm^{-1}, from which we extract $\alpha(\nu_0) = 1.37 \times 10^{-4}$ cm^{-1}, and $N_{J''} = \alpha(\nu_0)/\sigma_{12}(\nu_0) = 9 \times 10^8$. The total concentration N of the sample can also be estimated using partition functions,

$$N(J'') = N(2J''+1)\frac{\exp(-E_{J''}/k_BT)}{q(T)}.$$

With a rotational temperature T around 360 K (deduced from Doppler profiles), and rotational constant $B_{v''=0} = 7.9$ cm^{-1} [C50], the partition function $q(T)$ is given

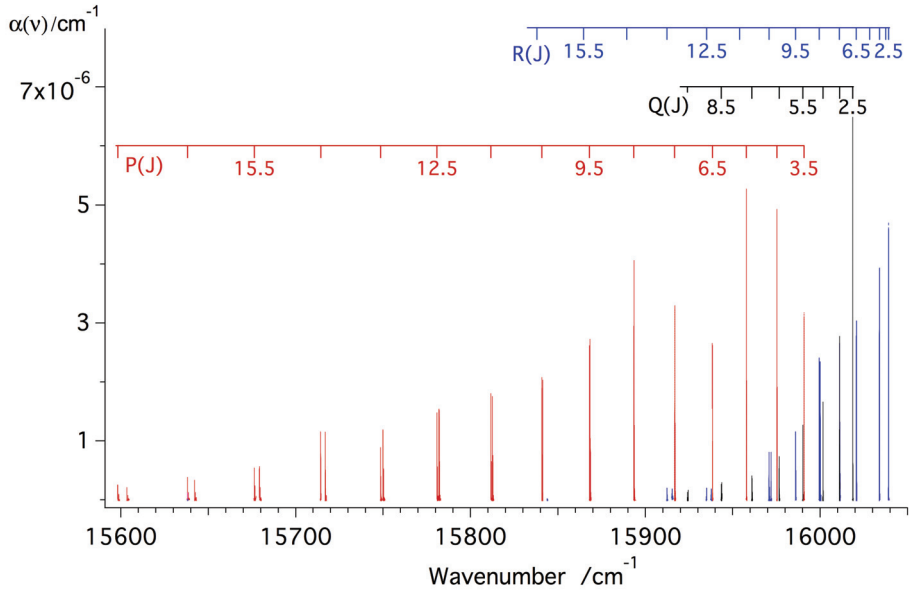

Figure 14.5 CRDS survey of the B-X (0-0) band of NiD. P, Q and R branches (drawn respectively in red, black and blue). The observed Λ-doubling is dominated by parity splittings in the excited state.

by

$$q(T) \approx \frac{k_B T}{B_{v''=0}},$$

assuming that only the $v'' = 0$ level of the ground state is populated. This gives $N \approx 9.8 \times 10^9\, cm^{-3}$.

The present discharge source was designed for LIF experiments, and one possible improvement in the context of CRDS would be to incorporate a long-discharge setup, to enhance the filling factor. This approach was successful in a White cell arrangement, reported in reference [C32]. We built a similar source for CRDS work, but it gave disappointing results. In this setup, the discharge emission (whose spectrum spreads beyond the wavelength range of the cavity mirrors) saturates the very sensitive APD detector, even when appropriate optical filtering is attempted. Carefully planned detection optics might reduce the contribution from the plasma, and could then take advantage of the absorption length. Indeed, even if the sputter source produces ten times more molecules per cm^3 than the coaxial discharge source, the absorption length of the latter increases by a factor of about 15, with additional benefit of a better definition of the sample length.

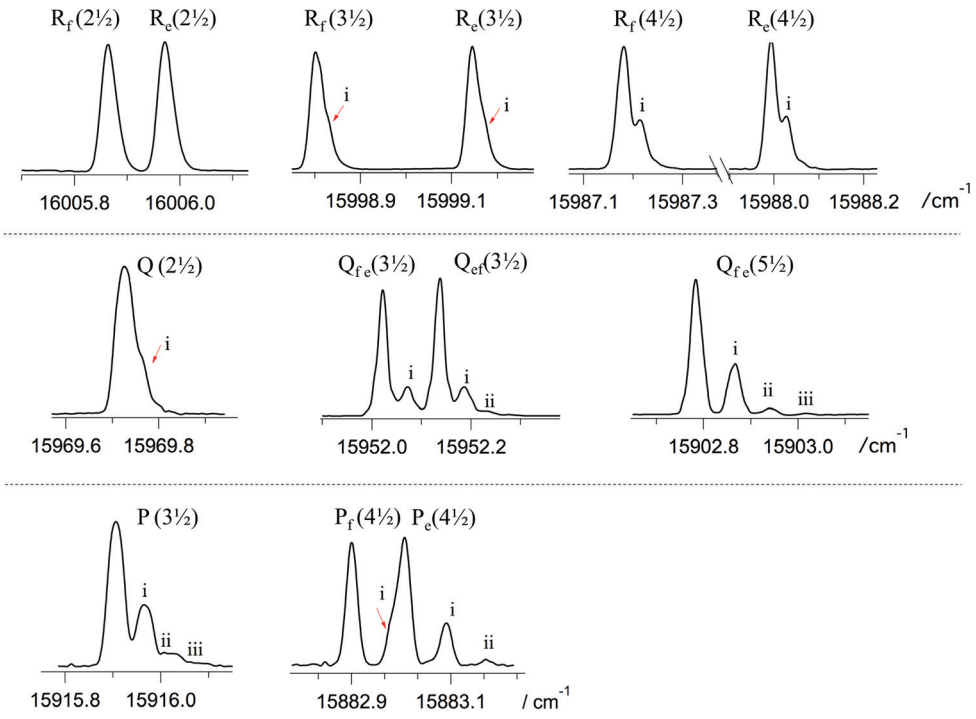

Figure 14.6 Isotope- and parity-splittings in the first lines of NiH B - X (0-0) band. Symbols i, ii, iii indicate contributions from ^{60}NiH, ^{62}NiH and ^{64}NiH.

14.4 Spectroscopic Results

This work allows us to compare spectra of NiH and NiD measured in a sputtering source with cw-CRDS with results from other techniques (absorption in a vacuum furnace, intracavity laser-absorption spectroscopy (ICLAS), laser induced fluorescence). In comparison to the ICLAS results from [C30], for which resolution is limited by the use of a grating spectrometer, the cw-CRDS spectra show improved resolution; Doppler-limited FWHM linewidths at 360 K are 0.028 cm^{-1}in the cw-CRDS spectra. Figure 14.6 demonstrates that the CRDS spectra resolve parity and/or isotope splittings except for the transitions of lowest J'', namely Q(2.5), P(3.5) and R(3.5). This performance matches that of the Fourier-transform dispersed-fluorescence (DF) experiment reported in ref. [C31]. However, the DF technique required separate experiments to excite selectively the different NiH isotopomers, and the overall sensitivity of the measurements was lower. The spectrum of ^{62}NiH, clearly observed in the cw-CRDS scans, could be just barely recorded this way; ^{64}NiH was not observed at all.

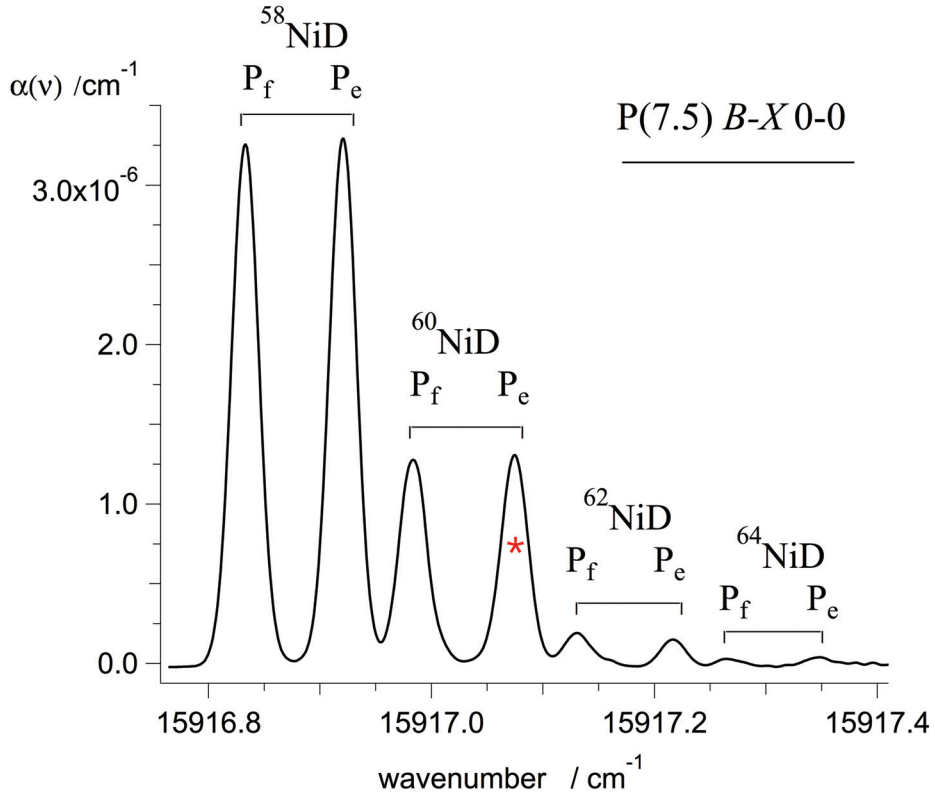

Figure 14.7 CRDS scan of the NiD B-X (0-0) P(7.5) line, where isotope and parity splittings are now completely resolved (see Table 1). The measured P_e, P_f (7.5) wavenumbers are 15917.076, 15916.984 cm^{-1} for ^{60}NiD and 15917.217, 15917.131 cm^{-1} for ^{62}NiD.

14.4.1 NiD

The CRDS measurements are shown as a composite spectrum in Figure 14.5, and listed in Table 14.1. The results led to some new assignments for this red band of NiD. Our calibration against the I2 atlas resulted in differences (reaching $\sim$ 0.1 cm^{-1} for some lines) with respect to the earlier work from Stockhlom [C49]. Some reassignments were possible because the NiD isotopomer structure is better resolved. Figure 14.7 shows the P(7.5) line on an expanded scale; in Ref. [C49], the line at 15917.074 cm-1 P_5(7.5), marked with an asterisk in Figure 14.7 and now obviously ^{60}NiD, had been assigned as P_e(7.5) of ^{58}NiD. Table 14.1 gives the list of assigned lines for ^{58}NiD, indicating the difference between this work and King furnace absorption where possible. The high-temperature work still gives the most extensive coverage of rotational levels.

Table 14.1 Observed transition wavenumbers (cm^{-1}) in the ^{58}NiD B-X (0-0) band. Entries quoted with three decimals are CRDS measurements (this work), those with only two decimals are taken from Ref. [C49]. e/f parity assignments assume that as in NiH, the ground state R(J)-P(J) combination differences are greater for f parity than for e. R_f lines were labelled R_d in ref. [C49], Q_{ef} were labelled Q_c.

J''	R_e	R_f	Q_{fe}	Q_{ef}	P_e	P_f
2.5	16039.108	16039.109	16018.668	16018.668		
3.5	16037.52	16037.52	16011.171	16011.171	15990.737	15990.737
4.5	16033.942	16033.942	16001.640	16001.640	15975.280	15975.280
5.5	16028.40	16028.25	15990.075	15990.110	15957.803	15957.803
6.5	16020.83	16020.645	15976.514	15976.603	15938.339	15938.299
7.5	16011.373	16011.048	15960.977	15961.156	15916.922	15916.834
8.5	16000.033	15999.493	15943.479	15943.813	15893.598	15893.414
9.5	15986.85	15986.017	15924.02	15924.59	15868.394	15868.065
10.5	15971.897	15970.706			15841.367	15840.822
11.5	15955.28	15953.86			15812.555	15811.724
12.5	15937.708	15935.055			15782.049	15780.840
13.5	15915.374	15912.394			15749.986	15748.566
14.5	15893.48	15889.42			15716.979	15714.325
15.5	15869.82	15864.62			15679.316	15676.339
16.5	15844.01	15837.96			15642.250	15638.193
17.5	15817.80	15809.37			15603.478	15598.252
18.8	15789.31	15778.72			15562.65	15556.59
19.5	15759.43	15746.60			15521.56	15513.05
20.5	15728.44	15712.81			15478.24	15467.60
21.5	15897.51	15677.13			15433.67	15420.82
22.5		15639.75			15388.09	15372.41
23.5		15600.82			15342.76	
24.5		15559.10				

14.4.2 Zeeman spectra of NiH and NiD

The potential for this setup to record Zeeman splittings was investigated, by inserting the permanent magnetic circuit (described in section 12.1), producing a local homogeneous field in the zone where the molecular plume crossed the laser beam inside the source chamber. The polarisation of the laser beam entering the cavity was not controlled (as an ordinary single-mode fiber was used that did not maintain beam polarization), so both σ and π polarizations of the radiation electric field were available to excite the molecules.

Figures 14.8 and 14.9 show the magnetic responses of the first rotational lines of NiH and NiD. The electronic Landé factors for the two species are clearly very different.

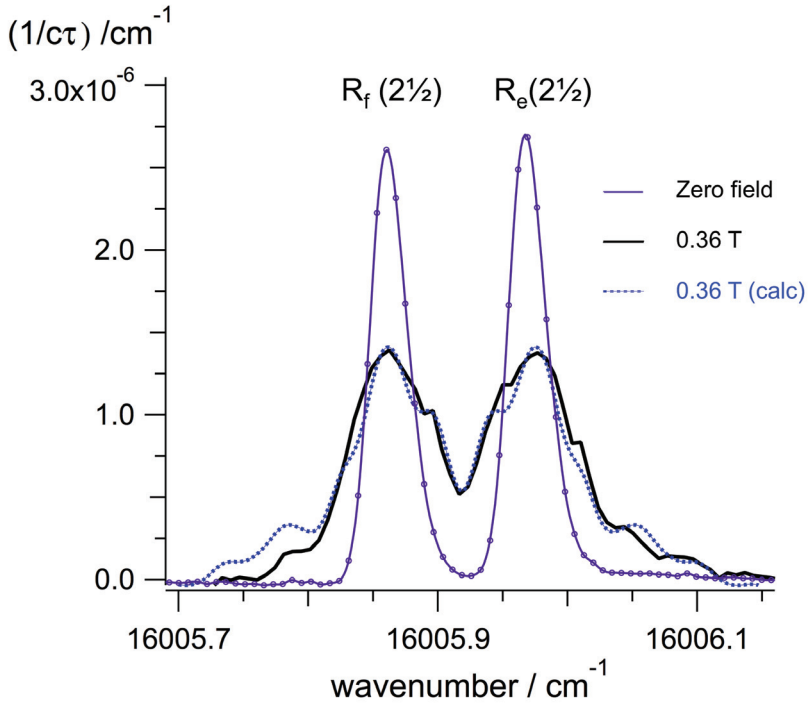

Figure 14.8 Comparison of zero-field and Zeeman spectrum on the NiH B–X (0-0) R(2.5) lines, recorded in zero-field conditions (thin solid line) and with B=0.36 Tesla (thick solid line). The broken line indicates a simulation of the Zeeman spectrum.

14.5 Conclusions

It was shown that the production of molecular metal hydride radicals by cathode sputtering is compatible with the use of CRDS super-mirrors and that quantitative spectroscopic data can be obtained from such a setup with a good signal/noise ratio. The wavelength range available naturally depends on the laser optics and cavity

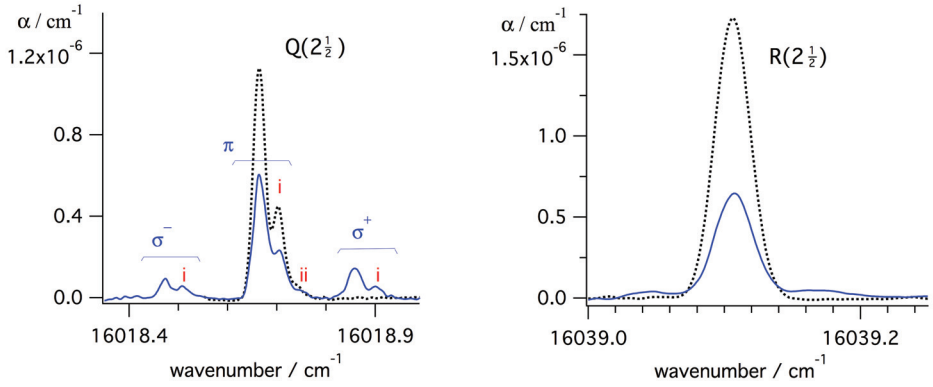

Figure 14.9 Comparison of zero-field and Zeeman (for B=0.47 Tesla) spectra of B–X (0-0) Q(2.5) and R(2.5) lines in NiD. Symbols i, ii, indicate contributions from ^{60}NiD and ^{62}NiD.

mirrors, but the heart of the cw-CRDS system (fiber, AOM, lenses, mirrors, detection chain) will remain the same.

The obvious weakness with the sputter source is that metal is removed less efficiently as the cathode progressively wears away. This means that the production of molecules will slowly decrease in time, as will the measured absorption coefficients, so that relative intensities derived over a few hours' continuous operation, in contrast with results from multiplex techniques, will NOT be consistent. There is therefore room for any improvement that can decrease the time required to make the measurements!

One option is to improve the filling-factor, by building a multi-head cathode aligned to the laser axis. Strategies to reduce recording time by reducing noise (and thus the number of ring-down events to be averaged) are also possible. Laser jitter would be reduced one-hundredfold if the laser were locked with a standard side-fringe locking system on a low-finesse reference cavity, and this would allow better control of the laser frequency, improving also calibration. If the cavity were modulated along its axis with a fast piezoelectric transducer, higher scan rates could be used for data acquisition (the current limitation is by the first resonance frequency of the laser galvoplates in the SpectraPhysics 380 dye laser : 250 Hz). This would also greatly improve the spectral resolution, which will be then limited by the laser linewidth.

The most promising approach to broadband intracavity measurements (covering $>$ 1000 cm^{-1}) involves coupling a femtosecond comb to a high finesse cavity. Recent work in Lyon [C51] has shown that Vernier coupling allows weak absorption features falling around the peak of a Ti:Sa fs laser gain curve to be recorded at Doppler resolution with recording times of the order of 1 second, fast enough that sputtering rate variation will not be a problem. The CRD spectra of NiH and NiD presented here prove that the sputtering discharge environment is compatible with supermirrors and high finesse cavity stability, so now frequency-comb intracavity absorption experiments are planned, using supermirrors optimised for the near IR and the sputter source, to investigate Zeeman patterns in other MH species.

References for Part III

[C1] N. Afram et al. "The FeH $F\,^4\Delta$ – $X\,^4\Delta$ system". *Astron. Astrophys.* 482.2 (2008), pp. 387–395.

[C2] L. Wallace et al. *An atlas of the sunspot umbral spectrum in the red and infrared from 8900 to 15 050 cm*$^{-}$1 *(6642 to 11 230 Å).* N.S.O. Technical Report 98-002. National Solar Observatory, 1998. URL: `ftp://nsokp.nso.edu/pub/atlas/spot3a`

[C3] M. Dulick et al. "Line Intensities and Molecular Opacities of the FeH $F\,^4\Delta$–$X\,^4\Delta$ Transition". *The Astrophysical Journal* 594.1 (2003), p. 651.

[C4] H. L. Nordh, B. Lindgren, and R. F. Wing. "A proposed identification of FeH in the spectra of M dwarfs and S stars". *Astron. Astrophys.* 56.1-2 (1977), pp. 1–6.

[C5] Jeremy J. Harrison and John M. Brown. "Measurement of the Magnetic Properties of FeH in Its $X\,^4\Delta$ and $F\,^4\Delta$ States from Sunspot Spectra". *The Astrophysical Journal* 686.2 (2008), p. 1426.

[C6] P. Crozet et al. "Laboratory determination of Landé factors for the molecular radical FeH". *EAS Publ. Ser.* 58.2012 (2013), pp. 63–67.

[C7] Y. Lyubchik et al. "Spectral analysis of high resolution near-infrared spectra of ultra cool dwarfs". *Astron. Astrophys.* 473.1 (2007), pp. 257–264.

[C8] J. A. Valenti and C. M. Johns-Krull. "Spectral analysis of high resolution near-infrared spectra of ultra cool dwarfs". *Proceedings of the 13th Cambridge Workshop on Cool Stars, Stellar Systems and the Sun* 560.1 (2005), pp. 261–270.

[C9] A. Reiners and G. Basri. "The First Direct Measurements of Surface Magnetic Fields on Very Low Mass Stars". *Astrophys. J.* 656 (2007), pp. 1121–1135.

[C10] P. Crozet et al. "Determination of Landé factors in the $F\,^4\Delta_{5/2,7/2}$ state of ^{56}FeH by laser excitation spectroscopy". *J. Mol. Spectrosc.* 303 (2014), pp. 46–53.

[C11] Nathan J. Deyonker and Wesley D. Allen. “Taming the low-lying electronic states of FeH”. *J. Chem. Phys.* 137.23 (2012).

[C12] J. J. Harrison et al. “The Zeeman effect on lines in the (1,0) band of the F $^4\Delta$ - X $^4\Delta$ transition of the FeH radical”. *Astrophys. J.* 679.1, Pt. 1 (2008), pp. 854–861.

[C13] Stuart P. Beaton et al. “Detection of the free radicals FeH, CoH, and NiH by far infrared laser magnetic resonance”. *J. Chem. Phys.* 89.7 (1988), p. 4446.

[C14] J. M. Brown et al. “The rotational and fine-structure spectrum of FeH, studied by far-infrared laser magnetic resonance”. *J. Chem. Phys.* 124.23 (2006).

[C15] R. T. Carter, T. C. Steimle, and John M. Brown. “The identification of a $^6\Phi$–X $^4\Delta$ intercombination system in the FeH radical at 448 nm”. *J. Chem. Phys.* 99.5 (1993), p. 3166.

[C16] D. A. Fletcher et al. “The green system of FeH recorded at ambient temperatures”. *J. Chem. Phys.* 93.12 (1990), p. 9192.

[C17] R. Vallon et al. “Room-temperature metal-hydride discharge source, with observations on NiH and FeH”. *J. Phys. Chem. A* 113.47 (2009), pp. 13159–13166.

[C18] J. G. Phillips et al. “The near-infrared spectrum of the FeH molecule”. *Astrophys. J. Suppl. Ser.* 65 (1987), p. 721.

[C19] I. Rüedi et al. “Interesting lines in the infrared solar spectrum. III. A polarimetric survey between 1.05 and 2.50 µm”. *Astron. Astrophys. Suppl. Ser.* 113 (1995), pp. 91–106.

[C20] D. Shulyak et al. “Modelling the molecular Zeeman-effect in M-dwarfs: methods and first results”. *Astron. Astrophys.* 523 (2010), A37.

[C21] R. Vallon et al. “Laboratory measurements of NiH by Fourier transform dispersed fluorescence”. *Astrophys. J.* 696.1 (2009), pp. 172–175.

[C22] I. Bozhinova et al. “Discharge tube with coaxial geometry for efficient production of metal hydrides”. *Review of Scientific Instruments* 84.9 (2013), p. 093107.

[C23] Helene Lefebvre-Brion and Robert W. Field. *The Spectra and Dynamics of Diatomic Molecules*. 2nd. Academic Pr, 2004.

[C24] Peter F. Bernath. *Spectra of Atoms and Molecules*. 2nd ed. Oxford University Press, 2005.

[C25] A. Hansson and J. K. G. Watson. “A comment on Hönl-London factors”. *J. Mol. Spectrosc.* 233 (2005), pp. 169–173.

[C26] W. Demtroder. *Laser Spectroscopy: Basic Concepts and Instrumentation*. 2nd. Springer-Verlag, 1996. ISBN: 9780387571713.

[C27] W. Zou and W. Liu. "Theoretical study on the low-lying electronic states of NiH and NiAt". *Journal of Computational Chemistry* 28.14 (2007), pp. 2286–2298.

[C28] H. Wöhl. "On molecules in sunspots". *Sol. Phys.* 16.2 (1974), pp. 362–372.

[C29] D. L. Lambert and E. A. Mallia. "Identification of NiH in the Sunspot Spectrum". *Mon. Not. R. Astron. Soc.* 151.4 (1971), pp. 437–447.

[C30] Leah C. O'Brien and James J. O'Brien. "Laboratory Measurements of NiH by Intracavity Laser Absorption Spectroscopy". *Astrophys. J.* 621.1 (2005), pp. 554–556.

[C31] A. J. Ross et al. "Resolved fluorescence spectra of NiH. Electronic structure, electronic energy transfer, and the Zeeman effect in low-lying states". *Mol. Phys.* 110.17 (2012), pp. 2019–2033.

[C32] M. Li, J. A. Gray, and R. W. Field. "A multipass, magnetically confined sputter source for absorption-based spectroscopy of transient molecules: the spectrum of NiH". *Chem. Phys.* 117.1 (1987), pp. 171–176.

[C33] S. Langhoff and Ch. Bauschlicher. "Theoretical study of the spectroscopy of FeH". *Journal of Molecular Spectroscopy* 141.2 (1990), pp. 243–257.

[C34] H. Harker et al. "Zeeman spectroscopy of NiH: Landé factors of three Ω=3/2 excited electronic states". *J. Mol. Spectrosc.* 292 (2013), pp. 28–34.

[C35] R. Vallon. "Fluorescence Laser Intracavité et Spectrométrie de Fourier : Développements expérimentaux et application au radical NiH". PhD thesis. Université Lyon 1, 2007.

[C36] A. Kramida et al. NIST Atomic Spectra Database (ver. 5.3), [Online]. Available: `http://physics.nist.gov/asd` [2016, April 22]. National Institute of Standards and Technology, Gaithersburg, MD. 2015.

[C37] S. V. Berdyugina and S. K. Solanki. "The molecular Zeeman effect and diagnostics of solar and stellar magnetic fields". *Astron. Astrophys.* 385.2 (2002), pp. 701–715.

[C38] Richard N. Zare. *Angular Momentum: Understanding Spatial Aspects in Chemistry and Physics*. Wiley, 1988.

[C39] J. D. Kirkpatrick et al. "An Improved Optical Spectrum and New Model FITS of the Likely Brown Dwarf GD 165B". *ApJ* 519 (1999), pp. 834–843.

[C40] B. Viswanathan et al. "Identification of CrH and CrD molecular lines in the sunspot umbral spectrum". *Sol. Phys.* 257.2 (2009), pp. 261–269.

[C41] J. Chen et al. "The Zeeman tuning of the A $^6\Sigma^+$–X $^6\Sigma^+$ transition of chromium monohydride." *Phys. Chem. Chem. Phys.* 9.8 (2007), pp. 949–957.

[C42] A. Burrows et al. "New CrH Opacities for the Study of L and Brown Dwarf Atmospheres". *Astrophys. J.* 577.2 (2002), pp. 986–992.

[C43] R. S. Ram, C. N. Jarman, and P. F. Bernath. "Fourier Transform Emission Spectroscopy of the A $^6\Sigma^+$–X $^6\Sigma^+$ System of CrH: Evidence for a $^4\Sigma^+$ Lowest Excited State". *J. Mol. Spectrosc.* 161.2 (1993), pp. 445–454.

[C44] O. Kuzmychov and S. Berdyugina. "Paschen-Back effect in the CrH molecule and its application for magnetic field measurements on stars, brown dwarfs, and hot exoplanets". *Astron. Astrophys.* 120 (2013), pp. 1–11.

[C45] M. Louviot et al. "Strong thermal nonequilibrium in hypersonic CO and CH4 probed by CRDS". *J. Chem. Phys.* 142.21 (2015), p. 214305.

[C46] J. Morville et al. "Effects of laser phase noise on the injection of a high-finesse cavity". *Appl. Opt.* 41.33 (2002), p. 6980.

[C47] Houssam Salami and Amanda J. Ross. "A molecular iodine atlas in ascii format". *J. Mol. Spectrosc.* 233.1 (2005), pp. 157–159.

[C48] J.A. Gray. "Laser spectroscopy and a supermultiplet structure model for Nickel Hydride". PhD thesis. 1988.

[C49] S. A. Kadavathu, S. Löfgren, and R. Scullman. "Rotational Analysis of Some New Transitions in NiD. A Comparison between NiH and NiD". *Phys. Scr.* 35.3 (1987), pp. 277–285.

[C50] J. A. Gray et al. "The electronic structure of NiH: The Ni+3d 9 2D supermultiplet". *J. Chem. Phys.* 95.10 (1991), p. 7164.

[C51] Lucile Rutkowski and Jérôme Morville. "Broadband cavity-enhanced molecular spectra from Vernier filtering of a complete frequency comb". *Opt. Lett.* 39.23 (2014), p. 6664.

Appendices

Appendix A

Authors's contributions

This thesis, prepared in co-tutelle between Univeristé Lyon 1 and Sofia University St. Kliment Ohridski, focuses on experimental realization of techniques in three distinct projects. They share a common ambition to achieve strict control of the quantum state in which atoms and molecules can be prepared, with applications in various scientific areas such as quantum computing, metrology and astrophysics. My contribution to this field has been essentially design, assembly and commissioning of scientific apparatus for spectroscopy and/or metrology. But a solid background in the physics behind all the measurements is obviously necessary to properly assess the performance of my prototype arrangements for molecular and atomic sources, or for laser stabilization and control. The chapters of the thesis therefore discuss these aspects also.

My first project was to construct an atomic beam apparatus operating with calcium, and to design and produce a laser source intended to probe the atoms in the beam. The system has been successfully used to record laser-induced intercombination transitions as fluorescence from ^{40}Ca atoms. Some further optimization of laser stability is still required, and then the set-up will be used to verify a mathematical model for coherent control developed at Sofia University. This will involve coherent manipulation of small quantum systems using composite pulses to control population transfer.

The second part of the thesis describes the effect of incorporating a modified low-velocity intense source (LVIS) of slow Cs atoms in the Cs fountain clock CSF2 at the primary frequency standard CSF2 (based at the German National Metrology Institute (PTB) in Braunsweig). A modified three-dimensional magneto-optical trap is used to provide an intense beam of slow atoms, increasing the number of atoms loaded in the optical molasses of the fountain clock by a factor of 40. This has had the desired impact on the clock stability, since the CSF2 clock instability $\sigma_y(\tau)$ is now $2.7 \times 10^{-14}\tau^{-1/2}$, where τ is the averaging time. This performance is comparable with the best Cs clocks in the world today.

The third part of the thesis is devoted to high resolution spectroscopy of some first-row transition metal hydrides, in particular to the determination of magnetic

constants (Landé factors) for specific transitions of astrophysical interest, supplying reliable absorption coefficients, as well as frequency measurements for the transitions. My goal was to optimize a workable method of production for these radicals, intended to be used in continuous regime of operation, creating a homogeneous distribution of molecules over a well-defined absorption pathlength of the order of 25 cm, ideally with a long operational lifetime, and allowing work with magnetic fields up to 0.5 Tesla. The prototype instrument allowed Zeeman features to be observed in the red bands of NiH, at 0.1 Tesla by differential laser absorption, but the signal/noise ratio was insufficient to allow investigation of the weaker system of interest (FeH bands around 900 nm). Ideas for further improvement of the source are presented in the thesis. The investigation of FeH used an existing design of sputter source, where the absorption pathlength and molecular homogeneity are less well defined, but signals are significantly stronger.

More than 50 transitions in the F-X (0–0) and (1–0) band systems of FeH were measured by laser excitation in the near infrared, allowing Landé g-factors to be determined for 33 rovibronic levels of the excited state, F $^4\Delta$, to within 2% uncertainty. CrH was observed with this set-up too.

To address the question of intensities (absorption coefficients) this dc-discharge based sputter source was placed inside a high finesse cavity, and cavity ring-down spectra (yielding absorption coefficients as a function of scanned laser wavelength) of NiH and NiD were recorded. The signal/noise ratio allowed the minor isotopes of Ni to be observed; this set-up holds much promise for future work on FeH and other metal hydrides.

The results from work performed as part of this thesis have been published in three scientific Papers, and reported at 8 conferences either as oral or poster presentations.

Publications in peer-reviewed journals

[1] G. Dobrev et al. "A CRDS sputter-source experiment to study MH radicals: application to NiH and NiD". *Molecular Physics* (2016). Pre-published.

[2] G. Dobrev, V. Gerginov, and S. Weyers. "Loading a fountain clock with an enhanced low-velocity intense source of atoms". *Physical Review A.* 93 (2016), p. 043423.

[3] P. Crozet et al. "Determination of Landé factors in the F $^4\Delta_{5/2,7/2}$ state of ^{56}FeH by laser excitation spectroscopy". *J. Mol. Spectrosc.* 303 (2014), pp. 46–53.

Conferences and seminars

[1] S. Weyers et al. "Improvements of the statistical and systematic uncertainty contributions of PTB's fountain clocks". *30$^{-\text{th}}$ European Frequency and Time Forum (EFTF)*. (Jork, United Kingdom, Apr. 4, 2016–Apr. 7, 2015). presentation.

[2] V. Gerginov et al. "Improving statistical and systematic uncertainties of PTB's caesium fountain clocks". *8$^{-\text{th}}$ Symposium on Frequency Standards and Metrology*. (Potsdam, Germany, Oct. 12–16, 2015). poster.

[3] G. Dobrev et al. "High Sensitivity Laser Spectroscopies Of Metal Hydride Radicals : Laboratory Measurements For Stellar Spectroscopy". *24$^{-\text{th}}$ Colloquium on High Resolution Molecular Spectroscopy*. (Dijon, France, Aug. 24–28, 2015). poster.

[4] P. Crozet et al. "High Sensitivity Laser Spectroscopies of Metal Hydride Radicals". *Spectroscopy of exoplanets - Exomol ERC-COST network meeting*. (Cumberland Lodge, Windsor, United Kingdom, July 24–26, 2015). poster.

[5] J. Morville et al. "A new broadband cavity enhanced frequency comb spectroscopy technique using GHz Vernier filtering". *70$^{-\text{th}}$ International Symposium on Molecular Spectroscopy (ISMS)*. (Illinois, United States, June 20–24, 2015). presentation.

[6] G. Dobrev, V. Gerginov, and S. Weyers. "Improved atom loading for CSF2 – PTB primary frequency standard". *576. WE-Heraeus Seminar on Designed Quantum States of Matter*. (Bad Honnef, Germany, Dec. 1–5, 2014). poster.

[7] G. Dobrev et al. "Astrophysique de laboratoire : Spectrométrie laser du radical FeH". *Colloque PAMO-JSM*. (Reims, France, July 7–10, 2014). poster.

[8] G. Dobrev et al. "Spectropolarimetry of the FeH molecule in the near-IR". *46$^{-\text{th}}$ Conference of the European Group on Atomic Systems (EGAS)*. (Lille, France, July 1–4, 2014). poster.